

Universitat de València  
DEPARTAMENT DE FÍSICA TEÒRICA



UNIVERSITAT DE VALÈNCIA

---

**Design and Performance Evaluation of Nonlinear Collimation  
Systems for CLIC and LHC**

TESIS DOCTORAL  
Javier Resta López  
Abril de 2007



Dra. ANGELES FAUS GOLFE, Científico Titular del Consejo Superior de Investigaciones Científicas (CSIC),  
Dr. DANIEL SCHULTE, miembro del European Organization for Nuclear Research (CERN),

CERTIFICAN:

Que la presente memoria *Design and Performance Evaluation of Nonlinear Collimation Systems for CLIC and LHC* ha sido realizada bajo nuestra dirección en el Departamento de Física Teórica de la Universidad de Valencia por D. Javier Resta López y constituye su Tesis para optar al Grado de Doctor en Física.

Y para que así conste, firmamos el presente Certificado.

Fdo: Angeles Faus Golfe

Fdo: Daniel Schulte





*A la memoria de Carlos Esteban Benito (1947–2007)*



## Abstract

The beam collimation systems are an essential part of the high energy colliders. A collimation system should remove beam halo to reduce detector background and ensure the machine protection, thus minimizing the activation and damage of sensitive accelerator components.

The mechanical and optics design of collimation systems is not simple, and they should fulfill some often conflicting constraints and requirements: high cleaning efficiency, high mechanical robustness, and low wakefields (impedances). The conventional collimation systems are generally based on linear optics. Nevertheless, several alternative advanced concepts on collimation have been proposed in the literature. In this thesis report we have studied in detail nonlinear collimation systems. These are based on a general scheme with a skew sextupole pair, which can be adapted to both linear and circular colliders.

In particular we have designed a nonlinear collimation system for the Compact Linear Collider (CLIC). This system fulfills the function of machine protection against mis-steered or errant beams with energy offset higher than 1.5 % of the nominal energy 1.5 TeV. The performance of this collimation system has been evaluated by means of tracking studies, and compared with that of the conventional baseline linear collimation system. Since the collimation requirements for linear colliders designed to operate at center-of-mass energy around TeV are similar to those for the Large Hadron Collider (LHC) at collision beam energy 7 TeV, it is thus close thought to apply a similar LHC nonlinear collimation scheme as that designed for CLIC. We have explored this possibility, and have proposed an alternative nonlinear system for the Phase-II betatron cleaning in the LHC. Its performance and cleaning efficiency have further been evaluated by tracking studies. Moreover a comparison of the features of the nonlinear collimation system and the linear collimation system has been made for the LHC.



# Contents

<b>1</b>	<b>Introduction</b>	<b>1</b>
<b>2</b>	<b>Collimation for High Energy Colliders</b>	<b>5</b>
2.1	Principle of beam collimation . . . . .	5
2.1.1	Collimation in linear colliders . . . . .	6
2.1.2	Collimation in circular colliders . . . . .	10
2.2	Advanced collimation concepts . . . . .	14
2.2.1	Consumable collimators . . . . .	14
2.2.2	Repairable collimators . . . . .	15
2.2.3	Crystal collimation . . . . .	16
2.2.4	Laser collimation . . . . .	17
2.2.5	Electron lens collimation . . . . .	18
2.2.6	Nonlinear collimation . . . . .	18
<b>3</b>	<b>Important Issues in Collimation for High Energy Colliders</b>	<b>21</b>
3.1	Beam halo and tail generation . . . . .	21
3.1.1	The concepts of beam and luminosity lifetime . . . . .	22
3.1.2	Scattering with residual gas . . . . .	23
3.1.3	Scattering off thermal photons . . . . .	28
3.1.4	Intra-bunch scattering processes . . . . .	30
3.1.5	Beam-beam interaction . . . . .	32
3.2	Collimator protection . . . . .	36
3.2.1	Limit for instantaneous temperature rise of a collimator . . . . .	36
3.2.2	Collimator-beam interaction mechanisms . . . . .	37
3.3	Collimator wakefields and impedances . . . . .	50
3.3.1	The wake function . . . . .	51
3.3.2	Impedances . . . . .	53
3.3.3	Collimator wakefield effects . . . . .	53
<b>4</b>	<b>Nonlinear Collimation for TeV Colliders</b>	<b>59</b>
4.1	Introduction . . . . .	59
4.2	Scheme with skew sextupoles pair . . . . .	61
4.2.1	Spoiler protection . . . . .	63
4.2.2	Nonlinear collimation for linear colliders . . . . .	63

4.2.3	Nonlinear collimation for circular colliders . . . . .	67
<b>5</b>	<b>Alternative Nonlinear Energy Collimation System with Skew Sextupole Pair for CLIC at 1.5 TeV</b>	<b>69</b>
5.1	Introduction to the CLIC accelerator . . . . .	69
5.1.1	The CLIC BDS . . . . .	70
5.1.2	The baseline linear collimation system of CLIC . . . . .	70
5.2	Benchmarking of tracking codes in the context of the CLIC BDS . . . . .	73
5.2.1	Tracking codes . . . . .	76
5.2.2	Tracking results . . . . .	76
5.2.3	Particle per particle comparison . . . . .	78
5.2.4	Chromatic effects . . . . .	79
5.2.5	Bandwidth . . . . .	81
5.3	An alternative nonlinear energy collimation system . . . . .	83
5.3.1	Collimation depth and collimator aperture . . . . .	84
5.3.2	Optics layout solution . . . . .	89
5.3.3	Optics optimization . . . . .	90
5.4	Tracking studies . . . . .	93
5.4.1	Performance . . . . .	94
5.4.2	Cleaning efficiency . . . . .	102
5.4.3	Collimator wakefield considerations . . . . .	105
<b>6</b>	<b>Alternative Nonlinear Cleaning Betatron Insertion with Skew Sextupole Pair for the LHC at 7 TeV</b>	<b>125</b>
6.1	Introduction to the LHC accelerator . . . . .	125
6.1.1	The baseline linear collimation system of LHC Phase-I . . . . .	126
6.2	An alternative nonlinear betatron collimation system . . . . .	128
6.2.1	Optics Layout . . . . .	130
6.2.2	Collimation boundaries . . . . .	131
6.2.3	Spoiler protection . . . . .	133
6.2.4	Two-Stage Collimation . . . . .	135
6.2.5	Cleaning Efficiency . . . . .	137
6.2.6	Decreasing the LHC Impedance . . . . .	139
<b>7</b>	<b>First Experimental Test on Nonlinear Collimation in the SPS</b>	<b>149</b>
7.1	Introduction . . . . .	149
7.2	Experimental setup . . . . .	149
7.2.1	Sextupolar bumps . . . . .	151
7.2.2	The Beam Loss Monitor (BLM) data acquisition system . . . . .	151
7.2.3	Beam intensity during the test . . . . .	152
7.3	Preliminary results . . . . .	152
<b>8</b>	<b>Summary and Conclusions</b>	<b>157</b>
<b>A</b>	<b>Maps in accelerators</b>	<b>161</b>
A.1	Reference system . . . . .	161
A.2	Taylor maps . . . . .	162
A.3	Lie algebra and symplectic maps . . . . .	163
A.3.1	Examples . . . . .	165

<b>Contents</b>	iii
<b>B Material properties</b>	<b>167</b>
<b>C Horizontal beam size at the spoiler considering up to third order dispersion</b>	<b>169</b>
<b>D Baseline Phase-I Collimation Database at Collision (7 TeV)</b>	<b>173</b>
<b>E Nonlinear Collimation IR7 Database at Collision (7 TeV)</b>	<b>177</b>
<b>F Coherent coupled-bunch head-tail tune shift</b>	<b>179</b>
F.1 Burov-Lebedev theory of linear resistive-wall wake field . . . . .	179
F.2 Coherent tune shift . . . . .	180
F.3 Tilted collimator contribution . . . . .	181
F.3.1 The transverse tensor impedance . . . . .	181
F.3.2 The tensor tune shift . . . . .	182
<b>Bibliography</b>	<b>182</b>





# Resumen

## Introducción y objetivos

El estudio de la física más allá del llamado Modelo Estándar de las partículas elementales exige de aceleradores de partículas que operen a escalas de energía del TeV. Se espera que las primeras respuestas a cuestiones tales como la existencia del bosón de Higgs, el origen del sabor (de quarks y leptones) y la unificación de las interacciones fundamentales en un único grupo vengan del ‘*Large Hadron Collider*’ (LHC) [1]. Este colisionador circular, actualmente en construcción en ‘*The European Organization for Nuclear Research*’ (CERN), hará chocar protones a energía en el centro de masas de 14 TeV, con la posibilidad adicional de colisión de iones.

En la actualidad existe consenso en la comunidad de física de altas energías de que la siguiente generación de aceleradores tras el LHC ha de ser un colisionador lineal leptón-antileptón, operando en un rango de energías 0.5–5 TeV. Los colisionadores lineales  $e^+e^-$ , además de minimizar el problema de pérdidas de energía debido a radiación sincrotrón, facilitarían la detección de partículas en el punto de interacción, ya que mientras que en una colisión protón-protón existe una partición de energía entre las partículas componentes, quarks y gluones, la colisión de  $e^+e^-$  sería puntual, dando lugar a reacciones muy bien definidas en los detectores. Se puede decir que los colisionadores lineales proporcionarían un excelente complemento al LHC, permitiendo estudiar con mayor resolución los descubrimientos físicos proporcionados por el LHC. Para detalles de la física de los colisionadores lineales  $e^+e^-$  véase, por ejemplo, la referencia [3].

Para alcanzar un gran número de sucesos en el punto de interacción se necesita una alta luminosidad. La luminosidad en el LHC será del orden de  $10^{34} \text{ cm}^{-2}\text{s}^{-1}$  en los experimentos a alta luminosidad (ATLAS y CMS) [1], y en los colisionadores lineales  $\sim 10^{34}\text{--}10^{35} \text{ cm}^{-2}\text{s}^{-1}$ . Esto se consigue con haces de gran intensidad ( $\sim 10^{14}$  partículas por haz en el caso del LHC,  $\sim 10^{11}$  partículas por haz en el caso de CLIC y  $\sim 10^{13}$  partículas por haz para el ILC) y tallas transversales de los haces en el punto de interacción muy pequeñas, que en el caso de los aceleradores lineales llegarán al orden del nanómetro, lo cual supone un reto en el transporte y focalización del haz en

el punto de interacción. La calidad del haz debe ser preservada a lo largo de la línea de transporte, evitando el aumento de la emitancia y minimizando el número de partículas viajando a gran amplitud con respecto a la partícula de referencia o con una energía diferente a la energía de diseño. Estas partículas constituyen lo que se denomina el *halo del haz*, y son las responsables de una gran parte del ruido de fondo en los detectores. Por tanto, las partículas del halo deben ser eliminadas. Los llamados *sistemas de colimación* están dedicados a tal fin.

Otra función importante del sistema de colimación es la protección de los componentes del acelerador. Con energías del orden del TeV y densidades de potencia del orden de  $\text{GWmm}^{-2}$ , es evidente la necesidad de un buen sistema de protección de la máquina en caso de fallo. Haces desviados de la órbita de diseño pueden irradiar en exceso elementos de la máquina y terminar dañándolos. Por tanto, el sistema de colimación debe ser capaz de interceptar esos haces. Además, en el caso de aceleradores basados en imanes superconductores, como el LHC, pérdidas excesivas de partículas en las llamadas regiones frías (los arcos que contienen dipolos superconductores), deben ser evitadas. De lo contrario, se rompe el régimen superconductor debido a un incremento de la temperatura del imán y tendremos una transición a la fase de conducción normal.

La forma usual de realizar la colimación de los haces es a través de bloques de material que a modo de barrera interceptan el halo. Éstos son localizados en regiones concretas de la máquina, con una óptica adecuada para dirigir las partículas del halo a los colimadores.

El sistema de colimación debe cumplir una serie de requisitos:

- La óptica del sistema no debe introducir aberraciones que desestabilicen el haz y degraden, por tanto, la luminosidad.
- La elección de las aperturas de los colimadores debe garantizar una limpieza eficiente del haz, y no introducir intolerables campos estela (o impedancias), que pueden comprometer la estabilidad del haz.
- Generalmente el sistema debe ser lo suficientemente robusto como para sobrevivir al impacto directo del haz.

Los sistemas de colimación estándar están basados en ópticas lineales. Ver, por ejemplo, una descripción del sistema lineal de colimación del LHC en [8], y del sistema lineal de colimación de CLIC en [10].

Sin embargo, otros conceptos alternativos de colimación han sido estudiados en la literatura, por ejemplo podemos citar: los colimadores desechables [19], los colimadores reparables [19], la colimación con láser [28], las lentes de electrones [30], la colimación por medio de cristales [21, 24–26], y la colimación no lineal [15, 33, 37–39].

El objetivo de esta tesis es el estudio detallado de los sistemas de colimación no lineales y su aplicación a CLIC y al LHC. Se llaman sistemas de colimación no lineal aquellos que incluyen elementos magnéticos no lineales, tales como *séxtupolos* y *octupolos*, con el propósito de eliminar el halo. Más concretamente en este trabajo se describe un diseño de sistema de colimación no

lineal basado en un par de sextupolos rotados (sextupolos ‘skew’). Estos sextupolos están girados transversalmente un ángulo de  $\pi/6$  rad respecto a un sextupolo normal.

El fundamento básico de la colimación no lineal es el siguiente: un primer elemento no lineal, en nuestro esquema un sextupolo rotado, inflaría el tamaño transversal del haz en el punto de impacto con el colimador o barrera que intercepta al haz primario, permitiendo así una mayor apertura del colimador. Esto reduciría a su vez la densidad de energía del halo en el momento de impacto, con el consiguiente aumento de probabilidad de supervivencia del colimador. Un segundo sextupolo de la misma intensidad y separado del primero por una matriz de transferencia  $-I$  (siendo  $I$  la matriz identidad) cancelaría las aberraciones ópticas de tipo geométrico introducidas por el primero. Es importante subrayar que el efecto del elemento no lineal afectará exclusivamente a las partículas del halo, i.e., aquellas viajando a grandes amplitudes o desviadas de la energía de diseño, dejando intacto el núcleo del haz.

## Discusión de los resultados

Como ya hemos mencionado en la introducción, en esta tesis hemos presentado un esquema general de colimación basado en colimadores primarios situados entre un par de sextupolos rotados. Las siguientes consideraciones son tenidas en cuenta:

- Ambos sextupolos tienen la misma intensidad.
- Los sextupolos están separados por una matriz de transferencia  $-I$ . Esto es esencial para que el segundo sextupolo cancele el efecto y las aberraciones de tipo geométrico introducidas por el primero.
- El colimador se ha situado con un avance de fase (en su movimiento betatrónico) de  $\pi/2$  rad respecto al primer sextupolo. El segundo sextupolo está localizado a su vez con un avance de fase de  $\pi/2$  rad respecto al colimador.
- Es preferible que la dispersión  $D_x$  en la posición del segundo sextupolo sea igual y de signo opuesto a la del primero. De este modo, es posible cancelar las aberraciones cromáticas de primer orden.

Partiendo del Hamiltoniano del sistema (ver capítulo 4) hemos calculado analíticamente el valor cuadrático medio de la talla transversal del haz en la posición del colimador. El sistema de ecuaciones para el cálculo de las aperturas del colimador a partir de los parámetros ópticos y de las profundidades de colimación ha sido también desarrollado.

Cabe resaltar que el esquema de colimación presentado en esta tesis es bastante general, y se puede aplicar, con las modificaciones oportunas, tanto a colisionadores lineales como a circulares.

En el caso de los *colisionadores lineales* hemos asumido que la componente dispersiva en energía de la amplitud transversal domina sobre las componentes betatrónicas. En nuestros cálculos también hemos asumido haces planos, con la talla horizontal  $\sigma_x$  mucho mayor que la vertical  $\sigma_y$ . Los colisionadores lineales suelen ser diseñados con haces planos para, por un lado, alcanzar una luminosidad elevada ( $\mathcal{L} \propto 1/(\sigma_x \sigma_y)$ ) y, por otro lado, minimizar los efectos del llamado ‘beam-strahlung’ [84], cuya intensidad se comporta como  $1/(\sigma_x + \sigma_y)$ .

En el caso de los *colisionadores circulares* o anillos de almacenamiento, para nuestros cálculos hemos asumido que la parte betatrónica de la amplitud transversal domina sobre la parte dispersiva y, por tanto, aplicaremos la colimación no lineal para la limpieza del halo en los planos betatrónicos.

### Un sistema de colimación no lineal para CLIC

Teniendo en cuenta las restricciones y requisitos para el sistema óptico impuestas en el capítulo 4, en el capítulo 5 mostramos diferentes soluciones ópticas para un sistema no lineal de colimación en energía para CLIC. Estos sistemas ópticos se diferencian esencialmente en su longitud y la intensidad (y longitud) de los imanes dipolares que crean la dispersión. El ajuste de la óptica ha sido realizado por medio de un programa informático de diseño de aceleradores llamado MAD [114].

Las características y eficiencia de tales sistemas han sido estudiadas por medio de simulaciones del haz a lo largo de la línea de transporte, desde la entrada del sistema de colimación hasta el punto de interacción. Para ello hemos usado los códigos MAD y Placet [119], asumiendo una distribución inicial de partículas Gausiana en el plano transversal, y plana en energía, con una anchura total de dispersión en energía del 1 %.

La luminosidad, calculada por medio de la simulación de la interacción haz-haz con el programa Guinea-Pig [86], decrece drásticamente con el aumento de la intensidad del sextupolo. Ello es debido al efecto de las aberraciones ópticas remanentes, geométricas y cromáticas, de segundo, tercer y cuarto orden. Con el objetivo de corregir tales aberraciones, dos nuevos imanes multipolares (un octupolo rotado y un sextupolo normal) fueron incorporados al sistema. La intensidad de estos multipolos fue calculada usando un algoritmo de minimización de aberraciones ópticas de alto orden denominado MAPCLASS [125]. De este modo, conseguimos suavizar la curva de decrecimiento de la luminosidad en función la intensidad del sextupolo rotado. Por ejemplo, tras la optimización del sistema, para una intensidad integrada del sextupolo rotado de  $K_s \simeq 20 \text{ m}^{-2}$  la luminosidad aumenta aproximadamente un factor 2 con respecto a su correspondiente valor sin optimización.

El comportamiento de la talla transversal del haz en el colimador también ha sido evaluada como función del error promedio en energía del haz. La talla en el plano vertical se ve considerablemente incrementada por el sextupolo, mientras que la horizontal permanece prácticamente no afectada. El objetivo incrementando la talla en el colimador es el de impedir el daño del colimador en caso de impacto directo de un haz con un cierto error de energía. Si denominamos por  $\sigma_{r,\min}$  a

la talla transversal mínima necesaria para evitar el daño del colimador, entonces se debe cumplir  $\sqrt{\sigma_x \sigma_y} \gtrsim \sigma_{r,\min}$  para la supervivencia del colimador. Para un colimador de berilio, por ejemplo, y suponiendo haces Gaussianos, este límite ha sido establecido en  $\sigma_{r,\min} \approx 120 \mu\text{m}$  [87]. De las simulaciones se deduce que los haces son no Gaussianos en el colimador, por lo que un mejor criterio sería comparar el pico de densidad transversal de energía del haz  $\rho_E(x, y)$  con el límite definido por la densidad  $\rho_{E,\max} = NE_0/(2\pi\sigma_{r,\min}^2)$ , con  $N$  el número de partículas por haz y  $E_0$  la energía nominal del haz. Al fin y al cabo, es la deposición de energía en la superficie del colimador lo que es relevante para la fractura del material.

La intensidad de los multipolos del sistema de colimación no lineal debe ser tal que garantice la reducción de la densidad transversal del haz por debajo del límite de fractura, a la vez que no degrade sobremanera la luminosidad en el punto de interacción. Un sextupolo con una intensidad integrada de alrededor de  $20 \text{ m}^{-2}$  garantizaría la supervivencia del colimador en el caso de impactos de haces con errores en energía  $\gtrsim 1.5 \%$ . En operación normal, i.e., sin errores de energía, con una intensidad del sextupolo de  $20 \text{ m}^{-2}$ , la luminosidad es  $\mathcal{L} \approx 5 \times 10^{34} \text{ cm}^{-2}\text{s}^{-1}$ . Este valor puede ser comparado con el computado para CLIC usando un sistema de colimación lineal:  $\mathcal{L} \approx 7 \times 10^{34} \text{ cm}^{-2}\text{s}^{-1}$ .

También podemos comparar la llamada *anchura de banda* en energía ('bandwidth') del sistema de colimación no lineal diseñado en esta tesis con la del sistema lineal. Por anchura de banda se entiende el error límite tolerado en energía antes de la degradación brusca de la luminosidad. Tras la optimización del sistema no lineal, mencionada anteriormente, hemos obtenido una anchura de banda para el sistema no lineal prácticamente comparable a la del sistema lineal.

Considerando colimadores perfectos, i.e., con absorción total y sin producción de haces secundarios, hemos estudiado y comparado la eficiencia de colimación del sistema lineal y no lineal. El porcentaje de pérdidas de partículas es muy similar en ambos tipos de sistema. Si bien, un nuevo estudio de optimización de las aperturas debe ser realizado, ya que el porcentaje de pérdidas en los colimadores betatrónicos, incluso considerando un caso ideal (sin error promedio de energía), es excesivamente alto, elevando así la probabilidad de producción de muones (en la interacción de la partícula con el colimador), tan indeseados a efectos de ruido de fondo en los detectores de la región de interacción.

## Un sistema de colimación no lineal para el LHC

El diseño del sistema de colimación del LHC está planeado para ser desarrollado por fases [8]. En una primera fase, el esfuerzo está centrado en la robustez del sistema, y está basado en una óptica lineal. Los colimadores primarios están contruidos con grafito y tienen una apertura de  $6\sigma$  (en unidades de valor cuadrático medio de la talla transversal del haz). Debido a la proximidad de los bloques de los colimadores al haz y a que el grafito tiene una baja conductividad eléctrica, se estima que las impedancias generadas pueden limitar considerablemente la luminosidad del

acelerador. Para solventar este problema han surgido propuestas alternativas para una segunda fase de desarrollo o mejora del sistema. A modo de ejemplo mencionaré la colimación a través de cristales [26] y la colimación usando lentes de electrones [30]. En esta tesis proponemos un sistema de colimación no lineal como solución para la segunda fase de desarrollo del sistema de colimación del LHC.

En el capítulo 6 se ha diseñado un sistema de colimación no lineal de la amplitud betatrónica para el LHC. Este sistema está basado en un concepto similar al sistema no lineal desarrollado para CLIC, teniendo en cuenta las siguientes diferencias: La dispersión en momento del LHC es casi dos órdenes de magnitud más pequeña que la de CLIC, por lo que la dispersión no puede ser explotada para inflar el haz; el crecimiento de la emitancia debido a radiación sincrotrón en el LHC es insignificante, y no será por tanto un factor restrictivo; y la emitancia geométrica vertical es aproximadamente unos 3 órdenes de magnitud mayor que en CLIC.

Con el fin de cumplir las condiciones para la colimación no lineal, hemos modificado los parámetros ópticos de la llamada región de interacción IR7 (versión 6.5), dedicada a la limpieza betatrónica del haz. Este ajuste fue realizado con el programa MAD sin afectar a las otras regiones de la máquina.

Para determinar el límite de protección del colimador nos hemos guiado por un criterio similar al utilizado anteriormente,  $\sigma_x \sigma_y \gtrsim \sigma_{r,\min}^2$ . En el caso del LHC, cuyos colimadores primarios están contruidos con grafito:  $\sigma_{r,\min}^2 \approx 200 \mu\text{m}$ . Sin embargo, para establecer un límite más preciso, sería necesario realizar simulaciones numéricas de la interacción de los protones del haz con el material del colimador y su correspondiente deposición de energía en el colimador.

Para el estudio de la eficiencia de colimación, hemos considerado un sistema de colimación no lineal de dos etapas, i.e., compuesto por colimadores primarios y secundarios. Estos últimos tienen como objetivo interceptar el halo secundario. En este diseño hemos colocado un colimador primario horizontal y otro vertical en el punto de interacción IP7. Las aperturas son de  $16 \sigma_x$  y  $8 \sigma_y$  para el primario horizontal y el primario vertical, respectivamente (comparar con los  $6 \sigma$  de apertura de un colimador primario en el sistema lineal). La eficiencia de colimación ha sido evaluada para ambos sistemas, el lineal y el no lineal. Para ello, halos de partículas fueron generados y transportados a lo largo de 200 vueltas diferentes usando el código de simulación SixTrack [145]. Considerando un halo en el plano vertical, la eficiencia de los dos sistemas es muy similar. Por otro lado, el sistema lineal se muestra más eficiente limpiando el halo en los planos horizontal y radial. Sin embargo, creemos que con un cuidadoso ajuste de la posición de los colimadores secundarios, así como de su orientación angular, sería posible incrementar la eficiencia del sistema no lineal al mismo nivel que el lineal.

El hecho de que un sistema de colimación no lineal permita aperturas mayores con respecto a los sistemas lineales convencionales, ayuda a reducir las impedancias de la máquina y, por consiguiente, a preservar la estabilidad del haz. A este respecto, se ha demostrado la reducción de las impedancias usando el sistema de colimación no lineal.

## **El primer experimento de colimación no lineal en el SPS**

El 8 de Noviembre de 2006, se llevó a cabo el primer experimento de colimación no lineal en el ‘Super Proton Synchrotron’ (SPS) del CERN. En este acelerador hay instalado un prototipo de colimador secundario tal como los que se utilizarán en la primera fase del LHC.

Para nuestro experimento hemos usado ocho imanes sextupolares que hay instalados en el SPS, y que en operaciones normales son usados para extracción lenta o resonante del haz. El objetivo de este primer experimento es determinar el efecto de los sextupolos en el patrón de pérdidas de las partículas del halo a lo largo del anillo. Este patrón de pérdidas ha sido comparado con el que existe cuando los sextupolos están desactivados.

Con los sextupolos de extracción hemos excitado términos resonantes. En ambos casos, con sextupolos activados y desactivados, encontramos un patrón similar de picos de pérdidas, estando el mayor de ellos localizado en la posición del colimador. Sin embargo, el análisis de los datos ha desvelado una clara diferencia: cuando los sextupolos están conectados, en las posiciones donde los términos resonantes son altos, encontramos picos de pérdidas adicionales. Esto es debido a la deflexión por los sextupolos de partículas del halo hacia aperturas que en operación normal (sin sextupolos) no son limitantes.

De esta primera prueba experimental podemos obtener ideas para configurar experimentos más sofisticados de colimación no lineal en el futuro. Estos deberán focalizar la atención, por un lado, en mejorar la eficiencia de colimación a la vez que se incrementa la apertura del colimador y, por otro lado, en la cancelación de aberraciones entre parejas de sextupolos.

## **Conclusiones**

Los sistemas de colimación son una parte esencial de los colisionadores operando a energías del orden del TeV. La colimación del haz es necesaria tanto para reducir el ruido de fondo en los detectores del punto de interacción, como para proteger los componentes de la máquina en caso de fallos en la operación.

El diseño de los sistemas de colimación no es nada sencillo y, generalmente, se debe amoldar a una serie de restricciones: alta eficiencia de colimación, colimadores resistentes y un efecto lo más débil posible de los ‘campos estela’ (impedancias).

Los sistemas de colimación están basados usualmente en secciones ópticas lineales. Aunque es posible encontrar conceptos alternativos en la literatura. En esta tesis hemos estudiado con detalle un sistema de colimación no lineal para aceleradores de altas energías, presentando un esquema general de colimación que es tanto aplicable a colisionadores lineales, tal como CLIC y ILC, como a colisionadores circulares, tal como el LHC. Este sistema está basado en imanes sextupolares rotados.

Una aplicación del concepto ha sido explorada para CLIC. En particular, hemos diseñado un sistema no lineal de colimación en energía. Las características de este sistema han sido estudiadas

con diversos códigos de simulación de la dinámica del haz. Este sistema garantiza la reducción de la densidad de la distribución transversal de energía en la posición del colimador para haces con errores en energía. La protección del colimador contra fractura está garantizada en caso de impacto directo de haces con errores promedios de energía  $\gtrsim 1.5\%$ .

Uno de los inconvenientes de los sistemas no lineales es el difícil control de las aberraciones ópticas de alto orden, que degradan considerablemente la luminosidad. Sin embargo, tras la optimización del sistema mediante una corrección local de las aberraciones, se consigue una luminosidad comparable a la del sistema lineal de CLIC. La anchura de banda en energía, i.e., el error límite tolerado en energía antes de la degradación brusca de la luminosidad, también fue mejorado tras la optimización, siendo ahora comparable a la del correspondiente sistema lineal.

Un esquema de colimación similar al de CLIC ha sido adaptado para colimación de las fases betatrónicas en el LHC. Para ello se ajustaron los parámetros del diseño óptico de la región IR7, que está dedicada a colimación betatrónica. Este ajuste fue realizado sin afectar a las otras secciones del acelerador.

El sistema de colimación no lineal, al igual que el lineal, incluyen colimadores primarios y colimadores secundarios, por lo que se le denomina sistema de colimación en dos etapas.

Hemos evaluado y comparado las características del sistema no lineal con las del sistema lineal. La eficiencia de colimación ha sido estimada a través de códigos de simulación de la dinámica del haz incluyendo la interacción del halo con los colimadores. Ambos sistemas, el lineal y el no lineal, muestran una eficiencia similar limpiando el halo en el plano vertical. Sin embargo, el sistema lineal, se muestra más eficiente limpiando partículas de un halo horizontal y radial. Cabe resaltar que, con un ajuste más fino de la orientación angular, así como de la posición, de los colimadores secundarios, se puede mejorar la eficiencia del sistema no lineal. En esta tesis hemos mostrado que el concepto de colimación no lineal trabaja aceptablemente para el LHC. Para refinar el rendimiento del sistema, un estudio de optimización del sistema sería conveniente en futuros trabajos.

Es también conveniente resaltar que el sistema de colimación no lineal descrito en este trabajo para el LHC permite mayores aperturas de los colimadores con respecto al sistema lineal. Esto es muy importante, ya que contribuye a reducir las impedancias generadas por los colimadores, que actualmente son un factor limitante para la luminosidad del LHC. Hemos reducido en un factor 2 el módulo de la impedancia efectiva en el plano horizontal, y en un factor 3 en el plano vertical con respecto a los correspondientes valores generados por el sistema de colimación lineal. Esta reducción de la impedancia contribuye a incrementar la estabilidad del haz.

Finalmente, podemos concluir, que en esta tesis hemos demostrado que los sistemas de colimación basados en ópticas no lineales pueden ser lo suficientemente competitivos, y pueden contribuir además a resolver algunos problemas clave que en la actualidad limitan el rendimiento de los aceleradores, como por ejemplo el de las impedancias en el LHC.



# Introduction

The new colliders at high energy physics, operating at beam energies around 1–10 TeV will explore the physics beyond the so-called Standard Model of the elementary particles. For instance, the Large Hadron Collider (LHC) [1], currently under commissioning at the European Organization for Nuclear Research (CERN), will operate at a center-of-mass collision energy of 14 TeV. This is the biggest hadron storage ring ever constructed, with possibility of proton-proton or ion-ion collisions.

At present, there is a general consensus among the particle physics community that the next large-energy particle accelerator ‘post LHC’ should be an  $e^+e^-$  linear collider. Two big projects are currently being studied: the International Linear Collider (ILC) [2] and the Compact Linear Collider (CLIC) [3,4]. These machines, operating with centre-of-mass collision energies ranging from 0.5 TeV to about 5 TeV, will provide an essential complement to hadron-hadron colliders. Unlike the hadron-hadron collisions, where the center-of mass energy is split among all the constituents (quarks and gluons), the point-like  $e^+e^-$  collisions provide a cleaner experimental environment and a more ‘democratic’ production of all particles within the accessible energy range. This will allow more precise physics measurements, helping thus to unravel the TeV physics, to be unveiled by the LHC. In both LHC and linear collider projects a very high luminosity is necessary to reach the physics goals, a luminosity of about  $10^{34} \text{ cm}^{-2}\text{s}^{-1}$  (high luminosity experiments) for the LHC and about  $10^{34}\text{--}10^{35} \text{ cm}^{-2}\text{s}^{-1}$  for the linear colliders. In order to reach such a high luminosity, beams with high intensity and very small transverse beam sizes collide at the interaction point (IP).

In order to keep the quality of the beam, particles at large betatron amplitudes or with a large momentum offset, what are generally referred to as the *beam halo particles*, should be eliminated. The halo particles are an important source of detector background, which limits the ultimate achievable luminosity, such as the experience of running the Stanford Linear Collider (SLC) [5] and the Large Electron Positron (LEP) collider [6] have shown. Therefore, collimation sections should be dedicated to the cleaning of the beam halo in order to reduce the experimental background.

Another important function of the collimation system is the protection of the machine components in case of failures. The LHC and the future linear colliders will store a transverse energy density per beam of about  $\text{GJ/mm}^2$  ( $\approx 6.2 \times 10^{18} \text{ GeV/mm}^2$ ). This advances the state of the art by three order of magnitude respect to recent achievements at TEVATRON (Fermilab, USA) and at HERA (DESY, Germany) [7], what means a higher damage potential of the beam.

In addition, the collimation system should not compromise the beam stability introducing intolerable wakefields (impedances).

The collimation systems are generally based on linear optics, see [1, 8] for the LHC collimation system and [9, 10] for the CLIC collimation system. Alternatively other concepts have been proposed in the literature. In this thesis we focus our study on the nonlinear collimation concept. It is denominated “nonlinear” because it is based on nonlinear magnets, such as sextupoles and octupoles. We have designed a scheme based on skew-sextupoles<sup>1</sup> for CLIC, and adapted a similar scheme for betatron collimation in the LHC. The performance of these systems is compared with that of the conventional linear one.

This thesis report is organized as follows:

The general principles of beam collimation for high energy colliders are presented in chapter 2. The criteria to determine the necessary collimation depths in both transverse and longitudinal (in energy) planes, and the necessary optics requirements are introduced. In a first approximation we assume a linear optics for collimation.

The chapter 3 is devoted to describe briefly some important issues related to collimation: different mechanisms which may contribute to the halo and tail generation; and other mechanisms from beam-collimator interaction which may contribute to the collimator damage. A brief introduction to the concepts of collimator wakefields and collimator impedances is also given.

In chapter 4 we describe the concept of nonlinear collimation of beam halo in both linear and circular colliders. In particular we studied an optics scheme based on a pair of skew sextupoles. We have derived analytically the equation system to evaluate the optics parameters and the required collimator aperture of the system. Several constraints have been used in order to, on one hand, ensure the beam stability and, on the other hand, guarantee the collimator survival in case of a direct beam impact in a failure scenario. In this chapter the resulting expressions to calculate the transverse beam spot sizes at the spoiler (primary collimator) are given up to second order matrix expansion, and up to third order in the appendix C.

Chapter 5 studies the particular case of the CLIC collimation system. After a brief introduction to the present status of the CLIC beam delivery system, we present our results on the study of an alternative nonlinear energy collimation system for CLIC: optics layout and its performance evaluation. We also discuss the optics constraints and requirements to choose the best optics solution candidate. This optics solution should allow a collimation efficiency as high as possible minimizing at the same time the luminosity degradation. The system properties, like chromatic bandwidth, collimator survival condition and cleaning efficiency, are evaluated and compared with those of the

<sup>1</sup>“skew” refers to sextupoles rotated an azimuthal angle of  $\pi/6$  rad with respect to a normal sextupole.

corresponding conventional linear collimation system.

In chapter 6, after a brief introduction to the LHC, we explore the viability of a nonlinear collimation system for betatron cleaning in the LHC. This system could be a possible solution to the difficult trade-off between cleaning efficiency, collimator robustness and collimator impedance in the LHC. We analyze the beam losses and calculate the cleaning efficiency of the system. Moreover, impedance studies have been also performed. All the results have been compared with those of the LHC conventional linear collimation system.

The chapter 7 presents some preliminary results from the first experimental test on nonlinear collimation, based on normal sextupoles, made in the Super Proton Synchrotron (SPS) at CERN.

Finally some conclusions are drawn in chapter 8.



# Collimation for High Energy Colliders

## 2.1 Principle of beam collimation

The collimation system of high energy colliders should fulfil the following main functions:

- Reduction of the background in the particle detectors by removing halo particles, i.e. particles at large betatron amplitudes or energy offsets.
- Protection of machine components, i.e. should minimize the activation and damage of accelerator components outside of the dedicated collimation section. In accelerators using superconducting magnet technology, as in the case of the LHC [1], the collimation system has the following additional protection functionality: efficient cleaning such that beam-induced quenches of the superconducting magnets are avoided during routine operation <sup>1</sup>.
- Protection of the collimation system itself. The collimators should be protected from being destroyed during normal and abnormal operational conditions.

The design of a collimation system with the above functions is not trivial, as it has to obey a number of often conflicting constraints:

- The optics of the system should not adversely affect the beam stability or degrade the nominal luminosity.
- The choice of the collimator apertures should guarantee a good cleaning efficiency of the beam halo and, at the same time, not introduce intolerable wakefields (impedances), which can compromise beam stability.

---

<sup>1</sup>The protection against quenches of the superconducting magnets can also be important in future linear colliders, such as the ILC, whose final doublet in the 2mrad crossing angle scheme contains a superconductive large bore defocusing quadrupole and nearby two superconductive sextupoles for local chromaticity correction [11]

- The collimation system should withstand the direct impact of mis-steered or errant beams. This requires robust collimators and an appropriate optics design.
- The choice of the material for the collimator jaws is critical regarding both the robustness and the impedance issues.
- The regeneration of halo due to beam particle scattering at the collimator, or due to optical and wakefield phenomena, should be limited.

The beam collimation is generally performed using a mechanical system and a dedicated optics. Such a system is constituted of blocks of material between the beam and the size of the vacuum pipe to intercept the beam halo particles. These blocks are commonly called *jaws*.

In the next section we study the general guide lines for collimation in linear and circular colliders based in linear optics. Other alternative schemes are briefly described in section 2.2.

### 2.1.1 Collimation in linear colliders

A conventional postlinac collimation system for future linear colliders usually consists of a scheme of *spoilers/absorbers*, as shown in Fig. 2.1. The halo particles are first intercepted using thin spoilers, with a length of some fraction of a radiation length of material. Thick ( $\geq 20$  radiation lengths) absorbers judiciously placed downstream of the spoiler(s) collect the debris generated. The purpose of the spoilers is to increase the angular divergence of an incident beam. This increases the beam size at the absorbers and reduces the risk of material damage.

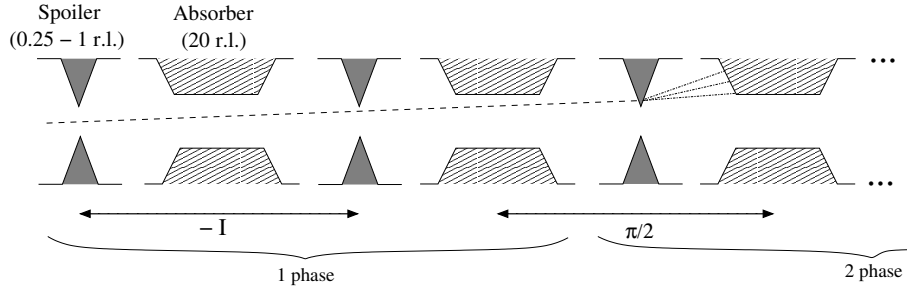


Figure 2.1: Schematic of a conventional collimation system consisting of a series of spoilers followed by absorbers.

The postlinac collimation system is generally composed of a section for betatronic collimation and another section for energy collimation <sup>2</sup>

<sup>2</sup>Unlike the ILC, where the betatron collimation section is followed by the energy collimators, in CLIC the energy collimation section is upstream of the betatron one.

### Betatron collimation amplitudes

How tight the betatron collimation has to be, i.e. how close to the core of the beam the apertures must be set, is determined predominantly by the geometry of the interaction region (IR) and the quadrupoles close to the IR, particularly the so-called final doublet (FD). The guiding principle is based on synchrotron radiation (SR) photons generated by the beam halo in the FD: all photons generated by the remaining halo particles should pass cleanly through the IR, rather than being intercepted by masks (which protect the detectors at the interaction point). This criterion defines a maximum allowed amplitude of particles at the entrance to the FD, which is referred to as the betatron collimation depth in the linear colliders, and it is measured in terms on the nominal core beam size ( $\sigma_{x,y} = \sqrt{\beta_{x,y}\epsilon_{x,y}}$ ).

In this section we study the betatron collimation depths using a linear optics. We do not consider the nonlinear effects coming, for example, from the sextupoles used for local chromaticity correction.

The betatron collimation system should perform collimation in the phase spaces  $x-x'$  and  $y-y'$ . To collimate exclusively in the betatronic planes, the collimators are usually located in a region with zero transverse dispersion<sup>3</sup>,  $D_{x,y} = 0$ . The necessary collimation depths  $n_{x,y}$  (in units of the rms transverse beam sizes  $\sqrt{\beta_{x,y}\epsilon_{x,y}}$ ) fix the transverse collimator half gaps:  $a_{x,y} = n_{x,y} \sqrt{\beta_{x,y}\epsilon_{x,y}}$ . The transverse phase-advance between the spoiler positions and the IP is generally set to be  $\ell\pi$  rad or  $(1/2 + \ell)\pi$  rad, with  $\ell = 0, 1, 2, 3, \dots$ . The IP is usually at  $\pi/2$  phase advance from the FD. Therefore, on one hand, spoilers at  $\ell\pi$  phase advance from the IP are said to collimate amplitudes at the IP phase and, on the other hand, collimators at  $(1/2 + \ell)\pi$  from the IP are said to collimate amplitudes at the FD phase. Figure 2.2 shows schematically an example of a possible transverse phase advance distribution between spoilers, FD and IP. Unlike circular collimators, where simultaneous collimation in both phase spaces  $x-x'$  and  $y-y'$  is provided, we consider rectangular collimators, i.e. by using horizontal and vertical jaws. A horizontal (H) spoiler is used for collimation of the region  $|x| \geq n_x \sqrt{\beta_x \epsilon_x}$ , and downstream, at  $\pi/2$  phase advance from the former, another spoiler clean the region  $|x'| \geq n_x \sqrt{\gamma_x \epsilon_x}$ . A similar arrangement with vertical (V) spoilers is used for cleaning of the phase space  $y-y'$ .

A detailed method to calculate the collimation depth is described in Ref. [13]. Here we will indicate the general guidelines.

At first order, the collimation depth at the IP is related to the collimated beam phase space corners at a distance  $s$  upstream from the IP by

$$\mathbf{x}_c^*(s^*) = R(s^*, s) \mathbf{x}_c(s), \quad (2.1)$$

where  $\mathbf{x}_c^*(s^*) = (n_x \sqrt{\beta_x^* \epsilon_x}, n_x \sqrt{\gamma_x^* \epsilon_x})$  is the collimation depth vector at the IP position  $s^*$ ,  $\mathbf{x}_c = (x_c, x'_c)$  is the amplitude vector of the envelope of the collimated halo at position  $s$ , and  $R(s^*, s)$  is

<sup>3</sup>An exceptional case was the optics of the collimation system of the NLC project [12], which was designed to perform collimation simultaneously in the plane  $x-x'$  and in energy with the following collimation depth:  $n_x = (x + D_x \delta) / \sqrt{\beta_x \epsilon_x}$ .

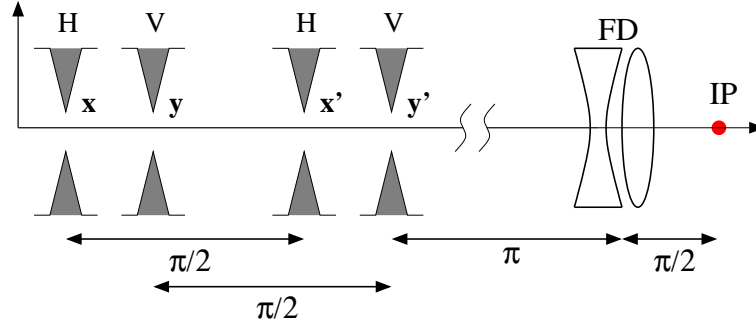


Figure 2.2: Schematic of the location in phase advance of spoilers.

the  $2 \times 2$  first order transfer matrix from the  $s$  position to the IP.

Beam particles in the collimated beam phase space which reaches the FD emit SR photons. These photons should cross the apertures in the interaction region without hitting any machine component. The limiting apertures may include the following: the bore of the incoming doublet itself, or the one of the opposite doublet, the narrow beampipe at the interaction point, forward instrumentation devices and protection masks. If  $s$  is the position of the FD,  $s^*$  the position of the IP, and  $L$  the distance from the IP to the limiting aperture (A) position, the corners of the SR fan envelope in this aperture are given by:

$$\begin{aligned} \mathbf{x}_c^y(s, L) &= D(s^* + L - s) \mathbf{x}_c(s) \\ &= D(s^* + L - s) R^{-1}(s^*, s) \mathbf{x}_c^*(s^*), \end{aligned} \quad (2.2)$$

where  $D(s^* + L - s)$  is the transfer matrix of a drift with length  $s^* + L - s$ , and in the second step the Eq. (2.1) has been inverted. Fig. 2.3 illustrates this situation. A similar development can be done for the phase space  $y-y'$ .

The maximum transverse radial displacement of the SR photon for a given emission point  $(x_c, x'_c)$  and  $(y_c, y'_c)$  is

$$r = \sqrt{x_c^{\gamma 2} + y_c^{\gamma 2}}. \quad (2.3)$$

This equation represents an elliptical curve in  $n_x-n_y$ . Considering a circular limiting aperture of radius  $A$  in the interaction region, the transverse collimation depths  $n_x$  and  $n_y$  for one particular emission point are determined by the constraint  $r \lesssim A$ . The solution usually chosen is that which maximizes the product  $n_x \cdot n_y$ . Note that this calculation recipe is made for a single emission point. Obviously, there are many emission points in the final doublet and thus many corresponding solution ellipses. Therefore, the collimation depths should be computed for many emission points through the final doublet. For a given limiting aperture the overall solution is the smallest pair of



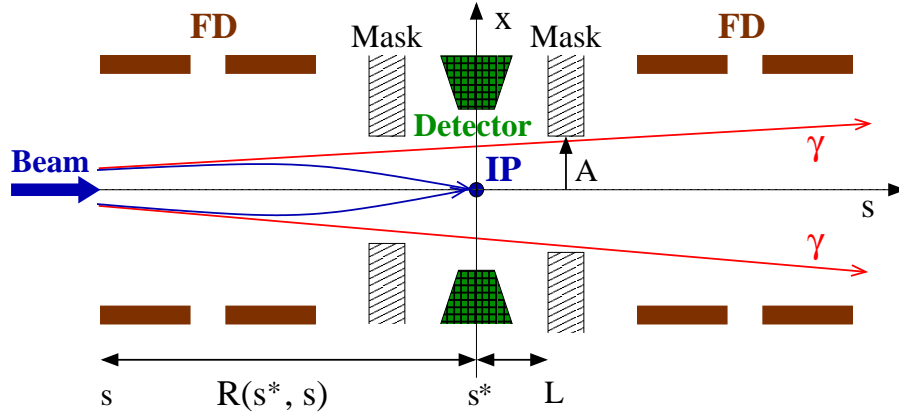


Figure 2.3: Schematic of the interaction region of a linear collider. The red lines represent the SR fan envelope generated in the final doublet. In this example the limiting aperture (A) is defined by the exit mask.

$(n_x, n_y)$  values. Moreover this calculation process should be repeated for each small aperture in the interaction region.

It is worth mentioning that in a real machine, the apertures in the interaction region may not impose circular symmetric constraints on the collimation depths, rendering the calculation more complicate.

Actually, the collimation amplitudes should usually be tighter than the calculated depths, due mainly to the following phenomena:

- A nonzero dispersion across the final doublet, which is an intrinsic feature of the so-called Raimondi-Seryi final focus optics [14]. Therefore, the horizontal beam size  $\sigma_x$  includes both betatron and dispersive components.
- If collimation is performed at  $\pi/2$  rad intervals, as for the case shown in Fig. 2.2, with amplitudes of  $\pm n_x \sigma_x$  in each phase, the phase space after collimation is the rectangle of Fig. 2.4 (left). Note that some particles, for instance particles with amplitudes  $\pm n_x \sigma_x \sqrt{2}$  are transmitted which are outside the region of  $\pm n_x \sigma_x$  amplitude. These particles may phase-rotate into the FD phase and generate SR. This problem can be solved by collimating at  $\pm n_x \sigma_x / \sqrt{2}$ , which ensures that the maximum particle amplitude permitted is  $\pm n_x \sigma_x$ . A similar configuration is chosen for the vertical phase space  $y-y'$ .

Above we have considered the case of a phase advance per spoiler of  $\pi/2$  rad. This solution is not the only choice, and lattice design with a different phase advance per spoiler can be conceived. For instance, in the TESLA post-linac collimation system design [15], the betatron spoilers were conceived to be separated by  $\pi/4$  rad horizontal phase advance and  $7\pi/4$  rad vertical phase advance. In this way, and using more collimators, instead of the transmitted phase space square of Fig. 2.4,

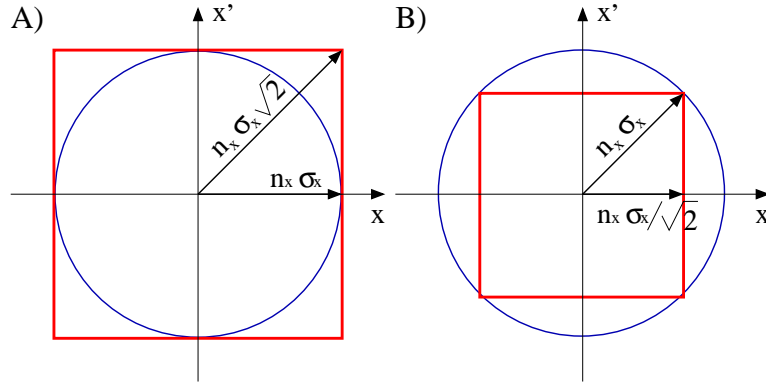


Figure 2.4: A) Collimation amplitude  $n_x \sigma_x$  in phase space  $x-x'$ . B) Collimation amplitude  $n_x \sigma_x / \sqrt{2}$ . The red square represents the phase space region which is transmitted after collimation.

the collimation depth would correspond to an octagon inside the ellipse defined by the collimation depth.

### Energy collimation amplitudes

The energy collimation depth is usually not determined by the background, but instead it is set by the failure modes in the linac. Momentum errors in the main linac can be caused, e.g., if the beam is injected at the wrong phase, or with the wrong charge. This may generate errant or missteered beams which must be intercepted. Otherwise, they can hit and damage magnets in the BDS or other important technical equipment. In this sense the energy collimation system can be considered as part of the machine protection system. Namely, it protects the machine equipment from energy errors. In some cases it also protects the downstream spoilers. For instance in CLIC, where the momentum collimation system is conceived with the additional function of avoiding the direct impact of errant beams in the downstream betatron spoilers. The momentum spoilers are located in high dispersion points, and generally their passive survival in case of direct beam impact is demanded.

In some cases, as in the NLC post-linac collimation design [16] additional kicker magnets are incorporated to extract the beam downstream of the main linac energy diagnostic station.

### 2.1.2 Collimation in circular colliders

The collimation of high energy storage rings, e.g. the LHC, is based on the so-called *multi-stage collimation system* [17, 18]. This system is illustrated in the schematic of Fig. 2.5. Particles of the primary halo are intercepted by the so-called primary collimators. By multiple Coulomb scattering many of these particles are scattered off the primary collimator with larger angular divergence. In

addition, by inelastic processes (see Chapter 3) secondary particles may be produced: in the case of hadronic beams, some halo particles can inelastically interact with the nuclear material of the collimator, generating thus hadronic showers (mesons and nucleons). These particles scattered off the primary collimators form the so-called secondary halo, which should be intercepted downstream of the primary collimators by additional thicker collimators. The latter are the so-called secondary collimators. In some cases, even tertiary (and quaternary) collimators can be used to further increase the efficiency of halo absorption and the protection of sensitive equipment.

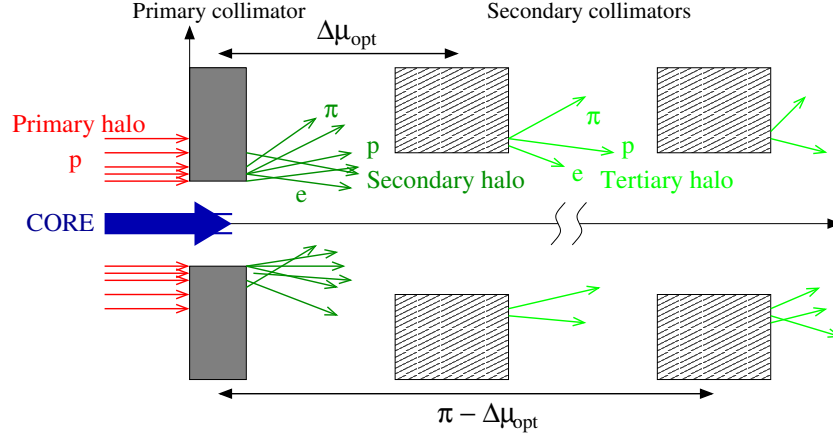


Figure 2.5: Schematic of a multi-stage collimation system.

### Betatron collimation amplitudes

In order to simplify the treatment, we consider here one dimensional betatronic collimation for on-energy ( $\delta \equiv \Delta E/E_0 = 0$ ) halo particles.

Let  $n_1$  and  $n_2$  be the normalized apertures (in units of rms transverse beam size) of the primary and secondary collimators, respectively. We further consider the impact points to be at the surface of the collimator, with the maximum transverse amplitude vector  $\mathbf{X}_0 = (X_0, X'_0) = (n_1, 0)$ . Here  $X_0$  and  $X'_0$  denote the normalized horizontal amplitudes  $X_0 \equiv x_0 / \sqrt{\beta_x \epsilon_x}$  and  $X'_0 \equiv (\alpha_x x + \beta_x x') / \sqrt{\beta_x \epsilon_x}$ . After scattering in the collimator, the particle gets an angular kick  $X'_1 = K$ , and then the new coordinates at the primary collimator are  $\mathbf{X}_1 = (n_1, K)$ .

The location of the secondary collimators is determined by optimizing the phase advance  $\Delta\mu_{\text{opt}}$  between the position of the primary collimator and the secondary collimator. The amplitude at the secondary collimator is given by the transport equation

$$\mathbf{X}_2 = \mathcal{R}(\Delta\mu_{\text{opt}})\mathbf{X}_1, \quad (2.4)$$

with  $\mathcal{R}(\Delta\mu_{\text{opt}})$  the normalized linear transport matrix

$$\mathcal{R}(\Delta\mu_{\text{opt}}) = \begin{pmatrix} \cos \Delta\mu_{\text{opt}} & \sin \Delta\mu_{\text{opt}} \\ -\sin \Delta\mu_{\text{opt}} & \cos \Delta\mu_{\text{opt}} \end{pmatrix}. \quad (2.5)$$

The optimum phase advance  $\Delta\mu_{\text{opt}}$  is chosen to minimize the maximum secondary halo amplitude escaping the two-stage collimation. This happens for the value [17]

$$\Delta\mu_{\text{opt}} = \arccos\left(\pm \frac{n_1}{n_2}\right), \quad (2.6)$$

if the minimum amplitude which cuts the secondary halo corresponds to the values  $X_{2,\text{cut}} = n_2$  and  $X'_{2,\text{cut}} = 0$ .

By using Eqs. (2.4), (2.5) and (2.6) one obtains

$$X_2 = n_1^2/n_2 + (1 - n_1^2/n_2^2)^{1/2} K. \quad (2.7)$$

Therefore, cutting at  $X_2 = n_2$ , the largest scattering angle which passes the secondary jaws is given by

$$K_c = K = (n_2^2 - n_1^2)^{1/2}. \quad (2.8)$$

Fig. 2.6 illustrates this situation for a two-stage collimation in the phase space  $X$ – $X'$ . Two secondary jaws are located at phase advance  $\Delta\mu_{\text{opt}} = \arccos(+n_1/n_2)$  and  $\Delta\mu_{\text{opt}} = \arccos(-n_1/n_2)$  respectively. Another solution is  $\pi - \Delta\mu_{\text{opt}}$ .

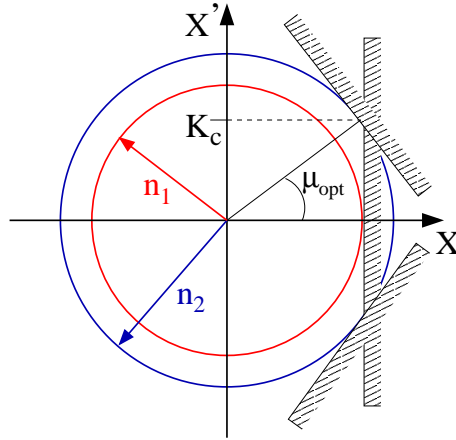


Figure 2.6: Example of a two-stage betatronic collimation system in phase-space  $X$ – $X'$ .

The optimum configuration is given by secondary collimators located at phase advance  $\Delta\mu_{\text{opt}}$  and at  $\pi - \Delta\mu_{\text{opt}}$  from the primaries. More details about two dimensional betatronic collimation can be found in [18], where the disposition of four secondaries per each primary is proposed to reach

an acceptable cleaning efficiency.

### Energy collimation amplitudes

In circular colliders an insertion can be dedicated to remove halo particles with large energy offsets. For this a horizontal collimator is usually placed in a region with horizontal dispersion  $D_x \neq 0$ . As in the previous case for betatron collimation, a two-stage collimation system can be arranged for energy collimation: primary and secondary collimators with normalized apertures  $n_1$  and  $n_2$ , respectively.

Following the prescriptions from Refs. [17, 18], we consider  $\mathcal{D}' = (\alpha_x D_x + \beta_x D'_x)/\sigma_x = 0$  at the primary collimator position<sup>4</sup>. This condition ensures that the cut made on the secondary halo does not depend on the relative momentum offset  $\delta$ . Fig. 2.7 shows the collimation depths of the primary ( $n_1$ ) and secondary ( $n_2$ ) collimators and an example phase space circle corresponding to a particle distribution with average energy offset  $\delta \neq 0$ .

If  $\mathcal{D}_1 = D_{x,1}/\sigma_x$  is the normalized dispersion at the primary collimator position, and using the slow diffusion approximation, i.e. considering the impact points to be at the surface of the collimator while the betatronic oscillation is at its maximum, the particles reach the primary collimator with amplitude

$$n_1 = \mathcal{D}_1 \delta + X_\beta, \quad (2.9)$$

where  $X_\beta$  is the normalized betatronic contribution. In addition we assume  $X'_\beta = 0$ . The largest momentum offset which can pass the primary collimator is given by  $\Delta = n_1/\mathcal{D}_1$  with  $X_\beta = 0$ .

After scattering with the primary collimator, taking the largest scattering angle which passes the secondary jaw as  $K_c = (n_2^2 - n_1^2)^{1/2}$  and using Eq. (2.9), the maximum horizontal betatronic amplitude is

$$A_{x,\beta}^{\max} = \sqrt{X_{\beta,2}^2 + X_{\beta,2}'^2} = \sqrt{(n_1 - \mathcal{D}_1 \delta)^2 + K_c^2}. \quad (2.10)$$

Therefore, if in the arc of the ring the normalized horizontal dispersion is  $\mathcal{D}_{\text{arc}}$ , the maximum transverse normalized excursion  $X_{\max} = \mathcal{D}_{\text{arc}} \delta + A_{x,\beta}^{\max}$  can be written as a function of the energy offset  $\delta$  and the apertures  $n_1$  and  $n_2$ :

$$X_{\max} = \mathcal{D}_{\text{arc}} \delta + \left( \mathcal{D}_1^2 \delta - 2n_1 \mathcal{D}_1 \delta + n_2^2 \right)^{1/2}. \quad (2.11)$$

The largest stable secondary excursion  $\mathcal{A}_{\text{arc}}$  is usually determined by the machine aperture: either by the geometrical aperture (inner mechanical apertures of the machine components) in the case of

---

<sup>4</sup>The following notation is used:  $\mathcal{D}'$  is the derivative of the dispersion with respect to the longitudinal coordinate  $s$ , normalized to the beam size,  $D_x$  is the horizontal dispersion and  $D'_x$  is the derivative of the horizontal dispersion with respect to  $s$

an ideal linear machine or the so-called dynamic aperture <sup>5</sup> in the case of a real machine. For the LHC, for example,  $\mathcal{A}_{\text{arc}} \simeq 12 \sigma$ . From Eq. (2.11) with  $X_{\text{max}} = \mathcal{A}_{\text{arc}}$  and  $\delta = \Delta(n_1)$ , one obtains

$$\Delta = \frac{\mathcal{A}_{\text{arc}} - (n_2^2 - n_1^2)^{1/2}}{\mathcal{D}_{\text{arc}}} . \quad (2.12)$$

Fixing  $n_1$  and inserting Eq. (2.12) into  $\mathcal{D}_1 = n_1/\Delta$ , the necessary dispersion at the primary collimator is given by

$$\mathcal{D}_1 = \frac{n_1 \mathcal{D}_{\text{arc}}}{\mathcal{A}_{\text{arc}} - (n_2^2 - n_1^2)^{1/2}} . \quad (2.13)$$

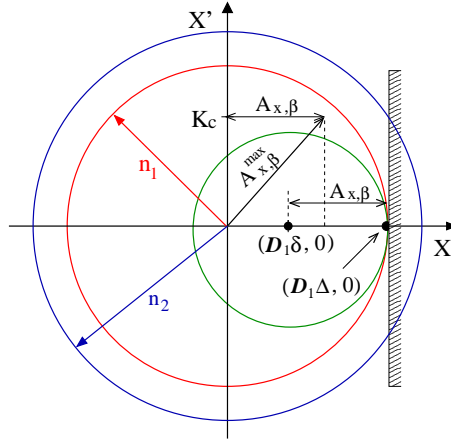


Figure 2.7: Example of a two-stage momentum collimation system in phase space  $X-X'$ . The point  $(\mathcal{D}_1\Delta, 0)$  indicates the largest momentum offset which can pass the primary collimator aperture  $n_1$ .

## 2.2 Advanced collimation concepts

Other ideas for fulfilling the often conflicting collimation constraints and requirements have been pursued in the literature. Some of these alternative concepts are listed below.

### 2.2.1 Consumable collimators

The concept of consumable collimator was first proposed for the Next Linear Collider (NLC) design [19], and it is also the solution adopted for the younger ILC project. The jaws of such a collimator can be moved to a new position a finite number of times after being damaged by the beam in case of direct impact.

<sup>5</sup>The dynamic aperture is defined as the maximum phase-space amplitude within which particles do not get lost as a consequence of single-particle-dynamics effects

The mechanical schemes considered in Ref. [19] are based on wheels, bars or tapes which can be transversally moved after damage. Schematics of these concepts are shown in Fig. 2.8. The wheel collimator requires vacuum bearings, but its mechanical design is simple compared with the tape collimator, which requires a complex vacuum mechanical system. The advantage of the tape collimator is its large usable area. Unlike the wheel and the tape concepts, the bar collimator does not require any vacuum moving parts, but is large for its active area. From all these candidates, a prototype based on rotating wheels has been chosen for the ILC. It is worth mentioning that a similar rotating collimator will be constructed for the LHC Phase-II collimation [20].

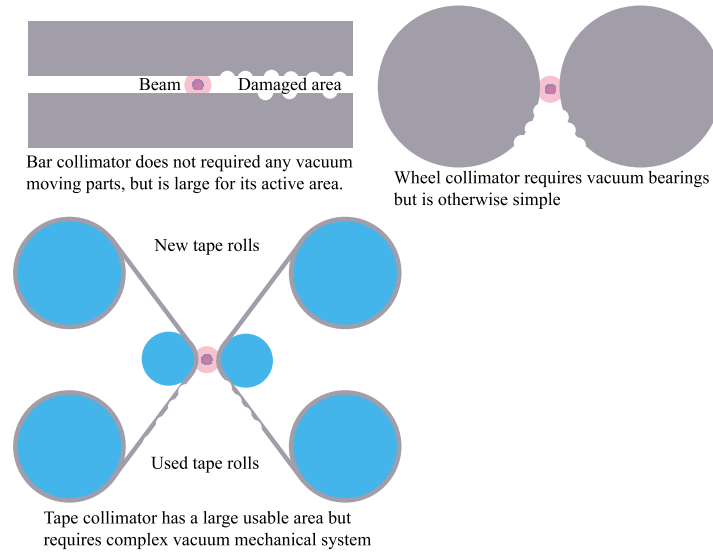


Figure 2.8: Schematic of consumable collimators with moving mechanical jaws: bars, wheels and tapes [19].

### 2.2.2 Repairable collimators

This kind of collimators is based on jaws which can be continuously repaired during operation an unlimited number of times after damage. A design with rotating jaws, whose surface is exposed to a bath of liquid metal, has been proposed in Ref. [19]. In this idea a liquid metal is frozen on the surface of slowly turning metal drums. The solidified surface is rolled flat with smoothing rollers. See the schematic of Fig. 2.9. Here the main problem is to find liquid metals with the required material properties: low vapor pressure at melting point; elemental in order to avoid fractional crystallization during solidification; no or low toxicity; and adherence to the jaw surface. Molybdenum rollers and a bath of liquid tin seem to be a good candidate [19].

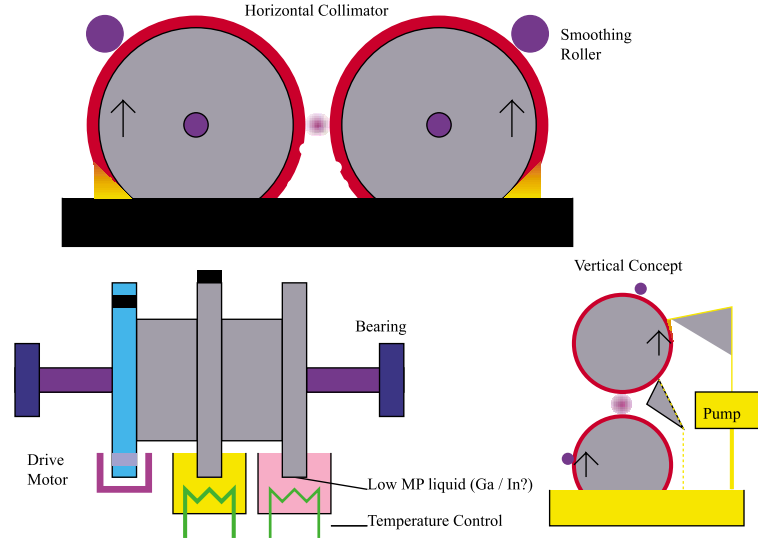


Figure 2.9: Schematic of repairable collimators with liquid metal which is solidified onto the collimator surface [19].

### 2.2.3 Crystal collimation

We have already mentioned that the simplest way to remove halo particles is to use a block of amorphous material, which interacts with the halo so that the particles lose enough energy to be removed from the beam. However, particles that do not have a large impact parameter can rescatter from the material, contributing to halo repopulation. So then, in order to remove this halo, another block of material (secondary collimator or absorber) is needed downstream of the former. But this block can cause the same problem. To alleviate such a problem, a so-called bent crystal can be used. In a crystal a particle will tend to follow the atomic planes, i.e. it is channeled. If in addition the crystal is bent, it is possible to steer the particles.

The basic schematic of the collimation principle using bent crystals is shown in Fig. 2.10. A bent crystal, serving as a primary collimator or scraper should coherently bend halo particles, which enter into the crystal at an appropriate angle, onto a secondary collimator or absorber. An advantage is that the angle of escape from the crystal is known. If a particle impacts tangentially to the atomic planes in the crystal, with some probability, it can be channeled; otherwise, it may be reflected by the coherent potential of bent atomic planes, and can again repopulate the halo.

Experiments on crystal collimation at IHEP (Protvino) [21, 22] demonstrated a collimation efficiency of 40 %, and a factor-of-2 reduction in the accelerator background by using a bent crystal incorporated into a proton beam cleaning system. Crystal extraction of Pb ions was earlier demonstrated at CERN SPS with efficiency of 4–11 % for a long (40 mm) Si crystal [23]. More recently, a (5mm O-shaped Si) crystal collimator efficiency of  $\approx 30$  % have been measured at RHIC for collimation of gold ions [24]. This modest efficiency  $\approx 30$  % has been attributed to the high



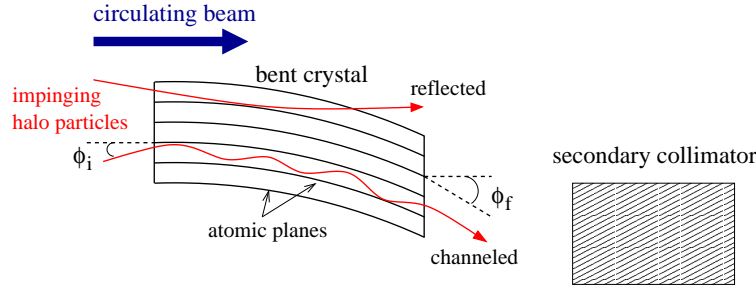


Figure 2.10: Schematic of bent crystal collimation.

angular spread of the beam that hits the crystal face due to the machine optics. Following the RHIC experiment, a similar O-shaped Si crystal was installed into the Tevatron [25]. In this experiment, using 980 GeV proton beams, a channeling efficiency of  $78 \% \pm 12 \%$  was obtained.

A highlight of recent experimental studies was the first successful test of crystal reflection with a 400-GeV proton beam at CERN in the SPS North Area by the H8-RD22 collaboration [26]. The demonstration of an extremely high effective field together with more than 95 % extraction efficiency opens up a completely new perspective for the upgrade of the LHC collimator system.

The Tevatron and the H8-RD22 (at SPS) experiments, besides demonstrating a very high efficiency of the crystal collimation in colliders, have revealed a new interesting physics of beam reflection on the coherent field of the atomic planes of bent crystal. This reflection, theoretically well understood (see for example [27]), causes a strong perturbation of the beam and it is observed as a very strong factor affecting particle loss in the accelerator ring. The reflection is less sensitive to incoming angle than channeling, and could serve as a basis of a new crystal collimation system at high energy.

#### 2.2.4 Laser collimation

Pioneering studies on postlinac laser collimation for high energy linear colliders were done by F. Zimmermann [28]. He proposed a linear collider based on the schematic of Fig. 2.11.

Laser collimation would consist in Compton scattering of electrons (positrons) in the transverse halo tails off a high power laser beam, avoiding the regime where pair production occurs. The scattered halo particles, which are off energy, would be intercepted in downstream absorbers, placed in a dispersive region. In the schematic shown, the dispersion would be created by using a bunch-combining half chicane.

A laser collimation system has the following advantages: a laser employed as a spoiler can neither be destroyed by the beam impact nor generate collimator wakefields. In addition, the postlinac collimation section, presently the longest part of the linear collider beam delivery systems, can be shortened. However, the laser technology has the following disadvantages: the high cost of the needed lasers, of high intensity and high power, and the necessary fine alignment of the laser. A

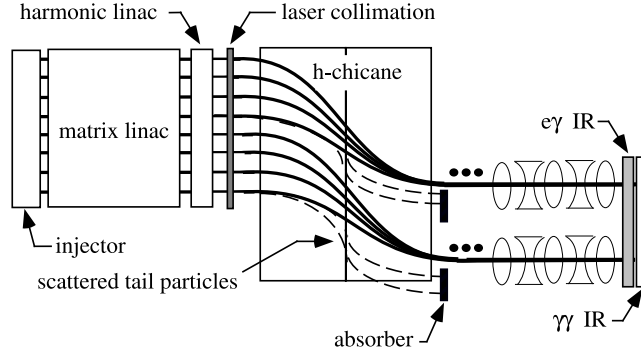


Figure 2.11: Schematic of a linear collider operating in the TeV energy scale, with linac energy compensation, laser collimation, bunch combination, sextupole-final focus, and  $e\gamma$  conversion. Courtesy of F. Zimmermann from [28].

failure in the laser could damage other accelerator components.

### 2.2.5 Electron lens collimation

Electron lenses have been built and used for beam-beam compensation studies in the Tevatron at Fermilab [29]. Recently, the use of electron lenses as electromagnetic primary collimators has been proposed by V. Shiltsev [30].

A hollow electron beam in an electron lens has very strong nonlinear field components, which can excite betatron motion of particles with larger amplitudes (halo), while smaller amplitude particles (core) are not affected at all.

The electron lens collimation may offer a possible solution to the problem of ion fragmentation in ion beam collimation. Unlike primary collimators made of usual material (for example C, Ti, W and Cu), an electron lens, used as a primary collimator, does not break an ion into fragments.

Fig. 2.12 shows a schematic of the principle, comparing the concept of two-stage collimation scheme, such as in Phase-I collimation in the LHC, and a possible LHC electron lens (LEL). The LEL would allow a fast diffusion of the halo particles and opening up the aperture of the usual collimators by  $\sim 2\sigma$ , reducing thus the collimator impedance effects.

### 2.2.6 Nonlinear collimation

The basic layout for a possible nonlinear collimation system is illustrated in Fig. 2.13. The purpose of the first nonlinear element is to blow up beam sizes and particle amplitudes, so that the collimator jaw can be placed further away from the nominal beam orbit (reducing the wakefields and resistive impedances) and the beam density at the collimator is decreased (for collimator survival). A second nonlinear element downstream of the spoiler, and at a phase advance of  $\pi$  from the first nonlinear

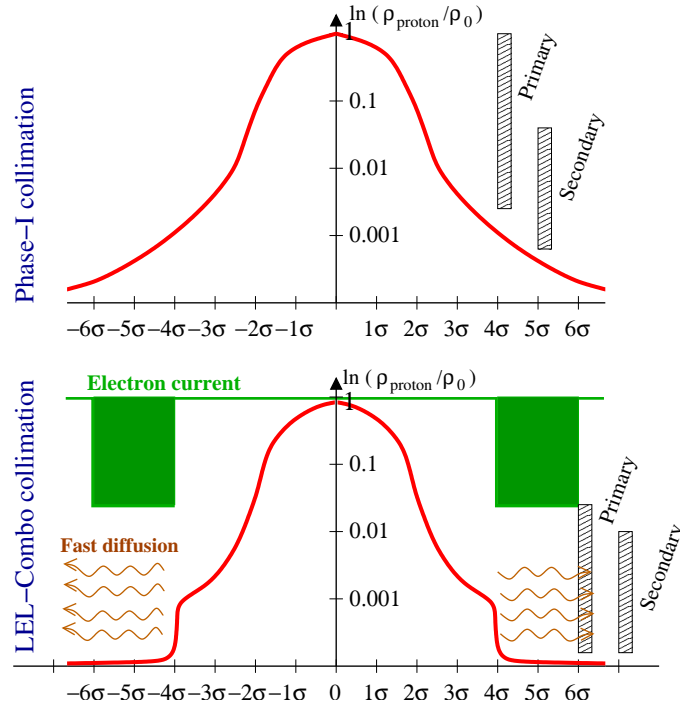


Figure 2.12: Diffusion enhanced by electron lens collimation. Picture is redrawn from [30].

element, cancels the geometric aberrations induced by the former.

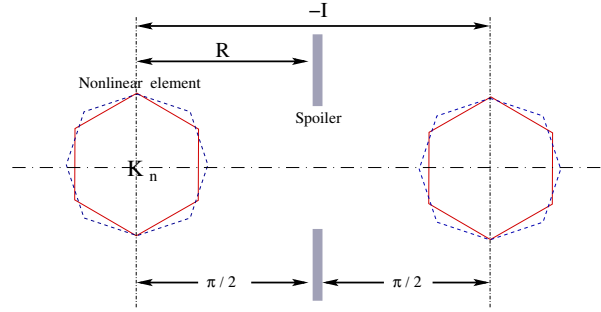


Figure 2.13: Schematic of a nonlinear collimation system.

Different types of nonlinear collimation systems for future linear colliders have been described in the literature [15, 31–33, 37–39]:

- For the NLC, in [31–33] a scheme with skew-sextupole pairs for nonlinear betatron collimation in the vertical plane has been proposed.
- Subsequently, in [37] a halo reduction method with the addition of “tail-folding” octupoles

(‘Chebyshev arrangement of octupoles’) in the NLC final focus system was presented (see also [38] for an earlier study with only 1 octupole in front of the final doublet).

- For the TESLA post-linac collimation system a magnetic energy spoiler (MES) has been suggested [15]. Here, an octupole is placed at a high dispersion point between a pair of skew sextupoles (at  $\pi/2$  phase advance from the octupole). The skew sextupoles are separated by a optical transfer matrix  $-I$ . The result is a significant increase in the vertical beam size at a downstream momentum spoiler.

A characteristic feature of all these systems is that they separate between energy and betatron collimation, and typically employ the nonlinear elements only in one or the other half.

A nonlinear collimation system for CLIC with three skew sextupoles was explored in [39]. It contains a single vertical spoiler which collimates simultaneously in the horizontal and vertical betatron amplitude at both betatron phases as well as in energy.

The nonlinear collimation is the main topic of this thesis. Detailed studies of alternative nonlinear collimation systems based on skew sextupoles for CLIC and LHC are presented in Chapters 4, 5 and 6.

# Important Issues in Collimation for High Energy Colliders

## 3.1 Beam halo and tail generation

The experience with SLC [5] and LEP [40, 41] showed that the ultimate luminosity was limited by detector background due to beam tails. In the SLC the beam halo was estimated to be about 0.1 % of the beam. The identification and the study of the beam halo sources are difficult subjects outside the scope of this thesis. The aim of this section, however, is to briefly mention some of the halo formation mechanisms. A more complete overview can for example be found in [42–44].

In the  $e^+e^-$  *linear colliders* the main sources of beam halo have been identified to be the following processes: scattering between beam particles in the beam core and scattering off the residual gas atoms in the vacuum chamber (beam-gas Coulomb scattering, beam-gas bremsstrahlung); Compton scattering between beam particles and thermal photons; linac wakefields which deflect beam core particles; injection errors in the sources and from the damping ring.

At high-energy  $e^+e^-$  *circular colliders*, such as the LEP, the halo formation arises mainly from beam-gas Coulomb scattering, beam-gas bremsstrahlung, beam-beam resonances, small tune drifts, and Compton scattering off thermal photons. A detailed explanation of some of these mechanisms for LEP can be found in [42].

In the case of *proton or ion storage rings* (e.g. LHC, Tevatron, RHIC) the halo can arise from space-charge forces, injection errors, Touschek effect, intrabeam scattering, diffusion driven by magnet nonlinearities, and beam-beam interaction. A detailed review of all these processes is given in [45]. Another contribution may arise from electron cloud effects (see for example [46] and [47]).

In the following sections I will briefly describe some scattering processes relevant for halo generation.

### 3.1.1 The concepts of beam and luminosity lifetime

#### Beam lifetime

The loss rates due to scattering processes scale as  $dN/N \propto \sigma_i$ , where  $\sigma_i$  is the corresponding scattering cross section. In the case of beam-gas scattering, the rate of scattered beam particles per time interval  $dt$  is given by

$$\frac{dN}{N} = \beta_v c dt n_{\text{gas}} \sigma_{\text{gas}} , \quad (3.1)$$

where  $n_{\text{gas}}$  is the local gas density,  $\beta_v c$  the speed of the incident beam particle, and  $\sigma_{\text{gas}}$  the beam particles cross section for scattering off gas molecules. If more than one gas species are present in the beam pipe, then summing over the different types of gas is required as

$$\frac{dN}{N} = \beta_v c dt \sum_i n_i \sigma_i , \quad (3.2)$$

where the index  $i$  indicates the gas species.

The evolution of the loss rates with time can be quantified by the so-called *beam lifetime*  $\tau$ ,

$$\frac{1}{\tau} = -\frac{1}{N} \frac{dN}{dt} , \quad (3.3)$$

which is defined as the time needed to reduce the number of beam particles to a fraction  $1/e$  of the initial intensity. The beam lifetime is a parameter commonly used in storage rings.

#### Emittance lifetime

The so-called *emittance lifetime* is another important concept in circular colliders. It is defined as

$$\frac{1}{\tau_{\epsilon_j}} = -\frac{1}{\epsilon_j} \frac{d\epsilon_j}{dt} , \quad j = x, y, z , \quad (3.4)$$

where  $\epsilon_x$  and  $\epsilon_y$  denote the horizontal and vertical normalized beam emittance, respectively, and  $\epsilon_z$  is the longitudinal normalized beam emittance. Among the main sources of emittance growth are the following scattering processes: beam-gas multiple Coulomb scattering, beam-beam elastic scattering at the interaction points, and the intrabeam scattering (see the section 3.1.2 for definitions). Additional optical processes, as magnet nonlinearities, dispersion, coupling and orbit mismatch can also lead to a substantial emittance growth in combination with scattering processes and synchrotron radiation.

The emittance growth is dominated by intrabeam scattering (see section 3.1.4) in the proton beam with small contribution from beam-beam effects. In lepton colliders, as LEP, the beam-beam effects have been identified as the most important source of emittance growth in the vertical plane [42].

### Luminosity lifetime

The luminosity lifetime is defined as

$$\frac{1}{\tau_{\mathcal{L}}} = \frac{1}{\tau_{B1}} + \frac{1}{\tau_{B2}} + \frac{1}{\tau_{BB}} + \frac{1}{2\tau_{\epsilon_x}} + \frac{1}{2\tau_{\epsilon_y}}, \quad (3.5)$$

where  $\tau_{B1}$  and  $\tau_{B2}$  denotes the lifetime contribution of the single beams 1 and 2, respectively. If we assume two similar opposing beams  $\tau_{B1} \equiv \tau_{B2}$ . The single beam lifetime is determined by (both elastic and inelastic) beam-gas scattering and intra beam scattering.  $\tau_{BB}$  refers to the lifetime relying on the beam-beam effects. The terms  $\tau_{\epsilon_x}$  and  $\tau_{\epsilon_y}$  denote the horizontal and the vertical emittance lifetime, respectively.

#### 3.1.2 Scattering with residual gas

The vacuum conditions of the accelerator chamber are not perfect. There is a certain residual gas density inside the chamber, and the beam particles can interact with the gas molecules.

The beam-gas scattering can be elastic or inelastic. The former changes the direction of the beam particle while its energy is not affected; the latter changes the beam particle energy. Information on the total cross section for different gases can be found in [48].

#### Elastic scattering processes

A charged particle traversing a medium is deflected by the Coulomb potential of the particles in the residual gas. This, alone or in combination with other nonlinear phenomena, for example optics nonlinearities, can lead to large betatron amplitudes and loss of particles at collimators or any other aperture restriction. We will survey the following elastic scattering phenomena: single Coulomb scattering of spin-1/2 beam particles off an unpolarized target nucleus, multiple Coulomb scattering and elastic nuclear scattering.

- *Single Coulomb scattering of spin-1/2 particles:*

The cross section for single Coulomb scattering, also denominated *Mott scattering*, is given by [50]

$$\left( \frac{d\sigma_{\text{el}}}{d\Omega} \right)_{\text{Mott}} = \left( \frac{Zr_q}{2\gamma} \right)^2 F^2(q) \frac{1 - \beta_v^2 \sin^2(\theta/2)}{\sin^4(\theta/2) \left( 1 + 2 \frac{E}{Mc^2} \sin^2(\theta/2) \right)}, \quad (3.6)$$

with  $Z$  and  $M$  the charge and the mass of the gas nuclei respectively,  $r_q$  the radius of the incident particle,  $E$  the energy of the incident particle,  $\gamma \equiv E/m_q c^2$  and  $\beta_v c$  the Lorentz factor and the speed of the incident particle respectively, and  $\theta$  the scattering angle. In addition,  $F(q)$  is the nuclear form factor, which for relatively small scattering angles can be approximated by 1. Note that in the nonrelativistic regime, i.e.  $\beta_v \ll 1$ , and for  $m_q \ll$

$M$ , one can approximate the expression (3.6) by the classical Rutherford scattering formula  $d\sigma_{\text{el}}/d\Omega \propto 1/\sin^4(\theta/2)$ , and for small angles  $d\sigma_{\text{el}}/d\Omega \propto 1/\theta^4$ .

- *Multiple Coulomb scattering:*

The random accumulation of a large number of small angle scatters is called multiple Coulomb scattering. Assuming small deflection angles, the angular distribution can be approximated by a Gaussian with a rms width [48]

$$\theta_{\text{mC}} = \frac{13.6 \text{ MeV}}{\beta_v c p} z_q \sqrt{L_R} [1 + 0.038 \ln(L_R)] , \quad (3.7)$$

where  $p$ ,  $\beta_v c$  and  $z$  are the momentum, velocity and charge number of the incident beam particle, and  $L_R \equiv z/z_R$  is the thickness of the scattering medium in units of radiation length (r.l.)  $z_R$ . The radiation length is defined as the mean distance over which a high energy electron loses all but  $1/e$  of its energy by bremsstrahlung.

The expression (3.7) is accurate to 11 % or better for  $10^{-3} < L_R < 100$ .

The beam-gas multiple Coulomb scattering can cause an increase of the transverse beam emittance, thus contributing to the population of the beam halo. A similar effect occurs when the beam particles strike a thin spoiler. In this case the particles acquire a net rms angle given in good approximation by the distribution of Eq. (3.7), thus increasing the number of halo particles, which will be intercepted by downstream absorbers or secondary collimators (see the spoiler/absorber scheme or the multi-stage collimation concept in sections 2.1.1 and 2.1.2, respectively).

- *Elastic nuclear scattering:*

This process is exclusively relevant for hadronic beams, such as in the LHC (with beams of protons or ions). The differential cross section of proton-nucleus elastic scattering can be parameterized as [51]

$$\frac{d\sigma_{\text{nuc}}^{\text{el}}}{dt} = \sigma_{pN}^{\text{el}} B_{\text{coh}} e^{-B_{\text{coh}}(A)|t|} + \sigma_{pn}^{\text{el}} B_{\text{incoh}} e^{-B_{\text{incoh}}|t|} . \quad (3.8)$$

Here  $t = -(p\theta)^2$  is the momentum transfer expressed in terms of the momentum  $p$  of the incoming proton and the scattering angle  $\theta$ . The coefficients  $\sigma_{pN}^{\text{el}}$  and  $B_{\text{coh}}$  represent the total cross section and the slope of proton coherent scattering, respectively. This process is called *coherent* because all the nucleons of the gas nuclei react as a single body, diffracting the incoming protons. A second term is added in expression (3.8), with the coefficients  $\sigma_{pn}^{\text{el}}$  and  $B_{\text{incoh}}$ , which represent the total cross section and the slope of the proton incoherent scattering, respectively. This process is denominated *incoherent* or *quasielastic*, since it describes the proton individual scattering with some of the nucleons forming the gas nuclei.



The slope  $B_{\text{coh}}$  can be obtained from experimental data on elastic scattering for 70, 125 and 175 GeV protons on various targets materials [52]. The log-linear fit to the scattering data of 175 GeV gives [51],

$$B_{\text{coh}} \simeq 12.85 A^{2/3} \text{ GeV}^{-2} . \quad (3.9)$$

Note the dependence of  $B_{\text{coh}}$  on the atomic number  $A$  of the target.

The slope of incoherent scattering is usually obtained from abundant experimental data on proton-proton elastic scattering <sup>1</sup> [53]. From the extrapolation of  $B_{\text{incoh}}$  to the region of the LHC beam-gas proton-proton collision energy (with center-of-mass energy  $\sqrt{s_{\text{coll}}} \approx \sqrt{2m_p p} = 114.59 \text{ GeV}$ , with  $m_p$  the proton mass and  $p = 7000 \text{ GeV}$ ), the following behavior is predicted [54]

$$B_{\text{incoh}} \simeq (8.5 + 1.086 \ln \sqrt{s}) \text{ GeV}^{-2} . \quad (3.10)$$

The elastic proton-proton cross section  $\sigma_{pp}^{\text{el}}$  ( $\sigma_{pp}^{\text{el}} \approx \sigma_{pn}^{\text{el}}$ ) can be obtained from experimental data [48], which are represented in Fig. 3.1 as a function of the momentum  $p$  (in the Lab frame) of the incoming proton. One can see that for  $p = 450 \text{ GeV}$  (the LHC beam energy at injection)  $\sigma_{pp}^{\text{el}} \approx 7.0 \text{ mb}$ . For  $p > 450 \text{ GeV}$ , the data varies slowly with the beam momentum, and can be fitted to a linear function on a logarithmic scale [45],

$$\sigma_{pp}^{\text{el}} \approx \sigma_{pp}^{\text{el}}(p = 450 \text{ GeV}) \left( \frac{p}{450 \text{ GeV}} \right)^{0.0479} , \quad (3.11)$$

where the cross-section at LHC injection momentum has been taken as reference. From Eq. (3.11), the value of the cross section at LHC collision energy can be estimated:  $\sigma_{pp}^{\text{el}}(p = 7000 \text{ GeV}) \approx 7.98 \text{ mb}$ .

### Inelastic scattering processes

- *Bremsstrahlung*:

In lepton accelerators, at high energy, the dominant process caused by inelastic beam-gas scattering is bremsstrahlung. The cross section for bremsstrahlung at high energies (assuming complete screening from the atomic electrons) can be approximated by [56]

$$\sigma_{\text{brem}} \simeq \frac{16}{3} \alpha Z(Z + 1.35) r_e^2 \ln \left( \frac{183}{Z^{1/3}} \right) \left[ \ln \left( \frac{\delta_{\text{max}}}{\delta_{\text{min}}} \right) + \delta_{\text{min}} - \delta_{\text{max}} \right] , \quad (3.12)$$

---

<sup>1</sup>Proton-neutron scattering is considered approximately equal to proton-proton scattering, the latter one being more exhaustively measured and characterized by more abundant data.

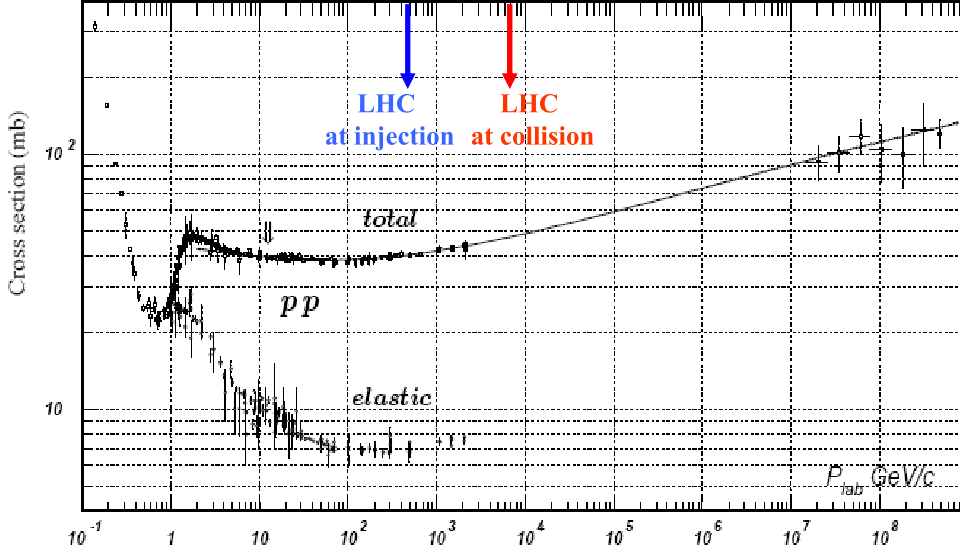


Figure 3.1: Total and elastic proton-proton cross sections [55]. The arrows indicates the LHC beam energy at injection and at collision.

where  $\alpha$  is the fine-structure constant,  $\delta_{\min}$  and  $\delta_{\max}$  are the minimum and maximum photon energies emitted in units of the beam energy. The factor  $Z(Z + 1.35)$  accounts for the nuclear charge and includes the contribution from the atomic electrons.

The angular cross section of this process scales as [57]

$$\frac{d\sigma_{\text{brem}}}{d\Omega} \sim \frac{\theta}{(1 - \cos \theta + \gamma^{-2})^2} . \quad (3.13)$$

Figure 3.2 compares the cross section of bremsstrahlung with the Mott scattering as a function of scattering angle. At small scattering angles  $\theta$ , the Mott scattering is the dominant process.

The number of scattered beam particles can be estimated by

$$\frac{\Delta N}{N} = n_{\text{gas}} L \sigma_{\text{brem}} , \quad (3.14)$$

where  $L$  is the distance travelled by the beam and  $n_{\text{gas}}$  is the residual gas density in the vacuum pipe, which can be expressed as  $n_{\text{gas}} = 3.2 \times 10^{22} P N_{\text{atom}} \text{ m}^{-3} \text{ Torr}^{-1}$  at 300 K, with  $P$  the vacuum pressure, and  $N_{\text{atom}}$  the number of atoms per molecule of gas. As an example, assuming  $N_2$  as the remanent gas inside of the vacuum pipe,  $\delta_{\min} = 0.01$  and  $\delta_{\max} = 1$ , one has  $\sigma_{\text{brem}} \simeq 5.2 \text{ barn}$ . Assuming further 10 nTorr pressure at 300 K of temperature,

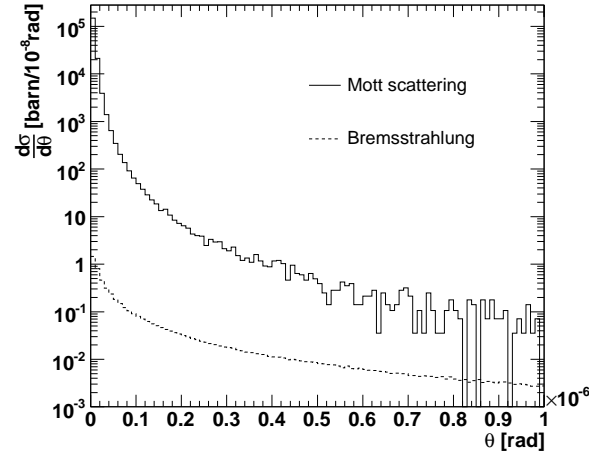


Figure 3.2: Cross sections for elastic Mott scattering (solid line) and bremsstrahlung (dashed line) as a function of the scattering angle. Courtesy of L. Neukermans.

then about 3000 particles per bunch train suffer scattering by bremsstrahlung in the CLIC Linac+BDS (16.5 km long). In this estimate the following CLIC parameters have been assumed:  $2.56 \times 10^9$  electrons (positrons) per bunch, and 220 bunches per train.

- *Inelastic nuclear scattering:*

This process is only relevant for hadronic machines, where protons or ions interact with the nucleus of the rest-gas in the vacuum pipe.

When a high energy proton (kinetic energy  $> 1$  GeV) strikes a nucleus there is a high probability of inelastic scattering. The circulating protons can interact either coherently with the nuclei of the rest-gas or incoherently with their individual nucleons. In these reactions secondary particles are emitted. The energy of such secondaries is much lower than the primary energy, and these particles are usually lost in downstream bending magnets. Losses may be distributed all around the machine and the dedicated global collimation sections be not effective against them. The number of losses produced in this way can be calculated from the inelastic nuclear cross-section, taking into account both the proton-nucleon ( $pn$ ) and the proton-Nucleus ( $pN$ ) scattering. The proton-nucleon scattering refers to both the proton-proton ( $pp$ ) scattering and the proton-neutron scattering.

The total  $pp$  cross-section, i.e. including both the elastic and the inelastic contributions, can be evaluated from experimental data of Fig. 3.1 as a function of the beam momentum. In the range  $> 20$  GeV the data are well represented by the Regge theory [58]:

$$\sigma_{pp}^{\text{total}} = 22 \cdot s^{0.079} + 56.1 \cdot s^{-0.46}, \quad (3.15)$$

with  $s \approx 2m_p p$  the square of the center-of-mass energy ( $m_p$  being the proton mass).

The cross section of the inelastic  $pp$  scattering can be evaluated by subtracting the elastic contribution from the total cross-section,

$$\sigma_{pp}^{\text{inel}} = \sigma_{pp}^{\text{total}} - \sigma_{pp}^{\text{el}} . \quad (3.16)$$

Fig. 3.3 compares the  $pp$  total cross section from Eq. (3.15) with the elastic  $pp$  cross section from Eq. (3.11) and the inelastic part from Eq. (3.16).

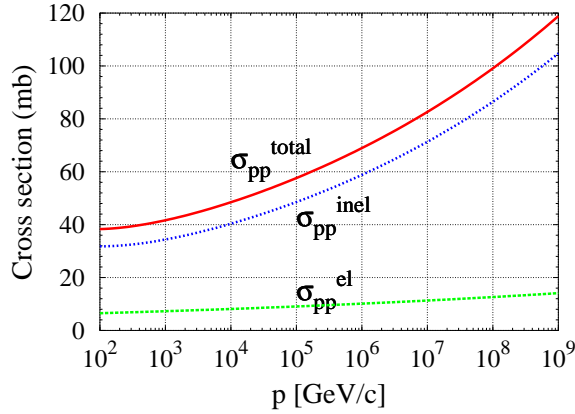


Figure 3.3: Total  $pp$  cross section as given by Eq. (3.15), elastic  $pp$  cross section as given by Eq. (3.11), and inelastic  $pp$  cross section as given by Eq. (3.16).

Another possible inelastic process is the diffractive proton-proton scattering. It consists of a coherent excitation of one of the protons in a gas nucleus into a resonance state, i. e.  $pp \rightarrow Xp$ , where  $X$  is an excited nucleon state with mass  $M_X > m_p$ . This process is dominant within the range  $m_0^2 < m_X^2 < 0.15s$ , where the lower limit is  $m_0 = (m_p + m_\pi) \approx 1 \text{ GeV}/c^2$ , with  $m_\pi$  the pion mass. The nucleus with excited nucleons can decay via the emission of lower energy particles in a so-called evaporation process (emission of neutrons,  $\alpha$  particles, deuteron, etc.). The diffractive nuclear effect has been studied extensively in [59].

Concerning the proton-nucleus inelastic scattering, experimental data of inelastic neutron-nucleus scattering have been analyzed in [60] for energies in the 160-375 GeV range. According to Ref. [60],  $\sigma_{pN}^{\text{inel}} \approx \sigma_{nN}^{\text{inel}}$  can be assumed. This cross section scales approximately with the atomic mass as  $A^{0.71}$ , and the total cross section (elastic + inelastic) scales as  $A^{0.77}$  [60].

### 3.1.3 Scattering off thermal photons

An important source of beam halo in electron or positron accelerators is Compton scattering off thermal photons. This effect was identified as the largest contribution to the beam lifetime without

collision in LEP [40–42]. This process has also been extensively studied for the NLC.

The total cross section for Compton scattering of a electron (positron) beam and a photon is given by [61]

$$\sigma_c = \frac{2\pi r_e}{u} \left[ \left( 1 - \frac{4}{u} - \frac{8}{u^2} \right) \ln(u+1) + \frac{1}{2} + \frac{8}{u} - \frac{1}{2(u+1)^2} \right], \quad (3.17)$$

with the scattering factor

$$u = \frac{4E\omega\hbar}{m_e^2 c^4} \cos^2(\theta/2), \quad (3.18)$$

where  $E$  and  $\hbar\omega$  are the beam and incident photon energy respectively,  $m_e$  the electron mass, and  $\theta$  is the angle of the incident photon with respect to the beam in the laboratory system.

The energy of the scattered photons,  $\hbar\omega'$ , extends between 0 and a maximum value  $\hbar\omega'_{\max}$

$$0 \leq \hbar\omega' \leq \hbar\omega'_{\max} = \frac{u}{1+u} E. \quad (3.19)$$

The thermal photon density is described by the well known Planck black-body formula

$$\frac{dn_\gamma}{d\omega} = \frac{\omega}{\pi^2 c^3 (e^{\hbar\omega/kT} - 1)}, \quad (3.20)$$

with a photon density of  $n_\gamma \approx 2 \times 10^7 T^3$  [ $\text{K}^{-3} \text{ m}^{-3}$ ] and an average photon energy of  $\hbar\langle\omega\rangle = 2.7kT$ , where  $k$  is the Boltzmann constant. If a beam of  $N$  particles is propagating through a distance  $L$ , its distribution of large-amplitude scatterings can be obtained by integrating the product of cross section and Planck spectrum over the solid angle  $d\Omega$  and over all photon energies, i.e. [61]

$$\frac{1}{N} \frac{dN}{d\omega'} = L \int_0^\pi \int_{\omega_{\min}}^\infty \frac{d\sigma_c}{d\omega'} (1 + \cos\theta) dn_\gamma(\omega, T) \hbar d\omega \frac{d\Omega}{4\pi}, \quad (3.21)$$

where the factor  $(1 + \cos\theta)$  accounts for the relative motion of the electron and the photon, and  $\hbar\omega_{\min}$  is the minimum photon energy capable of producing a fractional energy loss  $\hbar\omega'/E$ , given  $E$  and  $\theta$ ,

$$\hbar\omega_{\min} = \frac{\hbar\omega' m_e^2 c^4}{4(E - \hbar\omega')E \cos^2 \theta/2}. \quad (3.22)$$

Assuming that half the photons are scattered to the maximum energy, the number of large-amplitude scatterings off thermal photons can be roughly estimated by using the following simpler expression:

$$\frac{\Delta N}{N} = \frac{1}{2} n_\gamma L \sigma_c, \quad (3.23)$$

where  $n_\gamma$  is the photon density,  $L$  the distance the beam travels and  $\sigma_c$  is obtained from Eq. (3.17). As an example, at room temperature (300 K)  $n_\gamma = 5.4 \times 10^{14} \text{ m}^{-3}$ . The total cross section  $\sigma_c$  is

close to the Thomson cross section  $\sigma_{\text{th}} \approx 8\pi r_e^2/3 \approx 0.7$  barn. Therefore, for the 16.5 km CLIC Linac+BDS system about 200 particles per bunch train are scattered by thermal photons.

In the case of a circular  $e^+e^-$  collider, such as the LEP, assuming that all scattered particles are lost, the beam lifetime can be evaluated from

$$\tau = \frac{1}{cn_\gamma\sigma_c} \approx \frac{1}{cn_\gamma\sigma_{\text{th}}} , \quad (3.24)$$

where the cross section  $\sigma_c$  can be approximated by the Thomson cross section  $\sigma_c \approx 0.7$  mb. For LEP the beam lifetime due to Compton scattering on thermal photons has been estimated to be  $\tau = 60$  hours.

### 3.1.4 Intra-bunch scattering processes

Coulomb scattering processes suffered by particles inside the same circulating bunch induce an exchange of energy between the transverse (betatronic) and longitudinal oscillations. If the relative energy deviation after scattering exceeds the energy acceptance of the machine the particle is lost. Two kinds of processes can be distinguished: the so-called *intra-beam scattering* (IBS) and the so-called *Touschek effect*. The former is due to multiple Coulomb scattering, while the Touschek effect is a single scattering effect.

#### Touschek scattering

In storage rings, the Touschek effect refers to the single particle-particle Coulomb collision within the same bunch, where the energy transferred from the transverse to the longitudinal phase space could be as high as the scattered particles could leave the stable RF bucket. This effect was first seen in the small AdA storage ring [62] and explained by Bruno Touschek.

The Touschek effect is the main limitation of the beam lifetime for all low-energy  $e^+e^-$  rings and most synchrotron light sources. This effect is also important in the damping rings of future linear colliders, such as CLIC and ILC. It further causes proton beam loss and halo formation at the LHC.

The inverse Touschek lifetime can be obtained from the following expression [63]

$$\frac{1}{\tau_{\text{Tous}}} = \frac{r_q^2 c N_0}{8\pi\gamma^2 \delta_{\text{max}}^2 \sigma_z} \int_0^C \frac{D(\varepsilon)}{\sigma_x \sigma_y} ds , \quad (3.25)$$

where  $\tau_{\text{Tous}}$  is the beam lifetime limit owing to the Touschek effect, and the following parameter notation is used:

$$\varepsilon = \left( \frac{\delta_{\text{max}}}{\gamma \sigma_\delta} \right)^2 , \quad (3.26)$$

where  $\varepsilon$  is the momentum acceptance, with  $\delta_{\text{max}} \equiv (\Delta E/E)_{\text{RF}}$ , limited by dynamics or RF voltage, and  $\sigma_\delta$  the rms energy spread of the beam distribution. In Eq. (3.25) the average effect over the

whole circumference is taken into account by integrating over the longitudinal coordinate  $s$ .

For *round beams* the function  $D(\varepsilon)$  is given by [64]

$$D(\varepsilon) = \sqrt{\varepsilon} \int_0^\infty \frac{1}{u^{3/2}} \left[ \left( \frac{u}{\varepsilon} \right) - \frac{1}{2} \ln \left( \frac{u}{\varepsilon} \right) - 1 \right] e^{-u} du . \quad (3.27)$$

For *flat beams*, such as in the case of the damping rings of linear colliders,  $D(\varepsilon)$  is given by [63]

$$D(\varepsilon) = \sqrt{\varepsilon} \left[ -\frac{3}{2} e^{-\varepsilon} + \frac{\varepsilon}{2} \int_\varepsilon^\infty \frac{e^{-u} \ln u}{u} du + \frac{1}{2} (3\varepsilon - \varepsilon \ln \varepsilon + 2) \int_\varepsilon^\infty \frac{e^{-u}}{u} du \right] . \quad (3.28)$$

An expression for the general case with arbitrary ratio of horizontal to vertical betatron amplitudes, arbitrary energies, and non zero derivative of the lattice functions ( $\beta'_{x,y}$ ,  $D'_{x,y}$ ) can be found in Ref. [65].

Some quantitative examples of  $\tau_{\text{Tous}}$  are shown in Table 3.1 for the CLIC damping ring at 2.424 GeV, and the LHC (with the nominal parameters) at injection energy (450 GeV) and at collision energy (7 TeV).

Table 3.1: Touschek lifetime value estimated for the CLIC damping ring [66], and for the LHC at injection energy and the LHC at collision energy [67].  $E$  denotes the corresponding beam energy.

Accelerator	$E$ [GeV]	$\tau_{\text{Tous}}$ [h]
CLIC damping ring	2.424	$\sim 4.19$
LHC at injection	450	$\sim 4830.9$
LHC at collision	7000	$\sim 12077.3$

### Intrabeam scattering

The IBS refers to multiple Coulomb scattering between particles within the same bunch. This involves a continuous interchange of energy between the interacting particles and between the (transverse and longitudinal) degrees of freedom, leading to emittance growth in all three directions. In proton accelerators, such as the LHC, IBS causes the beam to grow slowly over a period of several hours. This limits the luminosity lifetime. In circular lepton accelerators, such as in the damping rings of future linear colliders, IBS is counteracted by radiation damping, resulting in a new equilibrium beam emittance with a relaxation time on the order of milliseconds.

Two theories exist for computing this effect: Piwinski's [68] and Bjorken-Mtingwa's [69]. Both of these theories give a recipe how to estimate the emittance growth rate due to IBS. Recently a more general formulae for the three intrabeam scattering growth rates, including non-ultrarelativistic terms and vertical dispersion, has been derived by Frank Zimmermann in [70]. Table 3.2 shows some examples of IBS growth rates for CLIC and LHC.

Table 3.2: IBS growth rates estimated for the CLIC damping ring [70], and for the LHC at 7 TeV [70].

Accelerator	$\tau_z$ [ms]	$\tau_x$ [ms]	$\tau_y$ [ms]
CLIC damping ring	2.2	2.1	2.0
LHC at collision	$2.11 \times 10^8$	$3.75 \times 10^8$	$15.7 \times 10^8$

### 3.1.5 Beam-beam interaction

#### Beam-beam effects in storage rings

When two beams cross at the interaction point, on one hand, elastic and inelastic particle-particle collision occurs and, on the other hand, the electromagnetic field created by a beam can interact incoherently with the particles of the opposite beam and coherently with the bunches of the opposite beam (considering the coherent motion of all particles in a bunch).

Considering the incoherent beam-beam effect, when a test particle passes through the opposite bunch, it receives a small transverse impulse as a result of the electromagnetic field associated to the opposite beam. A derivation of the beam-beam force for both round ( $\sigma_x = \sigma_y$ ) and elliptical beams ( $\sigma_x \neq \sigma_y$ ) with a Gaussian distribution in the two transverse directions can be found in [71]. As an example, for round beams ( $\sigma_x = \sigma_y = \sigma$ ) the corresponding beam-beam force is given by [71]

$$F_r(r) = -\frac{ne^2(1 + \beta_v^2)}{2\pi\epsilon_0} \cdot \frac{1}{r} \cdot \left[ 1 - \exp\left(-\frac{r^2}{2\sigma^2}\right) \right], \quad (3.29)$$

in function of the amplitude  $r = \sqrt{x^2 + y^2}$ , with  $\beta_v \equiv v/c$  the relativistic factor ( $\beta_v \approx 1$  for ultrarelativistic beams),  $n$  the longitudinal density of particles in the beam,  $e$  the elementary charge, and  $\epsilon_0$  the permittivity of the free space. Depending on the sign of the two colliding beams, the force can be attractive or repulsive. Figure 3.4 shows the force and its derivative as a function of the amplitude  $r$ . For small amplitudes  $F_r(r)$  is approximately linear, and this results in a quadrupole-like tune change. In this sense, the incoherent beam-beam effect can be treated as a static thin lens. For amplitudes higher than  $1\sigma$  the force is no longer linear and the tune change depends on the amplitude.

The instantaneous tune shift of a particle when it crosses the other beam is related to the derivative of the force with respect to the amplitude. For a test particle with a small amplitude, the tune shift is given by the slope of  $F_r$  at the origin, which is called the *beam-beam parameter*

$$\xi_{x,y} = \frac{Nr_q\beta_{x,y}^*}{2\pi\gamma\sigma_{x,y}(\sigma_x + \sigma_y)}. \quad (3.30)$$

with  $r_q$  the particle radius,  $N$  the beam intensity and  $\beta_{x,y}^*$  is the  $\beta$ -function at the interaction point. The beam-beam parameter is often used to quantify the strength of the beam-beam interaction at the interaction point. The total beam-beam parameter over all interaction points is defined as



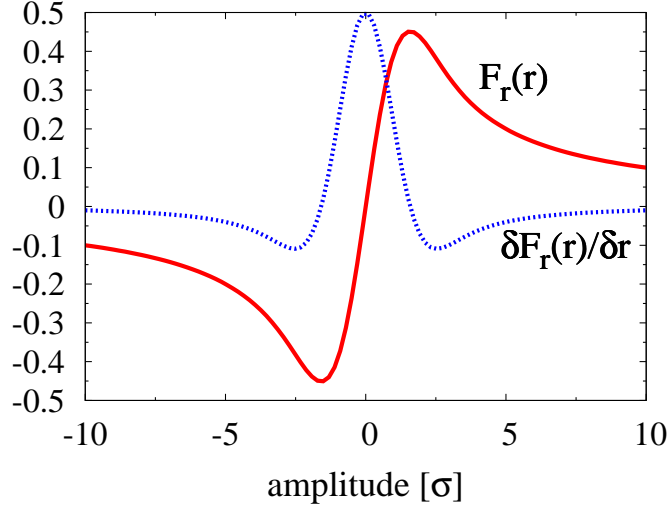


Figure 3.4: Beam-beam force (solid red line) and its derivative (dashed blue line) for round beams. Force in arbitrary units; amplitude in units of rms beam size.

$\xi_{\text{tot}} = n_{\text{IP}} \xi_{x,y}$ , with  $n_{\text{IP}}$  the number of interaction points.

In the majority of the colliders, *head-on* collisions occurs at the interaction point. However, in order to avoid the ‘parasitic’ collisions, in the LHC two bunches collide at a small angle (quasi head-on) at the centre, while the other bunches are kept separated by the crossing angle. The schematic of Fig. 3.5 illustrates this situation, where the crossing angle has been exaggerated. Actually in the LHC the value of the crossing angle is  $285 \mu\text{rad}$ . When the separation between opposite bunches is large, the beam-beam interaction receives the name of *long-range* beam-beam interaction. While the head-on collisions are strongest for small amplitude particles, the long-range one perturbs the motion at large amplitudes where particles come close to the opposing beam. They thereby may cause a denominated ‘diffusive’ (or dynamic) aperture [72], causing a fast particle loss at large aperture and possibly contributing thereby to a tail formation. Several diffusion models have been described in the literature to explain the proton tail formation. See, for example, Ref. [73] for a complete overview of the status of the studies on halo formation due to beam-beam collisions in both lepton and hadron accelerators.

In LEP the largest contribution to the halo formation (the shortest beam lifetime) in the vertical plane was the beam-beam bremsstrahlung at the interaction point [41, 42, 49]. The differential probability of incoherent bremsstrahlung for a single collision per particle is [74]

$$\frac{dN}{dE_\gamma} \approx 0.4 \frac{1}{E_\gamma} \alpha \left( \frac{r_e^2 N_2}{\sigma_x \sigma_y} \right) \left[ \ln \left( \frac{4\gamma^3 m_e c^2}{E_\gamma} \right) - \frac{1}{2} \right], \quad (3.31)$$

where  $E_\gamma > E_c \equiv 4\gamma^2 \hbar c / \sigma_z$ , and  $N_2$  denotes the bunch population of the opposing beam. The LEP halo was very sensitive to the residual vertical dispersion at the IP. Comparisons between

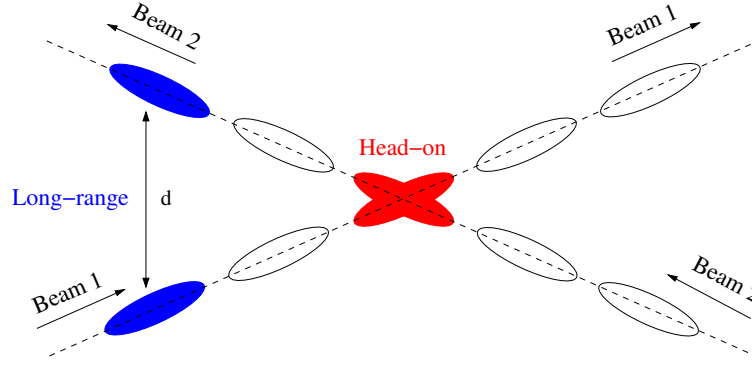


Figure 3.5: Head-on and long-range beam-beam interactions.

simulations and measurements at 45.6 GeV for a beam-beam parameter  $\xi_y \approx 0.025$  showed a reasonable agreement [42, 49] (see Fig. 3.6).

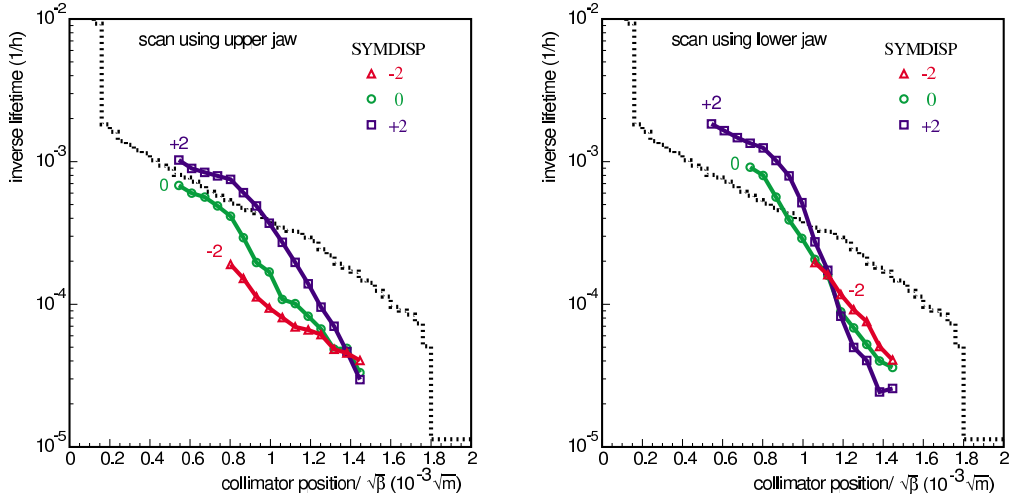


Figure 3.6: Vertical tails for different dispersions at the LEP interaction points at 45.6 GeV measured by upper jaw scan (left) and lower jaw scan (right) with  $\xi_y \approx 0.025$ . The dotted line corresponds to the simulation results for no dispersion at the IP and  $\xi_y = 0.025$  (Courtesy of Helmut Burkhardt from [49]).

Coherent bremsstrahlung, which occurs for  $E_\gamma < E_c \equiv 4\gamma^2\hbar c/\sigma_z$ , have been study for lepton-lepton scattering and for  $pp$  and  $p\bar{p}$  [75]. Most likely it does not much contribute to tail formation.

The lifetime due to beam-beam bremsstrahlung is given by [42]

$$\tau_{BB} = \frac{2r_e m_e}{n_{IP} f_{rev} \sigma_{BB}} \cdot \frac{\beta_y^*}{E \xi_y}, \quad (3.32)$$

where  $r_e$  and  $m_e$  are the radius and the mass of the electron, respectively,  $n_{IP}$  the number of collision

points (in LEP  $n_{\text{IP}} = 4$ ),  $f_{\text{rev}}$  the revolution frequency and  $\sigma_{BB}$  the total cross section leading to a loss of the scattered particle from the beam. Note the dependence on the beam energy  $E$  and the beam-beam tune shift  $\xi_y$ . For example, for LEP  $\tau_{BB} \approx 10 - 20$  hours depending on the beam energy and the beam-beam tune shift [42].

In hadron colliders, as the LHC, nuclear (elastic, inelastic, diffractive) interaction mechanisms take place at the IP. For what concerns emittance growth and emittance lifetime, only elastic and diffractive scatterings should be considered since inelastic interactions are designed to happen within the 4 detectors of the machine. For more details see the above description of the different nuclear scattering processes in this chapter. The corresponding transverse emittance growth rate can be calculated as [76]

$$\frac{1}{\epsilon_j} \frac{d\epsilon_j}{dt} = \frac{\sigma_{BB}^{\text{el}} \theta_{\text{el}}^2}{2\epsilon N_b N} \sum_i \beta_{ji}^* \mathcal{L}_i, \quad j = x, y, \quad (3.33)$$

where  $\beta_{ji}^*$  and  $\mathcal{L}_i$  are the  $\beta$ -functions and luminosity at the interaction point  $i$ . All the interaction points are added.  $\sigma_{BB}^{\text{el}}$  is the fraction of the elastic cross-section resulting in the emittance growth,  $\theta_{\text{el}}$  the rms projected elastic scattering angle,  $N_b$  the number of bunches, and  $N$  the number of particles per bunch.

In the case of ion-ion collisions, for example as in RHIC and LHC, two other incoherent collision processes, which are expected to contribute to the generation of tails and to limit the maximum reachable luminosity, are the  $e^+e^-$  pair production followed by electron capture, and the nuclear excitation with the subsequent neutron emission [77].

### Beam-beam effects in linear colliders

In linear colliders, where the bunches collide only once, intense  $e^+e^-$  beams and small cross sections are required in order to achieve high luminosity. This gives rise to intense electromagnetic fields that strongly affect the dynamics of the particles in the oncoming beam. Unlike for circular colliders, for linear colliders the generated beam-beam effects are not a halo and tail source, but an important background source and a cause of luminosity modification.

We can distinguish the following effects: the *disruption* [78, 79] and the *beamstrahlung* [80–82]. The primary effect of the disruption is a luminosity enhancement, i.e. the particles of the colliding beams are mutually focused by the electromagnetic force of the opposite beam towards the beam center. The result is a small effective beam size. This is also known as the *pinch effect*. All disruption effects can be described in terms of the horizontal and vertical *disruption parameters*

$$D_{x,y} = \frac{2r_e N \sigma_z}{\gamma \sigma_{x,y}^* (\sigma_x^* + \sigma_y^*)}, \quad (3.34)$$

where  $\sigma_{x,y}^*$  denotes the transverse rms beam sizes at the IP and  $N$  the number of particle per bunch. Note the similarities between Eq (3.34) and Eq (3.30). In linear colliders the parameter  $D_{x,y}$  plays a similar role that the beam-beam parameter  $\xi_{x,y}$  in circular colliders.

Since particles are bent by the field of the opposing beam charge (disruption effect), they emit synchrotron radiation, which is referred to as beamstrahlung. This causes the spread of the centre-of-mass energy. Thus, the luminosity is not peaked at the mean nominal energy but a luminosity spectrum is induced [83]. In addition, beamstrahlung is an important source of background. High-energy beamstrahlung photons can further interact with the beam fields and with each other through QED and QCD processes, generating  $e^+e^-$  pairs (coherent pair creation) and hadronic minijets. The latter are produced when a high energy photon produces a quark-antiquark pair.

Other sources of background due to beam-beam interaction include: incoherent pair creation and hadronic showers. The main contribution to the former process arise from  $ee \rightarrow ee(e^+e^-)$ ,  $e\gamma \rightarrow e(e^+e^-)$  and  $\gamma\gamma \rightarrow (e^+e^-)$ , with the photons coming from beamstrahlung. The hadronic showers can arise from high energy  $\gamma\gamma$  collisions. In addition, neutrons produced in the electromagnetic showers induced by the electrons and positrons lost in the final quadrupoles can also contribute to the detector background. A complete description of all these processes can be found in [84].

It is worthwhile to mention that excellent codes have been written to compute the beam-beam effects and beam-beam interactions in  $e^+e^-$  linear colliders, for example, CAIN [85] and GUINEA-PIG [86]. As an example, for CLIC, GUINEA-PIG predicts 700,  $3 \times 10^6$ ,  $7 \times 10^8$  and  $2 \times 10^9$  coherent  $e^+e^-$  pairs per bunch crossing for a center-of-mass energy of 0.5, 1, 3 and 5 TeV, respectively [84].

## 3.2 Collimator protection

The circular collider LHC and the linear colliders will store a transverse energy density per beam of the order of GJ/mm<sup>2</sup>. For this density energy the local deposition of heat can be so high that the collimator may be damaged. Therefore, in this section it is worth introducing some important issues for collimator protection as: the limit for instantaneous temperature rise of a collimator, and the main mechanisms for heat deposition in the collimator. Concerning the production of secondary particles due to a direct beam impact in the collimator, we also introduce briefly the muon production, which is relevant for the IP background.

### 3.2.1 Limit for instantaneous temperature rise of a collimator

Some criteria listed in the literature [16, 87] for estimating the maximum acceptable temperature rise in collimators are the following:

- Melting temperature point: the maximum allowed temperature excursion is given by

$$\Delta T_{\text{melt}} = T_{\text{melt}} - T_{\text{room}} , \quad (3.35)$$

with  $T_{\text{melt}}$  the melting temperature in Kelvin and  $T_{\text{room}} = 293.15$  K the room temperature.

- The mechanical fracture temperature:

$$\Delta T_{\text{fail}} = \frac{\zeta \sigma_{\text{uts}}}{\alpha_T Y}, \quad (3.36)$$

with  $\alpha_T$  the thermal expansion coefficient,  $\sigma_{\text{uts}}$  the ultimate tensile strength of the material and  $\zeta$  an empirical factor. For instance,  $\zeta = 1.5$  is adopted in Ref. [16] and  $\zeta = 2$  in Ref. [87].

- The vapor pressure of the collimator at its elevated operating temperature may be high enough to evaporate the surface of the material during the course of a run. The temperature for this process represents a higher limit than the melting and the fracture temperatures.

The safe limit is usually chosen as  $\Delta T_{\text{limit}} = \min[\Delta T_{\text{melt}}, \Delta T_{\text{fail}}]$ . Generally the minimum corresponds to  $\Delta T_{\text{fail}}$ . The limit temperature  $\Delta T_{\text{melt}}$  and  $\Delta T_{\text{fail}}$  are registered in Table 3.3 for several materials.

Table 3.3: The melting point temperature  $T_{\text{melt}}$ , the melting temperature excursion limit  $\Delta T_{\text{melt}} = T_{\text{melt}} - 293$  K, the thermal fracture temperature excursion limit  $\Delta T_{\text{fail}}$  (corresponding to the ultimate tensile strength from Eq. (3.36)), the elastic modulus  $Y$ , the coefficient of thermal expansion  $\alpha_T$  and the ultimate tensile strength  $\sigma_{\text{uts}}$ , for the following materials: beryllium (Be), graphite (C), titanium (Ti), titanium alloy (90 % Ti, 6 % Al, 4% V), copper (Cu) and tungsten (W). For Ti alloy we have assumed the same melting point as for pure Ti. Data obtained from [?, ?].

Material	$T_{\text{melt}}$ [K]	$\Delta T_{\text{melt}}$ [K]	$\Delta T_{\text{fail}}$ [K]	$Y$ [ $10^5$ MPa]	$\alpha_T$ [ $10^{-6}$ K $^{-1}$ ]	$\sigma_{\text{uts}}$ [MPa]
Be	1560	1267	370	2.87	11.3	600
C	3800	3507	14207	0.12	7.1	580
Ti (pure)	1941	1648	742	1.16	8.6	370
Ti alloy	1941(?)	1648(?)	1710	1.14	9.2	897
Cu	1358	1065	201	1.3	16.5	216
W	3695	3402	670	4.11	4.5	620

### 3.2.2 Collimator-beam interaction mechanisms

Next we will review the main sources which may contribute to the temperature rise at the collimators: image current heating and energy deposition by direct beam-matter interaction.

#### Image current heating

This is a collective effect. When a beam of charged particles passes through the aperture of the collimators, image currents are generated on the resistive surface of the collimator jaws.

Depending on the distance from the beam centroid to the jaw different cases can be distinguished (see Fig. 3.7):

- In the case  $a \gg \sigma_y$  (see Fig. 3.7 (A)), i.e. the beam is far away from the collimator and it can be considered as a transverse point-like beam. Assuming a Gaussian bunch of rms length  $\sigma_z$

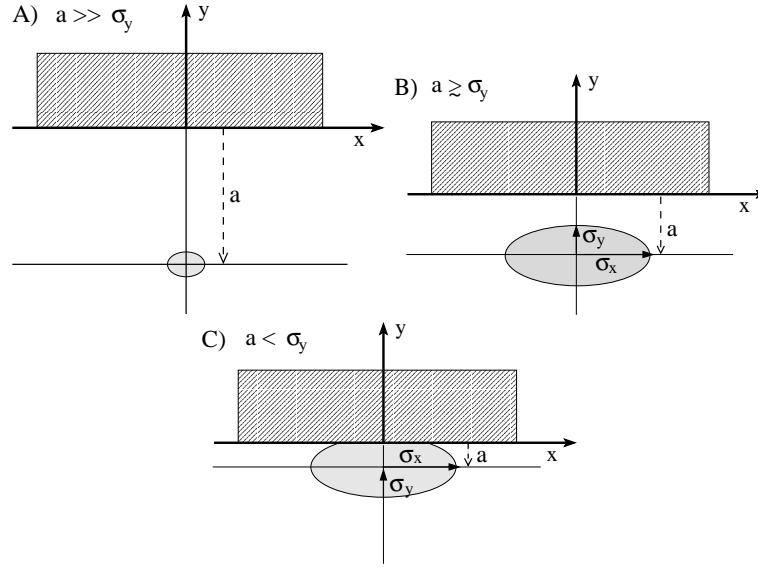


Figure 3.7: Schematic of a particle beam passing near a collimator jaw. Different cases for image current heating can be distinguished depending of the distance between the beam and the block of material.

and total charge  $Q = Nq$  (with  $N$  the number of particles per bunch and  $q$  the unit charge), the energy density deposited at the collimator surface by image current was calculated in Ref. [88] for a round pipe of radius  $r_0$ ,

$$E_d(x=0, y=0) = \frac{Z_0 c}{2\pi} \left( \frac{Q}{\pi \sigma_z} \right)^2 \frac{1}{4r_0^2}, \quad (3.37)$$

where  $Z_0 = 376.7 \, \Omega$  is the vacuum impedance and  $c$  the speed of light. We will make the assumption that the case of a beam centered in a rectangular collimator of half-gap  $r_0$  is comparable.

If  $a \ll r_0$  but the beam is still far enough away to be approximated as transverse point-like, the general expression for the energy density deposited by a single bunch centered at arbitrary position  $(x_0, y_0)$  is given by [87]:

$$E_d(x, y; x_0, y_0) = \frac{Z_0 c}{2\pi} \left( \frac{Q}{\pi \sigma_z} \right)^2 f^2(x; x_0, y_0) g(y/\delta(\omega_\sigma)), \quad (3.38)$$

where

$$f(x; x_0, y_0) = \frac{y_0}{y_0^2 + (x_0 - x)^2}, \quad (3.39)$$

and the called penetration function

$$g(y/\delta(\omega_\sigma)) = \int_0^\infty dz e^{-z} e^{-2\frac{y}{\delta(\omega_\sigma)} z^{1/4}}, \quad (3.40)$$

which depends on the skin depth  $\delta(\omega_\sigma) = \sqrt{2/(\omega_\sigma \mu_0 \sigma)}$ , with  $\omega_\sigma = c/\sigma_z$  the frequency spread,  $\mu_0$  the permeability of free space and  $\sigma$  the electrical conductivity of the collimator material.

It is necessary to mention that the expression (3.38) does not take into account the heat diffusion over the time scale  $\Delta t = \sigma_z/c$ , and it is then valid as long as the thermal diffusion length, defined by  $l_{\text{diff}} = \sqrt{(K/(\varrho C))(\sigma_z/c)}$ , is much smaller than the skin depth,  $l_{\text{diff}} \ll \delta(\omega_\sigma)$ . The parameters  $K$ ,  $\varrho$  and  $C$  are the thermal conductivity, density and specific heat, respectively, of the collimator material. Table 3.4 compares the values of  $l_{\text{diff}}$  and of  $\delta(\omega_\sigma)$  for the case of different accelerators. It is possible to see that the energy collimators for CLIC, ILC and LHC are in the regime  $l_{\text{diff}} \ll \delta(\omega_\sigma)$ . For details of the material properties, see the tables of Appendix B.

Table 3.4: The thermal diffusion length  $l_{\text{diff}}$  per bunch, the thermal diffusion per bunch train  $l_{\text{diff}}^{\text{train}}$ , the skin depth  $\delta(\omega_\sigma)$ , and the effective skin depth  $\delta_e$  in the case of the CLIC energy spoiler, the ILC energy spoiler and the LHC primary energy collimator. The nomenclature of the respective spoilers is indicated between brackets.

Accelerator	Material	$l_{\text{diff}}$ [ $\mu\text{m}$ ]	$l_{\text{diff}}^{\text{train}}$ [ $\mu\text{m}$ ]	$\delta(\omega_\sigma)$ [ $\mu\text{m}$ ]	$\delta_e$ [ $\mu\text{m}$ ]
CLIC (ENGYSPO)	Be	$2.47 \times 10^{-3}$	1.87	0.1	0.12
ILC (SPEX)	Ti	$3.59 \times 10^{-3}$	105.92	0.9	1.1
LHC (TPC.6L3.B1)	C	0.16	170.0	90.97	74.3

The single bunch pulsed heating can be approximately considered as an instantaneous energy deposition. In such a case, the instantaneous temperature rise becomes  $T_1(x, y) = E_d(x, y)/(\varrho C)$ .

From Eq. (3.40) it is straightforward to show  $g(y = 0) = 1$ , and assuming a point-like bunch centered at  $(x_0 = 0, y_0 = a)$ , one obtains

$$E_d(x = 0, y = 0) = \frac{Z_0 c}{2\pi} \left( \frac{Q}{\pi \sigma_z} \right)^2 \frac{1}{a^2}. \quad (3.41)$$

Therefore,  $T_1(x = 0, y = 0)$  can easily be estimated from:

$$T_1(x = 0, y = 0) = \frac{Z_0 c}{2\pi} \left( \frac{Q}{\pi \sigma_z} \right)^2 \frac{1}{a^2} \frac{1}{\varrho C}. \quad (3.42)$$

- Missteered beam can get close to the collimator surface, i.e.  $a \gtrsim \sigma_y$  (see Fig. 3.7 (B)). In such a case, the point-like transverse distribution approximation is no longer valid. Assuming a

bunch with Gaussian transverse distribution

$$\rho(x_0, y_0) = \frac{1}{2\pi\sigma_x\sigma_y} \exp\left(\frac{x_0^2}{2\sigma_x^2} - \frac{(y_0 - a)^2}{2\sigma_y^2}\right), \quad (3.43)$$

the energy density deposited instantaneously by the bunch passage is given by [87]

$$E_d(x, y) = \frac{Z_0 c}{2\pi} \left(\frac{Q}{\pi\sigma_z}\right)^2 g(y/\delta(\omega_\sigma)) \int_{-\infty}^{+\infty} dx_0 \int_{-\infty}^0 dy_0 f(x; x_0, y_0) \rho(x_0, y_0). \quad (3.44)$$

- When  $a \lesssim \sigma_y$  (see Fig. 3.7 (C)), part of the bunch penetrates the material surface. Other processes, such as radiation heating, which will be studied in the next section, will start to be important and they add to the image current heating. The maximum energy density deposition by image current before saturation can be estimated from [88]:

$$E_d^{\max}(x=0, y=0) = \frac{Z_0 c}{2\pi} \left(\frac{Q}{\pi\sigma_z}\right)^2 \frac{f_{\max}^2(\sigma_y/\sigma_x)}{\sigma_x\sigma_y}, \quad (3.45)$$

where the function  $f_{\max}$  is given by

$$f_{\max}(v) \approx \sqrt{\frac{1}{2\pi}} \frac{\ln(1 + \pi v)}{\sqrt{v}}. \quad (3.46)$$

The maximum temperature rise induced by a single bunch is then given by

$$T_1^{\max} = E_d^{\max}/(\rho C) \quad (3.47)$$

Using this equation we have represented  $T_1^{\max}$  as a function of the horizontal rms beam size  $\sigma_x$  for a fixed vertical rms beam size  $\sigma_y = 21.9 \mu\text{m}$  and for different materials, see Fig. 3.8 (top). The red point indicates  $T_1^{\max} \simeq 0.14 \text{ }^\circ\text{C}$ , which is the value calculated using the beam sizes at the CLIC energy spoiler ( $\sigma_x \simeq 1000 \mu\text{m}$  and  $\sigma_y \simeq 21.9 \mu\text{m}$ ). Another example of  $T_1^{\max}$  versus  $\sigma_y$  for different values of  $\sigma_x$  is shown in Fig. 3.8 (bottom) if the collimator is made of beryllium. The parameters of CLIC have been used for these calculations: the longitudinal beam size  $\sigma_z = 30.8 \mu\text{m}$  and  $N = 2.56 \times 10^6$  particles per bunch. We have used the material parameters of the Appendix B. Table 3.5 shows the values of  $T_1^{\max}$  induced by a single bunch in the energy collimators of CLIC, ILC and LHC.

Eq. (3.45) can be combined with Eq. (3.41) to roughly estimate the bunch-collimator distance at which the energy deposition by image current saturates. We obtain

$$a_{\max} \approx \sqrt{2\pi} \frac{\sigma_y}{\ln(1 + \pi\sigma_y/\sigma_x)}. \quad (3.48)$$



For future high energy linear colliders, such as CLIC and ILC, where the beam is transversely flat by design, i.e.  $\sigma_y/\sigma_x \ll 1$ , we can further approximate Eq. (3.48) by  $a_{\max} \approx \sqrt{2}\sigma_x/\sqrt{\pi}$ .

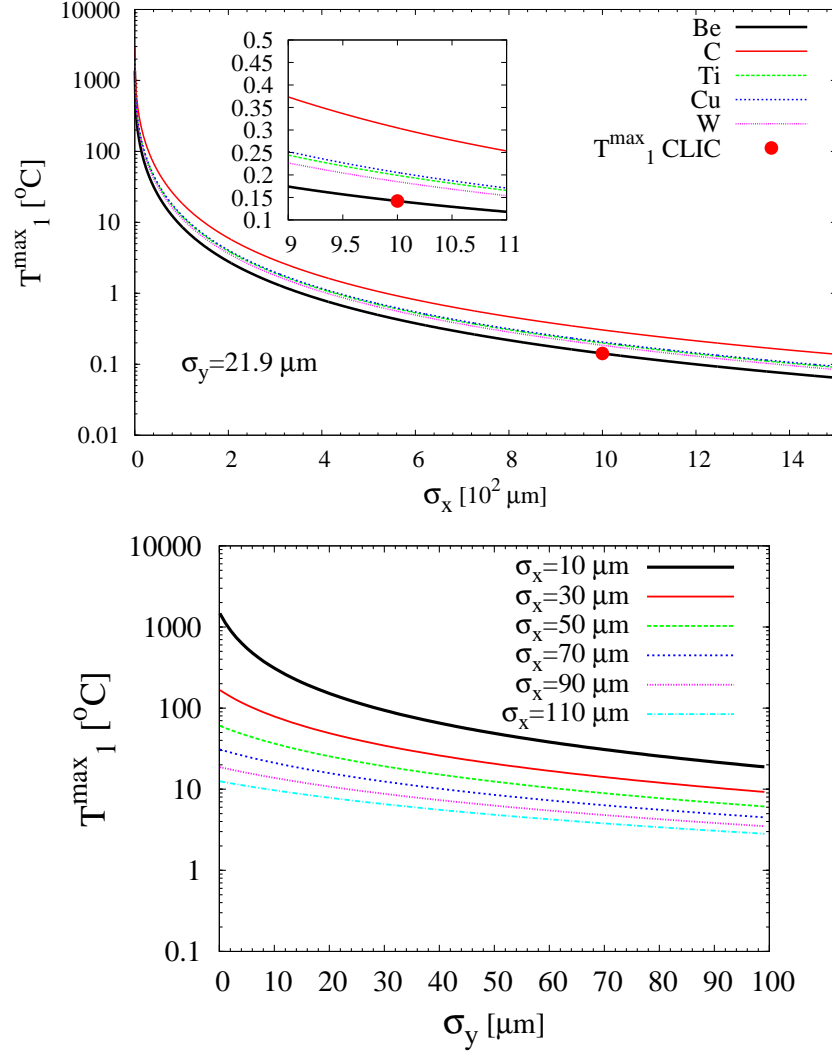


Figure 3.8: The maximum temperature rise induced by a single bunch versus the horizontal beam size  $\sigma_x$  fixed the vertical beam size,  $\sigma_y = 21.9 \mu\text{m}$ , for different collimator materials (top); the red point indicates the case of the CLIC energy spoiler. The maximum temperature rise versus  $\sigma_y$  for different values of  $\sigma_x$  if a Be collimator is chosen (bottom).

Until now we have considered a single bunch passage. Next we will give the corresponding expressions for the case of multibunch heating.

The thermal diffusion length of a bunch train is defined as  $l_{\text{diff}}^{\text{train}} = \sqrt{KN_b t_b / (\varrho C)}$ , with  $N_b$  the number of bunches per train and  $t_b$  the bunch separation in units of time. An effective skin depth of penetration is also defined:  $\delta_e = \Gamma(3/4) \sqrt{2\sigma_z / (c\mu_0\sigma)}$ . When  $\delta_e \sim l_{\text{diff}}^{\text{train}}$ , the general expression

for the temperature rise is given by [88]:

$$T_N(x=0, y=0, t) = \frac{E_d(x=0, y=0)}{\varrho C} \sum_{n=0}^{N_b-1} e^{\hat{x}_n^2} \text{erfc}(\hat{x}_n) H(t - nt_b) ,$$

$$\hat{x}_n = \sqrt{4D(t - nt_b)}/\delta_e , \quad (3.49)$$

where  $\text{erfc}(\hat{x}_n)$  is the complementary error function, which is defined by [89]

$$\text{erfc}(\hat{x}_n) = \frac{2}{\sqrt{\pi}} \int_{\hat{x}_n}^{\infty} e^{-t^2} dt . \quad (3.50)$$

Depending on the different cases listed above,  $E_d(x=0, y=0)$  of Eq. (3.49) is given by (3.37), (3.38), (3.41) or (3.45). The parameter  $D$  depends on the material and determines the diffusion length between pulses,  $l_{\text{diff}}^{\text{pulse}} = \sqrt{Dt_b}$ . The function  $H(t - nt_b)$  is the called Heaviside step function.

In the limit of short thermal diffusion length, i.e.  $l_{\text{diff}}^{\text{train}} \ll \delta_e$ , Eq. (3.49) can be reduced to

$$T_N = N_b T_1 , \quad (3.51)$$

where  $T_1$  is the temperature rise for a single bunch (see Eq. (3.42)).

On the other hand, in the limit of long thermal diffusion length, i.e.  $l_{\text{diff}}^{\text{train}} \gg \delta_e$ ,

$$T_N = 2\sqrt{N_b} \frac{E_d}{\sqrt{\pi K \varrho C t_b}} \frac{\delta_e}{2} , \quad (3.52)$$

and the maximum temperature rise induced by a multibunch train will be given by [88]

$$T_N^{\text{max}} = \frac{2\sqrt{N_b} Q^2}{\sqrt{\pi K \varrho C t_b}} \frac{f_{\text{max}}^2 (\sigma_y/\sigma_x)}{\pi^2 \sigma_x \sigma_y} \sqrt{\frac{\mu_0}{2\sigma}} \left( \frac{c}{\sigma_z} \right)^{3/2} \frac{\Gamma(3/4)}{2\pi} . \quad (3.53)$$

As an example, for the sake of comparison, we have calculated the values of  $l_{\text{diff}}^{\text{train}}$  and  $\delta_e$  for the case of the energy collimators of CLIC, ILC and LHC (see Table 3.4). For these three cases  $l_{\text{diff}}^{\text{train}} \gg \delta_e$ , and therefore the maximum temperature rise  $T_N^{\text{max}}$  can be calculated using the Eqs. (3.53). The corresponding results are written in Table 3.5.

Fig. 3.9 shows the maximum temperature rise due to multibunch heating as a function of the rms horizontal beam size for different collimator materials, as calculated using the expression (3.53) with the parameters of Table 3.6 for CLIC and the material property parameters from Appendix B.

### Energy deposition by direct beam-matter interaction

This corresponds to a deep beam impact on the collimator. We need to distinguish: the electron (positron) beam-matter interaction and the proton beam-matter interaction.

- *Electrons or positrons interacting* with the collimator material, at low energies ( $\leq 10$  MeV) primarily lose energy by *ionization*, resulting in soft X-rays, which are absorbed within short

Table 3.5: Beam sizes, maximum temperature rise by single bunch heating and maximum temperature rise by multibunch heating in the case of the CLIC energy spoiler, the ILC energy spoiler and LHC primary energy collimator. The nomenclature of the respective spoilers is indicated between brackets.

Accelerator	Material	$\sigma_x [\mu\text{m}]$	$\sigma_y [\mu\text{m}]$	$\sigma_z [\mu\text{m}]$	$T_L^{\text{max}} [^\circ\text{C}]$	$T_N^{\text{max}} [^\circ\text{C}]$
CLIC (ENGYSP)	Be	1000.	21.9	30.8	0.141	1.138
ILC (SPEX)	Ti	180.4	11.	300	3.54	58.12
LHC (TPC.6L3.B1)	C	246.17	246.17	$7.55 \times 10^4$	$3.59 \times 10^{-4}$	0.3046

Table 3.6: Bunch population, number of bunches, rms longitudinal beam size, and bunch separation for CLIC, ILC and LHC.

Accelerator	$N$ (part. per bunch)	$N_b$ (bunches per train)	$\sigma_z [\mu\text{m}]$	$t_b$ [ns]
CLIC	$2.56 \times 10^9$	220	30.8	0.267
ILC	$2. \times 10^{10}$	2820	300	307.7
LHC (7 TeV)	$1.15 \times 10^{11}$	2808	$7.55 \times 10^4$	100

distance. Additionally, at energies around 1 MeV other process also contribute to energy loss: Møller scattering, Bhabha scattering and positron annihilation. Electron or positron scattering is considered as ionization when the energy loss per collision is below 0.255 MeV, and as Møller ( $e^-$ ) or Bhabha ( $e^+$ ) scattering when it is above [48].

At energies  $> 10$  MeV the electrons predominantly lose energy in matter by bremsstrahlung. In addition to the energy loss from bremsstrahlung, the particles undergo multiple elastic Coulomb scattering, which results in an increase of the angular spread of the primary particles. The rms angle increase by multiple Coulomb scattering for a spoiler of  $L_R$  radiation lengths is given by Eq. (3.7). The photons generated by bremsstrahlung can interact with matter and produce electron-positron pairs. This process is commonly called electromagnetic cascade.

Figure 3.10 compares the mean energy deposition ratio of all the above processes as a function of the beam energy. While the ionization energy loss rate rises logarithmically with energy, the bremsstrahlung losses rise nearly linearly, i.e.  $(dE/dL_R)_{\text{brems}} \propto -E$ . In addition, if the energy of the photons from the electromagnetic cascade is high enough, other heavier particles, such as  $\mu^\pm, \pi^\pm \dots$  can also be produced.

The mean longitudinal profile of the energy deposition in an electromagnetic cascade can be well described by the following distribution [48]

$$\left( \frac{dE}{dL_R} \right)_{\text{EM}} = Eb \frac{(bL_R)^{a-1} e^{-bL_R}}{\Gamma(a)}, \quad (3.54)$$

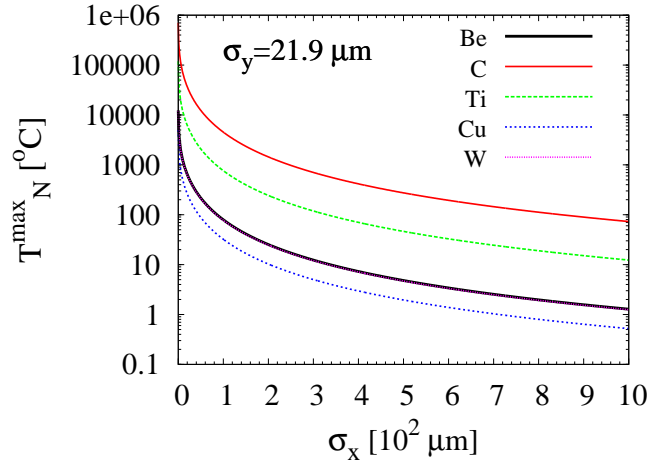


Figure 3.9: The maximum temperature rise induced by a multibunch train versus the horizontal beam size  $\sigma_x$  if  $\sigma_y = 21.9 \mu\text{m}$  for different collimator materials.

where  $a$  and  $b$  are fit parameters dependent on the material. The maximum deposition occurs at

$$L_R^{\max} = (a - 1)/b = \ln\left(\frac{E}{E_c}\right) + C_j, \quad j = e, \gamma, \quad (3.55)$$

with  $C_e = -0.5$  for electron-induced cascades and  $C_\gamma = +0.5$  for photon-induced cascades. The critical energy  $E_c$  is commonly defined as the energy at which the bremsstrahlung energy loss rate is equal to the ionization loss rate.  $E_c \simeq 610 \text{ MeV}/(Z + 1.24)$  in case of a solid target material and  $E_c \simeq 710 \text{ MeV}/(Z + 0.92)$  in the case of gases [48]. The parameter  $a$  can be calculated from Eq. (3.55) assuming  $b \approx 0.5$ ,

$$a \simeq 0.5 \left[ \ln\left(\frac{E}{E_c}\right) + C_j \right] + 1. \quad (3.56)$$

Figure 3.11 shows the longitudinal profile of the energy deposition taking a beam energy  $E = 1.5 \text{ TeV}$  and considering different collimator materials ( $Z$ ). For instance, if we consider a beryllium spoiler of 0.5 r.l. and a 1.5 TeV electron beam, the beam energy deposition by electromagnetic cascade is  $(dE/dL_R)_{\text{EM}} \simeq 0.023 \text{ GeV}$ . In the same conditions, for a beryllium spoiler of 1.0 r.l. we obtain  $(dE/dL_R)_{\text{EM}} \simeq 0.4 \text{ GeV}$ .

From electron-nucleus interaction hadronic cascades can be initiated. In the beam energy range  $6 \leq E \leq 60 \text{ MeV}$ , the electron can excite the nucleus, generating the so-called giant resonances. This is a collective nuclear excitation, where the neutrons oscillate against the protons. The de-excitation proceeds with high probability via neutron emission as a  $(\gamma, n)$  reaction. For higher energies also  $(\gamma, p)$  and  $(\gamma, np)$  channels are open. The resultant high

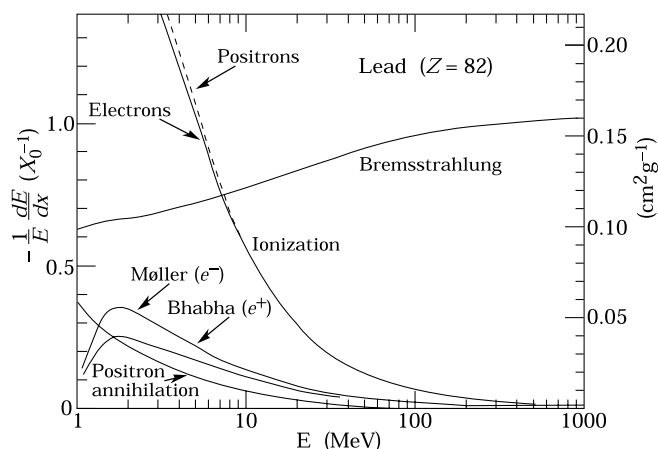


Figure 3.10: Fractional energy loss per radiation length in lead as a function of electron or positron energy. From Ref. [48].

energy neutrons and protons can then generate a hadronic cascade.

- *The interaction of high energy protons* with the collimator material is a complex process, including: ionization energy loss, multiple Coulomb scattering, elastic and inelastic proton-nucleon and proton-nucleus scattering, and electromagnetic cascades initiated by photons from the decay of secondary particles.

At high incident beam energies the inelastic scattering is the dominant process. When a high energy nucleon strikes a nucleus the collision gives rise to a large number of particles (by the strong interaction at the quark level), principally nucleons, pions and kaons, thus generating hadronic cascades. Fig. 3.12 (left) compares the ionization-range<sup>2</sup> of protons in various materials and their probability of inelastic interaction within that range, as a function of the proton energy. One sees that for energies above 1 GeV, the inelastic scattering probability rises to nearly 100 % before the proton reaches the end of its ionization-range. Most of the final channels of these nuclear reactions include neutron emission. As an example, for the stopping of one 1-GeV proton in copper or iron, ~ 10 fast neutrons are liberated. The neutron yield scales approximately with  $E$  for beam energies above 1 GeV, see Fig. 3.12 (right).

The principal mechanisms by which the flux of secondary particles is attenuated are ionization energy loss and multiple scattering. Neutrons above ~ 150 MeV take on the dominant role in the hadronic cascade propagation because they are the most penetrating particles. Additionally electromagnetic cascades can also be generated by the decay of pions and kaons, which can produce leptonic pairs ( $e^+e^-$  and  $\mu^+\mu^-$ ). It is important to mention that for protons with energy higher than a few tens TeV, the radiative mechanisms (bremsstrahlung and direct  $e^+e^-$  pair production) dominate on the ionization losses, especially in heavy materials.

<sup>2</sup>The ionization-range is defined as the distance travelled by the particle inside the block of material before deposition of its total energy by ionization.

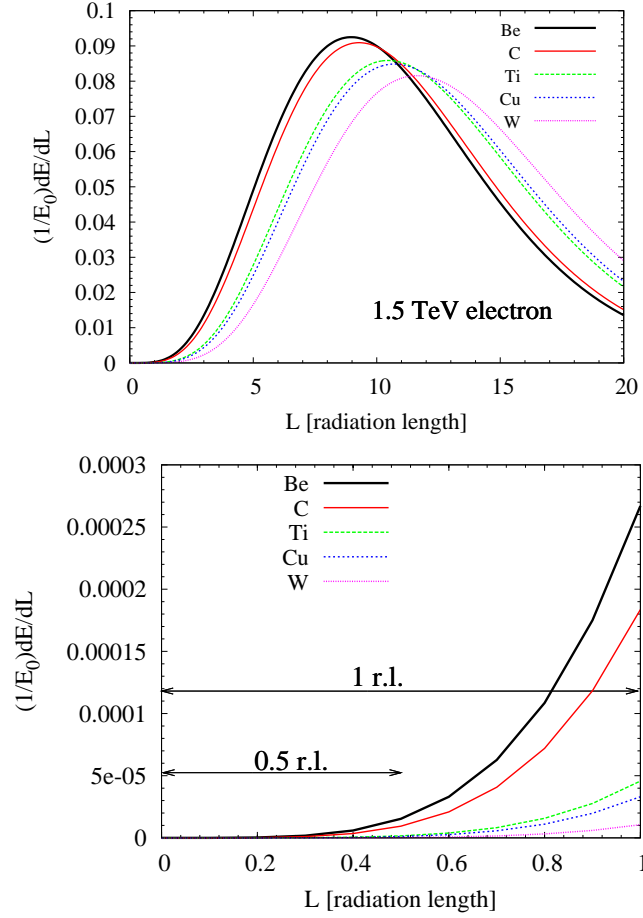


Figure 3.11: Energy deposition distribution per radiation length for different materials. From Eq. (3.54) with  $b = 0.5$ . Bottom: zoom of the range  $[0, 1]$  r.l.

The study of the multiplicity of the emitted secondary particles as well as their energy and angular distributions is complicated and all these quantities depend on the individual interaction cross sections. For this task, complex Monte-Carlo codes, such as FLUKA [91], are generally used. As an example, we will next show some results from a simulation with FLUKA of a direct interaction of an LHC beam at collision energy (7 TeV) with a square block made of graphite. The dimensions of this block of material are: height of 25 mm, length of 0.6 m and total width of 80 mm (the dimensions of an LHC primary collimator). A total energy of about 27 GeV is deposited in the material<sup>3</sup> This energy is deposited mainly by ionization from secondary particles (nucleons, pions, leptonic pairs, ...). The electromagnetic shower (all the photons, electrons and positrons which fall below the transport threshold of FLUKA) contribute with approximately 18.3 GeV. Different contributions to the energy balance are

<sup>3</sup>This quantity is simply estimated from the balance “entering-escaping” energy from the system.

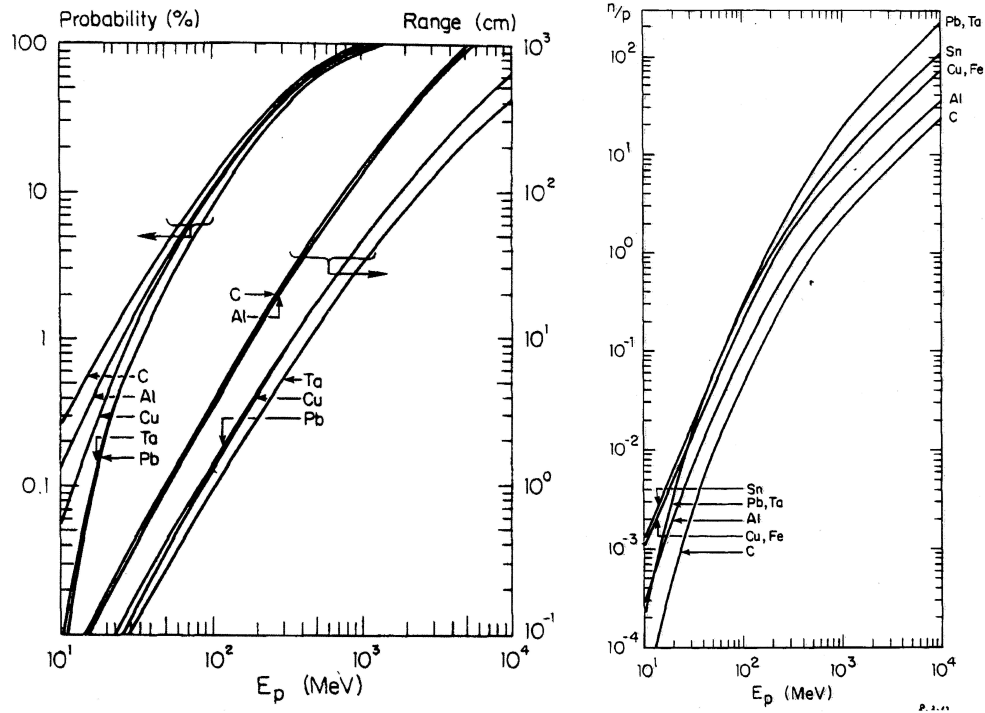


Figure 3.12: Left: Proton ionization ranges in various metals and probability of inelastic nuclear interaction within the range as a function of the proton kinetic energy. Right: Total number of neutrons per proton incident on a thick target of various metals as a function of the proton energy. From [90].

shown in Table 3.7

Table 3.7: Contribution from different secondaries to the total energy deposited by a single proton (at 7 TeV) hitting a block of graphite. The values have been estimated from a simulation with the code FLUKA.

Particles	Energy [GeV]
Hadrons, muons	7
EM cascade ( $e^+$ , $e^-$ , $\gamma$ )	18.3
Low energy neutrons	0.01
Nuclear fragments recoil ( $\text{He}_4$ , $\text{He}_3$ , deuteron, p, n)	0.9

Additionally every primary proton creates a hadronic cascade, which yields an average of  $\sim 60$  inelastic nuclear interactions. Out of these, about of 7.26 (12.1 %) nuclear interactions are due to protons. Table 3.8 summarizes the FLUKA results for the secondary particles which have a very high probability of making a nuclear interaction.

In our example with FLUKA an average of 572 secondaries are generated in inelastic inter-

Table 3.8: Proportion of particles from the hadronic cascade which contribute to the generation of inelastic nuclear interactions. The values have been estimated from a simulation with the code FLUKA, using an LHC proton beam (at 7 TeV) directly interacting with a block of graphite.

Particles	# nuclear interactions [%]
p	12.1
n	14
$\pi^+/\pi^-$	29.9/13.1
kaons	$\sim 30$

actions per beam particle. Table 3.9 shows the percentage of the different types of particles produced.

Table 3.9: Secondaries which have a high probability of being generated by an LHC beam (at 7 TeV) which directly interacts with a block of graphite. The values have been estimated from a simulation with the code FLUKA.

Secondaries	# [%]
p	15
n	17
$\gamma$	5
$\pi^+\pi^-$	29
$\pi^0$	17
Kaons, deuteron, $\text{He}_3$ , $\bar{n}$ , $\bar{p}$	$\lesssim 1$

### Temperature Increase Due to Energy Deposition by Direct Beam-Matter Interaction

The most severe scenario for spoiler/collimator damage is the instantaneous heat deposition by direct beam-spoiler interaction. In this Section we study the most critical case, which is the instantaneous temperature rise of the spoiler due to a deep beam impact on the collimator. Assuming spoilers whose thickness is significantly small in terms of radiation length, e.g. 0.25 r.l. or 0.5 r.l., the charged particles deposit energy mainly by ionization. In this case, the instantaneous temperature rise is given by

$$\Delta T_{inst}(x, y, t = 0) = \frac{1}{\rho C} \left( \frac{dE}{dz} \right) \rho(x, y) , \quad (3.57)$$

where  $\rho$  is the density of the spoiler material,  $C$  the heat capacity and  $\rho(x, y)$  is an arbitrary transverse beam density. The energy deposition per unit of length is denoted as  $(dE/dz)$ , whose value can be determined from the Bethe-Bloch formula [48] (for electrons and positrons we can use the approximation given by the formula (3.54)). Properties for several materials, including the radiation length and the minimum energy deposition for ionization, are shown in Table B.1 and



Table B.2 of Appendix B.

If we assume a Gaussian beam with horizontal and vertical rms sizes  $\sigma_x$  and  $\sigma_y$ , respectively, at the spoiler position, then the peak of instantaneous temperature rise by the impact of a full bunch train is given by

$$\Delta\hat{T}_{inst} = \frac{1}{\rho C} \left( \frac{dE}{dz} \right) \frac{N_e N_b e}{2\pi\sigma_x\sigma_y}, \quad (3.58)$$

where we have assumed a train with  $N_b$  bunches, each of them containing  $N_e$  electrons.

During the impact of a full bunch train, the passage of a bunch through the spoiler occurs at a certain repetition frequency (depending on a certain bunch separation  $t_b$ ). In order to determine the time evolution of the temperature in the spoiler, it is necessary to solve the heat equation with a periodic excitation:

$$\frac{\partial T}{\partial t} = \frac{K}{\rho C} \nabla^2 T + \sum_{n=0}^{N_b-1} \frac{\Delta T_{inst}}{t_b N_b} \delta(t - nt_b). \quad (3.59)$$

The first term on the right hand side of Eq. (3.59) represents the heat conductivity, and the second term, containing the Dirac delta function  $\delta(t - nt_b)$ , takes into account the periodic heating bunch after bunch in the train.  $\Delta T_{inst}$  can be obtained from Eq. (3.58). Possible cooling mechanisms, e.g. radiation cooling, can also contribute to the heat equation. At very high temperatures cooling by thermal radiation (black body radiation) becomes important. The radiated power per transverse area is given by:

$$h = \varepsilon \sigma_{SB} T^4, \quad (3.60)$$

where  $\varepsilon$  is the emissivity of the material and  $\sigma_{SB} = 5.67 \times 10^{-8} \text{ Wm}^{-2}\text{K}^{-4}$  the Stefan-Boltzmann constant. If we take into account this cooling mechanism, a term  $-2\varepsilon\sigma_{SB}T^4K/(\rho C)$  has to be added to the right hand side of Eq. (3.59). Here we will neglect the contribution of the thermal radiation energy versus the energy deposited by ionization. Indeed, the ionization energy deposited during the passage of a train, crossing a length  $L$  of spoiler material can be calculated from

$$E_{ion} = N_b N_e L \frac{dE}{dz}. \quad (3.61)$$

Taking into account that the duration of a bunch train is  $N_b t_b$ , the corresponding energy emitted by thermal radiation (black body) writes

$$E_{black} = N_b t_b S \sigma_{SB} T^4, \quad (3.62)$$

where the emission surface is given by  $S = 2\sigma_x L$ . Let us consider, for example, a CLIC spoiler with length  $L = 0.5$  r.l. made of Be, and the following beam parameters:  $\sigma_x = 796 \mu\text{m}$ ,  $N_b = 312$  bunches,  $N_e = 3.72 \times 10^9$  electrons/positrons per bunch and  $t_b = 0.5$  ns. Considering also the upper temperature limit  $T_{melt} \simeq 1560$  K and  $(dE/dz)_{min}$  from Table B.1, one obtains a ratio  $E_{black}/E_{ion} \simeq$

$1.5 \times 10^{-6}$ .

### Muon production

If the halo particles of an electron (positron) beam strike directly the collimator material, they may generate an unacceptable muon background. The muon generation occurs by a variety of mechanisms, the most important one being the Bethe-Heitler pair production [92]:  $\gamma Z \rightarrow Z\mu^+\mu^-$ , with photon energies  $\gtrsim 211$  MeV (the di-muon rest mass). The initial photon in this process is usually produced by an electromagnetic cascade. It is analogous to  $e^\pm$  pair production but with a production cross section smaller by a factor of  $\sim (m_e/m_\mu)^2 = 2.34 \times 10^{-5}$ . The probability for muon production has been estimated to be of the order of  $4 \times 10^{-4}$  per lost electron [93, 94].

The photo-produced muon fluence is highly peaked in the forward direction (angle  $\lesssim 10$  mrad). This means that many muons will propagate inside the vacuum pipe almost parallel to the beam. Moreover, if we take into account their long lifetimes, high energies, and high penetrating power (they only weakly interact with matter), the muons may easily arrive at the interaction region, and therefore they are a potentially significant source of background for the detectors in the  $e^+e^-$  linear colliders.

Performing the halo collimation as far as possible from the interaction region, the muon background can be reduced. However, a collimation section very far from the interaction region means a longer beam delivery system, which is not desired. Another possible cure for the muon background is adding material in the tunnel between the collimation system and the IP, as for example magnetised spoilers: tunnel-filling iron blocks with current windings, which produce a toroidal magnetic field to deflect muons away from the detector (see Fig 3.13). This solution was adopted in the design of the NLC [16]. Another alternative solution was proposed in [92] and consists of nested iron cylinders with opposite-polarity azimuthal magnetic fields as shown in Fig. 3.14. These nested cylinders would be located downstream of each muon source (collimators, critical apertures) and are long enough to either range out muons or at least cause enough energy loss so that the muons are unlikely to reach the detector.

In proton accelerators, muon production becomes energetically possible with primary kinetic energy above  $\sim 150$  MeV, and it is significant when the beam energy rises above 10–20 GeV. The beam can interact with the collimator material generating hadronic cascades, as explained previously. From these cascades, muons can then be produced by the decay of pions and kaons.

## 3.3 Collimator wakefields and impedances

A charged particle beam moving in an accelerator induces electromagnetic fields which interact with its environment. Depending on the discontinuities and variations in the cross-sectional shape of the vacuum chamber, the beam self field is perturbed and can be reflected onto the beam axis and interact with particles in the beam itself. These electromagnetic fields induced by the beam

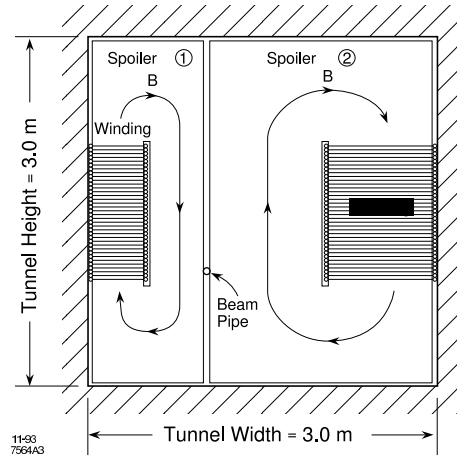


Figure 3.13: Schematic of a tunnel-filling toroidal spoiler magnets to intercept and deflect muons. From Ref. [92].

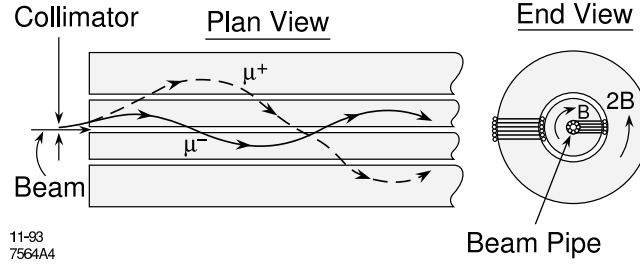


Figure 3.14: Sectional view of nested, magnetized iron cylinders of opposite polarity to channel muons. From Ref. [92].

are called *wakefields*, due to the fact that they are left mainly behind the driving charge (the source charge of the wakefield). In the limit of ultrarelativistic motion, i.e.  $\beta_v \approx 1$ , the wakefields can only stay behind the driving charge.

In the case of bunched beams, depending on whether the wakefields interact with the driving bunch itself or with the following bunches, they are denominated *short range wakefields* or *long range wakefields*, respectively. The former may degrade the longitudinal and transverse emittances of individual bunches and the latter may cause collective instabilities.

### 3.3.1 The wake function

The strength of the wake force at a distance  $z$  behind a driving point charge  $q$  is defined by a longitudinal wake function  $w_{\parallel}(\vec{r}, \vec{r}', s)$  and a transverse wake function  $\vec{w}_{\perp}(\vec{r}, \vec{r}', s)$ . The former is

given by:

$$w_{\parallel}(\vec{r}, \vec{r}', s) = -\frac{1}{q} \int_{-\infty}^{+\infty} dt \vec{v} \cdot \vec{E}(\vec{r}, z, t)|_{t=(z+s)/v} , \quad (3.63)$$

where  $\vec{v}$  denotes the speed vector of the driving charge and  $\vec{E}$  the electrical field excited by the driving charge, which satisfies the condition  $|\vec{E}| \rightarrow 0$  as  $z \rightarrow \infty$  [95]. The transverse offsets of the driving and test charges from the  $z$  axis are  $\vec{r}'$  and  $\vec{r}$ , respectively (see Fig. 3.15). The coordinate  $s = vt - z$  is the relative longitudinal coordinate moving with the bunch. The dimensions of the longitudinal wake function  $w_{\parallel}$  are volt per Coulomb (V/C) in the MKS system.

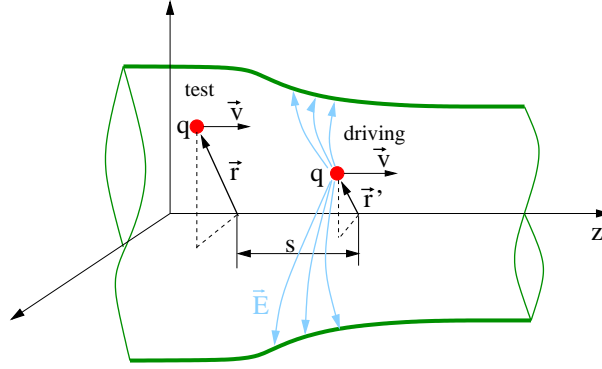


Figure 3.15: A driving charge  $q$  at transverse position  $\vec{r}'$ , moving at velocity  $\vec{v}$  parallel to the  $z$  axis and traversing a region of the vacuum pipe with variations in the cross-sectional shape. A test particle also moving at the same velocity  $\vec{v}$ , but at transverse position  $\vec{r}$  and at longitudinal distance  $s$  behind the former driving charge. The electric field lines of the driving charge are represented by the blue arrows.

The transverse wake function is defined as

$$\vec{w}_{\perp}(\vec{r}, \vec{r}', s) = -\frac{1}{q} \int_{-\infty}^{+\infty} dz \frac{1}{|\vec{r}'|} \left[ \vec{E} + \frac{\vec{v}}{c} \times \vec{H} \right]_{\perp}(\vec{r}, z, t)|_{t=(z+s)/v} , \quad (3.64)$$

where  $[\vec{E} + (\vec{v}/c) \times \vec{H}]_{\perp}$  denotes the transverse component of the radiated field, with  $\vec{H}$  the magnetic field. Note that for a source displaced transversely by  $|\vec{r}'|$ , the transverse electromagnetic field is proportional to  $|\vec{r}'|$ . This dependence is removed by dividing by  $|\vec{r}'|$  (see Eq. (3.64)). The wake is then defined as the integrated force normalized by the offset of the source charge. Note also that for relativistic beams, i.e.  $v \approx c$ , we should replace  $c$  by  $v$  in the above equations.

The relation between the longitudinal and the transverse wake functions is given by the *Panofsky-Wenzel theorem* [96]:

$$\frac{\partial w_{\perp}(s, \vec{r})}{\partial s} = \frac{1}{|\vec{r}'|} \nabla_{\perp} w_{\parallel}(s, \vec{r}) . \quad (3.65)$$

It is worthwhile to mention that the wake functions are time domain quantities, and the time domain analysis is usually adopted for linear accelerators. However, the frequency domain analysis is

usually preferred for circular accelerators because of the intrinsic periodicity in the beam dynamics. In this case, the frequency Fourier transform of the wake functions is computed. On one hand, the resulting quantity from the Fourier transform of the longitudinal wake function has units of Ohm, and is therefore called longitudinal impedance. On the other hand, the resulting quantity from the transform of the transverse wake function has units of Ohm per meter, and is called transverse impedance.

### 3.3.2 Impedances

A longitudinal impedance  $Z_{\parallel}(\omega, \vec{r})$  is defined as the Fourier harmonic of the wake function of Eq. (3.63)<sup>4</sup>, i.e.

$$Z_{\parallel}(\omega, \vec{r}) = \frac{1}{qc} \int_{-\infty}^{+\infty} ds w_{\parallel}(s, \vec{r}) e^{i\omega s/c} , \quad (3.66)$$

and the transverse impedance  $Z_{\perp}(\omega, \vec{r})$  is defined as the Fourier harmonic of  $-iw_{\perp}$ , which writes

$$Z_{\perp}(\omega, \vec{r}) = -\frac{i}{qc} \int_{-\infty}^{+\infty} ds w_{\perp}(s, \vec{r}) e^{i\omega s/c} . \quad (3.67)$$

By applying the Fourier transformation in the longitudinal coordinate  $s$  to both sides of Eq. (3.65), one obtains the expression for the transverse impedance in terms of the transverse gradient of the longitudinal impedance:

$$Z_{\perp}(\omega, \vec{r}) = \frac{c}{\omega |\vec{r}'|} \nabla_{\perp} Z_{\parallel}(\omega, \vec{r}) . \quad (3.68)$$

### 3.3.3 Collimator wakefield effects

Since the collimators are close to the beam orbit, the strong wakefield excited by the collimator can perturb the beam motion downstream of the collimator and thereby generate an additional emittance growth and jitter amplification of the collimated beam.

For future linear colliders, where we have flat beams, i.e.  $\sigma_x \gg \sigma_y$ , the sensitivity to the beam offset is larger in the vertical collimators.

#### Kick factor

Assuming a local transverse offset of the beam  $\Delta y$ , the deflection of a beam slice at position  $z$  is obtained by [97]:

$$\Delta y'(z) = \frac{r_q N}{\gamma} \tilde{\kappa}_{\perp}(z) \Delta y , \quad (3.69)$$

---

<sup>4</sup>Here we will assume relativistic beams,  $v \approx c$ .

where  $r_q$  is the classical radius of the charged particle,  $N$  is the number of particles per bunch, and the kick transverse factor  $\tilde{\kappa}_\perp$  is defined as the convolution of the transverse wake function with the longitudinal particle density  $\rho(z)$  along the bunch, i.e.

$$\tilde{\kappa}_\perp(z) = \int_z^\infty w_\perp(z - z') \rho(z') dz' . \quad (3.70)$$

Here the wake function has been integrated by all the leading bunch slices ( $z' > z$ ). The density  $\rho(z')$  is normalized so that  $\int \rho(z) dz = 1$ .

The centroid deflection of the beam is obtained by averaging the wakefield deflection over the longitudinal beam distribution:

$$\langle \Delta y' \rangle = \int_{-\infty}^\infty \Delta y' \rho(z) dz . \quad (3.71)$$

Therefore, the beam centroid deflection can be expressed in terms of a total kick transverse factor  $\kappa_\perp$  and the centroid position  $\Delta y_c$ .

$$\langle \Delta y' \rangle = \frac{r_q N}{\gamma} \kappa_\perp \Delta y_c , \quad (3.72)$$

with

$$\kappa_\perp \equiv \langle w_\perp(z - z') \rangle = \int_{-\infty}^\infty \int_{-\infty}^\infty w_\perp(z - z') \rho(z') \rho(z) dz' dz . \quad (3.73)$$

In addition to the centroid deflection, the wakefield will also increase the beam emittance and the beam divergence.

A similar kick factor can be defined for the longitudinal wakefield effect:  $\kappa_\parallel \equiv \langle w_\parallel(z - z') \rangle$ . The physical meaning of the longitudinal wake function  $w_\parallel$  is the energy loss  $\Delta\mathcal{E}$  of a test particle with charge  $e$ , that follows, at distance  $s = z - z'$ , a pointlike bunch having total charge  $q = eN$  [98, 99]:

$$\Delta\mathcal{E} \equiv eq w_\parallel(z - z') . \quad (3.74)$$

From this definition,  $\kappa_\parallel$  is then the energy loss per particle averaged over the particle distribution in the bunch.

The wakefield kick from a collimator has two contributions: (i) the geometric one arising from the geometrical aperture variation of the collimator, and (ii) the resistive wall one arising from the finite conductivity of the chamber wall.

In order to minimize the geometric wakefields, the collimators are tapered as shown in Fig. 3.16. The following notation is used:  $L_T$  is the length of the tapered part;  $b(s)$  is the radius of the tapered part, which depends of the longitudinal coordinate  $s$  (usually  $b > b(s) > a$ );  $b$  is the radius of the beam pipe;  $a$  denotes the radius or half gap of the collimator flat part;  $L_F$  the length of the flat part (in case of a spoiler or a scraper  $L_F = 0$ ) and  $\theta_T = \arctan((b - a)/L_T$ .

The flat part of the collimator contributes to resistive wall wakes, and the tapered parts con-

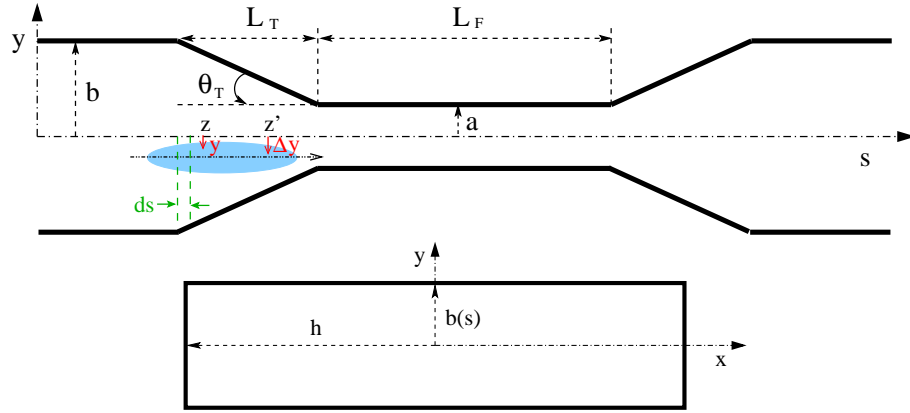


Figure 3.16: Top: longitudinal view of a tapered collimator. An oncoming particle bunch is schematically represented by the solid ellipse. Bottom: cross-sectional view in the case of a rectangular collimator.

tribute to both geometric and resistive wakes. We next review the expressions given in the literature for the transverse deflection caused by the wakefield effects, using round and rectangular transverse cross section collimators.

### Geometric wakefields

In the literature geometric wakes from tapered collimators have been studied for round geometries [97, 100] and flat geometries [97, 100, 101].

Depending on the dimensions of the collimator parameters and the longitudinal bunch length, different regimes can be distinguished [97]:

- Inductive regime:

The inductive regime for *tapered and round cross section collimators* is defined by the applicability limit  $a\theta_T/\sigma_z < 2\sqrt{\pi}$  (smooth tapering). This regime for tapered cylindrical beam pipe geometry was first studied by K. Yokoya [100]. In this case, the transverse deflection felt by a particle situated at  $z$  coordinate of a Gaussian bunch with rms size  $\sigma_z$  is given by:

$$\Delta y'_G = \frac{2Nr_q}{\gamma\sqrt{2\pi}\sigma_z} e^{-z^2/(2\sigma_z^2)} I_1 \Delta y, \quad (3.75)$$

with

$$I_1 = \int_0^{L_T} \frac{b'^2(s)}{b^2(s)} ds. \quad (3.76)$$

For a constant  $b'$  and writing  $b'ds = db$  the integral  $I_1$  is straightforward to evaluate, giving

$$I_1 = \theta_T \left( \frac{1}{a} - \frac{1}{b} \right) . \quad (3.77)$$

In this case, the vertical average deflection is then given by

$$\langle \Delta y'_G \rangle = \frac{Nr_q}{\gamma} \frac{\theta_T}{\sqrt{\pi}\sigma_z} \left( \frac{1}{a} - \frac{1}{b} \right) \Delta y_c . \quad (3.78)$$

Assuming *flat tapered collimators* with a width (height) <sup>5</sup>  $h$  ( $b(s) \ll h$ ), the inductive regime is defined in the limit  $\sqrt{a\theta_T/\sigma_z} < 3.1a/h$ , and the result is [101]:

$$\Delta y'_G = \frac{2Nr_q}{\gamma \sqrt{2\pi}\sigma_z} [(\pi h I_2 - I_1) \Delta y + I_1 y] e^{-z^2/(2\sigma_z^2)} , \quad (3.79)$$

where  $I_1$  is the same integral from Eq. (3.76) and

$$I_2 = \int_0^{L_T} \frac{b'^2(s)}{b^3(s)} ds . \quad (3.80)$$

Now we have the dependence on the displacement  $\Delta y$  of the source particle from the axis <sup>6</sup> (kick dipole part) and on the position  $y$  of the test particle (kick quadrupole part).

Solving  $I_2$  yields

$$I_2 = \frac{\theta_T}{2} \left( \frac{1}{a^2} - \frac{1}{b^2} \right) , \quad (3.81)$$

and the average transverse deflection is given by

$$\langle \Delta y'_G \rangle = \frac{Nr_q}{\gamma} \frac{\theta_T h \sqrt{\pi}}{2\sigma_z} \left( \frac{1}{a^2} - \frac{1}{b^2} \right) \Delta y_c . \quad (3.82)$$

Usually one assumes  $b \gg a$  and then  $\langle \Delta y'_G \rangle \simeq Nr_q \theta_T h \Delta y_c / (2\gamma \sigma_z a^2)$ .

- **Diffractive regime:**

The diffractive regime is defined in the limit  $a\theta_T/\sigma_z > 2\sqrt{\pi}$  for round collimators. For *round tapers*, the average transverse kick is given by:

$$\langle \Delta y'_G \rangle = \frac{\sqrt{2}Nr_q}{\gamma a^2} \Delta y_c . \quad (3.83)$$

---

<sup>5</sup>The collimator variable  $h$  is evidently the collimator width or the height depending it collimates in the vertical or horizontal plane respectively.

<sup>6</sup>Note that if the beam offset is assumed as a constant along the bunch,  $\Delta y$  is equivalent to the centroid bunch displacement  $\Delta y_c$ .



For the *flat tapers*, the diffractive regime limit is established as  $\sqrt{a\theta_T/\sigma_z} > 0.37$ , and the expression of the transverse deflection is:

$$\langle \Delta y'_G \rangle = \frac{Nr_q}{\gamma a^2} \Delta y_c . \quad (3.84)$$

- Intermediate regime:

If  $0.37 > \sqrt{a\theta_T/\sigma_z} > 3.1a/h$  (not very smooth tapering), then a rectangular collimator is in the intermediate regime, and the average transverse kick is given by the following expression:

$$\langle \Delta y'_G \rangle = \frac{2.7Nr_q}{\gamma} \sqrt{\frac{\theta_T}{\sigma_z a^3}} \Delta y_c . \quad (3.85)$$

### Resistive wall wakefields

The resistive wall wakefields are due to the finite conductivity of the collimators (resistance of the metallic material). This phenomenon is even present for a perfectly regular vacuum pipe. The theory of the resistive wall wakefields was developed by Piwinski for flat vacuum chambers [102], round vacuum chambers [103] and elliptical vacuum chambers [104].

For a collimator with a tapered part of length  $L_T$  and a flat part of length  $L_F$  (see Figure 3.16) and electrical conductivity  $\sigma$ , the average kick for a bunch with centroid amplitude offset  $\Delta y_c$  and length  $\sigma_z$  is given by [104]

$$\begin{aligned} \langle \Delta y'_R \rangle = & F_G \frac{Nr_q}{\gamma} \frac{2\Gamma\left(\frac{1}{4}\right)}{\pi^2} \sqrt{\frac{2}{\sigma_z \sigma Z_0}} \left[ \overbrace{L_F \frac{\sin\left(\frac{\pi\Delta y_c}{a}\right) + \frac{\pi\Delta y_c}{a}}{a^2 \left(1 + \cos\left(\frac{\pi\Delta y_c}{a}\right)\right)}}^{\text{flat part contribution}} \right. \\ & \left. + \overbrace{\frac{L_T}{b-a} \left( \frac{\tan\left(\frac{\pi\Delta y_c}{2a}\right)}{a} - \frac{\tan\left(\frac{\pi\Delta y_c}{2a}\right)}{b} \right)}^{\text{taper part contribution}} \right] , \end{aligned} \quad (3.86)$$

where  $F_G = 1$  for round collimators and  $F_G = \pi^2/8$  for flat collimators.

For very small beam offset, i.e., in the case of near axis bunches ( $\pi\Delta y_c/a \ll 1$ ), one can make the following approximation:

$$\langle \Delta y'_R \rangle \simeq F_G \frac{Nr_q}{\gamma} \frac{\Gamma\left(\frac{1}{4}\right)}{\pi a^2} \sqrt{\frac{2}{\sigma_z \sigma Z_0}} \left[ \frac{L_F}{a} + \frac{1}{\theta_T} \right] \Delta y_c , \quad (3.87)$$

with the term  $L_F/a$  being the contribution from the flat part and the term  $1/\theta_T$  the contribution from the tapered part.



# Nonlinear Collimation for TeV Colliders

## 4.1 Introduction

Many nonlinear magnets based ideas for beam collimation have been proposed in the literature. The basic principle of nonlinear collimation has been briefly exposed in section 2.2.6. It is based on a first nonlinear element to drive the beam halo to large amplitudes to be caught by the collimator jaws, which can be placed further away from the nominal beam orbit. This permits higher collimator apertures than for the linear collimation systems, reducing thereby the effects from the collimator wakefields or collimator impedances. Other possible advantages of the nonlinear collimation systems are the reduction of the transverse beam density at the collimators, increasing therefore the collimator survival probability in case of direct beam impacts during failure scenarios. A second nonlinear element of the same or opposite polarity, depending on their multipolarity, downstream of the collimator and at a phase advance  $\pi$  from the first nonlinear element, cancels the geometric aberrations induced by the former.

Pioneering studies on nonlinear collimation for linear colliders were made by N. Merminga *et al.* [31–33]. They investigated the possibility to apply sextupole pairs, octupoles pairs and decapole pairs for betatron and energy collimation in the NLC [31], arriving to the conclusion that decapoles and higher order multipolar magnets can not be useful for collimation in TeV linear colliders, because they don't penetrate to the small necessary distances [33]. Then they focused the effort on the study of a nonlinear collimation with skew sextupole pairs in the NLC for vertical betatron collimation, applying usual mechanical linear collimation for the horizontal betatronic plane and for energy collimation. This system is schematically represented in Fig. 4.1

Another application of skew sextupole pairs for postlinac nonlinear collimation was proposed in [15]. This system, called Magnetic Energy Spoiler (MES), was designed to protect the machine

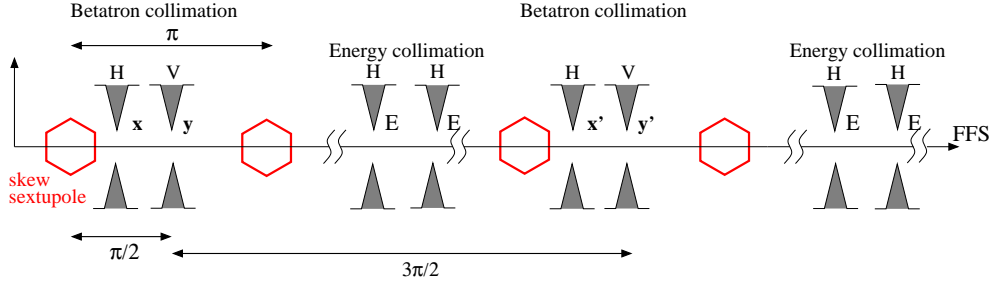


Figure 4.1: Schematic representation of the nonlinear collimation system in the NLC proposed in [33] for the collimation in the horizontal phase  $x$  and  $x'$ , in the vertical phase  $y$  and  $y'$ , and in energy  $E$ .

against mis-steered bunches because of failures in the linac. The MES was located downstream of the betatron collimation system of TESLA, and it also includes an octupole at a high dispersion point in between of two skew sextupoles, as shown in Fig. 4.2. The octupole introduces third order dispersion at the second skew sextupole position, which contributes to significantly increase the vertical beam size at the downstream momentum spoiler.

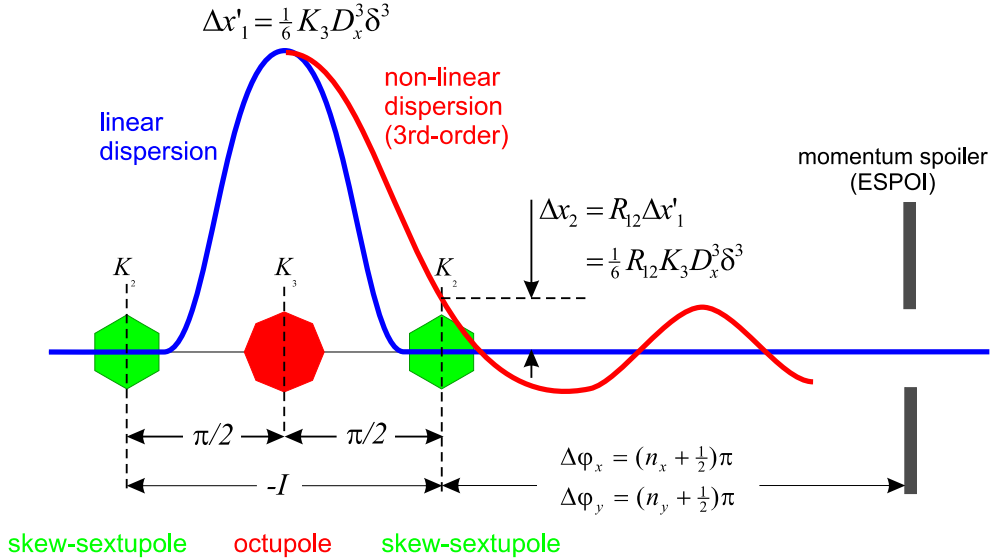


Figure 4.2: Schematic of the Magnetic Energy Spoiler (MES) for TESLA. Courtesy of Nicholas Walker from [15].

Unlike the previous nonlinear collimation system designs, which employ the skew sextupoles either for betatron collimation or for energy collimation separately, a nonlinear collimation system for CLIC was proposed in [39] for simultaneously to collimate in energy and in the betatronic phases.

On the other hand, the possibility of using octupoles for tail folding in the final focus of linear colliders has been also explored in [34–38]. Particularly, the performance of a system using “Chebyshev arranged octupole doublets” for the NLC was study in [37], where the octupole doublets were incorporated in the final focus, providing a significant reduction of the halo amplitude.

More recently a study on octupole tail folding was done for CLIC [135], concluding that an acceptable tail folding performance for CLIC without luminosity loss would require a new final focus optics.

Other interesting alternative idea involving octupoles is the nonlinear resonant collimation in the main Linac [136]. This system consists of octupoles added to the FODO lattice of the main linac of linear colliders. These octupoles are arranged to resonantly disestablish particles at large betatron amplitudes. These halo particles are then dispersed by the nonlinear field and caught by absorbers before they reach the end of the linac. However, it is important to point out that this scheme would be only practicable in a “warm” RF cavities based linear accelerator. Evidently, in an accelerator as the ILC, whose linac is composed of superconducting cavities, no collimation system can be located in the linac. Particles scattered off the collimators and secondary showers may be deposited in the cavity walls causing quenches.

For TeV circular colliders a nonlinear collimation system based on a skew sextupole pair for betatron cleaning has also been studied [137], and particularly for the LHC [138–140] (see Chapter 7).

## 4.2 Scheme with skew sextupoles pair

In this section we describe a nonlinear collimation system using a pair of skew sextupoles and a single spoiler, based on the layout of Figure 4.3.

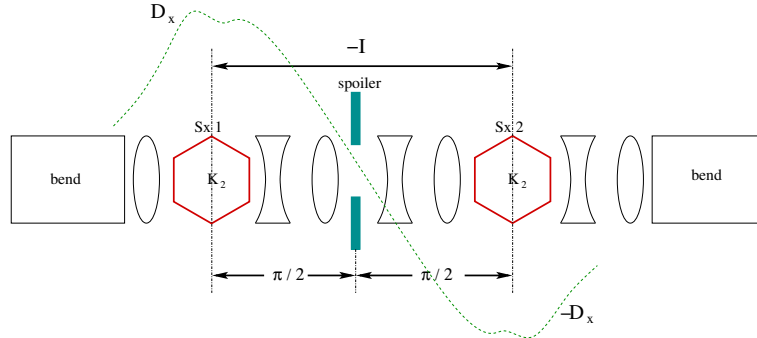


Figure 4.3: Schematic of a nonlinear collimation system using a pair of skew sextupoles and a single spoiler.

The beam motion in a skew sextupole at a location with horizontal dispersion  $D_{x,s}$  is given by the Hamiltonian

$$H_s = \frac{1}{6} K_s (y_s^3 - 3(x_s + D_{x,s}\delta)^2 y_s) , \quad (4.1)$$

where  $x_s$  and  $y_s$  are the transverse amplitudes at the sextupole, and  $\delta$  the relative momentum offset. The subindex ‘s’ means first skew sextupole. We assume no dispersion in the vertical plane. The integrated sextupole strength  $K_s$  can be expressed in terms of the sextupole length  $l_s$ , the pole-tip field  $B_T$ , the magnetic rigidity  $B\rho$  and the sextupole aperture  $a_s$  as

$$K_s = \frac{2B_T l_s}{(B\rho) a_s^2} . \quad (4.2)$$

Then the sextupole deflects a passing particle by

$$\Delta x' = -\frac{\partial H_s}{\partial x} = K_s (D_{x,s}\delta + x_s) y_s , \quad (4.3)$$

$$\Delta y' = -\frac{\partial H_s}{\partial y} = -\frac{1}{2} K_s (y_s^2 - x_s^2 - D_{x,s}^2 \delta^2 - 2D_{x,s}\delta x_s) , \quad (4.4)$$

and the transverse position at the downstream spoiler is obtained from

$$x_{\text{sp}} = x_{0,\text{sp}} + R_{12} \Delta x' , \quad (4.5)$$

$$y_{\text{sp}} = y_{0,\text{sp}} + R_{34} \Delta y' , \quad (4.6)$$

where  $x_{0,\text{sp}} = x_{\beta,\text{sp}} + D_{x,\text{sp}}\delta$  and  $y_{0,\text{sp}} = y_{\beta,\text{sp}}$  are the horizontal and vertical position of the particle at the spoiler without the sextupole, written in terms of the betatronic parts,  $x_{\beta,\text{sp}}$  and  $y_{\beta,\text{sp}}$ , and the horizontal dispersion at the spoiler,  $D_{x,\text{sp}}$ .  $R_{12}$  and  $R_{34}$  denote the linear optical transport matrix elements between the skew sextupole and the spoiler (see Appendix A for the transport matrix notation).

The transverse root mean squared beam sizes at the spoiler are given by the expressions

$$\sigma_{x,\text{sp}} = \sqrt{\langle x_{\text{sp}}^2 \rangle - \langle x_{\text{sp}} \rangle^2} , \quad (4.7)$$

$$\sigma_{y,\text{sp}} = \sqrt{\langle y_{\text{sp}}^2 \rangle - \langle y_{\text{sp}} \rangle^2} , \quad (4.8)$$

where  $x_{\text{sp}}$  and  $y_{\text{sp}}$  are computed from expressions (4.5) and (4.6), and the brackets  $\langle \dots \rangle$  indicates the average over the transverse distribution.

The second skew sextupole in Fig. 4.3 downstream of the spoiler with the same strength  $K_s$ , located at a position with horizontal dispersion  $-D_{x,s}$  and  $\pi$  phase advance from the first sextupole, cancels the geometric aberrations and the first order chromatic aberrations induced by the former one.

### 4.2.1 Spoiler protection

An important issue of the collimator system is the protection of the spoiler against mis-steered or errant beams which may hit and possibly damage it. Considering Gaussian beams, a minimum transverse rms beam size  $\sigma_{r,\min}$  is required for spoiler survival in case of full beam impact, and then the beam area at the spoiler must satisfy

$$\sigma_{x,\text{sp}}\sigma_{y,\text{sp}} \geq \sigma_{r,\min}^2 . \quad (4.9)$$

The minimum beam size  $\sigma_{r,\min}^2$  depends on the spoiler material and constrains the values of  $K_s$ ,  $R_{12}$  and  $R_{34}$  for the optics design of the nonlinear collimation system. If  $\sigma_{r,\min}^2$  is known, the maximum transverse beam energy density can be estimated by

$$\rho_{E,\max} = \frac{NE_0}{2\pi\sigma_{r,\min}^2} , \quad (4.10)$$

where  $N$  is the number of particles per bunch and  $E_0$  the nominal beam energy. Then the condition (4.9) can be express as  $NE_0/(2\pi\sigma_{x,\text{sp}}\sigma_{y,\text{sp}}) \lesssim NE_0/(2\pi\sigma_{r,\min}^2)$ .

Assuming Gaussian beams, the values of  $\sigma_{r,\min}$  have been evaluated for the 3 TeV center-of-mass energy CLIC parameters [87].

Following this criterium we can quickly estimate the relative collimator survival probability between the nonlinear and the linear collimation systems. Of course, for more precise studies energy deposition, collimator heating and heat propagation along the collimator material need to be considered. For these issues, usually powerful simulation software has been developed. As examples we can mention the simulation tools FLUKA [91] and BDSIM [105]. In this thesis, nevertheless, the aim is to compare roughly the collimator survival improvement of the nonlinear system respect to the linear one, and we will consider the approximative criterium (4.9) as sufficient for our purpose.

### 4.2.2 Nonlinear collimation for linear colliders

For linear colliders we assume that the betatronic components  $x_\beta$  and  $y_\beta$  are small compared with  $D_x\delta$  both at the spoiler and at the sextupole position. We assume further flat beams with  $\sigma_x \gg \sigma_y$ . The reason of the flat beams is to achieve high luminosity ( $\mathcal{L} \propto 1/(\sigma_x\sigma_y)$ ) and low beamstrahlung (the beamstrahlung parameter  $\Upsilon \propto 1/(\sigma_x + \sigma_y)$ ).

#### Transverse beam size at spoiler position

Considering the above approximations, and using the Eqs. (4.3) and (4.5) the horizontal mean squared position of particles and the average horizontal beam offset at the spoiler are given by

$$\langle x_{\text{sp}}^2 \rangle \simeq D_{x,\text{sp}}^2 \langle \delta^2 \rangle + R_{12}^2 K_s^2 D_{x,s}^2 \langle \delta^2 \rangle \langle y_{\beta,s}^2 \rangle, \quad (4.11)$$

$$\langle x_{\text{sp}} \rangle \simeq D_{x,\text{sp}} \langle \delta \rangle. \quad (4.12)$$

In a similar way, from Eqs. (4.4) and (4.6) the vertical mean squared position and the average vertical offset at the spoiler are given by

$$\langle y_{\text{sp}}^2 \rangle \simeq \frac{1}{4} R_{34}^2 K_s^2 D_{x,s}^4 \langle \delta^4 \rangle, \quad (4.13)$$

$$\langle y_{\text{sp}} \rangle \simeq \frac{1}{2} R_{34} K_s D_{x,s}^2 \langle \delta^2 \rangle. \quad (4.14)$$

From Eqs. (4.7), (4.8), (4.11), (4.12), (4.13) and (4.14), considering first a *Gaussian momentum distribution*:

$$P(\delta) = \frac{1}{\sqrt{2\pi}\sigma_\delta} e^{-1/2 \left( \frac{\delta - \delta_0}{\sigma_\delta} \right)^2}, \quad (4.15)$$

with a width  $\sigma_\delta$  and with an average momentum offset  $\delta_0$ , the transverse beam sizes at the spoiler take the form:

$$\sigma_{x,\text{sp}} \simeq \left( D_{x,\text{sp}}^2 \sigma_\delta^2 + R_{12}^2 K_s^2 D_{x,s}^2 (\delta_0^2 + \sigma_\delta^2) \beta_{y,s} \epsilon_y \right)^{1/2}, \quad (4.16)$$

$$\sigma_{y,\text{sp}} \simeq \left( \frac{1}{2} R_{34}^2 K_s^2 D_{x,s}^4 (\sigma_\delta^4 + 2\delta_0^2 \sigma_\delta^2) \right)^{1/2}. \quad (4.17)$$

On the other hand, if we consider the case of a *uniform flat momentum distribution*:

$$P(\delta) = \begin{cases} 0 & \text{for } \delta < -\frac{\delta_{\text{flat}}}{2} + \delta_0 \\ \frac{1}{\delta_{\text{flat}}} & \text{for } -\frac{\delta_{\text{flat}}}{2} + \delta_0 < \delta < \frac{\delta_{\text{flat}}}{2} + \delta_0 \\ 0 & \text{for } \delta > \frac{\delta_{\text{flat}}}{2} + \delta_0, \end{cases}$$

with a full width  $\delta_{\text{flat}}$  and an average momentum offset  $\delta_0$ , the transverse beam sizes at the spoiler take the form:

$$\sigma_{x,\text{sp}} \simeq \left( D_{x,\text{sp}}^2 \frac{\delta_{\text{flat}}^2}{12} + R_{12}^2 K_s^2 D_{x,s}^2 \left( \frac{\delta_{\text{flat}}^2}{12} + \delta_0^2 \right) \beta_{y,s} \epsilon_y \right)^{1/2}, \quad (4.18)$$

$$\sigma_{y,\text{sp}} \simeq \left( \frac{1}{4} R_{34}^2 K_s^2 D_{x,s}^4 \left( \frac{\delta_{\text{flat}}^4}{180} + \frac{1}{3} \delta_{\text{flat}}^2 \delta_0^2 \right) \right)^{1/2}. \quad (4.19)$$



### Collimation depth and collimator apertures

The transverse collimation depth for  $e^-e^+$  linear colliders is set by SR and beam loss in the final doublet quadrupoles (see Chapter 2). The SR generated in final doublet must pass cleanly through all apertures on the incoming side of the IP.

If we denote by  $n_x$  and  $n_y$  the horizontal and the vertical transverse normalized collimation amplitudes, our sextupole must deflect passing leptons whose amplitude offsets  $|x_{\beta,s}| \gtrsim n_x \sigma_{x,\beta}$  and/or  $|y_{\beta,s}| \gtrsim n_y \sigma_{y,\beta}$ , with  $\sigma_{x,\beta} = \sqrt{\beta_x \epsilon_x}$  and  $\sigma_{y,\beta} = \sqrt{\beta_y \epsilon_y}$ .

On the other hand, the energy collimation amplitude, which we call  $\Delta$  in units of  $\delta \equiv \Delta E/E$ , is not determined by the background, but instead it is set by the failure modes in the linac. These failure modes may result in mis-steered or errant beams which will hit the energy spoiler. In this way the energy collimation section fulfils the function of machine protection, and particles with energy offsets  $|\delta| \gtrsim |\Delta|$  will be intercepted by the energy spoiler.

If we employ a vertical spoiler of half gap  $a_y$ , the condition for collimation implies  $\Delta_{y,sp} \geq a_y$ .

For linear colliders we assumed that the dispersive term is dominant in Eqs (4.3) and (4.4). In this case we can employ the vertical spoiler for nonlinear energy collimation setting the jaws with half gap

$$a_y \simeq \frac{1}{2} R_{34} K_s D_{x,s}^2 \Delta^2. \quad (4.20)$$

The nonlinear terms in the sextupolar deflection also may yield a weak collimation for horizontal or vertical betatron amplitudes, at a collimation depth in units of  $\sigma_{x,\beta}$  or  $\sigma_{y,\beta}$  respectively of

$$n_x = \frac{D_{x,s} \Delta}{\sqrt{\epsilon_x \beta_{x,s}}}, \quad (4.21)$$

$$n_y = \frac{D_{x,s} \Delta}{\sqrt{\epsilon_y \beta_{y,s}}}, \quad (4.22)$$

In this case to get high betatronic collimation efficiency<sup>1</sup>, the betatron functions at the sextupole have to be increased. This was the approximation chosen in Ref. [39] for the first study of a nonlinear collimation system for CLIC, where  $\beta_{x,s}$  and  $\beta_{y,s}$  of the order of 100 km were required. This solution tended to introduce large chromaticity.

Additionally, we can collimate in the other betatron phase, using the linear optics. Denoting the horizontal and the vertical spoiler half gaps by  $a_x$  and  $a_y$ , respectively, and assuming that the

---

<sup>1</sup>For CLIC at 3 TeV center-of-mass energy we have  $n_x \simeq 10$  and  $n_y \simeq 80$  [9], and for ILC at 0.5 TeV center-of-mass energy  $n_x \simeq 9.6$  and  $n_y \simeq 74$  [106]

vertical gap is adjusted for collimation at the same offset  $\Delta$  as the horizontal one, we obtain

$$n_{x2} = \frac{a_x}{\sqrt{\epsilon_x \beta_{x,sp}}} \simeq \frac{D_{x,sp} \Delta}{\sqrt{\epsilon_x \beta_{x,sp}}}, \quad (4.23)$$

$$n_{y2} = \frac{a_y}{\sqrt{\epsilon_y \beta_{y,sp}}} \simeq \frac{1}{2} \frac{R_{34} K_s D_{x,s}^2 \Delta^2}{\sqrt{\epsilon_y \beta_{y,sp}}}, \quad (4.24)$$

where the subindex 2 refers to the orthogonal betatron phase, considering that the spoiler and the skew sextupole are placed roughly  $\pi/2$  out of phase. These equations can be matched for the beta functions at the spoiler.

In principle, by combining Eqs. (4.21), (4.22), (4.23) and (4.24), we could collimate in both betatron phases and in energy using a single spoiler. If we opt for nonlinear betatron collimation, the other phase could also be collimated by installing a “pre” skew sextupole with a phase advance of about  $\pi/2$  in front of the first skew sextupole, as proposed in [39].

### Emittance growth due to synchrotron radiation

In order to use a skew sextupole as weak as possible to avoid introducing strong optics aberrations, which may degrade the luminosity, one could think about increasing the dispersion  $D_{x,s}$  as much as possible. However the achievable value of  $D_{x,s}$  is limited by the emittance growth  $\Delta(\gamma\epsilon_x)$  due to synchrotron radiation in the dipole magnets. The quantum excitation of beam energy spread along path of length  $L$  is [107]

$$(\Delta\delta_E)^2 = \frac{55(\hbar c)^2}{48\sqrt{3}} \gamma^7 \int_0^L \left( \frac{1}{|\rho_x^3|} + \frac{1}{|\rho_y^3|} \right) ds, \quad (4.25)$$

with  $\gamma \equiv E/mc^2$  the Lorentz factor and  $\rho_u$  ( $u = x$  or  $y$ ) the radius of curvature of the design orbit.

Here I will be concerned only with deflections by dipole magnets in the horizontal plane, and then only the term  $1/|\rho_x^3|$  inside the integral will be considered.

That quantum excitation leads to the following statistical increase of the normalized emittance:

$$\Delta(\gamma\epsilon_x) = \frac{55r_e\hbar c}{48\sqrt{3}mc^2} \gamma^6 \int_0^L \frac{\mathcal{H}}{|\rho_x^3|} ds. \quad (4.26)$$

The curvature  $\rho_x(s)$  is a function of the longitudinal coordinate  $s$ . However, one can approximate  $\rho_x$  by a constant value within a given bending magnet. The integral of Eq. (4.26) is called the radiation integral  $I_5$ , and it can be written as [108]

$$I_5 = \int_0^L \frac{\mathcal{H}}{|\rho_x^3|} ds = \sum_i L_i \frac{\langle \mathcal{H} \rangle_i}{|\rho_{x,i}^3|}, \quad (4.27)$$

where the sum runs over all bending magnets, with bending radius  $\rho_i$ , length  $L_i$ , and the “curly H” function as defined in Ref. [107].

The Eq. (4.26) can then be written as

$$\Delta(\gamma\epsilon_x) = CE^6 I_5 , \quad (4.28)$$

where

$$C = \frac{55r_e\hbar c}{48\sqrt{3}(mc^2)^7} \simeq 4.13 \times 10^{-8} \text{ m}^2 \text{ GeV}^{-6} . \quad (4.29)$$

In order to avoid the degradation of the emittance we have then to get acceptable values for the bending magnet strengths, which limits the integral  $I_5$  at the same time that the dispersion  $D_{x,s}$  is maximized. This restricts the value

$$\Delta(\gamma\epsilon_x) \simeq (4.13 \times 10^{-8} \text{ m}^2 \text{ GeV}^{-6}) E^6 I_5 < f(\gamma\epsilon_x) \quad (4.30)$$

to a fraction  $f$  of the initial normalized emittance  $\gamma\epsilon_x$ .

### 4.2.3 Nonlinear collimation for circular colliders

For circular colliders we will assume the dispersive component  $D_x\delta$  to be smaller than the betatron amplitudes  $x_\beta$  and  $y_\beta$  both at the sextupole and at the spoiler, and we will apply the nonlinear collimation system for betatron collimation.

#### Transverse beam size at spoiler position

In the above approximation, and using Eqs. (4.3) and (4.5) the horizontal mean squared position of particles at the spoiler is given by

$$\langle x_{\text{sp}}^2 \rangle \simeq \langle x_{\beta,\text{sp}}^2 \rangle + R_{12}^2 K_s^2 \langle x_{\beta,s}^2 \rangle \langle y_{\beta,s}^2 \rangle , \quad (4.31)$$

$$\langle x_{\text{sp}} \rangle \simeq 0 , \quad (4.32)$$

and using Eqs. (4.4) and (4.6) the vertical mean squared position and the average vertical offset at the spoiler is

$$\langle y_{\text{sp}}^2 \rangle \simeq \langle y_{\beta,\text{sp}}^2 \rangle + \frac{1}{4} R_{34}^2 K_s^2 (\langle x_{\beta,s}^4 \rangle + \langle y_{\beta,s}^4 \rangle - 2 \langle x_{\beta,s}^2 \rangle \langle y_{\beta,s}^2 \rangle) , \quad (4.33)$$

$$\langle y_{\text{sp}} \rangle \simeq -\frac{1}{2} R_{34} K_s (\langle y_{\beta,s}^2 \rangle - \langle x_{\beta,s}^2 \rangle) . \quad (4.34)$$

From Eqs. (4.7), (4.8), (4.31), (4.32), (4.33) and (4.34), and assuming a transverse Gaussian distribution, the transverse beam sizes at the spoiler take the form:

$$\sigma_{x,\text{sp}} \simeq \left( K_s^2 R_{12}^2 \beta_{x,s} \beta_{y,s} \epsilon_x \epsilon_y + \beta_{x,\text{sp}} \epsilon_x \right)^{1/2}, \quad (4.35)$$

$$\sigma_{y,\text{sp}} \simeq \left( \frac{1}{2} K_s^2 R_{34}^2 (\beta_{x,s}^2 \epsilon_x^2 + \beta_{y,s}^2 \epsilon_y^2) + \beta_{y,\text{sp}} \epsilon_y \right)^{1/2}. \quad (4.36)$$

### Collimation depth and collimator apertures

Let  $\pm n_x \sqrt{\beta_{x,s} \epsilon_x}$  and  $\pm n_y \sqrt{\beta_{y,s} \epsilon_y}$  be the collimation amplitudes for the horizontal and vertical betatron motion respectively, and  $\pm n_{x2} \sqrt{\beta_{x,\text{sp}} \epsilon_x}$  and  $\pm n_{y2} \sqrt{\beta_{y,\text{sp}} \epsilon_y}$  the physical transverse apertures of the primary spoiler. Then for the collimation to function in either transverse plane, we must have [139]

$$n_{y2} \sqrt{\beta_{y,\text{sp}} \epsilon_y} = \frac{1}{2} K_s R_{34} n_x^2 \beta_{x,s} \epsilon_x, \quad (4.37)$$

$$n_{x2} \sqrt{\beta_{x,\text{sp}} \epsilon_x} = \frac{1}{2} K_s R_{34} n_y^2 \beta_{y,s} \epsilon_y. \quad (4.38)$$

Particles at transverse amplitudes  $|x_\beta| \gtrsim n_x \sqrt{\beta_{x,s} \epsilon_x}$  and  $|y_\beta| \simeq 0$ , or  $|y_\beta| \gtrsim n_y \sqrt{\beta_{y,s} \epsilon_y}$  and  $|x_\beta| \simeq 0$ , will be deflected by the skew sextupole and are caught by a vertical spoiler of normalized half gap  $n_{y2}$ . On the other hand, particles with  $|x_\beta| \approx |y_\beta|$  will not be collimated by the vertical spoiler. Instead these particles will receive a horizontal kick by the skew sextupole and can be caught by the spoiler set to the normalized horizontal aperture  $n_{x2}$ , i.e.

$$n_{x2} \sqrt{\beta_{x,\text{sp}} \epsilon_x} = K_s R_{12} n_x n_y \sqrt{\beta_{x,s} \epsilon_y} \sqrt{\beta_{y,s} \epsilon_x}. \quad (4.39)$$

Therefore, the aperture at the spoiler  $n_{x2}$  can be adjusted to improve the cleaning efficiency for particles with offsets in both transverse planes.

# Alternative Nonlinear Energy Collimation System with Skew Sextupole Pair for CLIC at 1.5 TeV

## 5.1 Introduction to the CLIC accelerator

In basic form, a Linear Collider consists of two linear accelerators pointed at each other in 180 degree opposition <sup>1</sup>. After obtaining the nominal energy the beams collide at the interaction point, where the particle detectors are located.

It is worth mentioning that the beam is not recirculated as it happens in the circular machines; instead, it is dumped after the collision point, following a single acceleration pass. Therefore, the repetition of the acceleration process and the beam collision is required as frequently as possible.

The CLIC technology is based on the two beam acceleration method. An overall layout for the centre-of-mass energy of 3 TeV is shown in Figure 5.1. This method consists in extracting RF power from a low energy and high intensity electron beam (so-called *Drive Beam*) by Power Extraction and Transfer Structure (PETS). The *linear accelerator* (linac) is based on a modular design and has no active components such as modulators or klystrons. Each RF power structure accelerates electron and positron beams (so-called *Main Beam*) with accelerating gradients of 150 MV/m at room temperature and are arranged in sectors providing an acceleration of  $\sim 70$  GeV over 624 m [4]. The main parameters of CLIC are listed in Table 5.1 for center-of-mass energies 0.5 TeV

---

<sup>1</sup>The Stanford Linear Collider (SLC) [5], the sole linear collider built to date, did not actually consist of two opposing machines. The SLC, at a relatively low beam energy of approximately 30 GeV, used only one linac instead a pair of opposing linacs for the sake economy. The linac accelerated both electrons and positrons via a process involving the generation of positrons by bombardments of a target, then electrons and positrons were sent in two separate arcs and steered into collision. However, this scheme is not feasible for beam energies of the order of hundreds of GeV.

and 3 TeV. The two first columns corresponds to old parameters set previous to the year 2005. The third column shows parameters set as of mid 2005 [109].

Table 5.1: Overall parameters of CLIC for centre-of-mass energies 0.5 TeV and 3 TeV.

parameter	value		
Centre-of-mass energy (TeV)	0.5 TeV	3 TeV	3 TeV (updated 2005)
Design luminosity ( $10^{34} \text{ cm}^{-2}\text{s}^{-1}$ )	2.1	8.0	6.5
Mean energy loss (%)	4.4	21	10
Photons/electron	0.75	1.53	1.1
Main linac RF frequency (GHz)	30	30	30
Linac repetition rate (Hz)	200	100	150
Particles/bunch at IP ( $\times 10^9$ )	4.0	4.0	2.56
Bunches/pulse	154	154	220
Bunch length ( $\mu\text{m}$ )	35	35	30.8
Bunch separation (ns)	0.67	0.67	0.267
Bunch train length ( $\mu\text{s}$ )	0.102	0.102	0.0587
Emittances $\epsilon_x/\epsilon_y$ ( $10^{-8} \text{ rad}\cdot\text{m}$ )	200/1	68/1	68/1
Unloaded/loaded gradient (MV/m)	172/150	172/150	172/150
Beam power/beam (MW)	4.9	14.8	20.3
Total site AC power (MW)	175	410	418
Overall length (km)	7.7	33.2	33.2

The total length of the CLIC will be around 33 km. However, due to its modular structure the collider could start generation at lower energy simply with a shorter length and then be upgraded in stages to reach the maximum energy of 5 TeV [4]. Operating at this centre-of-mass energy, the CLIC linear collider should be designed with a luminosity  $\mathcal{L} \sim 10^{35} \text{ cm}^{-2}\text{s}^{-1}$ .

### 5.1.1 The CLIC BDS

The latest design of the lattice for the CLIC beam delivery system (CLIC BDS) [10] is based on a compact FFS “a la Raimondi” [14], adapted to the CLIC requirements [110]. This lattice has been matched to the twiss parameters of Table 5.2. The corresponding twiss parameters are shown in Figure 5.2. Here  $\beta_x^* = 7 \text{ mm}$  and  $\beta_y^* = 0.09 \text{ mm}$  have been chosen for the interaction point.

The baseline linear collimation system [9], whose optics is shown in Fig. 5.3, includes a region of 1375 m with high horizontal dispersion for energy collimation, and a section of 625 m for betatron collimation upstream of the FFS. Next we will focus our study on the collimation system of CLIC.

### 5.1.2 The baseline linear collimation system of CLIC

Two sections upstream the final focus system are dedicated to collimation:

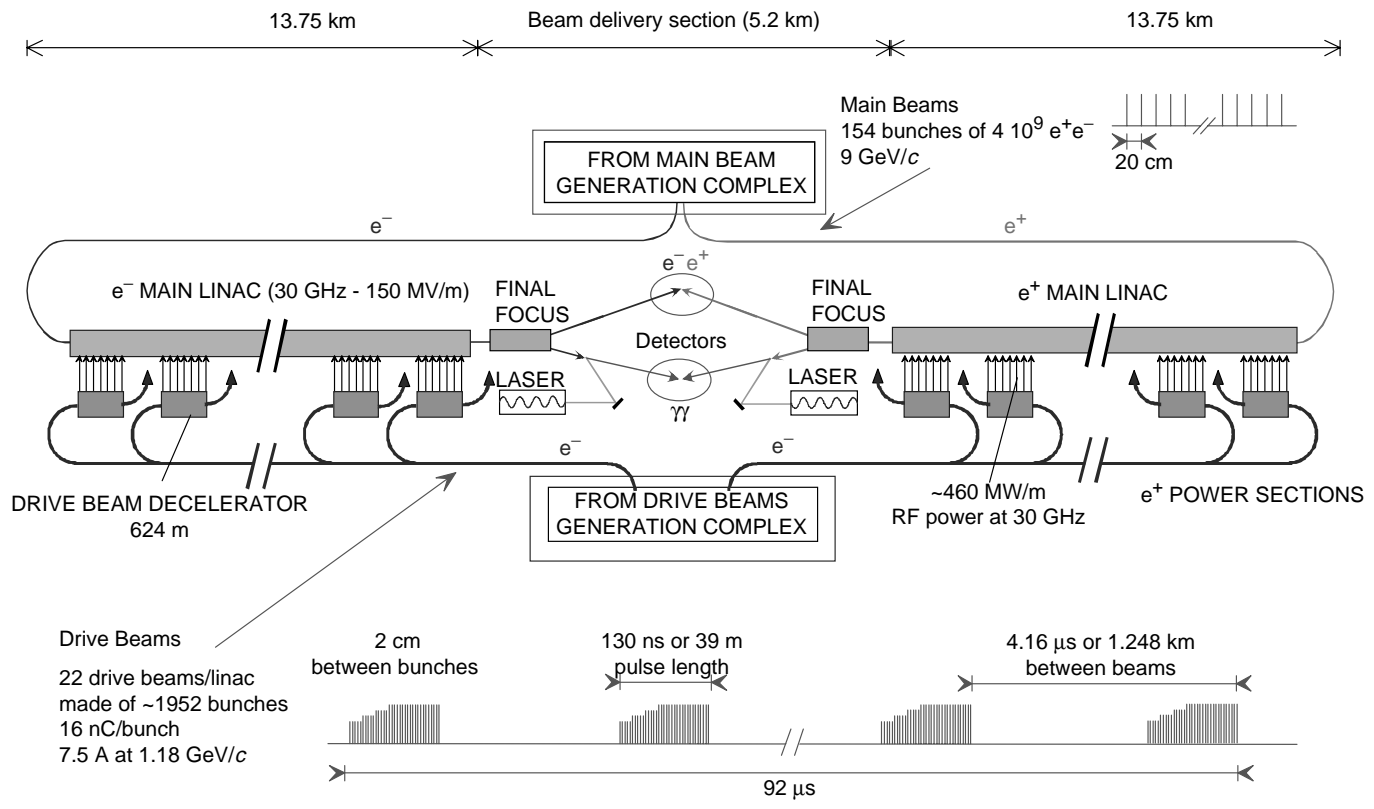


Figure 5.1.1: Overall layout of CLIC for the centre-of-mass energy of 3 TeV.

Table 5.2: System lengths and beam parameters at the entrance and at the IP of the CLIC Beam Delivery System. The nominal energy spread is a flat square distribution with 1 % full width.

Lattice lengths		
FF length		0.5 km
CS length		2.0 km
BDS length		2.5 km
BDS entrance		
Beam energy	$E$	1500 GeV
Energy spread	$\delta = \Delta E/E$	1 % (full width square)
Hor. beta function	$\beta_x$	64.171 m
	$\alpha_x$	-1.951
Ver. beta function	$\beta_y$	18.244 m
	$\alpha_y$	0.606
Hor. emittance	$\gamma\epsilon_x$	680 nm
Ver. emittance	$\gamma\epsilon_y$	10 nm
Bunch length	$\sigma_z$	35 $\mu\text{m}$
IP		
Hor. beta function	$\beta_x^*$	7 mm
Ver. beta function	$\beta_y^*$	90 $\mu\text{m}$
Hor. beam size	$\sigma_x^*$	40.12 nm
Ver. beam size	$\sigma_y^*$	0.55 nm

- As explained in chapter 2, section 2.1.1, the collimation depth for the CLIC *betatron collimation* is determined from the conditions that beam particles and synchrotron radiation photons emitted in the final quadrupoles should not hit any magnet apertures on the incoming side of the IP. According to this criterion, the collimation depths were estimated to be less than  $14 \sigma_x$  (horizontal plane) and  $83 \sigma_y$  (vertical plane) [13]. Due to nonzero dispersion across the final doublet, the number for the horizontal beam size  $\sigma_x$  includes both betatron and dispersive components, roughly equal in magnitude, such that the actual horizontal collimation depth at a place with zero dispersion needs to be  $\sqrt{2}$  smaller, or about  $10 \sigma_x$ . Scaling to lower energies, we need to replace the permanent final open quadrupole by a weaker magnet. In principle, the aperture of this magnet can be opened like the inverse of the beam energy. This suggests that, for constant normalized emittances and beta functions, the collimation depth quoted in numbers of root mean square (rms) beam sizes could be increased in proportion to the inverse square root of energy. However, the horizontal normalized emittance does increase at 500 GeV, and both IP beta functions decrease somewhat. Background studies [111] indicate that, at 500 GeV, the direct impact of synchrotron radiation on the vertex detector could limit the permissible collimation depth to smaller values.

It is worthwhile to mention that the spoilers in the betatron collimation section were designed to be sacrificial, and will certainly be destroyed (*consumable collimators*), if they are hit by



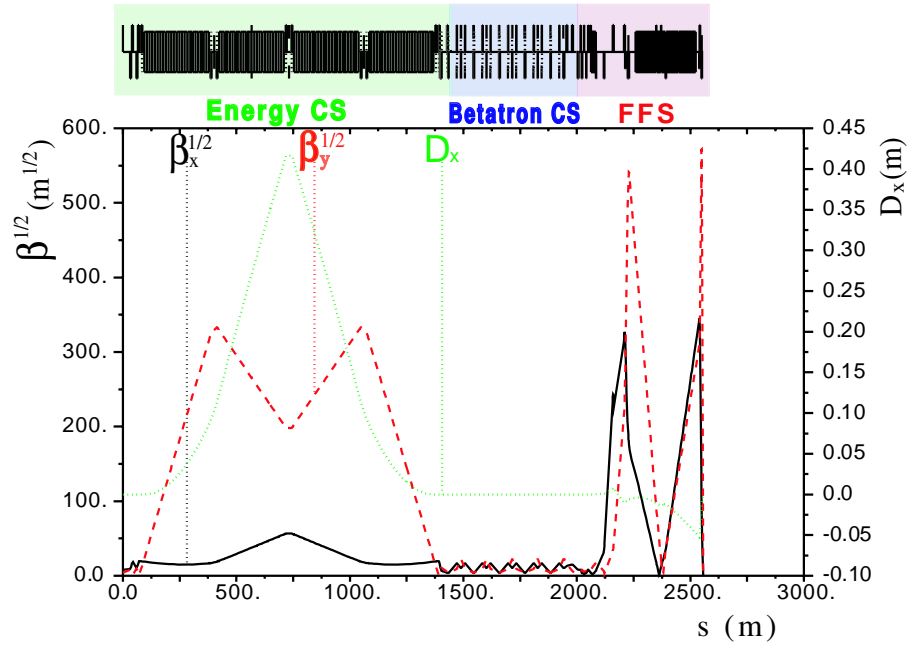


Figure 5.2: Horizontal dispersion and square root of the betatron functions for the CLIC BDS, using the linear CS, matched to the twiss parameters of Table 5.2.

a bunch train (for example, if the momentum collimators are not positioned properly).

- The *energy collimation* depth is not determined by the background, but instead it is set by failure modes in the linac (see chapter 2, section 2.1.1). For CLIC a value of about  $\pm 1\text{--}1.5\%$  was estimated [112]. This setting ensures, for all failure scenarios studied, that mis-steered or errant beams will either hit the energy spoiler, where the beam size is sufficiently large for collimator survival, or will pass all the way through the interaction point, without impacting on a betatron collimator.

The collimator parameters for the standard linear system are listed in Table 5.3, and the collimator database in Table 5.4.

## 5.2 Benchmarking of tracking codes in the context of the CLIC BDS

Different tracking and optics design simulation codes have been implemented with different methods. While some codes as MAD [114] use the TRANSPORT formalism [115] based on Taylor maps up to second order, the Strategic Accelerator Design (SAD) program [116] uses a symplectic formalism. Therefore, benchmarking the codes could be useful to assess the confidence in the simulations.

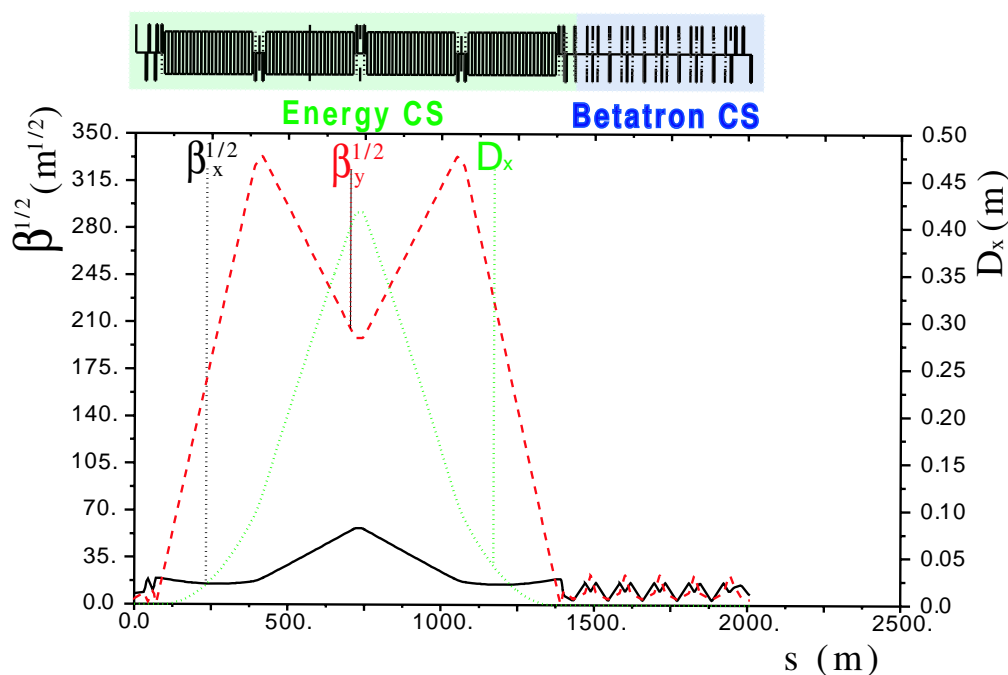


Figure 5.3: Horizontal dispersion and square root of the betatron functions for the CLIC linear CS (figure on the bottom) matched to the twiss parameters of Table 5.2.

Table 5.3: Collimation parameters for CLIC.

CM energy	3 TeV	500 GeV
energy spoiler gap	$\pm 3.51$ mm	$\pm 4.8$ mm
$\beta_x$ spoiler gap	$\pm 80$ $\mu$ m ( $10\sigma_x$ )	$\pm 300$ $\mu$ m ( $9\sigma_x$ )
$\beta_y$ spoiler gap	$\pm 104$ $\mu$ m ( $80\sigma_y$ )	$\pm 215$ $\mu$ m ( $69\sigma_y$ )
spoiler material	Be (or C)	Be (or C)
spoiler length	177 mm (0.5 r.l. C)	177 mm (0.5 r.l. C)
absorber material	Ti (Cu coated)	Ti (Cu coated)
no. of energy spoilers	1	1
no. of $\beta_{x,y}$ spoilers	4	4

In the context of the CLIC Beam Delivery System (BDS) [10] several tracking tools have been compared in previous works [117, 118]. The code Placet [119] is even able to simulate a whole linear machine, joining the linac and the Beam Delivery System.

In this section we study the performance of the CLIC BDS for centre-of-mass energy 3 TeV, using the linear collimation system and comparing the results of three tracking tools: SAD, MAD and

Table 5.4: CLIC post-linac collimator parameters. Longitudinal position, horizontal and vertical  $\beta$ -functions, dispersion, horizontal and vertical half gaps, geometry of the collimator and material.

s[m]	Name	$\beta_x$ [m]	$\beta_y$ [m]	$D_x$ [m]	$a_x$ [mm]	$a_y$ [mm]	Geometry	Material
566.502	ENGYS	1406.33	70681.9	0.27	3.51	25.4	rect	Be
731.502	ENGYS	3213.03	39271.5	0.417	5.4	25.4	rect	Ti(Cu coated)
1490.28	YSP1	114.054	483.253	0.	10.	0.102	rect	Be
1506.1	XSP1	270.003	101.347	0.	0.08	10.	rect	Be
1583.3	XAB1	270.102	80.9043	0.	1.	1.	ellip	Ti(Cu coated)
1601.12	YAB1	114.054	483.184	0.	1.	1.	ellip	Ti(Cu coated)
1603.12	YSP2	114.054	483.188	0.	10.	0.102	rect	Be
1618.94	XSP2	270.002	101.361	0.	0.08	10.	rect	Be
1696.14	XAB2	270.105	80.9448	0.	1.	1.	ellip	Ti(Cu coated)
1713.96	YAB2	114.055	483.257	0.	1.	1.	ellip	Ti(Cu coated)
1715.96	YSP3	114.054	483.253	0.	10.	0.102	rect	Be
1731.78	XSP3	270.003	101.347	0.	0.08	10.	rect	Be
1808.98	XAB3	270.102	80.9043	0.	1.	1.	ellip	Ti(Cu coated)
1826.8	YAB3	114.054	483.184	0.	1.	1.	ellip	Ti(Cu coated)
1828.8	YSP4	114.054	483.188	0.	10.	0.102	rect	Be
1844.63	XSP4	270.002	101.361	0.	0.08	10.	rect	Be
1921.83	XAB4	270.105	80.9448	0.	1.	1.	ellip	Ti(Cu coated)
1939.65	YAB4	114.055	483.257	0.	1.	1.	ellip	Ti(Cu coated)

Placet.

In this chapter we do not include studies at the interaction region, such as extraction lines, crossing angles, crab cavities, etc.

### 5.2.1 Tracking codes

The computer tracking code used for the comparison in the context of the CLIC BDS are: SAD MAD and Placet.

- SAD is a 6D-symplectic tracking tool. In the presence of synchrotron radiation each magnet is split into several slices, and the radiation occurs at the borders between the slices. A particle obeys symplectic dynamics within every slice [120].
- MAD uses the TRANSPORT formalism up to order two. In the case of synchrotron radiation, MAD computes the energy radiated at the entrance and the exit of the element [121]. In this paper the version MAD8 is used. A new synchrotron radiation generator has been recently implemented for MADX based on integrals of Chebyshev polynomials [122].
- Placet is a tracking code originally written for linac simulations [119] and later extended to cover also the Beam Delivery System [123]. Placet implements the Monte Carlo generator for synchrotron radiation of Ref. [124].

It is worthwhile to mention some differences between the different codes when the synchrotron radiation is active. In order to maintain the beam nominal energy and the beam matched with the downstream lattice, MAD accounts for energy losses due to photon emission by artificially re-accelerating the beam after the bending magnets in the final focus system. Placet can simulate beam re-acceleration and magnet rescaling. For SAD with synchrotron radiation neither artificial re-acceleration nor magnet rescaling have been added. The values of the luminosity have been computed with GuineaPig [86]. This program performs detailed simulations of the beam-beam interactions at the IP including the hourglass effect, the pinch effect beamstrahlung and  $e^+e^-$  production. The interface between the tracking codes and GuineaPig has been done off line. The output files from the tracking simulations with the above codes are used as input beam particles distributions to perform beam-beam calculations with GuineaPig.

### 5.2.2 Tracking results

A distribution of 40000 particles and 1 % full width energy spread for a flat square energy distribution has been tracked along the CLIC beam delivery system. The nominal beam parameters are shown in Table 5.2.

Figure 5.4 shows an example of the beam transversal profile at the IP. The beam sizes have been calculated taking the size of the beam core by means of a gaussian fit. For the case of the CLIC BDS, the transverse tails of the particles distribution at the IP are long and may provide an

important background source. It was estimated in Ref. [117] that the beam population of those tails is about 10 % of the total bunch particles. Some of these particles are at very large amplitude and contribute to increase the value of the standard deviation of the particle position. Therefore, because of the non-gaussian nature of the beam distribution at the CLIC IP, the standard deviation is not a good indication of the beam size.

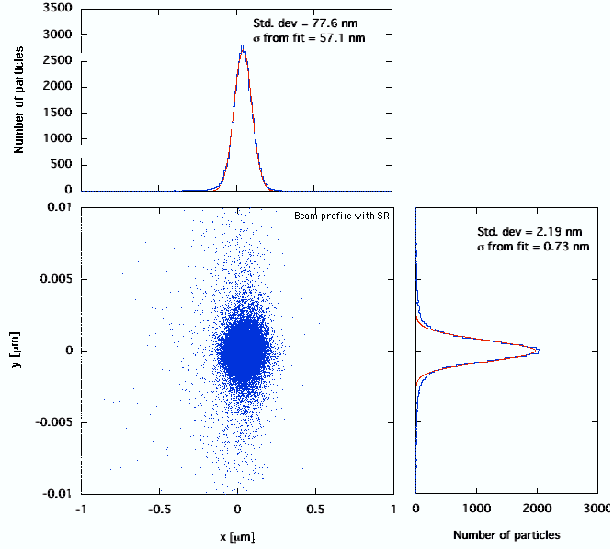


Figure 5.4: Sample of transverse beam profile at the IP after the tracking with Placet, including the effects of the synchrotron radiation. The core beam sizes is calculated by means of gaussian fit to the particles distribution in both planes  $x$  and  $y$ .

Figures 5.5 and 5.6 are a sample of the phase space at the IP as given by Placet for the horizontal and vertical transversal plane, respectively. The cases without and with synchrotron radiation have been considered.

Table 5.5 summarizes the results for the beam size at the IP as given by SAD, MAD, and Placet. We compare the values of the standard deviation and the values obtained by a gaussian fit.

In the lattice with MAD the collimation aperture is defined and we have halo particles losses up to 4 % from the total number for a beam with 1 % energy spread. This explains why the standard deviation given by MAD is lower than the result with Placet and SAD, where the collimators are not defined.

When the synchrotron radiation is switched off, the result from the three codes for the core beam size is very similar or the same. With synchrotron radiation, we find a discrepancy for the vertical beam size with SAD up to 14 % from the other two codes, and discrepancies of about 15 % for the horizontal standard deviation. At this point, it is worthwhile to remind the reader that the

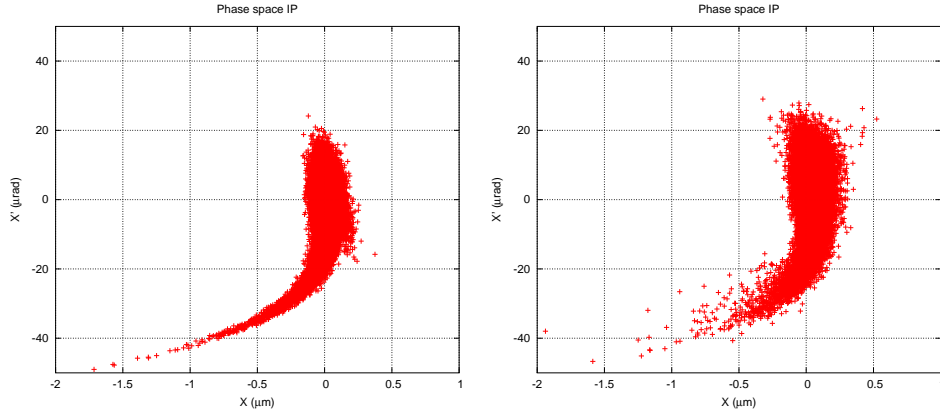


Figure 5.5: Horizontal phase space without the synchrotron radiation effects (figure on the left) and with the synchrotron radiation effects (figure on the right) as given by simulation with Placet.

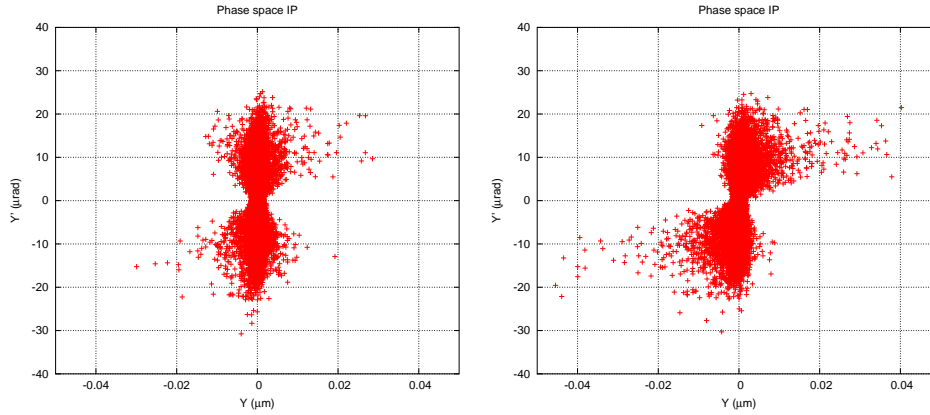


Figure 5.6: Vertical phase space without the synchrotron radiation effects (figure on the left) and with the synchrotron radiation effects (figure on the right) as given by simulation with Placet.

compensation for energy losses due to photon emission is implemented in the BDS lattice with MAD for the final focus system and Placet, and is missing in SAD. This could be the source of discrepancy when the synchrotron radiation is active.

Table 5.6 shows the values obtained for the luminosity without and with synchrotron radiation. Placet gives the higher values in comparison to the other two codes.

### 5.2.3 Particle per particle comparison

We have calculated the difference of the horizontal and vertical particle positions at the IP from the tracking results with the different codes as a function of the energy. A strong correlation with energy offset is found for the cases  $x_{MAD} - x_{SAD}$ ,  $x_{Placet} - x_{MAD}$ ,  $y_{MAD} - y_{SAD}$  and  $y_{Placet} - y_{MAD}$ .

Table 5.5: Comparison of the standard deviation (Std. dev.  $i$  for  $i = x, y$ ) of the beam distribution at the IP as given by the three tracking codes, and comparison of the transversal beam size ( $\sigma_i$  for  $i = x, y$ ) calculated by means of gaussian fit to the particles distribution at the IP. For the tracking a beam of 40000 particles and 1 % full width flat square energy spread was considered.

<b>w/o SR</b>				
	Std. dev. x	$\sigma_x$ (gaus. fit)	Std. dev. y	$\sigma_y$ (gaus. fit)
SAD	84.8 nm	48.0 nm	1.28 nm	0.65 nm
MAD	69.6 nm	47.3 nm	1.11 nm	0.65 nm
Placet	84.0 nm	48.0 nm	1.27 nm	0.65 nm
<b>with SR</b>				
	Std. dev. x	$\sigma_x$ (gaus. fit)	Std. dev. y	$\sigma_y$ (gaus. fit)
SAD	82.8 nm	57.1 nm	2.63 nm	0.85 nm
MAD	70.1 nm	57.5 nm	1.96 nm	0.73 nm
Placet	77.6 nm	57.1 nm	2.19 nm	0.73 nm

Table 5.6: Luminosity values calculated for the case without and with synchrotron radiation.

	SAD	MAD	Placet
$\mathcal{L}_{w/o\ SR} [\times 10^{34} \text{ cm}^{-2} \text{ s}^{-1}]$	11.35	10.714	11.655
$\mathcal{L}_{with\ SR} [\times 10^{34} \text{ cm}^{-2} \text{ s}^{-1}]$	7.171	7.441	8.214

Figure 5.7 shows the dependence on energy for  $x_{MAD} - x_{SAD}$  and  $y_{MAD} - y_{SAD}$ . For  $x_{MAD} - x_{SAD}$  maximum differences of up to about 10 nm are found for particles with  $\pm 0.4$  % energy offset. For the vertical position  $y_{MAD} - y_{SAD}$  maximum differences up to about 0.5 nm are found. For the case of  $x_{Placet} - x_{MAD}$  and  $y_{Placet} - y_{MAD}$  (see Figure 5.8) similar differences up to about 10 nm and 0.5 nm are found, respectively.

Figure 5.9 shows the case  $x_{Placet} - x_{SAD}$  and  $y_{Placet} - y_{SAD}$ . Here  $|x_{Placet} - x_{SAD}| < 5$  nm, and a light correlation is observed for a large energy offset lower than the nominal energy. For  $y_{Placet} - y_{SAD}$  no correlation with energy is observed.

The standard deviations found for the differences of the particles positions are summarized in Table 5.7. The minimum standard deviations correspond to the differences of position between the codes Placet and SAD.

#### 5.2.4 Chromatic effects

We consider monochromatic particle distributions arranged to form ellipses in phase space. These ellipses are matched to the entrance twiss parameters of Table 5.2. The ellipses are tracked for different energies from the nominal energy. Here we give the example for offset energies  $\Delta E/E = \pm 0.3$  % and  $\Delta E/E = \pm 0.4$  %.

Table 5.7: The data standard deviation for the difference of the particle positions between the different codes.

$x_{code1} - x_{code2}$	Std. dev. [nm]	$y_{code1} - y_{code2}$	Std. dev. [nm]
$x_{Placet} - x_{SAD}$	1.027	$y_{Placet} - y_{SAD}$	$9.639 \times 10^{-3}$
$x_{Placet} - x_{MAD}$	1.393	$y_{Placet} - y_{MAD}$	$8.701 \times 10^{-2}$
$x_{MAD} - x_{SAD}$	2.067	$y_{MAD} - y_{SAD}$	$8.412 \times 10^{-2}$

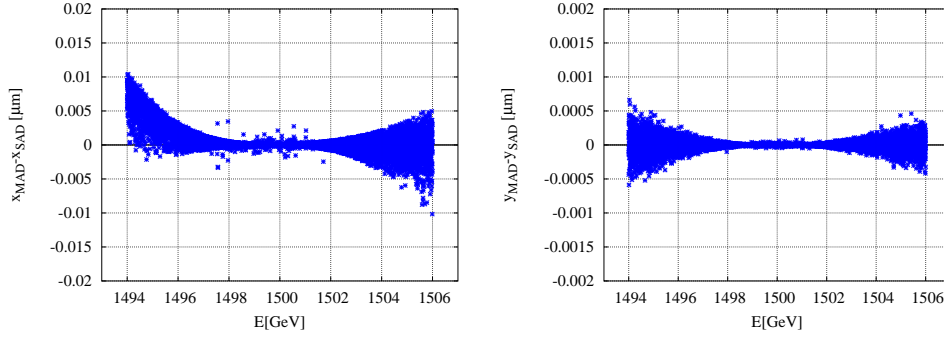


Figure 5.7: Difference of the horizontal (figure on the left) and the vertical (figure on the right) particle position at the IP as a function of the particle energy, as calculated by MAD and SAD.

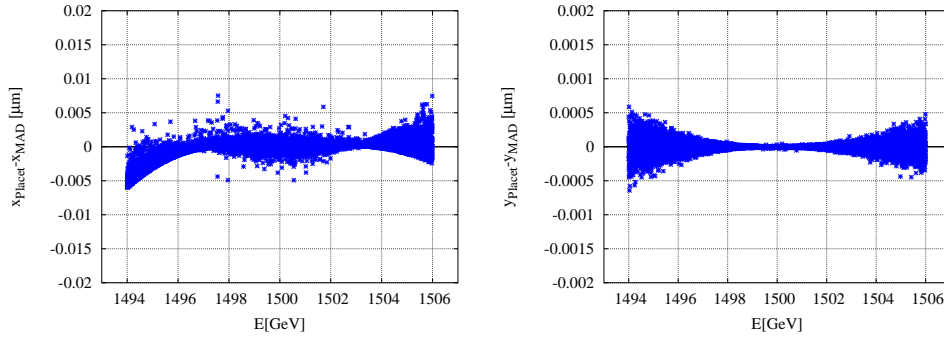


Figure 5.8: Difference of the horizontal (figure on the left) and the vertical (figure on the right) particle position at the IP as a function of the particle energy, as calculated by Placet and MAD.

If we have in the horizontal phase space an initial ellipsoidal particle distribution with vertical initial coordinates  $y_0 = 0$  and  $y'_0 = 0$ , the center of the ellipse at IP is determined by the Taylor map

$$\begin{aligned} x_c(\delta \equiv \Delta E/E) &= R_{16}\delta + T_{166}\delta^2 + U_{1666}\delta^3, \\ x'_c(\delta \equiv \Delta E/E) &= R_{26}\delta + T_{266}\delta^2 + U_{2666}\delta^3, \end{aligned} \quad (5.1)$$

where we consider terms only up to third order. The convention of Ref. [155] has been used for



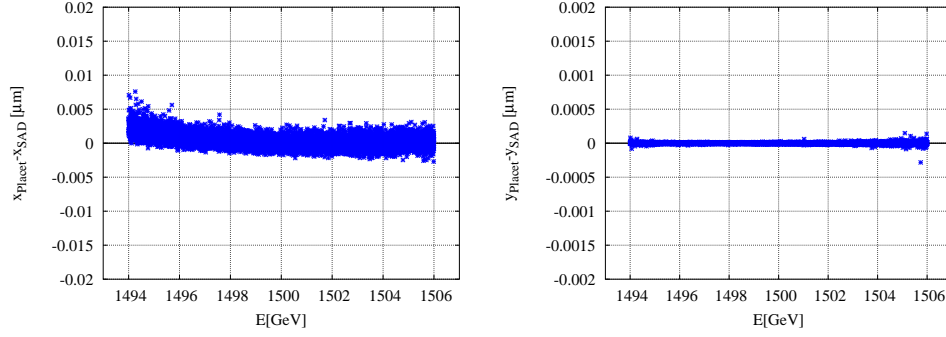


Figure 5.9: Difference of the horizontal (figure on the left) and the vertical (figure on the right) particle position at the IP as a function of the particle energy, as calculated by Placet and SAD.

the coefficients  $R_{ij}$ ,  $T_{ijk}$  and  $U_{ijkl}$  (see Appendix A). Figure 5.10 shows an example for the tracking for ellipses at  $1\sigma$  in the  $x - x'$  phase space using the program Placet. Note that the Taylor map up to third order dispersion gives a good description of the center ellipse transport in phase space for  $\Delta E/E \gtrsim -0.3\%$ . For lower energies from the nominal, strong deformations of the ellipses are observed. Particles with an offset energy  $\lesssim -0.3\%$  bear strong geometric aberrations and contribute to the long tail of the transversal phase space. Figure 5.11 shows the chromatics effects for the horizontal phase space at IP, where different colours have been used to distinguish the position of the particle depending on the energy around the nominal beam energy of 1500 GeV.

For the  $y - y'$  phase space we show in Figure 5.12 an example for the tracking with ellipses at position amplitudes of  $1\sigma$  and  $3\sigma$ , considering the nominal energy and the energy offset  $\Delta E/E = \pm 0.3\%$ . The particles at high position amplitude of several sigmas contribute to the population of the long tails. For the case of the ellipses at  $3\sigma$  in the vertical phase space, it is possible to observe a strong deformation of the shape caused by the sextupoles located in the final focus system.

The MAD program can calculate the matrix elements up to second order. We have calculated the third order with a elliptical fit to the tracked points which allows us to determine the ellipse center. Table 5.8 shows the result for the matrix elements from Eq. (5.1) corresponding to the CLIC BDS, FFS and CS separately. For the FFS a description up to second order is enough. The addition of CS introduces important third order coefficients.

### 5.2.5 Bandwidth

A way to estimate the importance of the residual high-order chromatic aberrations introduced from the BDS optics is to evaluate the momentum acceptance of the system. This acceptance is commonly denominated as the momentum or energy *bandwidth*, and is defined as the tolerable range of central momentum errors, or the tolerable range of energy spread. Outside this range the system performance is strongly degraded.

The tracking was made with 10000 particles for different energy spreads, considering a flat

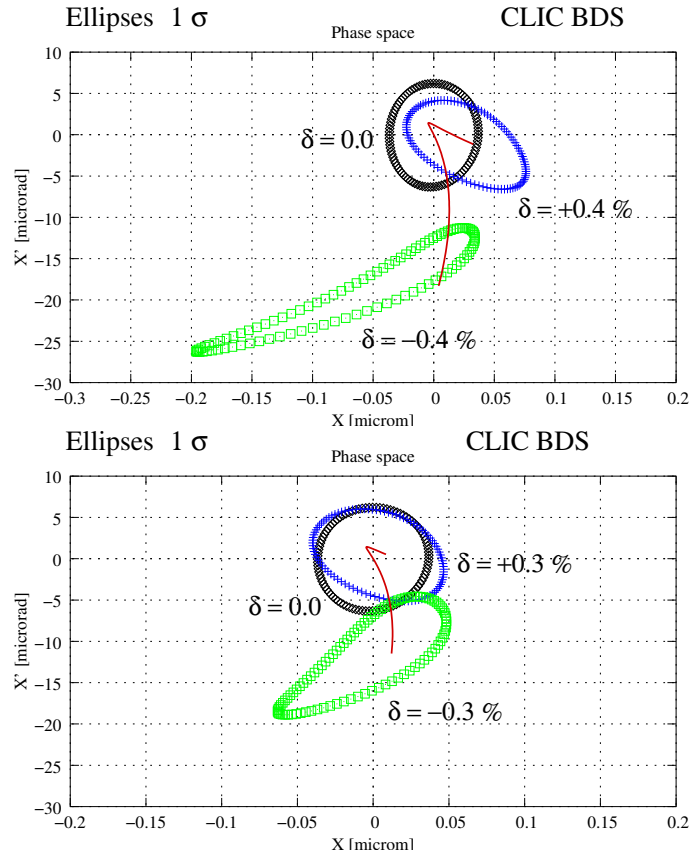


Figure 5.10: Phase space  $x - x'$  at IP for ellipsoidal particles distributions at  $1\sigma$ , using the tracking program Placet. Figure on the top shows the tracking result with Placet for nominal energy (black ellipse) and offset energies  $+0.3\%$  (blue ellipse) and  $-0.3\%$  (green ellipse). Figure on the bottom shows the tracking result with Placet for nominal energy (black ellipse) and off energy  $+0.4\%$  (blue ellipse) and  $-0.4\%$  (green ellipse). The red line is the center ellipse change as a function of the energy off-set, see Eq. (5.1).

square energy distribution. Both cases with and without synchrotron radiation have been considered.

Figure 5.13 shows the beam sizes as a function of the beam energy spread for the horizontal (figure on the top) and vertical (figure on the bottom) plane without synchrotron radiation. The bandwidth with synchrotron radiation is shown in Figure 5.14 for the horizontal beam size (on the top) and for the vertical (on the bottom). The results have been normalized to the value given by Placet at  $0\%$  energy spread without synchrotron radiation.

The lattice for the CLIC BDS in MAD includes the aperture of the collimators. Because of this, particle losses are observed with MAD from  $0.9\%$  energy spread on. For the nominal energy spread of  $1\%$  about  $4\%$  of the total particles are removed. For values of energy spread  $> 1\%$  the beam size

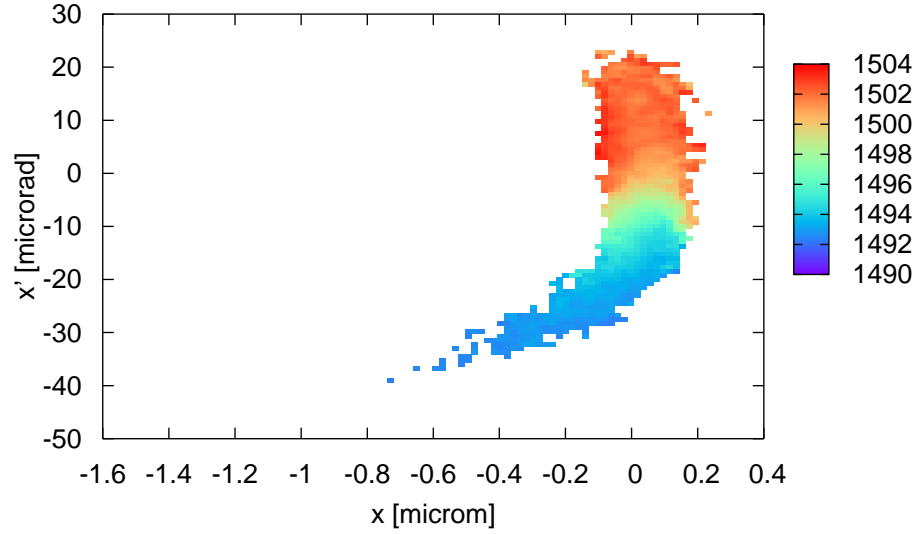


Figure 5.11: Horizontal phase space including synchrotron radiation effects. The color scale on the right represents the energy of the different particles given in GeV.

remains approximately constant because of the collimation using MAD. Figure 5.15 shows the result for the luminosity as a function of energy from the tracking simulation using the three simulation codes. At 1 % full width energy spread we have a luminosity loss  $\approx 30\%$  with respect to the ideal value. On the other hand, if we compare the values between the cases with and without radiation, the synchrotron radiation (bending magnets + final quadrupoles) causes about 40 % luminosity loss from the ideal value. Therefore, the synchrotron radiation is a limitation factor more important than the beam energy spread. In the next section, the limitation of the radiation in the strong final telescope will be evaluated.

As it was observed in previous sections, the values obtained from SAD are higher than those from the simulations with MAD and Placet for the beam sizes with radiation, and therefore lower for the luminosity.

### 5.3 An alternative nonlinear energy collimation system

As we have already mentioned in section 4.2.2, high horizontal dispersion and high betatron functions at the skew sextupoles are necessary to collimate simultaneously in energy and transverse beam amplitude. This solution, first proposed for CLIC in Ref. [39], tends to introduce large chro-

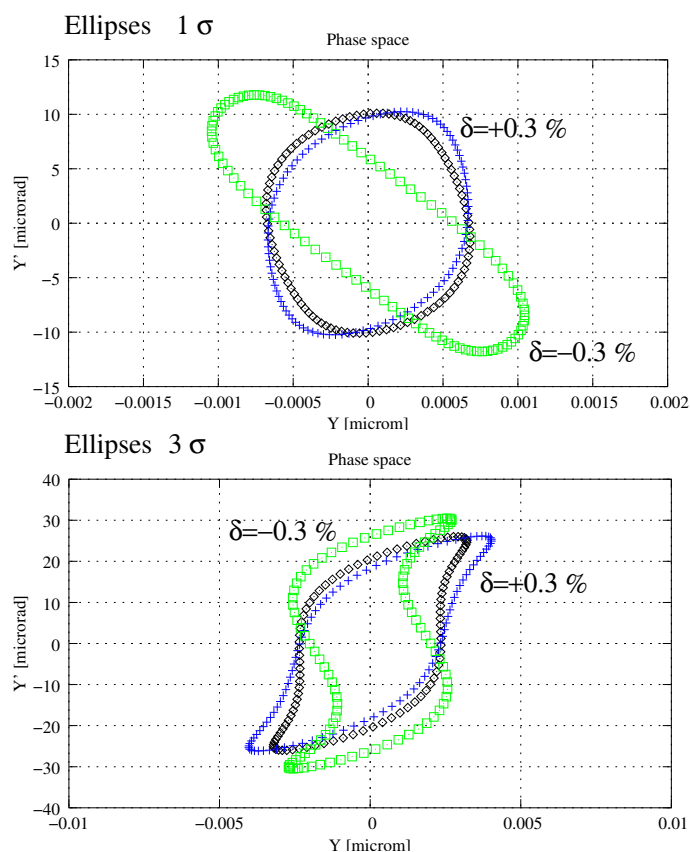


Figure 5.12: Phase space  $y - y'$  at IP for ellipsoidal particles distributions at  $1\sigma$  (figure on the top) and  $3\sigma$  (figure on the bottom) using the tracking program `PLAcet`. The tracking result for nominal energy (black ellipse) is compared with the tracking results for offset energies  $+0.3\%$  (blue ellipse) and  $-0.3\%$  (green ellipse).

maticity, which requires local correction. However the addition of other sextupoles for this correction introduced residual optics aberrations which degraded dramatically the luminosity. Then we decided to reduce the optical constraints for the nonlinear collimation system design, and to perform only collimation in energy using the scheme with a pair of skew sextupoles as described in section 4.2. For betatron collimation we will use exactly the same linear optics as in the baseline design of section 5.1.2.

### 5.3.1 Collimation depth and collimator aperture

The purpose of the first skew sextupole is to increase the vertical spot size at the spoiler, and from Eqs. (4.8), (4.13) and (4.14) we can rewrite the latter as

Table 5.8: Matrix elements for the dispersion up to third order for the CLIC Final Focus system (FFS) and Collimation System (CS) separately, and the Beam Delivery System (BDS): CS + FFS.

	FFS	CS	BDS
$R_{16}$ [m]	$-6. \times 10^{-6}$	0.	$-6. \times 10^{-6}$
$R_{26}$ [rad]	$1.818 \times 10^{-3}$	0.	$1.818 \times 10^{-3}$
$T_{166}$ [m]	$-0.183 \times 10^{-2}$	0.457	$0.114 \times 10^{-2}$
$T_{266}$ [rad]	$0.195 \times 10^{-2}$	$0.273 \times 10^{-2}$	-0.607
$U_{1666}$ [m]	0.	-6.735	0.598
$U_{2666}$ [rad]	0.	0.246	20.382

$$\sigma_y \simeq \frac{1}{2} R_{34} K_s D_{x,s}^2 \sqrt{\langle \delta^4 \rangle - \langle \delta^2 \rangle^2}, \quad (5.2)$$

In a similar way, from Eqs. (4.7), (4.11) and (4.12) the horizontal spot size at the spoiler takes the form

$$\sigma_x \simeq D_{x,sp} \sigma_\delta (1 + C_s)^{1/2}, \quad (5.3)$$

where  $\sigma_\delta = \sqrt{\langle \delta^2 \rangle - \langle \delta \rangle^2}$ , and the nonlinear effect of the sextupole is given by

$$C_s = R_{12}^2 K_s^2 \frac{D_{x,s}^2}{D_{x,sp}^2} \frac{\langle \delta^2 \rangle}{\sigma_\delta^2} \langle y_{\beta,s}^2 \rangle. \quad (5.4)$$

Assuming  $C_s \ll 1$ , then we can approximate

$$\sigma_x \approx D_{x,sp} \sigma_\delta + C'_s, \quad (5.5)$$

where  $D_{x,sp} \sigma_\delta$  is the linear dispersion component and

$$C'_s = \frac{1}{2} R_{12}^2 K_s^2 \frac{D_{x,s}^2}{D_{x,sp}} \frac{\langle \delta^2 \rangle}{\sigma_\delta} \langle y_{\beta,s}^2 \rangle \quad (5.6)$$

the sextupolar effect. This term will be small compared with  $D_{x,sp} \sigma_\delta$  (we recall that we have assumed the betatronic component  $y_{\beta,s}$  to be much smaller than the energy dispersion term  $D_{x,s} \delta$  at the sextupole position). Therefore, the effect of the skew sextupole can be neglected in the horizontal plane.

The increase of the transverse spot sizes at the spoiler translates into a the decrease of the transverse energy density ( $\rho_E \propto 1/\sigma_x \sigma_y$ ). This increases the probability for spoiler survival in case of full beam impact, which will be studied in section 5.4.1.

Recognizing that the energy collimation depth is set by the failure modes in the linac to a value in the range  $\pm 1$ – $1.5$  % [112], in this thesis we have tightened the energy collimation depth to  $\Delta = \pm 1.3$  %. A vertical spoiler with half gap  $a_y$  can be employed to intercept beams with average

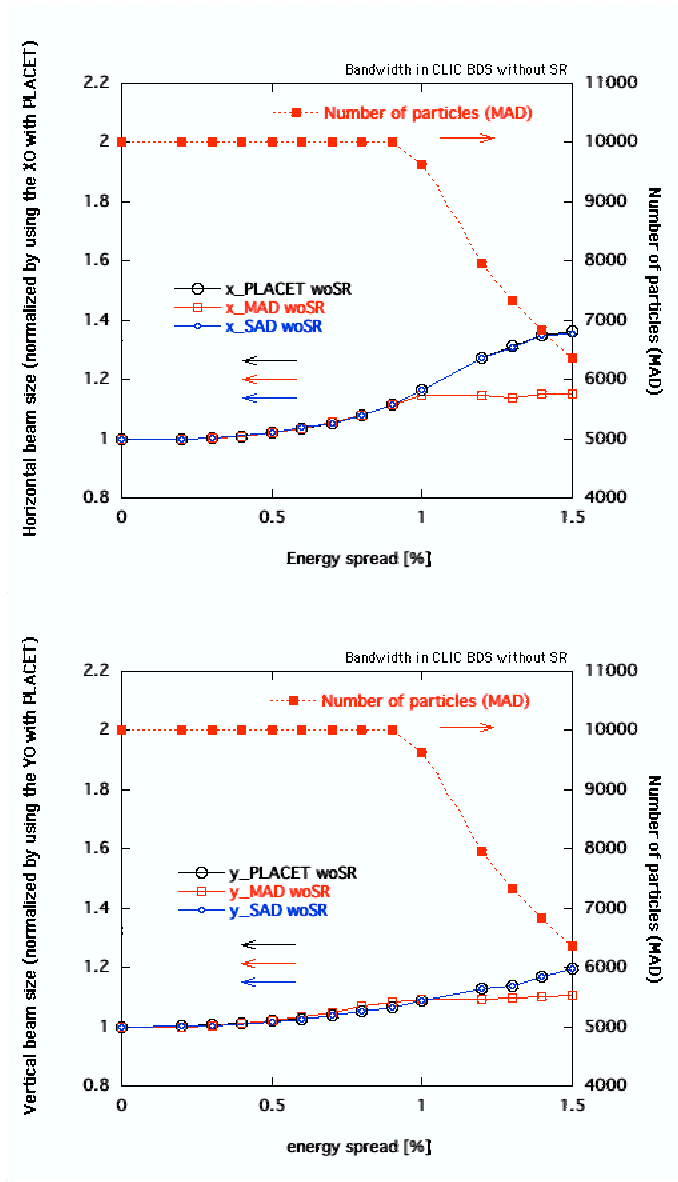


Figure 5.13: Horizontal (figure on the top) and vertical (figure on the bottom) IP spot sizes as a function of the full beam energy spread from the tracking with Placet (black line), MAD (red line) and SAD (blue line). The dashed line with red squared points indicates the number of particles with MAD. In this case the synchrotron radiation is not considered. The results have been normalized to the value given by Placet at 0 % energy spread without synchrotron radiation.

energy off-set  $|\delta_0| \gtrsim |\Delta|$ , giving a relation between  $a_y$ ,  $\Delta$  and the skew sextupole strength:

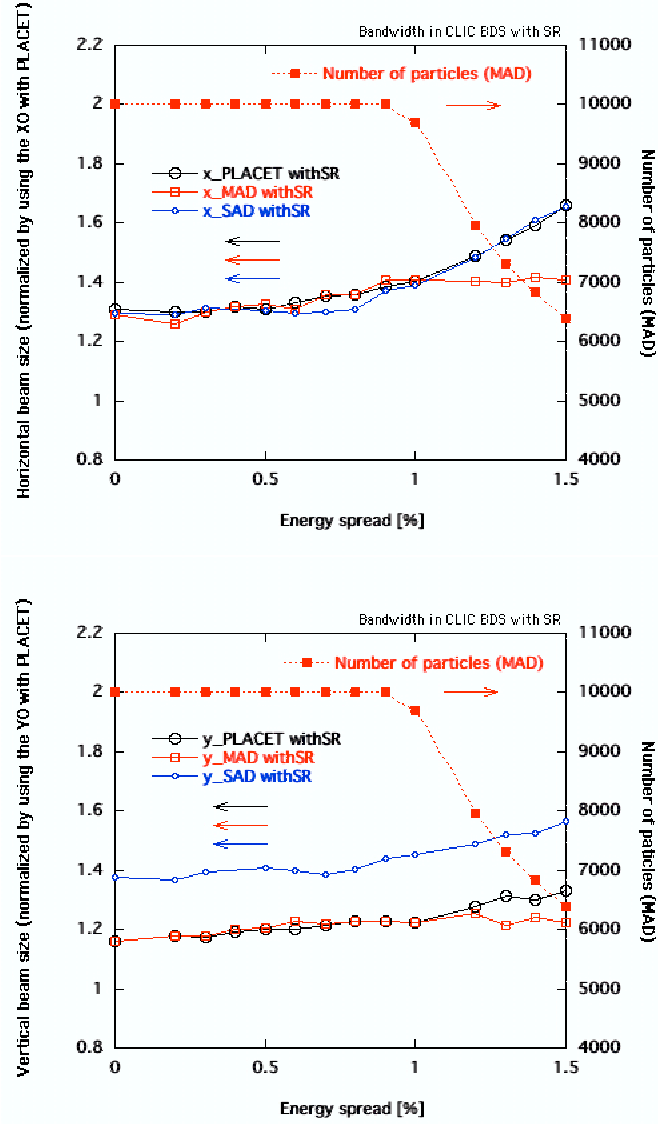


Figure 5.14: Horizontal (figure on the top) and vertical (figure on the bottom) IP spot sizes as a function of the full beam energy spread from the tracking with Placet (black line), MAD (red line) and SAD (blue line). The dashed line with red squared points indicates the number of particles with MAD. In this case the synchrotron radiation is considered. The results have been normalized to the value given by Placet at 0 % energy spread without synchrotron radiation.

$$a_y \simeq \frac{1}{2} R_{34} K_s D_{x,s}^2 \Delta^2 . \quad (5.7)$$

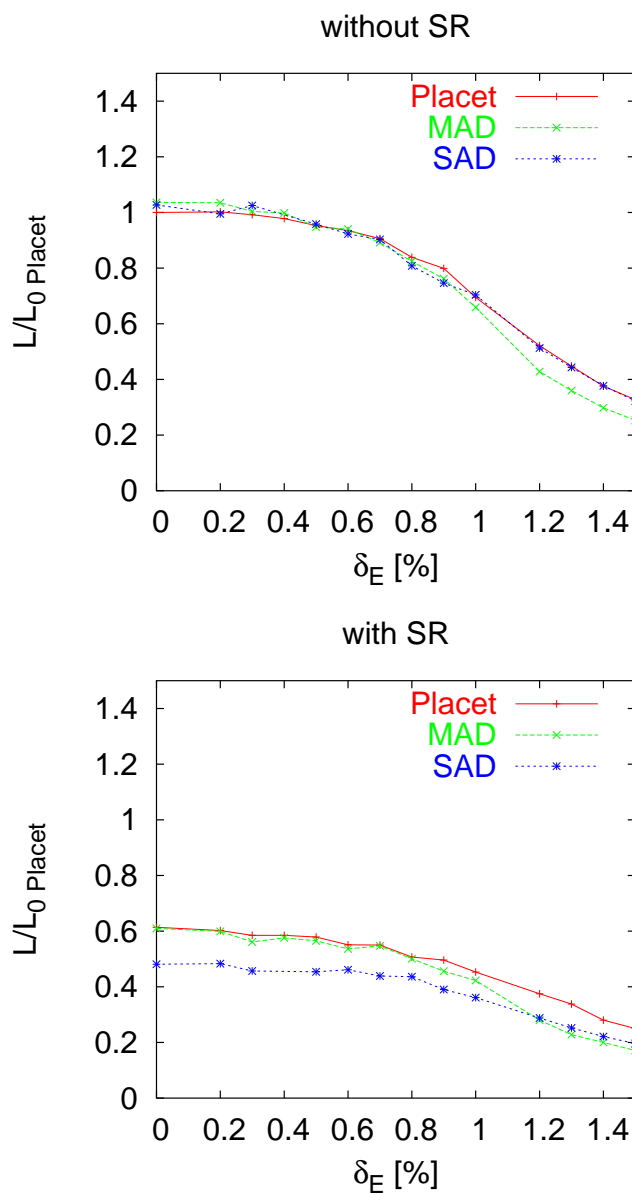


Figure 5.15: Luminosity as a function of the beam energy spread from the tracking with Placet (red line), MAD (green line) and SAD (blue line). Figure on the top corresponds to the case without synchrotron radiation. Figure on the bottom corresponds to the case with synchrotron radiation. The results have been normalized to the value given by Placet at 0 % energy spread without synchrotron radiation.

Alternatively, we can use the linear optics for energy collimation if a horizontal spoiler is set to the half gap



$$a_x \simeq D_{x,sp} \Delta . \quad (5.8)$$

### 5.3.2 Optics layout solution

Various optics designs for nonlinear energy collimation at CLIC were developed by using the code MAD. Table 5.9 lists the optics parameters for the different optics designs: the total length of the nonlinear energy collimation section; the betatron functions  $\beta_{x,s}$  and  $\beta_{y,s}$  at the skew sextupoles; the betatron functions  $\beta_{x,sp}$  and  $\beta_{y,sp}$  at the momentum spoiler; the absolute value of the horizontal dispersion  $|D_{x,s}|$  at the skew sextupoles; the horizontal dispersion  $D_{x,sp}$  at the momentum spoiler; the value of the dipole angle  $\theta_b$  at the nonlinear energy collimation section; and the synchrotron radiation integral  $I_5$  calculated along the nonlinear energy collimation lattice. The main features of those optics are:

- The dispersion  $D_{x,s}$  at the first skew sextupole and the skew sextupole strength  $K_s$  were chosen so as increase the vertical spot size at the spoiler enough to guarantee the scraper or spoiler survival in case of full beam impact. This issue will be studied with some detail in section 5.4.1.
- The stronger effect of the first skew sextupole is in the vertical spot size, which will be increased at the spoiler, in this way decreasing the transverse energy density at the spoiler. The sextupolar effect on the horizontal beam size will be small compared with the first order linear dispersive term (see Eq. (5.5)).
- We have maximized the overall fraction of the system occupied by bends and decreased the bending angle  $\theta_b$  to a point where the effect of synchrotron radiation became reasonably small. At the same time the dispersion at the sextupole position,  $D_{x,s}$ , was maximized as much as possible for good collimation effectiveness.
- One could think to increase  $D_{x,s}$  and decrease the SR effects with a big bending angle  $\theta_b$  and using larger dipole length  $l_b$ , since the energy spread due to SR is proportional to  $\theta_b^3/l_b^2$ . However, an important constraint is the length of the total system, which should be as short as possible if we take into account the considerable cost of the tunnel construction per km [113]. Therefore the length of the system was adjusted to the reasonable value for which emittance growth due to SR does not degrade the collider performance. The bending angles were adjusted accordingly to minimize the emittance growth due to the synchrotron radiation.

From Eq. (4.30) a value of the radiation integral  $I_5 = 10^{-19} \text{ m}^{-1}$  corresponds to a normalized emittance growth  $\Delta(\gamma\epsilon_x) \simeq 0.047 \mu\text{m}$ , i.e. about 7 %, for CLIC at center-of-mass energy of 3 TeV. We have taken the value  $I_5 = 10^{-19} \text{ m}^{-1}$  as constraint for the dispersion function, so that the value of emittance growth is restricted by  $\Delta(\gamma\epsilon_x) < f\gamma\epsilon_x$  with  $f \simeq 0.07$ .

- The transformation matrix  $-I$  between the skew sextupoles was chosen in order to cancel the geometric aberrations.
- No bends were installed between the skew sextupoles, i.e.,  $R_{16}^{s_1 \rightarrow s_2} = 0$  (where  $R_{16}^{s_1 \rightarrow s_2}$  denotes the optical transport matrix element between the two skew sextupoles). Hence the dispersion will propagate between the skew sextupoles exactly like a betatron oscillation. In this condition, the dispersion at each sextupole has the opposite sign and same absolute value which cancels the first order chromatic aberrations, reducing thus the luminosity degradation.
- Very strong skew sextupoles may introduce important third, fourth and higher order optics aberrations, which may dramatically degrade the luminosity at the IP. The criterion for selecting the sextupole strength was a trade-off between the minimum beam peak density at the scraper and the maximum luminosity. In the next section we will carefully discuss this issue presenting results from multiparticle tracking studies.

Table 5.9: Summary of some parameters for the different optics solutions of a nonlinear energy collimation system for CLIC.

parameters	optics #1	optics #2	optics #3	optics #4	optics #5
length [m]	2536.0	1717.035	2036.0	1730.763	1730.763
$\beta_{x,s}$ [m]	896.046	369.433	540.012	436.603	436.603
$\beta_{y,s}$ [m]	266.001	110.184	160.697	110.184	110.184
$\beta_{x,sp}$ [m]	650.0	650.0	650.0 65.0	550.0	550.0
$\beta_{y,sp}$ [m]	65.0	65.0	65.0	65.0	65.0
$ D_{x,s} $ [m]	0.085	0.097	0.094	0.097	0.078
$D_{x,sp}$ [m]	0.085	0.097	0.094	0.097	0.078
$\theta_b$ [rad]	$1.4 \times 10^{-4}$	$2.5 \times 10^{-4}$	$2.0 \times 10^{-4}$	$2.5 \times 10^{-4}$	$2.0 \times 10^{-4}$
$I_5$ [m <sup>-1</sup> ]	$1.643 \times 10^{-21}$	$4.87 \times 10^{-20}$	$1.261 \times 10^{-20}$	$4.71 \times 10^{-20}$	$1.543 \times 10^{-20}$

Table 5.10 compiles the beam, optics and collimation parameters for the nonlinear collimation system #4. For this system the betatron functions and the horizontal dispersion as a function of the longitudinal variable  $s$  are shown in Fig. 5.16. The betatron functions and the dispersion versus  $s$ , for the total CLIC BDS at 3 TeV using the nonlinear collimation system #4, are plotted in Fig. 5.17. We have considered  $\beta_x^0 = 65$  m,  $\beta_y^0 = 18$  m and  $D_x = 0$  m at the entrance of the BDS. The twiss parameters at the IP are exactly the same as for the BDS with linear collimation, i.e.  $\beta_x^* = 7$  mm,  $\beta_y^* = 0.09$  mm and  $D_x = 0$  m.

### 5.3.3 Optics optimization

The luminosity drops as the strength of the skew sextupole excitation increases. The arrangement of the skew sextupoles from Fig 4.3 allows the cancellation of first order geometric and chromatic aberrations. However, there are remanent higher order aberrations which may cause a strong

Table 5.10: Beam, optics and collimation parameters for the nonlinear collimation system #4

variable	symbol	value	units
Beam energy	$E$	1500	GeV
Energy spread full width (uniform distribution)	$\delta_{\text{flat}}$	0.01	
rms momentum spread	$\sigma_\delta$	$2.8 \times 10^{-3}$	
Hor. normalized emittance	$\gamma\epsilon_x$	680	nm
Ver. normalized emittance	$\gamma\epsilon_y$	10	nm
Total length	$l_t$	1730.763	m
Dipole angle	$\theta_b$	$2.5 \times 10^{-4}$	rad
Skew sextupole strength	$K_s$	20.8	$\text{m}^{-2}$
Hor. beta function at entrance	$\beta_x^0$	65.0	m
Ver. beta function at entrance	$\beta_y^0$	18.0	m
Hor. phase advance from sext. to spo.	$\mu_x$	0.25	$2\pi$
Ver. phase advance from sext. to spo.	$\mu_y$	0.25	$2\pi$
Transport matrix from sext. to spo.	$R_{12}$	490.032	m
Transport matrix from sext. to spo.	$R_{34}$	84.628	m
Hor. dispersion function at sext.	$D_{x,s}$	0.097	m
Ver. dispersion function at spo.	$D_{x,\text{sp}}$	0.097	m
SR integral	$I_5$	$4.71 \times 10^{-20}$	$\text{m}^{-1}$
Energy collimation depth	$\Delta$	0.013	
Hor. spoiler half gap	$a_x$	1.266 (112.552)	mm ( $\sigma_{\beta,x}$ )
Ver. spoiler half gap	$a_y$	1.414 (3008.681)	mm ( $\sigma_{\beta,y}$ )
Transverse energy beam density limit (beryllium spoiler survival)	$\rho_{E,\text{max}}$	11.156	$\text{kJ mm}^{-2}$ per bunch

degradation of the luminosity. For the CLIC nonlinear collimation system we have dominant high chromatic aberrations of second, third and fourth order.

Two additional thin multipoles (one skew octupole and one normal sextupole) have been added behind the second skew sextupole, such as shown in Fig. 5.18, in order to locally cancel the higher order aberrations. This minimization of aberrations was computed using a Python based code called MAPCLASS [125]. This optimization algorithm takes as figure of merit the rms beam sizes at the end of the beam line, calculated from the coefficients of the transfer map up to an arbitrary order, i.e. [126]

$$\sigma_f^2 = \sum_{\substack{jklmn \\ j'k'\ell'm'n'}} C_{jklmn} C_{j'k'\ell'm'n'} \int x_i^{j+j'} p_{xi}^{k+k'} y_i^{\ell+\ell'} p_{yi}^{m+m'} \delta_i^{n+n'} \rho_i dv_i, \quad (5.9)$$

where  $x_i$ ,  $p_{x,i}$ ,  $y_i$  and  $p_{y,i}$  represent the initial transverse phase space coordinates and  $\delta_i$  the initial average energy offset. The coefficients  $C_{jklmn}$  are the map coefficients of the corresponding final state, and can be obtained by MADX-PTC [127] up to any order.  $dv_i$  represents the differential volume of the initial phase space, and  $\rho_i$  the initial transverse beam density. Assuming that the transfer map

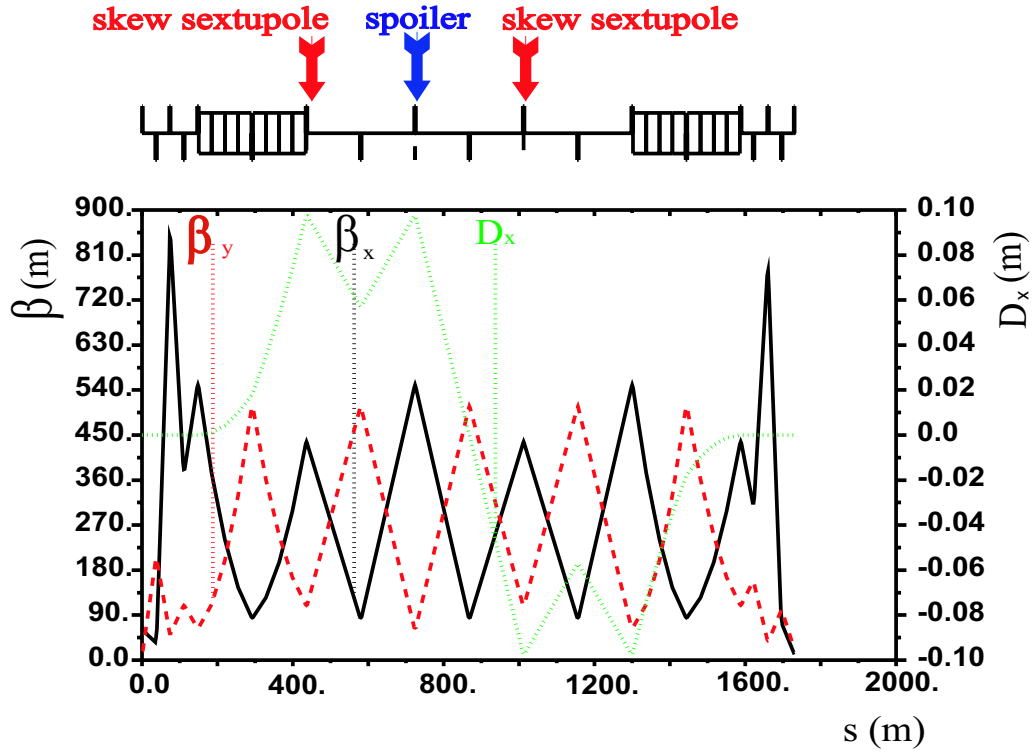


Figure 5.16: Twiss functions of the nonlinear energy collimation optics #4 proposed for CLIC at 3 TeV.

is symplectic  $\rho_i dv_i = \rho_f dv_f$ , where the subindex  $i$  denotes the initial phase space and the subindex  $f$  the final phase space.

The minimization of the transverse spot sizes  $\sigma_f$  at the end of the nonlinear collimation system is done by the Simplex method implemented in MAPCLASS. For reasons of computing time we limited the optimization considering the transfer map up to fourth order. Assuming an integrated sextupole strength of  $20.8 \text{ m}^{-2}$ , the minimum spot size at the end of the collimation lattice was found for the following strengths of the added multipole magnets:  $K_{o,\text{skew}} = -5445 \text{ m}^{-3}$  (skew octupole) and  $K_{s,\text{normal}} = -0.675 \text{ m}^{-2}$  (normal sextupole). Fig. 5.19 shows the result from this optimization for the nonlinear collimation optics #4, comparing the transverse rms beam sizes as function of the maximum order considered in the map before and after the optimization. There is clearly a significant reduction of the second, third and fourth order contributions to the horizontal and vertical beam sizes.

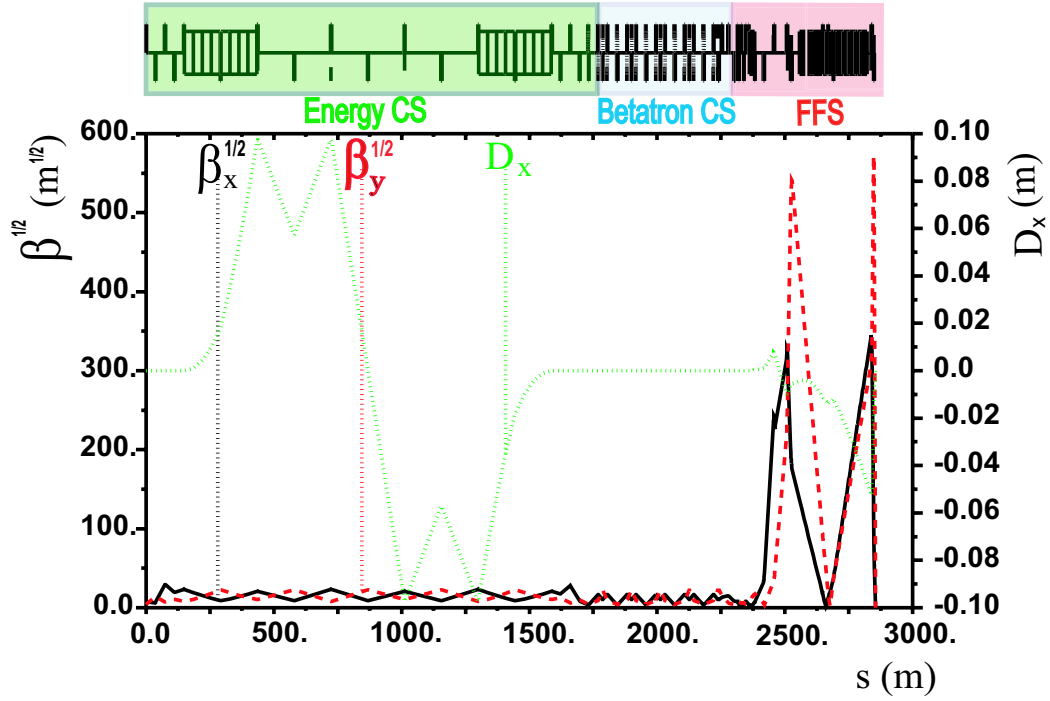


Figure 5.17: Twiss functions of the entire CLIC BDS optics including the nonlinear energy collimation system of Fig. 5.16.

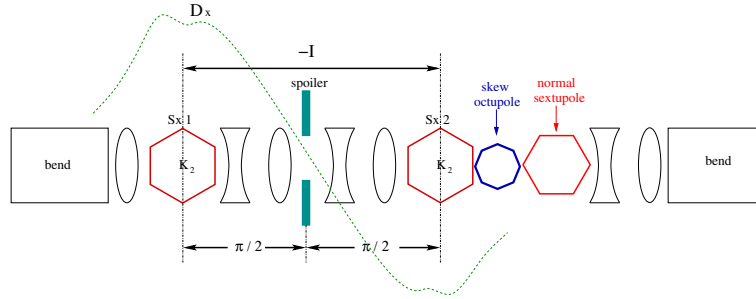


Figure 5.18: Schematic of a linear collimation system using a pair of skew sextupoles and adding a skew octupole and a normal sextupole for local correction of high order geometric and chromatic aberrations.

## 5.4 Tracking studies

Multiparticle tracking studies were done in order to study the performance of the various collimation systems proposed in this thesis (see Table 5.9). These studies allow us to choose the optics

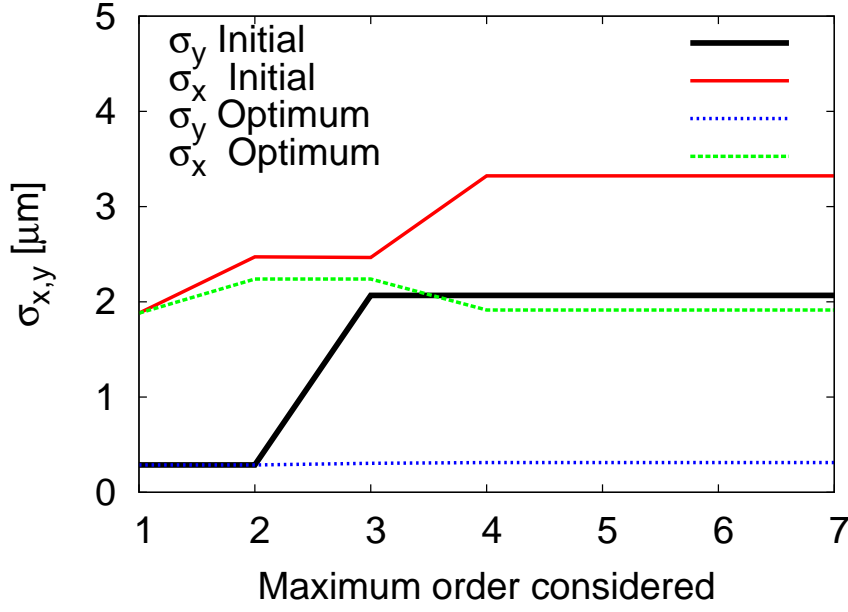


Figure 5.19: Horizontal and vertical rms beams sizes at the end of the CLIC nonlinear energy collimation system #4 as function of the maximum order considered in the transfer map. Both the initial case before optimization and the optimized case using MAPCLASS [125] are compared.

that best fulfils the nonlinear collimation requirements listed above, and the obtained preliminary results can guide the further optics improvement.

The codes MAD [114] and Placet [119] were used for the tracking (see section 5.2 for code comparison). From the tracking results, we have computed, on one hand, the luminosity and, on the other hand, the transverse rms beam sizes and the transverse beam energy density at the spoiler.

The output files from the tracking simulations with the above codes are used as input beam particle distributions to compute the luminosity with the beam-beam interaction code GuineaPig [86].

Both the luminosity at the IP and the beam energy density at the spoiler were calculated for different scenarios, i.e. for different skew sextupole strengths. The goal is to find the most favorable scenario, i.e. the optimum trade-off between maximum luminosity and minimum transverse beam energy density at the spoiler.

### 5.4.1 Performance

#### Luminosity

Multiparticle tracking studies were done from the entrance of the BDS to the IP using the different nonlinear energy collimation systems from Table 5.9. We have assumed an initial Gaussian distri-

bution in transverse phase space of 40000 macro-particles with an uniform flat energy distribution of  $\delta_{\text{flat}} = 1 \%$  (full width energy spread) centered at the nominal beam energy  $E_0 = 1500$  GeV.

The luminosity was computed using Guinea-Pig as a function of the integrated strength of the skew sextupoles. The luminosity is degraded with higher skew sextupole excitation. The results before and after optimization are registered in Table 5.11 for the different nonlinear collimation optics solutions considering a skew sextupole strength  $K_s = 20.8 \text{ m}^{-2}$ . Two curves of the luminosity, namely *without* and *with* optimization, versus the skew sextupole strength have been compared in Fig. 5.20 for the candidate solution #1 and in Fig. 5.21 for the candidate #4. Assuming an integrated skew sextupole strength  $K_s = 20.8 \text{ m}^{-2}$  for optics #1, the luminosity increases approximately a factor 3 after optimization, and for optics #4 approximately a factor 2.

Table 5.11: Results using the different optics for nonlinear collimation with an integrated skew sextupole strength of  $K_s \approx 20.8 \text{ m}^{-2}$ : luminosity,  $L$ ; luminosity after optimization,  $L_{\text{opt}}$ .

Optics #	$L$ [ $\times 10^{34} \text{ cm}^{-2} \text{ s}^{-1}$ ]	$L_{\text{opt}}$ [ $\times 10^{34} \text{ cm}^{-2} \text{ s}^{-1}$ ]
1	2.579	6.193
2	2.475	5.364
3	2.544	5.2
4	2.560	5.144
5	3.499	6.174

### Optical bandwidth

We have studied the IP bandwidth of the system by means of multiparticle tracking using the code Placet. Transverse Gaussian initial distributions of 40000 macro-particles were tracked along the CLIC BDS. A flat energy distribution with  $\delta_{\text{flat}} = 1 \%$  (full width energy spread) has been considered. The tracking was performed for different centroid energies within  $\pm 1 \%$  of the nominal beam energy.

We have evaluated the rms transverse spot sizes and the luminosity at the IP. The results have been normalized to the values obtained at 0 % centroid energy offset. The IP bandwidth before and after optimization is compared in Fig. 5.22 for the optics #4. Here the transverse rms normalized beam sizes at the IP and the normalized luminosity are plotted as a function of the beam centroid energy offset. After optimization the figure shows a significantly wider bandwidth, which is approximately comparable to the performance of the linear collimation system, whose bandwidth is shown in Fig. 5.23.

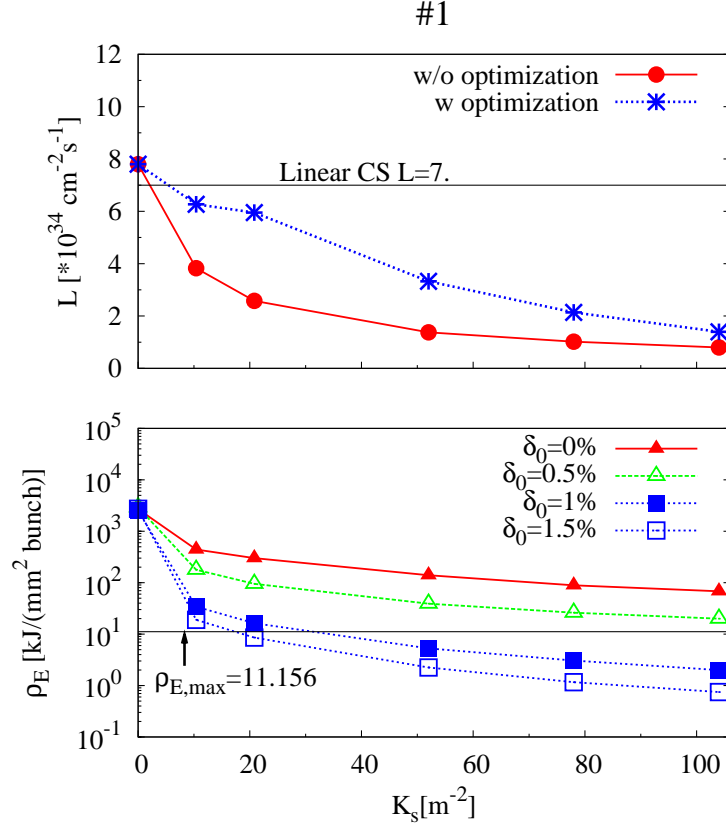


Figure 5.20: Top: luminosity versus integrated skew sextupole strength for the optics solutions #1; curves without optics optimization and with optics optimization are shown. Bottom: beam peak density at the spoiler versus integrated skew sextupole strength for the optics solutions #1; we show the cases for beams with average energy offset  $\delta_0 = 0.0, 0.005, 0.01$  and  $0.015$ . For all the cases an uniform energy distribution of 1 % full width energy spread has been considered in the simulations. The limit for spoiler survival  $\rho_{E,\text{max}}$  corresponds to a collimator made of Be.

### Transverse beam spot size at the spoiler

Sets of 10000 macro-particles were tracked in order to study the chromatic properties of the particle distribution at the spoiler position. Initial particle distributions with  $\delta_{\text{flat}} = 1 \%$  were considered, and the beam centroid energy was taken as a variable.

In addition, the rms horizontal and vertical beam sizes can analytically be calculated from Eqs. (4.18) and (4.19), respectively, up to first order. Both the tracking result and the analytical result of the rms transverse beam sizes as a function of the average beam energy offset  $\delta_0$  are compared in Fig. 5.24. These results have been obtained for  $K_s = 20.8 \text{ m}^{-2}$ .

The rms horizontal beam size at the spoiler  $\sigma_{x,\text{sp}}$  from tracking is in good agreement with the analytical expression only if the second order dispersion  $T_{166}$  is taken into account, i.e.



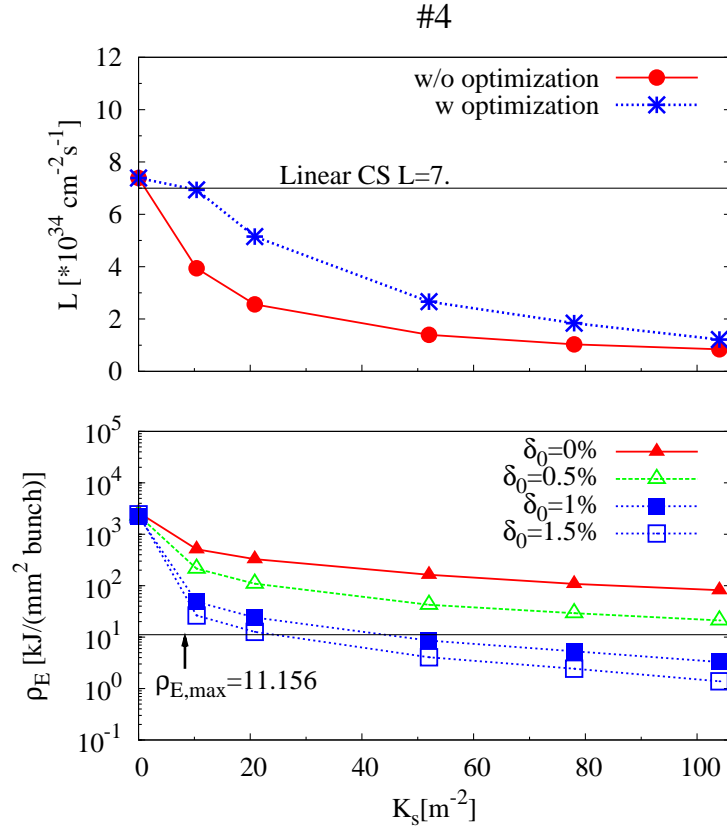


Figure 5.21: Top: luminosity versus integrated skew sextupole strength for the optics solutions #4; curves without optics optimization and with optics optimization are shown. Bottom: beam peak density at the spoiler versus integrated skew sextupole strength for the optics solutions #4; we show the cases for beams with average energy offset  $\delta_0 = 0.0, 0.005, 0.01$  and  $0.015$ . For all the cases a uniform energy distribution of 1 % full width energy spread has been considered in the simulations. The limit for spoiler survival  $\rho_{E,\text{max}}$  corresponds to a collimator made of Be.

$$\begin{aligned} \sigma_{x,\text{sp}} \simeq & \left( D_{x,\text{sp}}^2 \frac{\delta_{\text{flat}}^2}{12} + R_{12}^2 K_s^2 D_{xs}^2 \left( \frac{\delta_{\text{flat}}^2}{12} + \delta_0^2 \right) \beta_{y,s} \epsilon_y \right. \\ & \left. + T_{166}^2 \left( \frac{\delta_{\text{flat}}^4}{180} + \frac{1}{3} \delta_{\text{flat}}^2 \delta_0^2 \right) + \frac{1}{3} T_{166} D_{x,\text{sp}} \delta_{\text{flat}}^2 \delta_0 \right)^{1/2}. \end{aligned} \quad (5.10)$$

(See Appendix C for detailed calculation).

In Fig. 5.25 the transverse particle density is presented for optics #4. In this case an initial particle distribution with  $\delta_{\text{flat}} = 1 \%$  and  $\delta_0 = 1 \%$  has been used for the tracking. The goal is to study the effect of the skew sextupole on the transverse particle distribution for off-energy

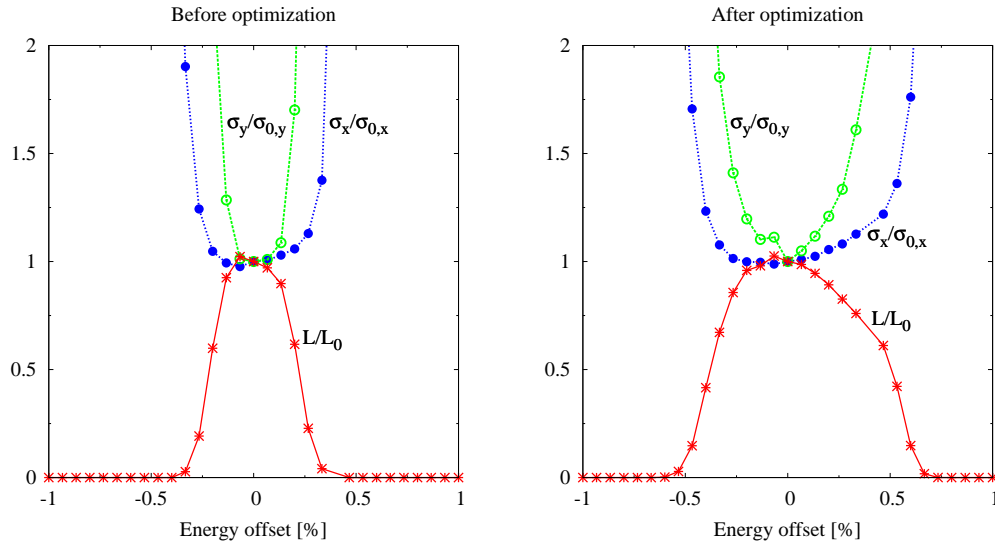


Figure 5.22: IP bandwidth of the CLIC BDS using the momentum nonlinear collimation system of #4. Normalized transverse rms beam sizes and normalized luminosity versus the average beam energy offset. The case before optics optimization (on the left) and the case after optics optimization (on the right) are shown.

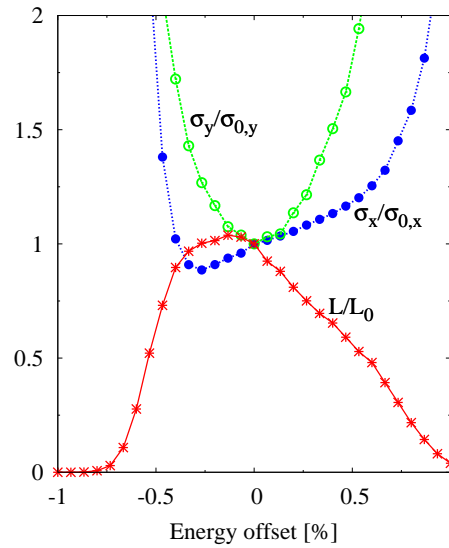


Figure 5.23: IP bandwidth of the CLIC BDS using the conventional baseline linear collimation system. Normalized transverse rms beam sizes and normalized luminosity versus the average beam energy offset.

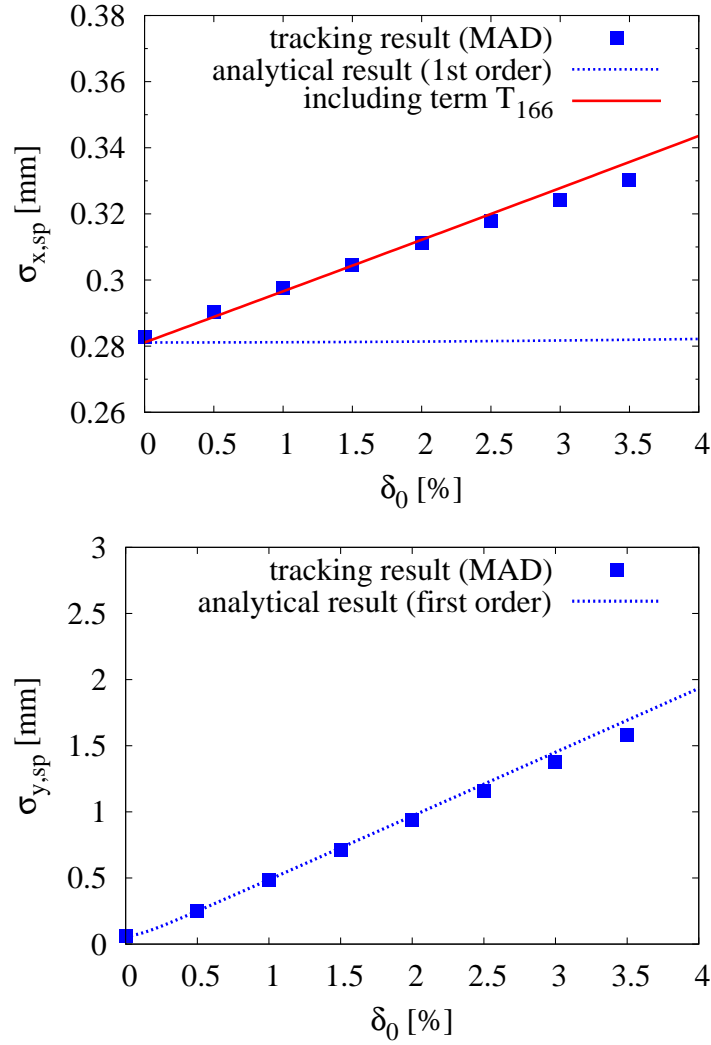


Figure 5.24: Horizontal (top) and vertical (bottom) beam sizes at the spoiler as a function of the average beam energy offset  $\delta_0$ , for the optics #4. The blue solid squares represent the rms beam size computed from the multiparticle tracking results using the code MAD. The lines represent the analytical results. The dotted blue line is the first order calculation and the red solid line is the calculation introducing also the second order dispersion  $T_{166}$  for the case of the horizontal beam size.

beams. Different cases are compared: with skew sextupole switched off ( $K_s = 0.0 \text{ m}^{-2}$ ), with skew sextupole switched on ( $K_s = 20.8 \text{ m}^{-2}$ ), without spoiler, with horizontal spoiler ( $a_x = 1.266 \text{ mm}$ ) and with vertical spoiler ( $a_y = 1.414 \text{ mm}$ ). In this study the spoilers are treated as perfect “hard-edges”, i.e. all particles hitting a spoiler were stopped, generating no secondary particles. The spoiler half gaps were set to the values given by Eqs. (5.7) and (5.8), and calculated in Table 5.10.

In the horizontal plane the effect of the skew sextupole is very weak as expected. In this case the horizontal particle distribution may be cut as for linear collimation by jaws set at location  $a_x = \pm D_{x,sp}\Delta$ . On the other hand, the vertical plane suffers a strong kick from the sextupole. For an initial particle distribution with  $\delta_{flat} = 1\%$  and  $\delta_0 = 1\%$ , the vertical beam density is approximately reduced by a factor  $10^3$  and the vertical beam average position acquires a nonzero value of order 1 mm. It is possible to see in Fig. 5.25 that, using nonlinear collimation, the vertical jaws play a similar role as the horizontal jaws.

Another example of transverse beam densities is shown in Fig. 5.26 for the case  $\delta_{flat} = 1\%$  and  $\delta_0 = 1.5\%$ .

### Beam energy peak density at the spoiler

In case of full beam impact in the spoiler, a smallest safe beam size  $\sigma_{r,min}$  was defined in section 4.2.1. This beam size is the rms cross-sectioned beam area for onset of mechanical fracture of the collimator surface. Hence one can establish  $\sigma_{x,sp}\sigma_{y,sp} \gtrsim \sigma_{r,min}^2$  as an approximative criterium for spoiler protection. Assuming transverse Gaussian beams, the limit  $\sigma_{r,min}$  has been computed in Ref. [87] for CLIC at 1.5 TeV beam energy. The boundaries limiting the spoiler damage onset for a full bunch train impact are shown in Fig. 5.27, where we have also compared the rms transverse beam size at the energy spoiler of the nonlinear system with beam centroid energy errors  $\delta_0 = 0\%$  and  $\delta_0 = 1.5\%$ . It is possible to see that for an errant beam with  $\delta_0 = 1.5\%$ , the rms transverse beam size  $\sigma_r = \sqrt{\sigma_{x,sp}\sigma_{y,sp}}$  is outside the critical regions, taking the boundaries for the following materials: Cu, Ti, Be, C and no conducting C.

However, since it is the beam energy loss in the material which matters for spoiler survival, a better criterium may be the comparison of the transverse energy peak density at the spoiler. The maximum acceptable transverse energy density was given in Eq. (4.10), which we rewrite below in units of Joule:

$$\rho_{E,max} = \frac{N}{2\pi\sigma_{r,min}^2} \frac{E_0}{(\text{GeV})} 1.6 \times 10^{-10} \text{ J} , \quad (5.11)$$

The values of  $\rho_{E,max}$  are given in Table 5.12 for different materials. The values  $\sigma_{r,min}$  have been taken from Ref. [87] and the following CLIC beam parameters have been assumed: number of electrons per bunch  $N = 4.2 \times 10^9$  and nominal energy  $E_0 = 1500 \text{ GeV}$ .

From multiparticle tracking results using MAD we have evaluated the 2-D transverse energy density at the spoiler,  $\rho_E(x, y)$  and compared it with  $\rho_{E,max}$ . For spoiler survival one should have  $\max(\rho_E(x, y)) \lesssim \rho_{E,max}$ , i.e. the maximum peak of transverse energy density at the spoiler should be lower than the value calculated from Eq. (5.11) depending on the spoiler material. The peak energy density  $\rho_E(x, y)$  is given in Fig. 5.28 as a function of the average off-set of energy  $\delta_0$  for the different nonlinear collimation optics considered in Table 5.9. When an energy error  $\delta_0 \gtrsim 1.3\%$  is considered and the nonlinear collimation lattices (#1, #2, #3, #4 and #5) are used, the peak energy density at the spoiler is lower than for the linear collimation case. This is desired in order to

Table 5.12: Minimum rms transverse beam size  $\sigma_{r,\min}$ , maximum trasverse beam density of particles  $\rho_{e,\max}$  and maximum transverse beam density of energy at the spoiler position, calculated for several materials: conducting and no conducting graphite (C), beryllium (Be), Titanium (Ti) and tungsten (W). These values correspond to the onset of the melting process of the spoiler surface because of beam impact.

Material	$\sigma_{r,\min}$ [ $\mu\text{m}$ ]	$\rho_{e,\max}$ [ $\times 10^9$ p/(mm <sup>2</sup> bunch)]	$\rho_{E,\max}$ [kJ/(mm <sup>2</sup> bunch)]
C (conducting)	58	198.707	47.755
C (no conducting)	32	652.784	156.884
Be	120	46.42	11.156
Ti	100	66.845	16.065
Cu	200	16.711	4.016
W	270	9.169	2.204

increase the spoiler survival probability. Fig. 5.29 shows the evolution of the peak energy density versus the skew sextupole strength  $K_s$  and the centroid beam energy offset  $\delta_0$  for the case of the nonlinear lattice #4.

The 2-D histogram of the transverse density of energy  $\rho_E(x, y)$  at the spoiler position for the linear system is shown in Fig. 5.30 from multiparticle tracking from the entrance of the BDS to the energy spoiler. An initial transverse Gaussian beam of 10000 macro-particles with a full width energy spread of 1 % and an average energy offset of 1.5 % has been used for such a tracking. Note that this beam is not gaussian any more when it arrives at the spoiler position. Similarly, Fig. 5.31 shows the 2-D histogram of  $\rho_E(x, y)$  for a beam with the same initial conditions as before, which is tracked from the entrance to the energy spoiler of the nonlinear system #4. In this case the maximum peak density has been reduced by a factor 1/2 with respect to the linear collimation, and the strong vertical deflection is clearly visible.

Table 5.13 summarizes the performance parameters corresponding to the different optics for nonlinear collimation with an integrated skew sextupole strength of  $K_s \simeq 20.8 \text{ m}^{-2}$ : horizontal root mean square beam size at the spoiler,  $\sigma_{x,\text{rms}}$ , from tracking result using the code MAD; vertical root mean square beam size at the spoiler,  $\sigma_{y,\text{rms}}$ , from tracking result using the code MAD; horizontal beam size at the spoiler,  $\sigma_{x,\text{theory}}$ , from analytical calculation; vertical beam size at the spoiler,  $\sigma_{y,\text{theory}}$ , from analytical calculation;  $\sigma_{r,\text{rms}} = \sqrt{\sigma_{x,\text{rms}}\sigma_{y,\text{rms}}}$  from tracking result;  $\sigma_{r,\text{theory}} = \sqrt{\sigma_{x,\text{theory}}\sigma_{y,\text{theory}}}$  from analytical calculation; transverse particle peak density of particles at the spoiler,  $\rho_e$ , from tracking result using the code MAD and transverse energy peak density at the spoiler,  $\rho_E$ , from tracking result using the code MAD. We have considered an initial uniform particle energy distribution of 1 % full width with an average energy beam offset of 1.5 %.

Table 5.13: Performance of the different optics studied for nonlinear collimation in CLIC.

parameters	optics #1	optics #2	optics #3	optics #4	optics #5
$\sigma_{x,\text{rms}}$ [ $\mu\text{m}$ ]	266.213	304.687	294.793	304.541	243.829
$\sigma_{x,\text{theory}}$ [ $\mu\text{m}$ ]	263.196	304.354	294.403	304.354	242.519
$\sigma_{y,\text{rms}}$ [ $\mu\text{m}$ ]	841.457	711.963	804.102	712.026	455.955
$\sigma_{y,\text{theory}}$ [ $\mu\text{m}$ ]	947.975	727.480	821.173	727.480	465.59
$\sigma_{r,\text{rms}}$ [ $\mu\text{m}$ ]	473.293	465.753	486.871	465.662	333.429
$\sigma_{r,\text{theory}}$ [ $\mu\text{m}$ ]	499.503	470.544	491.687	470.544	336.027
$\max(\rho_e(x, y))$ [ $10^9$ p/(mm <sup>2</sup> bunch)]	35.209	53.713	41.732	52.206	88.8
$\max(\rho_E(x, y))$ [kJ/(mm <sup>2</sup> bunch)]	8.542	13.036	10.141	12.659	21.538

## 5.4.2 Cleaning efficiency

### Machine protection

In order to study the machine protection function and the cleaning efficiency of the energy collimation system we have chosen the nonlinear collimation system #4, because of its trade-off between high luminosity and relative short lattice length.

The goal is to spoil the mis-steered or errant beams coming from the linac with large absolute momentum error ( $\gtrsim 1.3$  %). For this study we have tracked initial Gaussian distributions of  $10^5$  macro-particles along the CLIC BDS lattice by using the code `Placet`. These initial distributions were generated with a flat square energy distribution with  $\delta_{\text{flat}} = 1$  % full width energy spread and varying the average energy offset  $\delta_0$ . It is also important to mention that in our simulations the spoilers have been treated as perfect ‘hard-edges’, i.e., all particles hitting a spoiler were stopped, generating no secondary particles.

Figure 5.32 shows the simulated relative losses versus the beam centroid energy error. The relative losses are higher in the nonlinear system than in the baseline linear system, as we expected. In the case of the nonlinear system, considering an errant beam with  $\delta_0 = 1.5$  % about 68 % of the initial beam is intercepted by the energy spoiler, and only 26 % of the initial beam is stopped at the vertical betatron spoilers YSP1 and YSP3. On the other hand, in the case of the linear system, and for the same initial errant beam distribution, about 63 % of the initial beam is stopped at the energy spoiler ENGYP and about 24 % at the horizontal betatron spoilers XSP1, XSP2 and XSP3. The corresponding loss maps along the beam line are shown in Fig. 5.33 and Fig. 5.34 for the cases with  $\delta_0 = 0.5$  % and  $\delta_0 = 1.5$  %, respectively.

At this point, it is necessary to stress that in the case of  $\delta_0 = 0$  % (well centered beam), one would expect the core beam to pass through the collimation section without interacting with the spoilers, but this is not the case observed in our results. Instead, from an initial beam with  $\delta_0 = 0$  % tracked along the linear lattice a total of  $\approx 5.5$  % of the initial macro-particles is lost: 0.85 % at the energy spoiler ENGYP and about 4.7 % at the betatron spoilers XSP1, XSP2 and XSP3. By

contrast, for the nonlinear lattice, a total of about 19 % is lost in the collimation section: 1 % at the energy spoiler and 18 % at the vertical betatron spoilers. This situation of losses from the beam core is not convenient in terms of background increase in the detectors located at the interaction region. Muons may be generated at a rate of about  $10^{-4}$  per lost electron or positron [16, 128]. For this reason, in order to avoid or at least, to reduce the losses during normal operation (0 % centroid energy error), we have decided to increase the half gap of the vertical betatron collimators in the nonlinear system. For instance, for a new vertical half gap  $a_y = 150 \mu\text{m}$  (note that the previous value was  $a_y = 102 \mu\text{m}$ , see Table 5.4), a total of about 13 % of the initial halo is lost when  $\delta_0 = 0$  %, which is still an unacceptable number of losses for a normal operation.

Here, we have only considered the rough approximation of ‘hard-edges’ spoilers and hence all particles hitting a spoiler have been taken to be lost in the simulation. Nevertheless, in a more realistic case, a big proportion of those interacting particles would reenter the beam pipe after multiple Coulomb scattering in the spoiler, and then these particles would either contribute to the halo repopulation or be absorbed at the downstream absorbers. Therefore, in order to perform more realistic studies of the cleaning efficiency, details of the beam-spoiler scattering processes need to be considered.

### Betatron cleaning

The effectiveness of the collimation system can be quantified in terms of the number of halo particles that lie outside the collimation depth when they reach the final doublet. In the case of CLIC, the dimensions of the transverse window for collimation, defined by the final doublet aperture, are:  $A_x^{\text{FD}} = 14 \sigma_x$  and  $A_y^{\text{FD}} = 83 \sigma_y$ .

In order to study the betatron cleaning efficiency of the system, one can define a cleaning inefficiency  $\eta_l$  for linear colliders, given by

$$\eta_l = \frac{N(A_{x,y} > A_{x,y}^{\text{FD}})}{N_{\text{ab}}} , \quad (5.12)$$

where  $N(A_{x,y} > A_{x,y}^{\text{FD}})$  is the number of halo particles with initial amplitude  $A_{x,y}$  which reach the final doublet with higher amplitude than  $A_{x,y}^{\text{FD}}$  (the collimation depth limits), and  $N_{\text{ab}}$  is the total number of absorbed particles by the collimation section.

A toy halo model has been used for the tracking studies. Initial particles are distributed in ellipses with different transverse amplitude. The horizontal and vertical plane are separately treated, i.e. without initial coupling. Each ellipse contains a number of  $10^5$  macro-particles. Fig. 5.35 shows the initial transverse distribution at the entrance of the CLIC BDS.

These sets of ellipses are tracked along the CLIC BDS using the code *Placet*. The following cases have been considered:

- Initial ellipses with a Gaussian energy distribution of  $\sigma_\delta = 0.5$  % width energy spread, in order to take into account the chromatic effects. The ratio  $N_{\text{survival}}/N_{\text{initial halo}}$ , i.e. the

surviving particles (which reach the final doublet) divided by the initial number, and the cleaning inefficiency (such as defined in Eq. (5.12)) have been computed as a function of the initial amplitude of the ellipse.

On one hand the results are compared in Fig. 5.36 using the horizontal ellipses for both the linear and the nonlinear case. A similar ratio  $N_{\text{survival}}/N_{\text{initial halo}}$  is found for both the linear and the nonlinear system. At  $A_x = 14 \sigma_x$  about 10 % of the initial halo survives the collimation, and  $\eta_l \approx 5 \times 10^{-3}$ . If we compare  $N_{\text{survival}}/N_{\text{initial halo}}$  with  $\eta_l(A_x)$  as function of the horizontal amplitude  $A_x$ , one can observe that for  $A_x \lesssim 11 \sigma_x$  (linear case) and for  $A_x \lesssim 12.5 \sigma_x$  (nonlinear case) the inefficiency is  $\eta_l \lesssim 10^{-5}$ , which means that practically all the surviving particles are inside the collimation limits. The particles inside these limits are not potentially dangerous in terms of SR emission. The number of particles which are outside these limits increase with the rise of the initial amplitude  $A_x$ .

On the other hand, using the vertical ellipses (see Fig. 5.37), the ratio  $N_{\text{survival}}/N_{\text{initial halo}}$  is equal to 70 % for the nonlinear system and 30 % for the linear one at  $A_y = 80 \sigma_y$ . If  $A_y \gtrsim 109 \sigma_y$ , for the nonlinear case  $N_{\text{survival}}/N_{\text{initial halo}}$  is smaller than for the linear case. For instance, at  $A_y = 110 \sigma_y$  about a 3 % of the initial vertical halo survives for the nonlinear case and about a 5 % for the linear one.

We have obtained  $\eta_l > 10^{-2}$  for the nonlinear system in the interval  $A_y \in [80 \sigma_y, 110 \sigma_y]$ , in comparison with  $\eta_l \approx 10^{-4}$  obtained for the linear system.

- Monochromatic initial ellipses ( $\sigma_\delta = 0$  % energy spread) with nominal energy  $E_0 = 1500$  GeV. For this case the results are shown in Fig. 5.38 for horizontal ellipses and in Fig. 5.39 for vertical ellipses.

Taking the horizontal halo (monochromatic ellipses of  $10^5$  particles in the horizontal phase space  $x-x'$ ) at  $A_x = 14 \sigma_x$  the values  $N_{\text{survival}}/N_{\text{initial halo}} \simeq 3$  % and 6 % are obtained for the nonlinear and the linear case, respectively. It is worthwhile to mention that in the nonlinear case,  $N_{\text{survival}}/N_{\text{initial halo}}$  drops quickly for  $A_x \gtrsim 13.5 \sigma_x$ .

The cleaning inefficiency  $\eta_l(A_x)$  as a function of the initial amplitude of the horizontal ellipses is practically zero for  $A_x \lesssim 12.5 \sigma_x$  in the nonlinear case and for  $A_x \lesssim 13.5 \sigma_x$  in the linear case.

Similarly, taking the vertical halo (monochromatic ellipses in the vertical phase space  $y-y'$ ), at  $A_y = 110 \sigma_y$  we obtain  $N_{\text{survival}}/N_{\text{initial halo}} \simeq 0.4$  % and 5 % for the nonlinear and the linear case, respectively. In the nonlinear case,  $N_{\text{survival}}/N_{\text{initial halo}}$  drops quickly for  $A_y \gtrsim 105 \sigma_y$  compared with the linear case, whose slope is smoother.

The cleaning inefficiency  $\eta_l(A_y)$  as a function of the initial amplitude of the vertical ellipses is found to be zero for  $A_y \in [80 \sigma_y, 110 \sigma_y]$  in the case of the linear collimation system. However,  $\eta_l(A_y) > 10^{-3}$  for  $A_y \in [84 \sigma_y, 110 \sigma_y]$  in the case of the nonlinear collimation system.



Concerning collimation efficiency, one can conclude from these studies that the betatron cleaning efficiency in the horizontal phase space ( $x-x'$ ) is roughly similar for both linear and nonlinear systems. However, in the vertical phase space ( $y-y'$ ) the nonlinear system shows a higher collimation inefficiency ( $\eta_l(A_y) \gtrsim 10^{-3}$ ) than the linear one. This means that a big number of high vertical amplitude particles are not absorbed by the nonlinear collimation system and are outside the collimation window at the FD. This may be basically caused by non cancelled geometric high order aberration terms introduced by the nonlinear elements. We have to take into account that the vertical amplitude are highly sensitive to the sextupolar effects as we have shown in previous sections.

### 5.4.3 Collimator wakefield considerations

In chapter 3, section 3.3.3, we saw that for near-center beams, the transverse centroid deflection, because of collimator wakefields, is linearly proportional to the beam centroid position through a total kick factor  $\kappa_\perp \equiv \langle w_\perp \rangle$ , with  $w_\perp$  the transverse wake function.

- In the case of collimators placed where  $D_x = 0$ , we can rewrite the Eq. (3.72) as

$$\tilde{n}_{y'} \sqrt{\frac{\epsilon_y}{\beta_y}} = \frac{Nr_e}{\gamma} \kappa_\perp \tilde{n}_y \sqrt{\beta_y \epsilon_y} , \quad (5.13)$$

where  $\tilde{n}_{y'} = \langle \Delta y' \rangle / \sqrt{\epsilon_y / \beta_y}$  and  $\tilde{n}_y = \Delta y_c / \sqrt{\beta_y \epsilon_y}$  are normalized amplitudes.

Here the figure of merit is the so-called jitter amplification factor, which can be evaluated from Eq. (5.13) as

$$A_\beta \equiv \frac{\tilde{n}_{y'}}{\tilde{n}_y} = \frac{Nr_e}{\gamma} \kappa_\perp \beta_y , \quad (5.14)$$

and gives information about the amplification of the overall incoming jitter by the collimator wakefield effect.

- In the case of a collimator which is placed where  $D_x \neq 0$ , the generated transverse jitter is proportional to the energy jitter:

$$\tilde{n}_{y'} \sqrt{\frac{\epsilon_y}{\beta_y}} = \frac{Nr_e}{\gamma} \kappa_\perp D_x \delta_0 , \quad (5.15)$$

and the jitter enhancement factor is then given by

$$A_\delta = A_\beta \frac{D_x \delta_0}{\sqrt{\beta_y \epsilon_y}} . \quad (5.16)$$

We have calculated the wakefield jitter enhancement parameters,  $A_\beta$  and  $A_\delta$  from the above expressions for the CLIC collimators. The factor  $A_\delta$  has been calculated for a centroid energy offset  $\delta_0 = 1\%$ . The results are shown in Table 5.14 for the different kinds of CLIC collimators. ‘Nonlinear-E-SP’ denotes the energy spoiler of the nonlinear collimation system #4. This spoiler is composed by vertical jaws, while the energy spoiler in the linear collimation system is horizontal. From the table we can see that the jitter factor  $A_\beta$  for the nonlinear system is lower than for the linear one. Nevertheless, since the beam is flat,  $\sigma_y \ll \sigma_x$ , the vertical amplitude is more sensitive to the wakefields effects.

According to the limits for the different regimes (see section 3.3.3), the energy spoilers ENGYSP (linear system) and Nonlinear-E-SP (nonlinear system) are in a diffractive regime for the geometric wakefields, the betatronic spoilers are in an intermediate regime, and the betatronic absorbers (round absorbers) are in an inductive regime.

Table 5.14: Wakefield jitter amplification factors for CLIC collimators.

Collimator	Plane	$A_\beta$				$A_\delta$ $\delta_0 = 1\%$
		geometric	$\Omega$ taper	$\Omega$ flat	Total	
ENGYSP (linear CS)	X	0.000438	$6.68 \times 10^{-5}$	0.	0.000505	0.0668
ENGYAB (linear CS)	X	0.000423	0.000034	0.000122	0.000579	0.0888
Nonlinear-E-SP	Y	0.000125	0.000019	0.	0.000144	0.298
$\beta_y$ spoilers	Y	0.178	0.0272	0.	0.2052	0.
$\beta_x$ spoilers	X	0.162	0.0247	0.	0.1867	0.
$\beta_y$ absorbers	Y	0.0169	0.000121	0.00234	0.0194	0.
$\beta_x$ absorbers	X	0.0169	0.0000676	0.00131	0.0183	0.

Recently in Ref. [129] the collimator wakefields effects in the luminosity of CLIC (using the baseline linear collimation system) have been computed. A module for particle tracking along the BDS including the effect of wakefields was implemented in `Placet`. For more details see Refs. [129, 130]. We have used such a version of the code `Placet` to compute the luminosity degradation due to the misalignment of each collimator.

The impact of the wakefields on the luminosity has been computed assuming a perfect centered beam and collimator misalignments. This study has been made using the tracking code `Placet`, introducing wakefield effects. Fig. 5.40 shows the evolution of the normalized luminosity with the misalignment of each horizontal collimator respect to the nominal trajectory. Similarly, Fig. 5.41 shows the evolution of the normalized luminosity with the misalignment of each vertical collimator. The nonlinear collimation system presents a similar behavior and misalignment acceptance as the linear system in the horizontal plane. In the Fig. 5.41 (top) the misalignment acceptance in the vertical plane for the nonlinear system is better than that for the linear one (bottom), because in this case the half gap of  $\beta_y$ -collimators has been open up to  $150\ \mu\text{m}$ , while for the linear system this half gap is  $102\ \mu\text{m}$ .

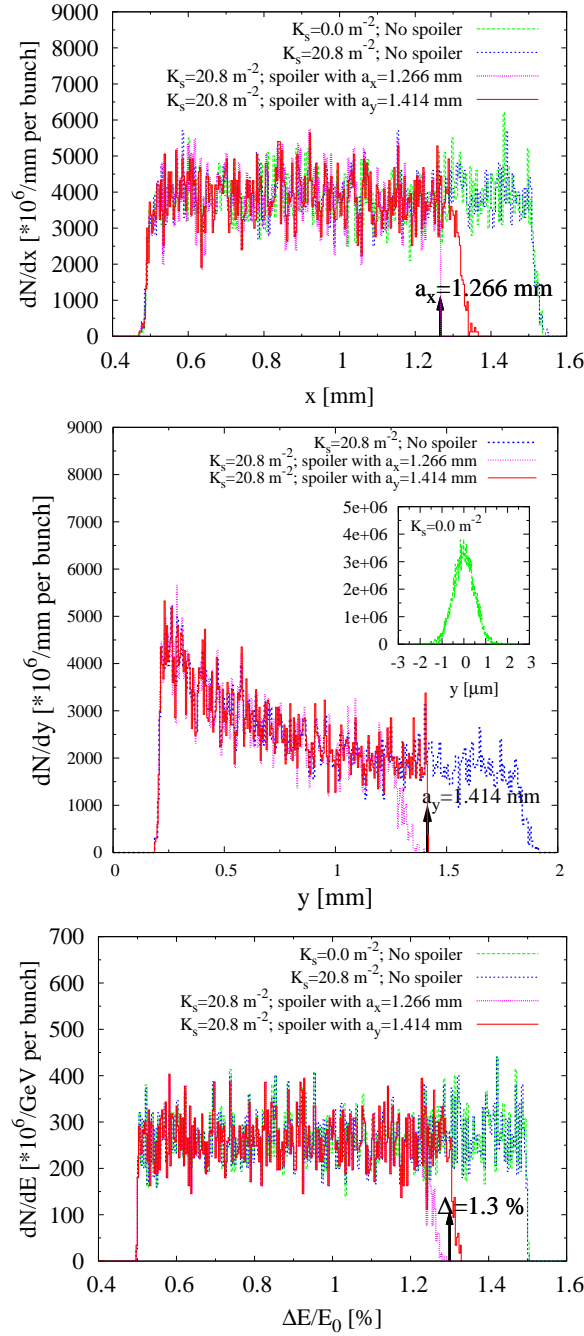


Figure 5.25: Horizontal particle density (top), vertical particle density (middle) and energy particle density (bottom) at the spoiler using the optics #4 and an initial particle distribution with  $\delta_{\text{flat}} = 1 \%$  and  $\delta_0 = 1 \%$ . Different cases are compared: with skew sextupole switched off ( $K_s = 0.0 \text{ m}^{-2}$ ), with skew sextupole switched on ( $K_s = 20.8 \text{ m}^{-2}$ ), without spoiler, with horizontal spoiler ( $a_x = 1.266 \text{ mm}$ ) and with vertical spoiler ( $a_y = 1.414 \text{ mm}$ ). The particle distributions have been normalized to a number of  $4 \times 10^9$  particles per bunch.

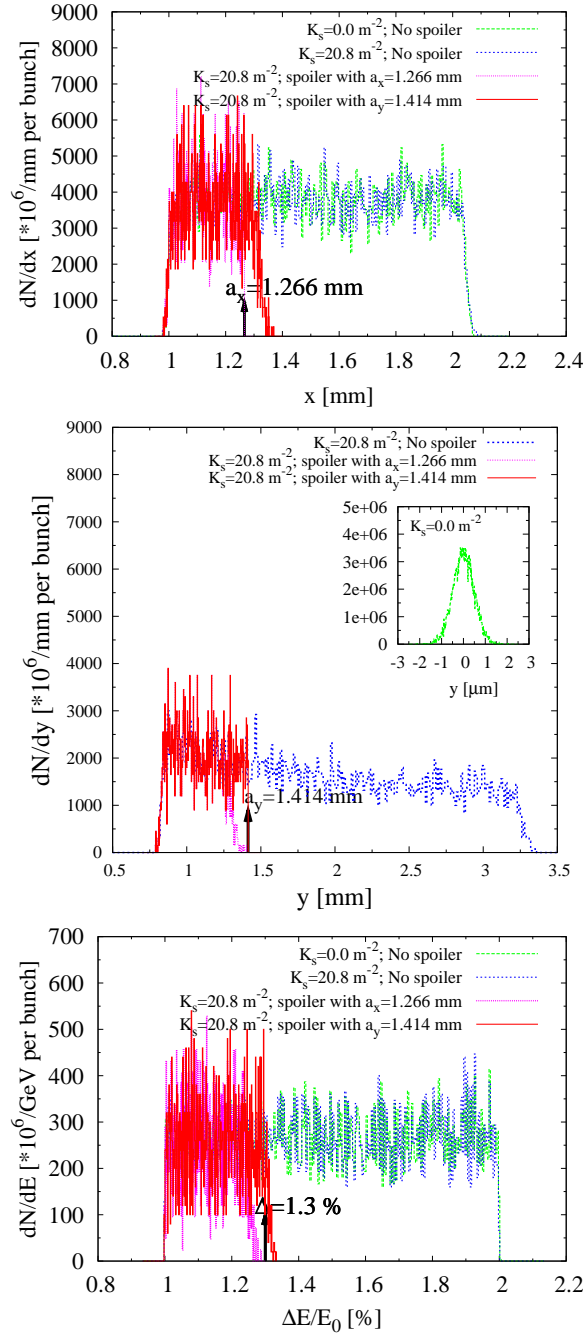


Figure 5.26: Horizontal particle density (top), vertical particle density (middle) and energy particle density (bottom) at the spoiler using the optics #4 and an initial particle distribution with  $\delta_{\text{flat}} = 1 \%$  and  $\delta_0 = 1.5 \%$ . Different cases are compared: with skew sextupole switched off ( $K_s = 0.0 \text{ m}^{-2}$ ), with skew sextupole switched on ( $K_s = 20.8 \text{ m}^{-2}$ ), without spoiler, with horizontal spoiler ( $a_x = 1.266 \text{ mm}$ ) and with vertical spoiler ( $a_y = 1.414 \text{ mm}$ ). The particle distributions have been normalized to a number of  $4 \times 10^9$  particles per bunch.

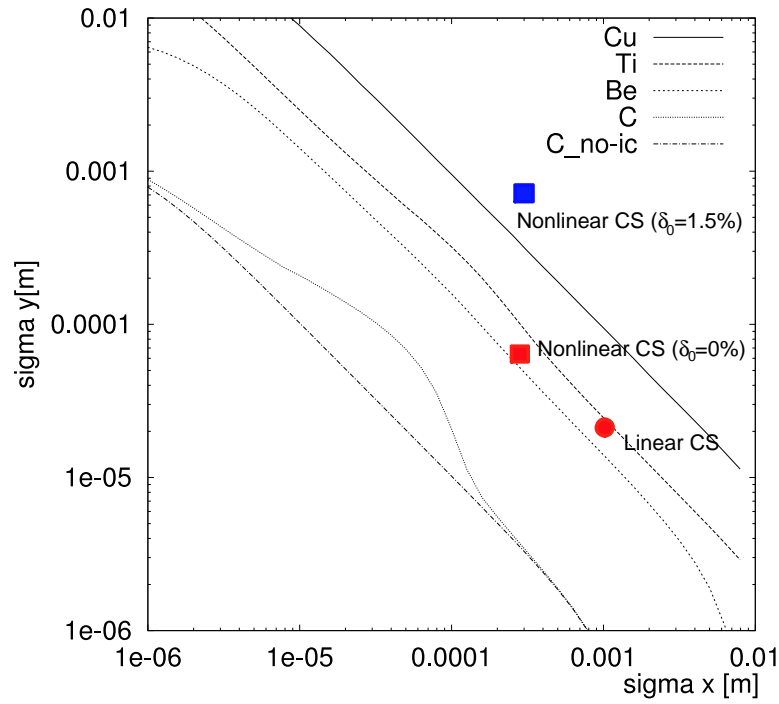


Figure 5.27: Vertical vs. horizontal beam size required for spoiler survival with different spoiler materials [87], and the values at the energy spoiler locations computed for the design beta functions, emittances and a beam energy spread  $\delta_{\text{flat}} = 1\%$ . The cases of beam centroid energy errors  $\delta_0 = 0\%$  and  $\delta_0 = 1.5\%$  in the nonlinear energy collimation system are compared with the case of the linear energy collimation system.

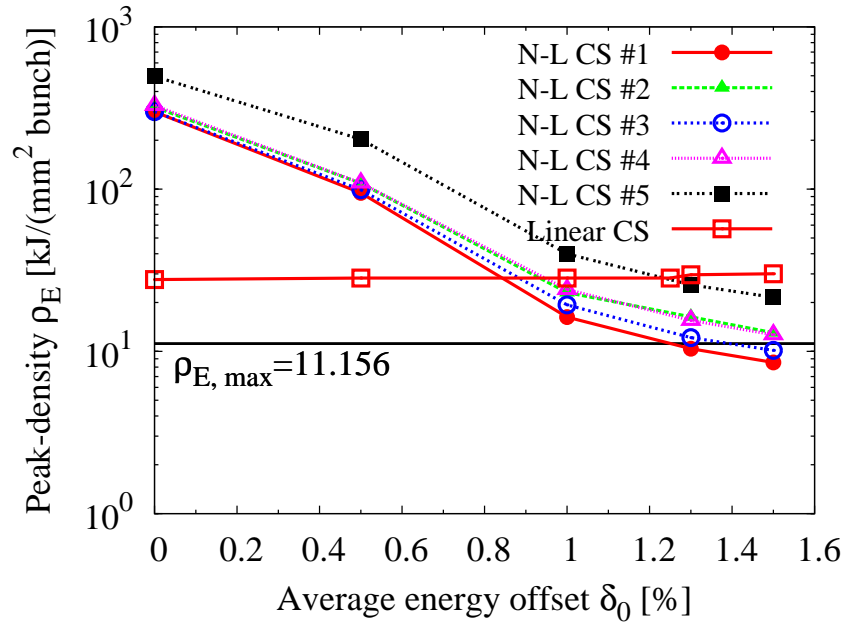


Figure 5.28: Peak energy density at the spoiler as function of the average beam energy offset  $\delta_0$  for the different optics solutions studied, using an integrated skew sextupole strength of  $K_s = 20.8 \text{ m}^{-2}$ . The results are compared with that from the linear collimation system (solid red line with open squared points), and with the density limit for spoiler survival in case of full beam impact for beryllium,  $\rho_{E,\text{max}}$  (solid black line).

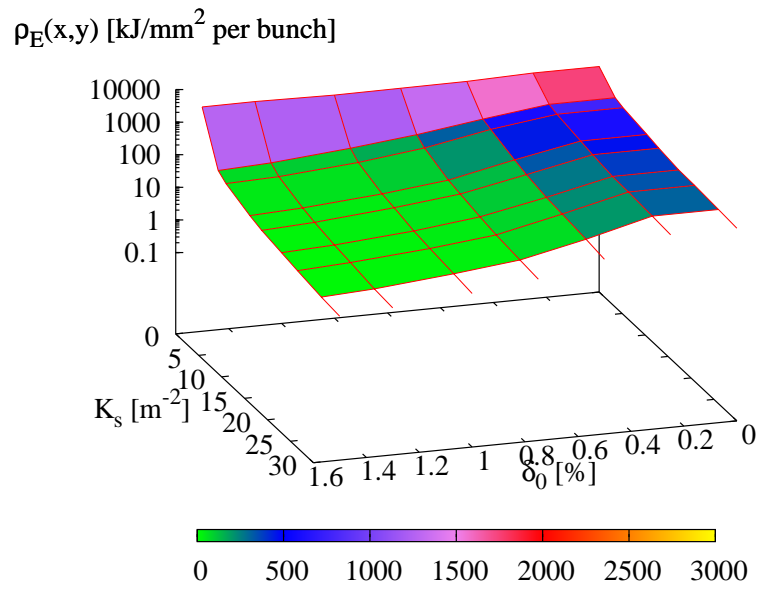


Figure 5.29: Evolution of the energy peak density  $\max(\rho_E(x,y))$  at the spoiler as a function of the skew sextupole strength  $K_s$  and of the beam energy error  $\delta_0$  in the nonlinear collimation lattice #4.

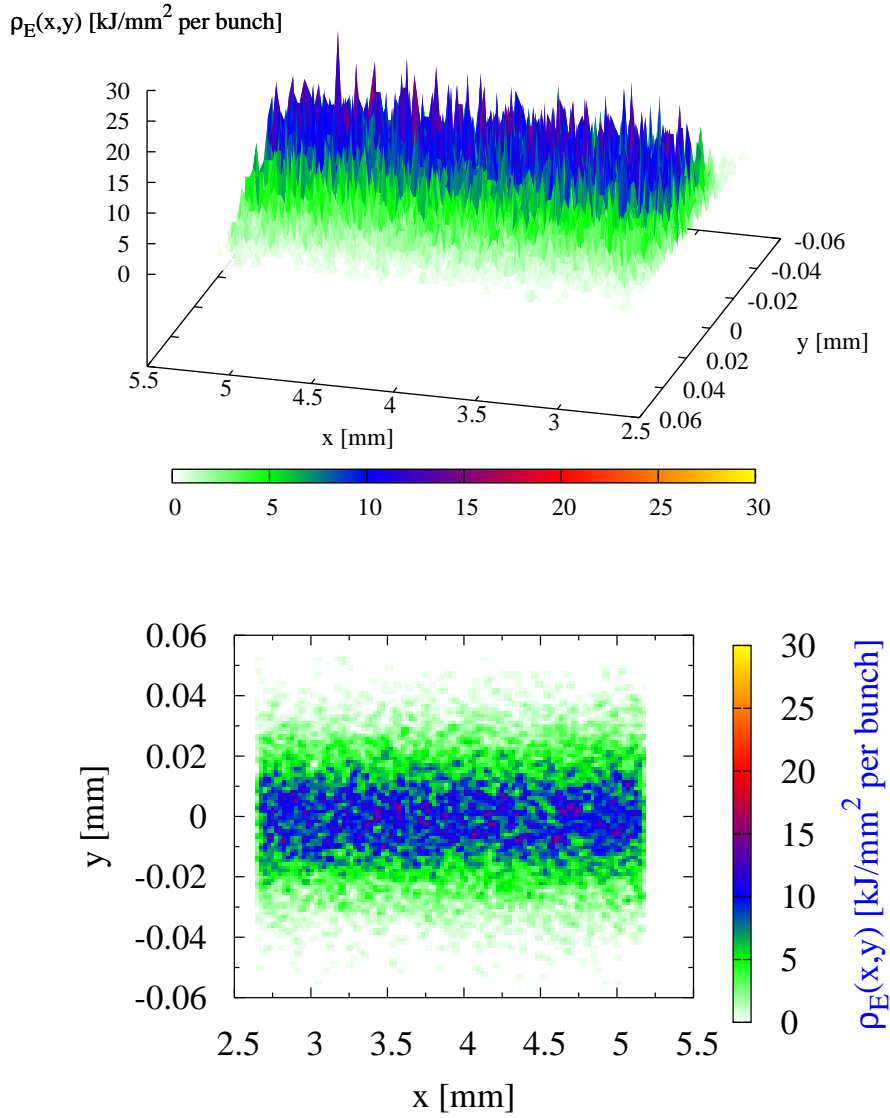


Figure 5.30: Transverse energy density at the energy spoiler position versus the plane  $x$ - $y$ , from tracking of an initial transverse Gaussian distribution of 10000 particles with a uniform energy distribution, and a full width energy spread of 1 % and a centroid energy offset of 1.5 %, for the case of the *linear collimation lattice*. The result is normalized to  $4.0 \times 10^9$  particles per bunch.



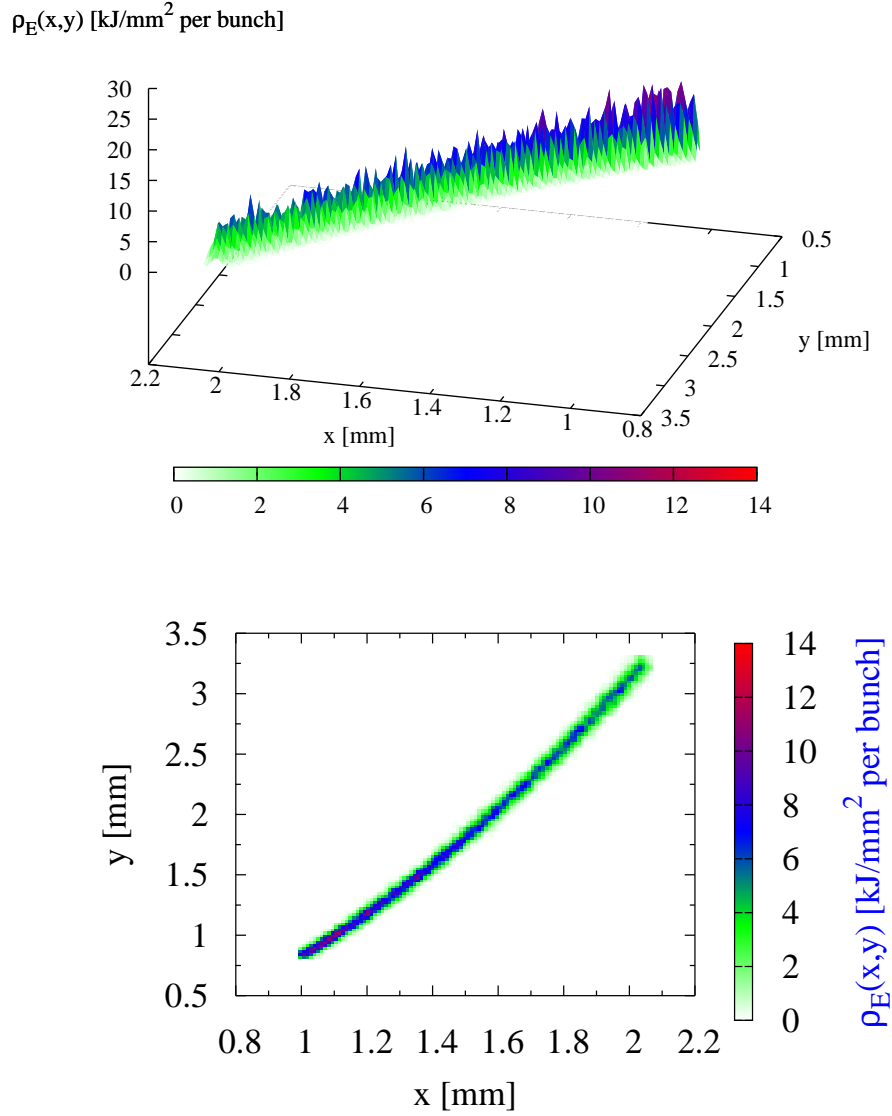


Figure 5.31: Transverse energy density at the energy spoiler position versus the plane  $x$ - $y$ , from tracking of an initial transverse Gaussian distribution of 10000 particles with a uniform energy distribution, and a full width energy spread of 1 % and a centroid energy offset of 1.5 %, for the case of the *nonlinear collimation lattice*. The result is normalized to  $4.0 \times 10^9$  particles per bunch.

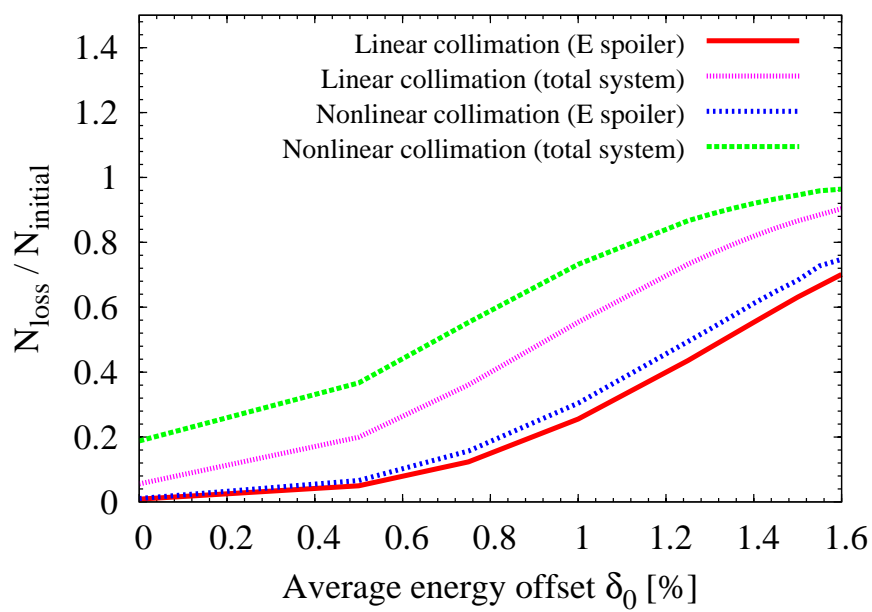


Figure 5.32: Relative particle loss of errant beams as a function of the average energy offset  $\delta_0$ , such as obtained from simulations with the tracking code `Placet`. The losses at the energy spoiler and in the total collimation system are compared for both linear and nonlinear collimation systems.

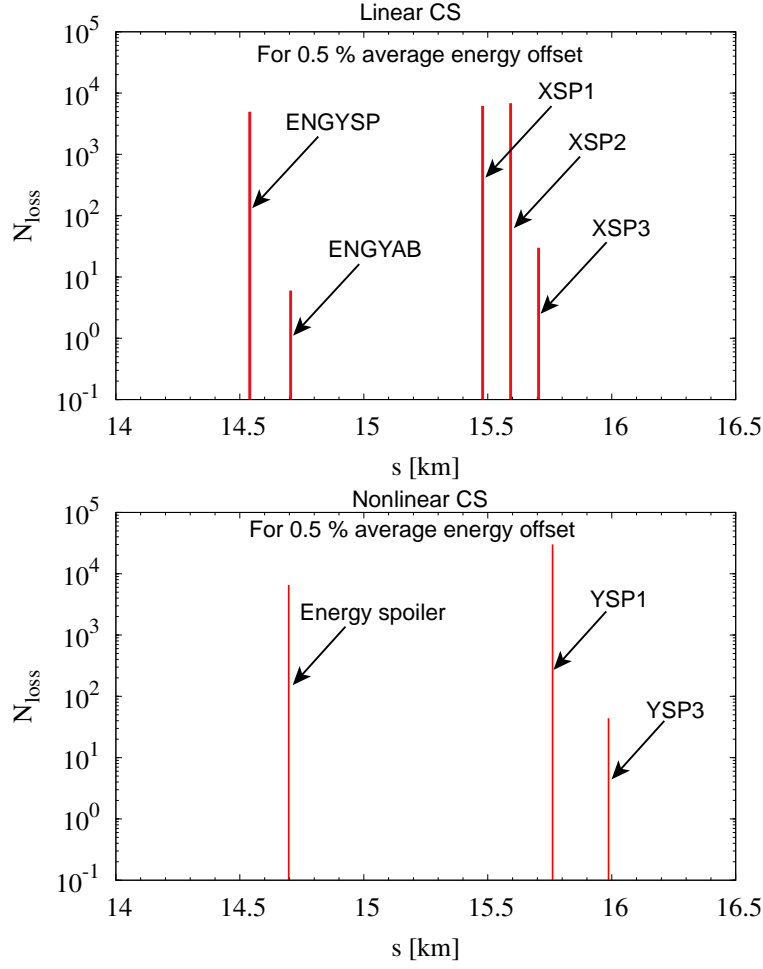


Figure 5.33: Number of particles lost along the BDS using the linear collimation lattice (top) and the nonlinear collimation lattice (bottom). The tracking has been done by using the code Placet and an initial Gaussian distribution of  $10^5$  particles with  $\delta_{\text{flat}} = 1$  % full width energy spread and  $\delta_0 = 0.5$  % average energy offset.

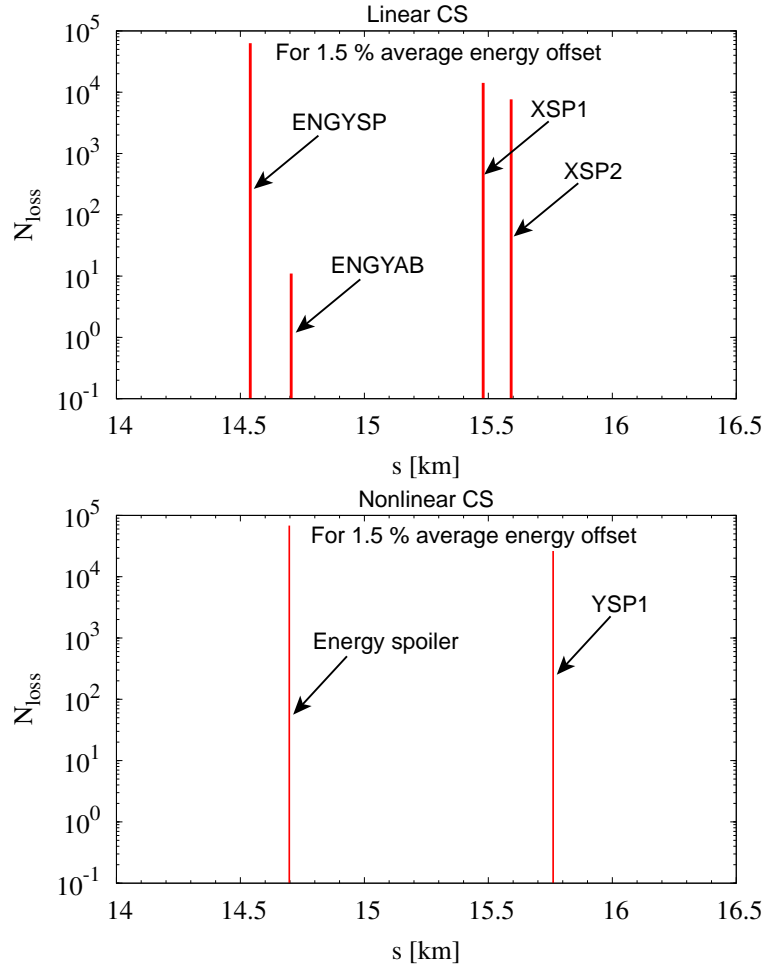


Figure 5.34: Number of particles lost along the BDS using the linear collimation lattice (top) and the nonlinear collimation lattice (bottom). The tracking has been done by using the code Placet and an initial Gaussian distribution of  $10^5$  particles with  $\delta_{\text{flat}} = 1\%$  full width energy spread and  $\delta_0 = 1.5\%$  average energy offset.

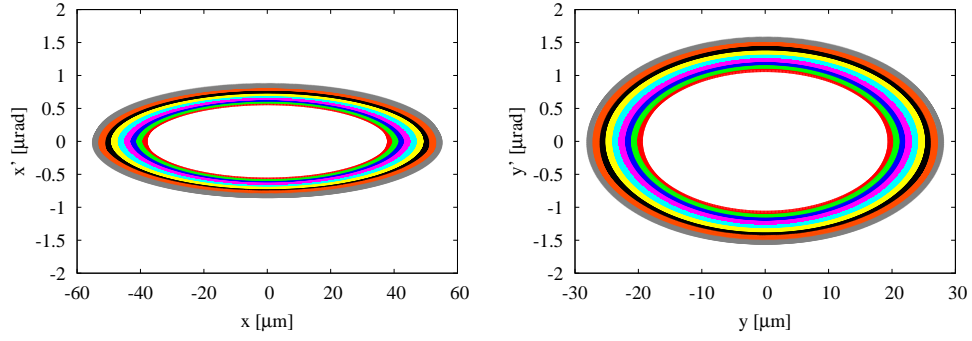


Figure 5.35: Sets of particle distributions in the horizontal (on the left) and the vertical (on the right) phase space at the entrance of the CLIC BDS. Each set contains  $10^5$  particles distributed in an ellipse. In the figure on the left, the following horizontal amplitudes are considered:  $10 \sigma_x$ ,  $10.5 \sigma_x$ ,  $11 \sigma_x$ ,  $11.5 \sigma_x$ ,  $12 \sigma_x$ ,  $12.5 \sigma_x$ ,  $13 \sigma_x$ ,  $13.5 \sigma_x$  and  $14 \sigma_x$ . In the figure on the right, the following vertical amplitudes are considered:  $80 \sigma_y$ ,  $84 \sigma_y$ ,  $88 \sigma_y$ ,  $92 \sigma_y$ ,  $96 \sigma_y$ ,  $100 \sigma_y$ ,  $104 \sigma_y$ ,  $108 \sigma_y$  and  $112 \sigma_y$ .

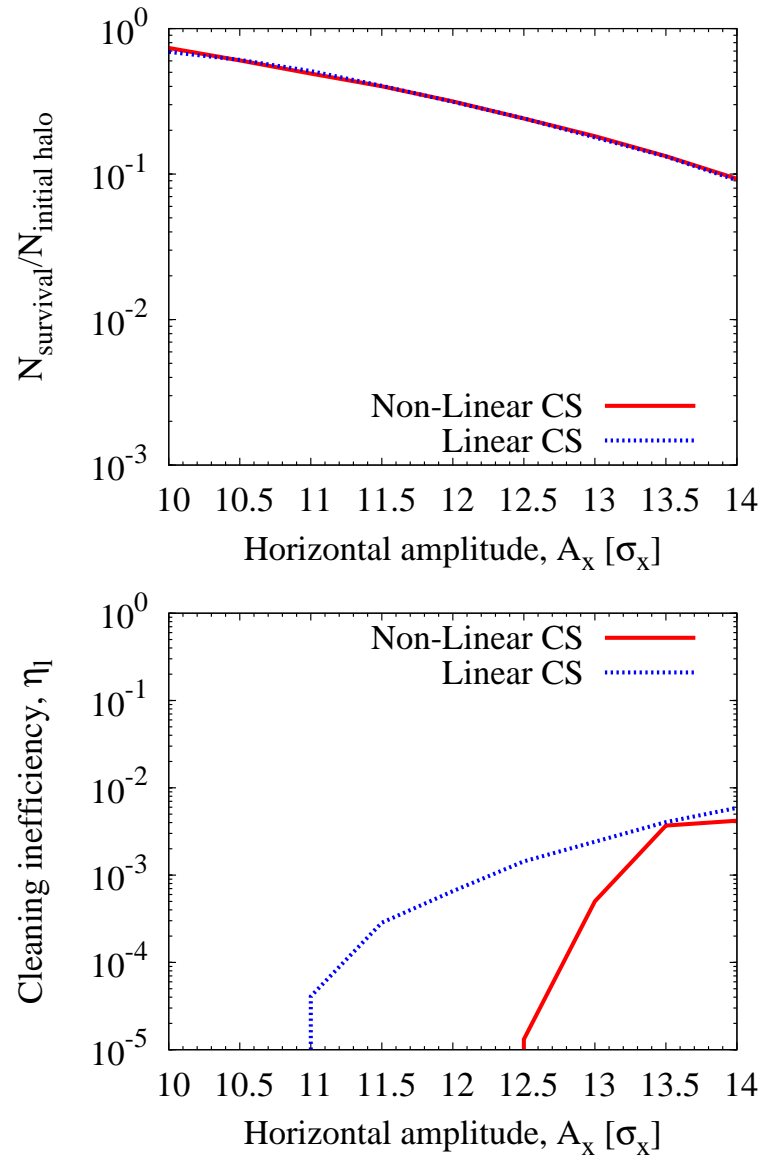


Figure 5.36: Number of particles which are not collimated and reach the final doublet divided by the initial population of the halo versus the initial horizontal amplitude  $A_x$  of the ellipse (top). The corresponding cleaning inefficiency  $\eta_l$ , such as defined in Eq. (5.12), versus  $A_x$  (bottom). The cases with nonlinear collimation (solid and red curve) and with linear collimation (dotted and blue curve) are compared. Here ellipses with a Gaussian distribution in energy of  $\sigma_\delta = 0.5\%$  (energy spread) have been used as a toy initial halo.

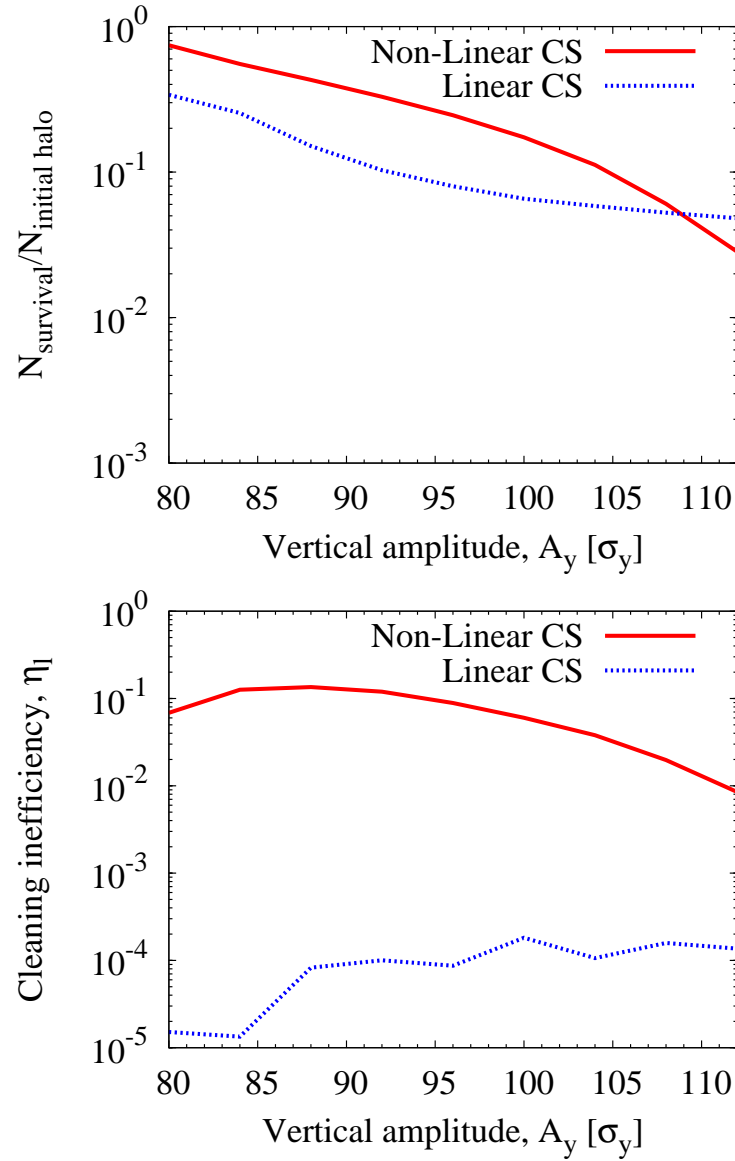


Figure 5.37: Number of particles which are not collimated and reach the final doublet divided by the initial population of the halo versus the initial vertical amplitude  $A_y$  of the ellipse (top). The corresponding cleaning inefficiency  $\eta_l$ , such as defined in Eq. (5.12), versus  $A_y$  (bottom). The cases with nonlinear collimation (solid and red curve) and with linear collimation (dotted and blue curve) are compared. Here ellipses with a Gaussian distribution in energy of  $\sigma_\delta = 0.5\%$  (energy spread) have been used as a toy initial halo.

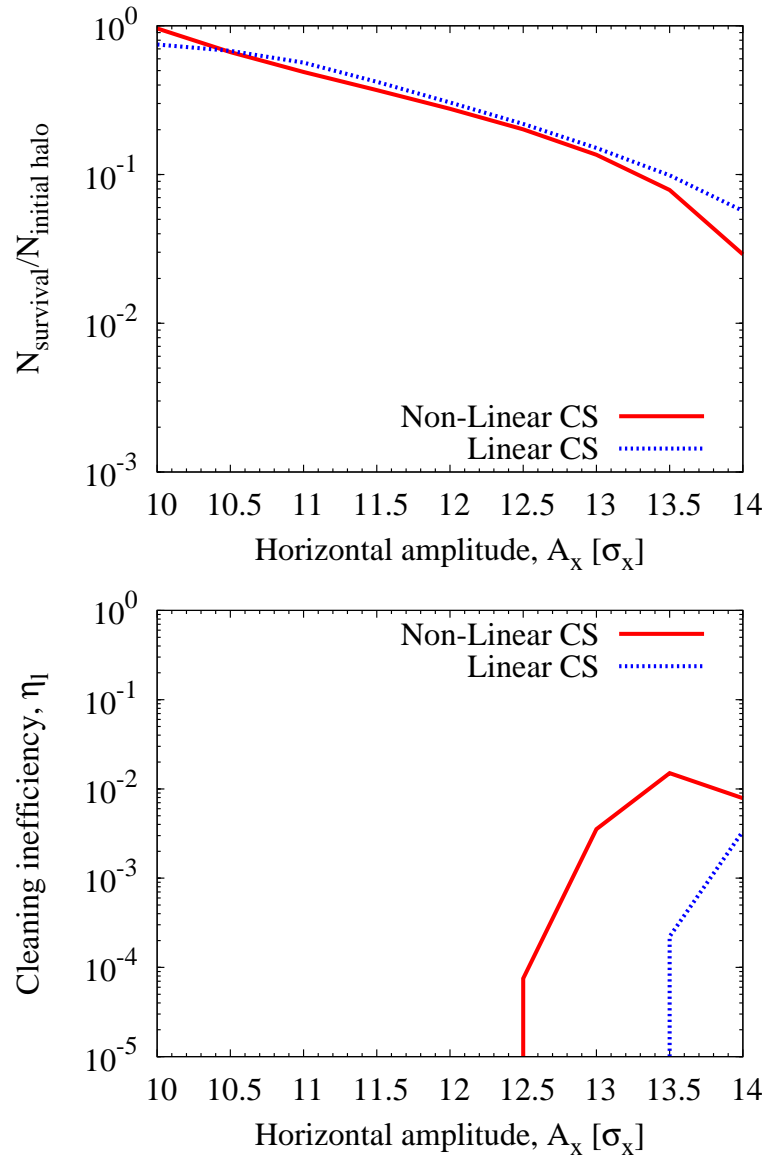


Figure 5.38: Number of particles which are not collimated and reach the final doublet divided by the initial population of the halo versus the initial horizontal amplitude  $A_x$  of the ellipse (top). The corresponding cleaning inefficiency  $\eta_l$ , such as defined in Eq. (5.12), versus  $A_x$  (bottom). The cases with nonlinear collimation (solid and red curve) and with linear collimation (dotted and blue curve) are compared. Here, unlike Fig. 5.36, monochromatic ellipses ( $\sigma_\delta = 0.0\%$ ) have been used as a toy initial halo.



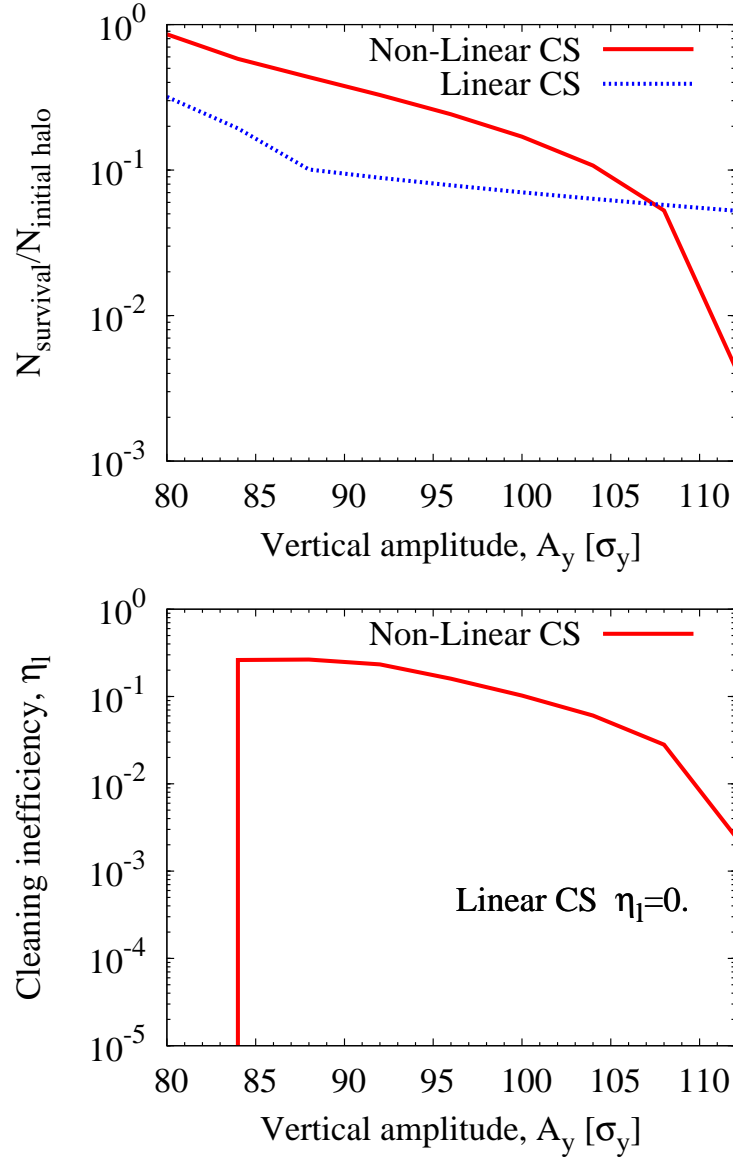


Figure 5.39: Number of particles which are not collimated and reach the final doublet divided by the initial population of the halo versus the initial vertical amplitude  $A_y$  of the ellipse (top). The corresponding cleaning inefficiency  $\eta_l$ , such as defined in Eq. (5.12), versus  $A_y$  (bottom). The cases with nonlinear collimation (solid and red curve) and with linear collimation (dotted and blue curve) are compared. Here, unlike Fig. 5.37, monochromatic ellipses ( $\sigma_\delta = 0.0$  %) have been used as a toy initial halo.

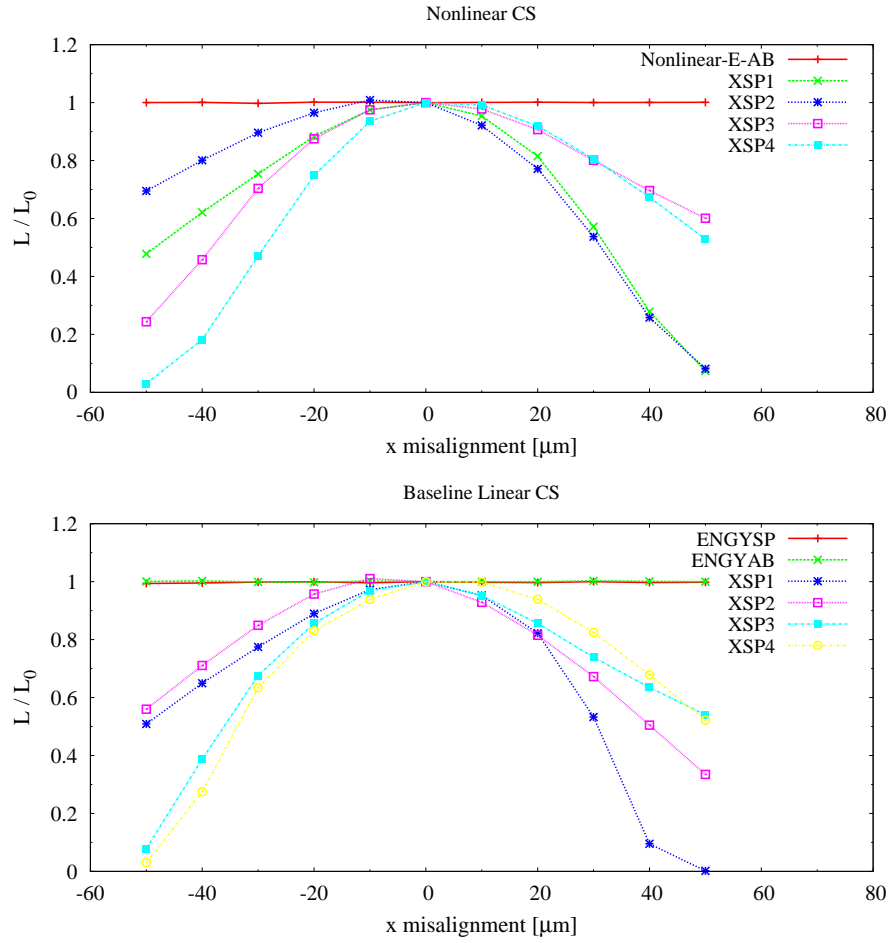


Figure 5.40: CLIC Luminosity as a function of the horizontal collimator offset when the nonlinear collimator system is used (at the top) and when the linear collimation system is used (at the bottom) in the simulations.

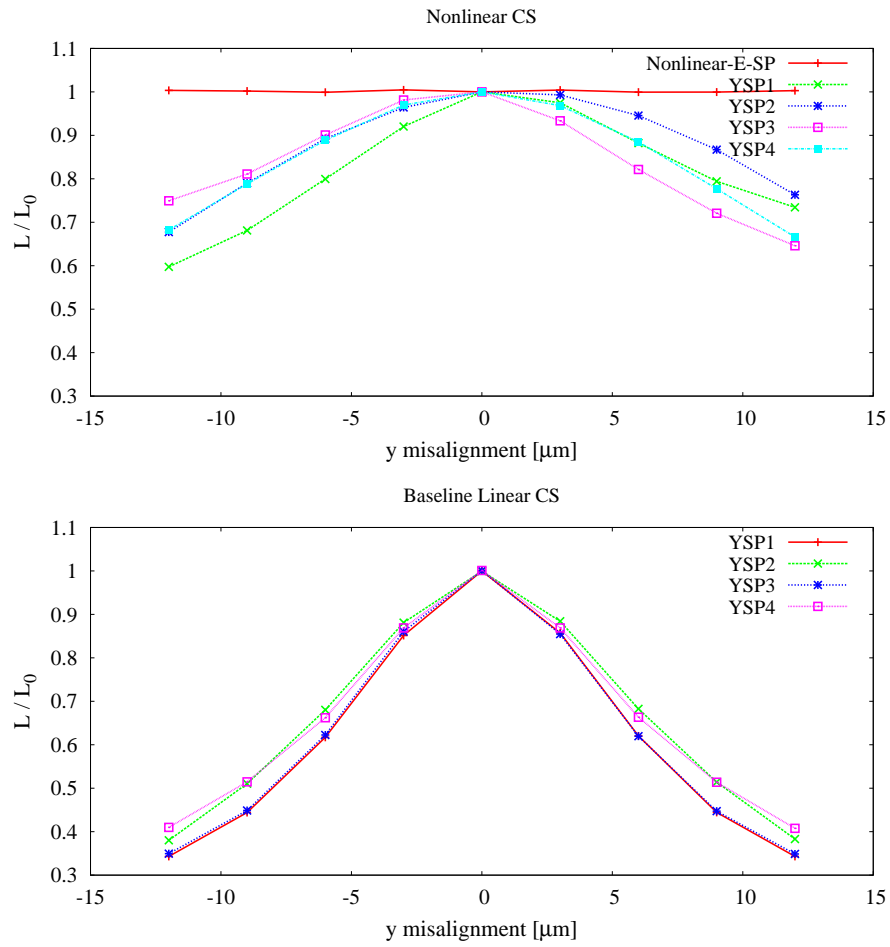


Figure 5.41: CLIC Luminosity as a function of the vertical collimator offset when the nonlinear collimator system is used (on the top) and when the linear collimation system is used (on the bottom) in the simulations.



# Alternative Nonlinear Cleaning Betatron Insertion with Skew Sextupole Pair for the LHC at 7 TeV

## 6.1 Introduction to the LHC accelerator

In this section a brief overview of the LHC is given. For more details the reader is invited to see Ref. [1].

The LHC, presently under construction at CERN, is a superconducting proton and ion collider with design luminosity of  $\sim 10^{34} \text{ cm}^{-2} \text{ s}^{-1}$ , nominal beam intensity of  $3 \times 10^{14}$  protons and beam energies ranging from 450 GeV (at injection) and 7 TeV (at collision). This machine is being installed in the 27.7 km long tunnel of its predecessor, the CERN Large Electron Positron collider (LEP) [6].

The LHC consists of 2 rings divided in 8 octants or regions, such as it is shown in Fig. 6.1. The rings cross in four of those interaction regions dedicated to high energy particles experiments: the Interaction Region 1 (IR1) containing the called ATLAS detector; the Interaction Region 2 (IR2) containing the called ALICE detector; the Interaction Region 5 (IR5) the CMS detector; and the Interaction Region 8 (IR8) the LHC-B detector. ATLAS and CMS will be experiments with high luminosity, while ALICE and LHC-B will be experiments with low luminosity.

The energy stored in each LHC beam exceeds by more than 2 orders of magnitude that of any existing machine: 360 MJ stored/each beam ( $3 \times 10^{14}$  protons at 7 TeV), and the transverse energy density is even a factor 1000 higher that of the other existing machines in the world. This makes the LHC beams highly destructive. Therefore, the high intensity LHC beams and the associated high loss rates of protons requires a powerful collimation system, allowing a peak loss of 1 % of the

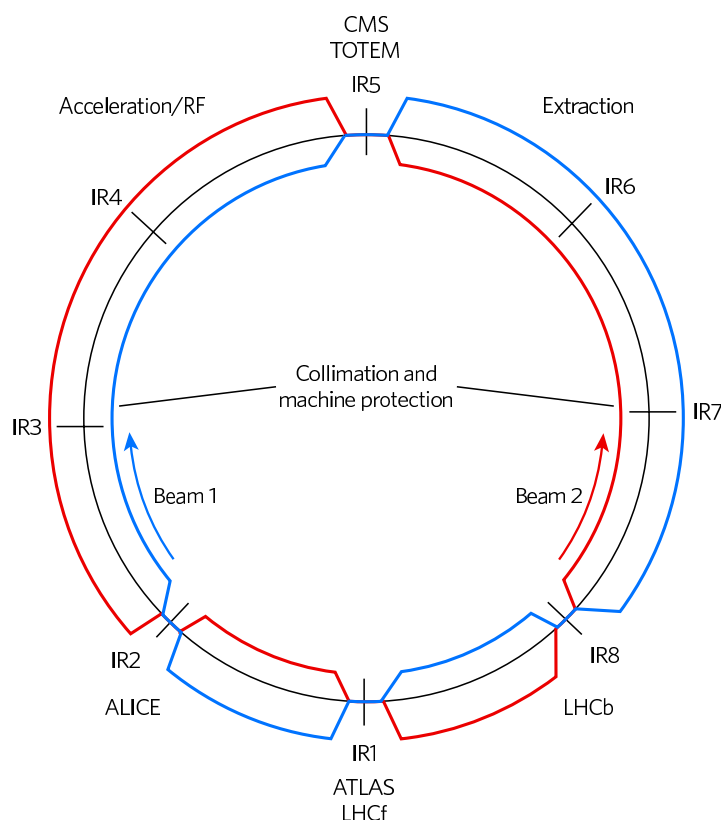


Figure 6.1: Schematic of the LHC ring.

beam within 10 s, a peak power load of 500 kW must be handled at 7 TeV [8]. At the same time, the maximum allowed energy deposition into the super-conducting magnets before quenching is 8.5 W/m. The interaction points 3 and 7 (IR3 and IR7) are dedicated to beam halo cleaning.

### 6.1.1 The baseline linear collimation system of LHC Phase-I

The design of the LHC collimation system is based on the concept of a *phased approach*. It relies on the fact that difficulties and performance goals for the LHC are distributed in time. This means that the collimation system will be improved into different phases in order to reach the necessary robustness and cleaning efficiency without compromising the nominal performance goals.

The first phase of LHC collimation focus the effort on the robustness and flexibility of the system against the specified regular beam losses and accident scenarios [131]. It includes two specific insertions: the IR7 insertion dedicated to betatron collimation, and the IR3 insertion dedicated to momentum collimation. This insertions are based in a multi-stage cleaning system, including primary, secondary and tertiary (absorber) collimators. The collimator database at collision can be found in the tables of the Appendix D. To name the collimators, the following notation is used [1,8]:

- Primary collimators (TCP): for intercepting protons from the primary halo. These collimators are made of two carbon-based jaws with a length <sup>1</sup> of 60 cm. The interacting halo is converted into a secondary off-momentum halo with larger divergence.
- Secondary collimators (TCSG): made of carbon with a length of 1 m. Their function is to stop the almost totality of protons from the secondary halo. The number of protons that escape this second stage collimation forms the tertiary halo.
- Tertiary collimators or absorbers (type TCLA): made of Tungsten (W) that are located at the end of the cleaning insertions (IR3 and IR7) for protecting the superconducting arcs.
- Special collimators or absorbers (type TCT): made of Tungsten (W) for local protection and cleaning at the triplets in the experimental insertions.

In addition, the LHC collimation system includes several other collimators for local protection during injection and for dump problems [132]: special injection protection collimators in IR2/IR8 protecting the main ring from injection kicker magnets faults; beam abort protection collimators in IR6 protecting the machine from errors of beam dump kicker magnets. Furthermore, there are also collision debris collimators protecting the machine from particle showerings coming from the IR1/IR5 experimental insertions.

Because of its high robustness to resist beam impacts, the graphite was chosen as the material to make the primary and secondary collimators of Phase-I. However, this material is a poor conductor, and a high conductivity would be desired to reduce impedance. Calculations have shown that the total LHC impedance is strongly dominated by this kind of collimators [133, 134]. This is expected to limit the total intensity to about 30–40 % of its nominal value.

For future upgrades of the system to reach the nominal machine performance, a Phase-II LHC collimation system has been planned. Different solutions are being studied, for example low impedance hybrid material for the secondary jaws and consumable collimators with Cu-based jaws (see Chapter 1). It is worth mentioning that a rotating consumable collimator will be constructed and tested at CERN for the LHC Phase-II collimation, under the auspicious of the LARP project [20], a task force collaboration between CERN and laboratories in the USA (SLAC, BNL, Fermilab).

### The LHC linear betatron cleaning insertion

The Fig. 6.2 shows the longitudinal distribution of primary and secondary collimators in the LHC linear betatron cleaning insertion IR7. The space reserved for the future secondary collimators of Phase-II is marked in the figure (see key “*Secondary coll. (phase2)*”). The system also includes other space ‘reservoir’, marked as *placeholders*, for location of new collimators in the future system upgrades. The features of the collimators are shown in the list of Table D.2 (Appendix D). The

<sup>1</sup>These lengths refer to the effective length of material, i.e. the one ‘seen’ by the incoming beam

nominal half gaps in the linear betatron cleaning system are set to  $6\sigma$  and  $7\sigma$  for primary and secondary collimators, respectively, and  $10\sigma$  for the absorbers.

The collimators are placed in warm regions, i.e. in regions with normal conducting dipole magnets. Unlike the superconducting magnets, warm magnets can tolerate higher local beam losses. Moreover, the warm magnets can redirect the secondary halo out of the machine aperture close to the collimation region, thus limiting the propagation of losses into the downstream arc.

The optics considered in this section for the IR7 is the LHC version 6.5 [1]. The corresponding betatron and dispersion functions as a function of the longitudinal coordinate are shown in Fig. 6.3. The performance of this linear collimation system will be compared with our proposed nonlinear collimation section.

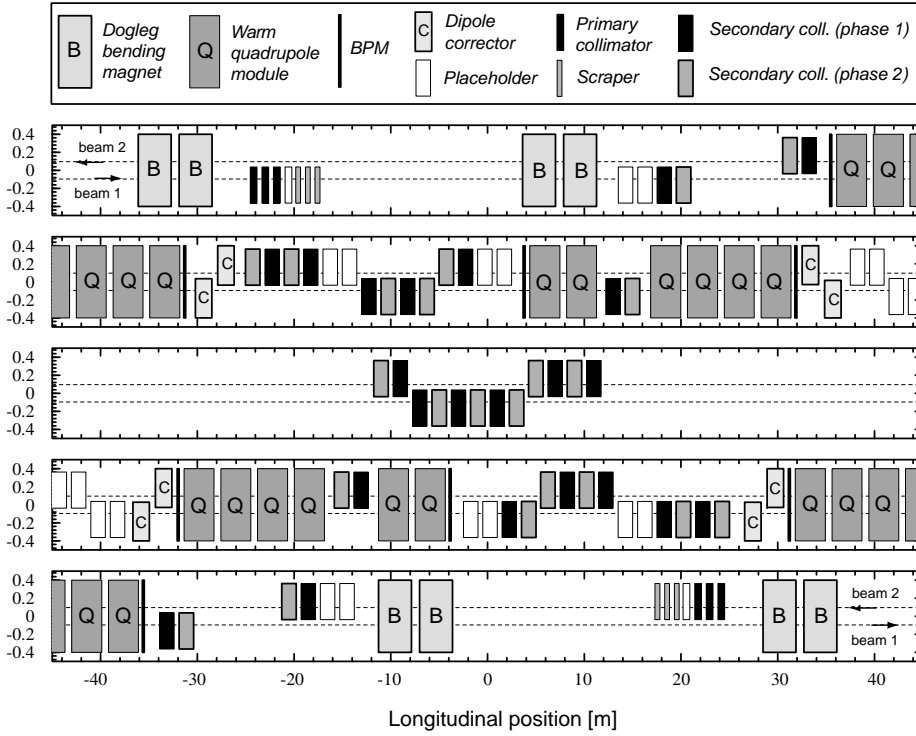


Figure 6.2: Longitudinal layout for the betatron cleaning insertion in IR7 [1].

## 6.2 An alternative nonlinear betatron collimation system

For  $e^+e^-$  linear colliders designed to operate at center-of-mass energy of the order of TeV, the collimation requirements are similar to those for the LHC. It is thus a close thought to apply a



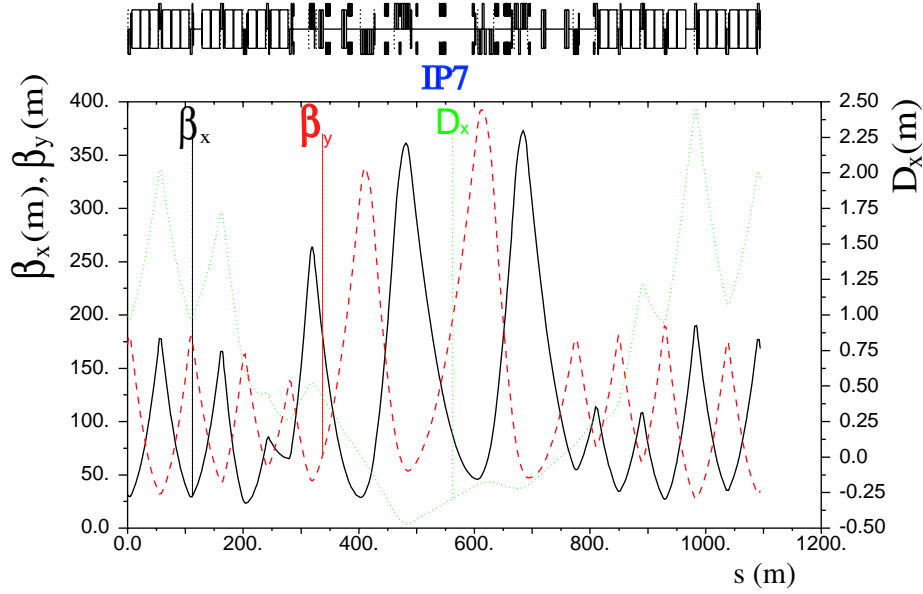


Figure 6.3: Betatron functions and dispersion versus the longitudinal position ( $s$ ) for the LHC IR7 Phase-I.

similar nonlinear collimation scheme as that designed for CLIC. The main differences from CLIC are the following:

- the LHC momentum spread is almost two orders of magnitude smaller, and, hence, cannot be exploited for widening the beam during collimation;
- emittance growth from synchrotron radiation is insignificant, and does not constrain the design of the collimation system;
- the geometric vertical emittance is about 3 orders of magnitude larger than in CLIC.

In this chapter we present a nonlinear collimation system for betatron cleaning in the LHC at collision energy (7 TeV). This system could be a possible solution to the difficult trade-off between cleaning efficiency, collimator robustness and collimator impedance.

We will discuss an optics based on a skew sextupole pair as shown in the schematic of Figure 6.4, which represents the long straight section LSS7 of the LHC IR7 region, adapted for nonlinear betatron cleaning. In this lattice, the spoilers or primary collimators are placed at (or near) the interaction point IP7. The first skew sextupole blows up the particle amplitudes, thereby allowing larger collimator gaps which may avoid an unacceptable high transverse resistive wall impedance from the collimator material. A skew sextupole downstream of the spoiler, and at  $\pi$  phase advance from the first sextupole, cancels the geometric aberrations induced by the former.

After placing secondary collimators downstream of the primary collimators, we will analyze the beam losses and calculate the so-called cleaning inefficiency of the system from tracking studies.

Finally, the impedance of the proposed design will also be studied. The results are compared with those of the conventional linear collimation system of Phase-I [1].

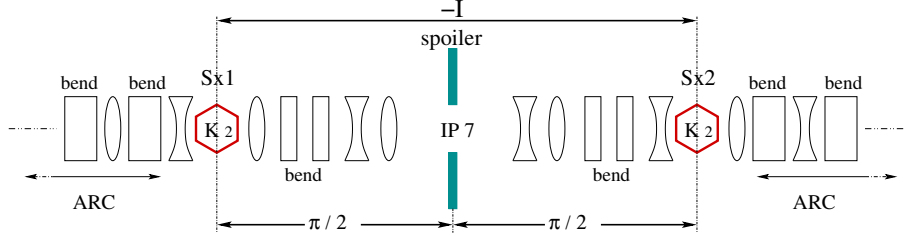


Figure 6.4: Schematic of a nonlinear collimation layout for the LHC.

## 6.2.1 Optics Layout

### Collimation depth and collimator apertures

The Eqs. (4.37), (4.38) and (4.39) provide the relation between the collimation depth in units of the rms beam size and the spoiler (primary collimator) aperture as function of the optics parameters.

A vertical aperture  $n_{y2}$  of the spoiler at IP7 will collimate halo particles located in the horizontal and vertical planes, while a horizontal spoiler aperture  $n_{x2}$  can be adjusted to improve the collimation of halo particles with amplitude offsets in both transverse planes, as we already mentioned in section 4.2.3.

In order to approximate a circular collimation aperture in the normalized  $x$ - $y$  plane we can choose  $\beta_{x,s} = \beta_{y,s}$  at the skew sextupoles and  $R_{12} \approx R_{34}$ . In this case, from the system of Eqs. (4.37), (4.38) and (4.39), we have  $n_{x2} = 2n_{y2}$ . Taking into account that the collimation depth for the LHC is established at  $n_x = n_y = 6$  [1], we have looked for optics solutions that allow the setting of the vertical and horizontal spoiler jaws with half gaps  $n_{y2} = 8$  and  $n_{x2} = 2n_{y2} = 16$ , respectively.

### Optics solution

The optics for the betatronic cleaning insertion IR7 in LHC optics version 6.5 has been matched to fulfil the nonlinear collimation requirements. The matching was done without affecting the optics of the other LHC insertions, and involved only existing quadrupole magnets.

Different optics solutions were found. They differ in the beta functions at the skew sextupoles and in the  $R_{12}$ ,  $R_{34}$  matrix elements between the first skew sextupole and the spoiler. To elucidate which of the different optics solutions is best suited for our application, we can choose a number of criteria:

- minimize the normalized sextupole strength  $K_s$ ,

- minimize the product of normalized sextupole strength and the larger of the two beta functions at the skew sextupole (which is equivalent to minimizing the sextupole pole-tip field),
- minimize the nonlinear aberrations introduced by the first skew sextupole, which scale as  $\beta_{y,s}^{3/2} K_s$  and as  $\beta_{y,s} \beta_{x,s}^{1/2} K_s$  (and in our case  $\beta_{x,s} = \beta_{y,s} \equiv \beta_s$ ).

The histogram of Fig. 6.5 compares the values of  $K_s$  and  $\beta_s K_s$  for the different optics solutions. From the 12 obtained candidate solutions, we have selected an optics for which both the sextupole strength and the product of sextupole strength and beta function at the sextupole are minimum.

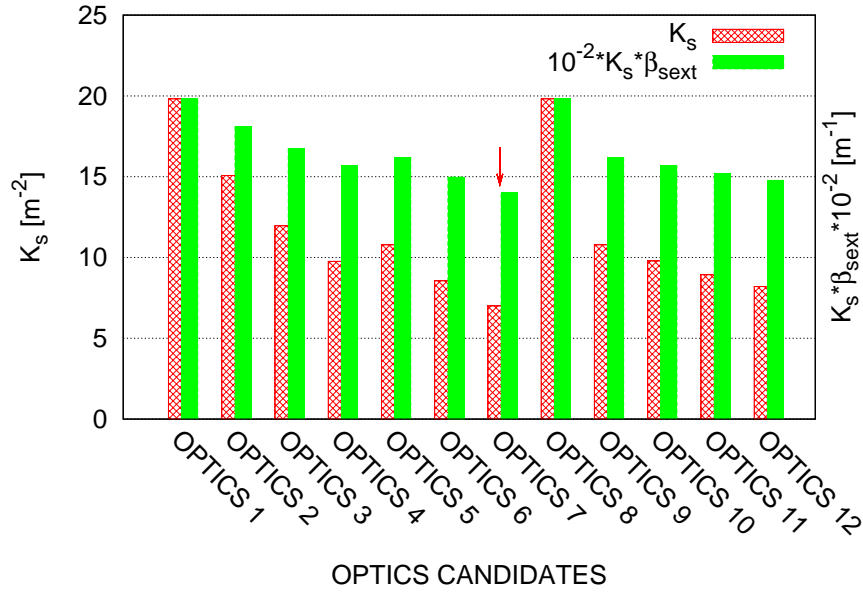


Figure 6.5: Comparative histogram for the values of the quantities  $K_s$  and  $10^{-2}\beta_s K_s$  in the 12 optics candidates solutions found for a nonlinear LHC collimation system. The solution OPTICS 7 gives the minimum values both for  $K_s$  and for the product  $K_s \beta_s$ . For all optics solutions shown  $\beta_{x,s} = \beta_{y,s} \equiv \beta_s$ .

Fig. 6.6 shows the betatron functions and dispersion as function of the longitudinal coordinate  $s$  for the optimum optics solution OPTICS 7. Table 6.1 summarizes the main parameters of this optics.

### 6.2.2 Collimation boundaries

From the collimator apertures  $n_{x2} = 16$  and  $n_{y2} = 8$  and using the optics parameters of Table 6.1, we can compute the collimation contours, given by the equations:

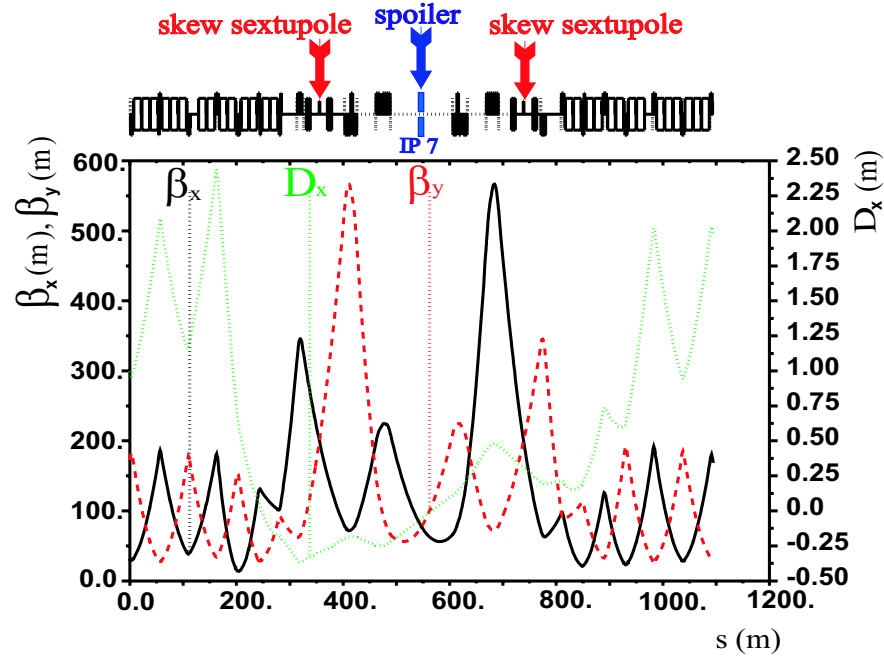


Figure 6.6: Betatron functions and dispersion versus the longitudinal coordinate ( $s$ ) for LHC IR7 with a nonlinear section based on two skew sextupoles.

Table 6.1: Optics parameters for a nonlinear collimation section in IR7 of LHC.

variable	value
beta functions ( $x, y$ ) at skew sext.	200.0, 200.0 m
product of skew sextupole pole-tip field and length ( $B_T l_s$ )	8.1823 T·m
skew sextupole aperture $a_s$	10 mm
skew sextupole strength $K_s$	7.0063 m <sup>-2</sup>
$R_{12}, R_{34}$ from sext. to spoiler	124.403, 124.404 m
beta functions ( $x, y$ ) at spoiler	77.381, 77.381 m
rms spot size ( $x, y$ ) at spoiler	215.89, 263.96 $\mu$ m

$$n_{x2} = \frac{\beta_{x,s}\epsilon}{\sqrt{\beta_{x,sp}\epsilon}} R_{12} K_s XY, \quad (6.1)$$

$$n_{y2} = \frac{\beta_{x,s}\epsilon}{\sqrt{\beta_{x,sp}\epsilon}} \frac{1}{2} R_{34} K_s (X^2 - Y^2), \quad (6.2)$$

expressed in normalized coordinates (in units of  $X = x / \sqrt{\beta_x \epsilon_x}$  and  $Y = y / \sqrt{\beta_y \epsilon_y}$ ).

Figure 6.7 shows the resulting collimation boundaries. Particles incoming at the sextupole with amplitude offsets  $\gtrsim 6\sigma$  will be deflected and, in the ideal case, lost in the downstream collimators. Note that the boundaries here shown refer to vanishing initial slopes, and they would be modified for trajectories with initial  $x'$  or  $y'$  unequal zero.

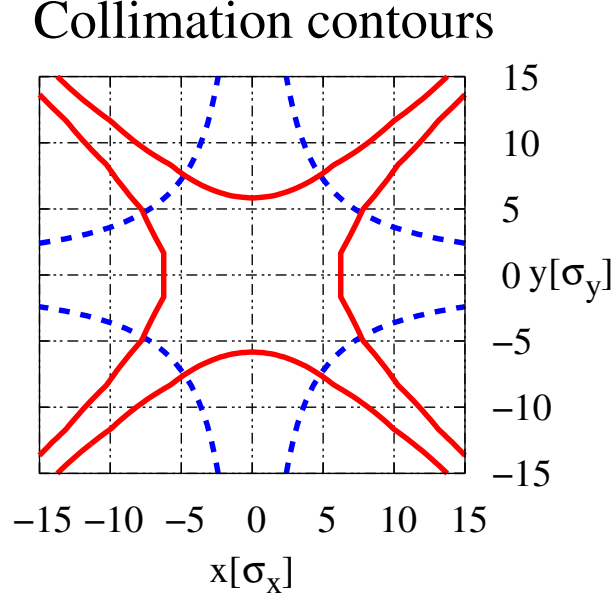


Figure 6.7: Collimation boundaries for  $x' = y' = 0$ , with  $n_x = 6$ ,  $n_y = 6$ ,  $n_{y2} = 8$  and  $n_{x2} = 2n_{y2}$ .

### 6.2.3 Spoiler protection

In Chapter 4 we pointed out that the condition  $\sigma_{x,\text{sp}}\sigma_{y,\text{sp}} \gtrsim \sigma_{r,\text{min}}^2$  could be established as a possible criterium for avoiding the spoiler damage in case of full beam impact. In the case of the LHC primary collimators (made of graphite), a minimum rms beam size  $\sigma_{r,\text{min}}$  of about  $200 \mu\text{m}$  has been estimated [141].

The above condition can be rewritten using the Eqs. (4.35) and (4.36), with  $\beta_{x,s} = \beta_{y,s}$  and  $\epsilon_x = \epsilon_y \equiv \epsilon$ , as

$$(K_s^2 R_{12}^2 \beta_{x,s}^2 \epsilon + \beta_{x,\text{sp}})(K_s^2 R_{34}^2 \beta_{x,s}^2 \epsilon + \beta_{y,\text{sp}}) \epsilon^2 \gtrsim \sigma_{r,\text{min}}^4. \quad (6.3)$$

From Eq. (4.39) we have

$$\beta_{x,s} = \left( \frac{n_{x2}^2 \beta_{x,\text{sp}}}{K_s^2 R_{12}^2 n_x^4 \epsilon} \right)^{1/2}. \quad (6.4)$$

Combining Eq. (6.3) and Eq. (6.4), one obtains the spoiler survival condition in terms of the colli-

mation depth  $n_x$  and of the collimator aperture  $n_{x2}$ , i.e.

$$\left(\frac{n_{x2}^2}{n_x^4} + 1\right) \left(\frac{\beta_{y,sp}}{\beta_{x,sp}} + \frac{R_{34}^2 n_{x2}^2}{R_{12}^2 n_x^4}\right) \beta_{x,sp}^2 \epsilon^2 \gtrsim \sigma_{r,min}^4, \quad (6.5)$$

and in the particular case of our optics solution, where  $\beta_{y,sp} = \beta_{x,sp}$  and  $R_{34} \simeq R_{12}$ , then one has

$$\left(\frac{n_{x2}^2}{n_x^4} + 1\right)^2 \beta_{x,sp}^2 \epsilon^2 \gtrsim \sigma_{r,min}^4. \quad (6.6)$$

Figure 6.8 shows the product  $\sigma_{x,sp}\sigma_{y,sp}$  in units of  $\sigma_{r,min}^2$  as a function of  $n_x$  and  $n_{x2}$ . The quadratic behavior of  $n_{x2}$  versus  $n_x$  is shown in Figure 6.9, where the working point here considered ( $n_x = 6$ ,  $n_{x2} = 16$ ) is compared with the limit for spoiler survival.

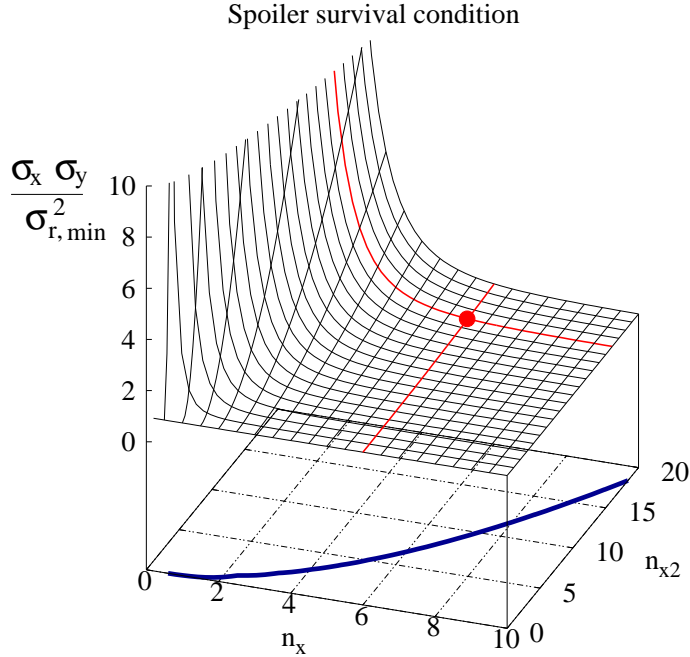


Figure 6.8: Surface  $\sigma_x \sigma_y / \sigma_{r,min}^2$  as function of  $n_x$  and  $n_{x2}$ . The point represents the working point  $n_x = 6$ ,  $n_{x2} = 2n_{y2} = 16$  and  $\sigma_x \sigma_y / \sigma_{r,min}^2 = 1.158$ . The solid line in the plane  $n_{x2}$  vs.  $n_x$  represents the limit  $\sigma_x \sigma_y / \sigma_{r,min}^2 = 1$  for spoiler survival when  $n_{x2} = 2n_{y2}$ .

At this point, it is necessary to warn that in the interaction of the protons, unlike for electron interactions, at the collision energy of 7 TeV per beam not only electromagnetic cascades of electron-positron pairs and photons occur, but also inelastic nuclear interactions with production of muons and hadronic matter, such as pions, kaons or neutrons. In addition, the secondary particles can give rise to new interactions. Therefore, in order to study the energy deposition in the collimators by protons, detailed numerical simulations are necessary. These would allow establish a more accurate limit for the collimator damage. Related to this topic see for example [142, 143].

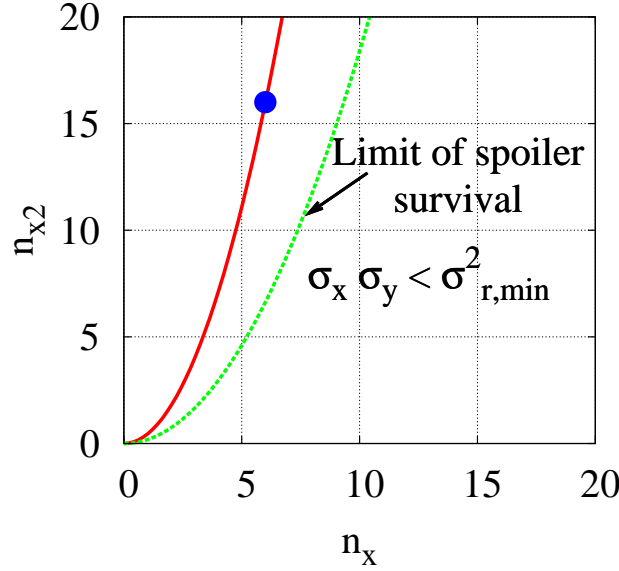


Figure 6.9: Mechanical spoiler aperture vs. collimation amplitude. The solid red line is the relation  $n_{x2}$  vs.  $n_x$  as given by Eq. (4.37). The dashed line represents the limit  $\sigma_x \sigma_y / \sigma_{r,min}^2$  for spoiler survival when  $n_{x2} = 2n_{y2}$ . In this thesis the point  $n_x = 6$  and  $n_{x2} = 2n_{y2} = 16$  is considered.

#### 6.2.4 Two-Stage Collimation

Until now we have only considered spoilers or primary collimators located at IP7. However, protons which are not absorbed can be scattered elastically off the jaw, thus generating a secondary halo which can induce quenches of the superconducting magnets. Therefore, secondary collimators are necessary to intercept the secondary halo. The gaps of the existing collimators in the IR7 insertion of the LHC [8] were set to the required apertures for nonlinear collimation. A total of 12 secondary collimators are retained downstream the primary collimators. Notably a vertical collimator is located at the optimum phase advance  $\Delta\mu_0 \approx 0.476$  rad from IP7, calculated from  $\Delta\mu_0 = \pm \arccos(n_{y2}/n'_{y2})$  [18], assuming a primary vertical aperture  $n_{y2} = 8$  and a secondary vertical aperture  $n'_{y2} = 9$ . The other possible solutions  $\Delta\mu_0 = 0.476 + \pi$  rad and  $\Delta\mu_0 = \pi - 0.476$  rad have been rejected, since at these phase advances one is in the arc downstream of the collimation region, where superconducting dipoles are located.

Information on the selection and setting of the primary and secondary collimators for the nonlinear system is compiled in Table 6.2. The secondary collimators between IP7 and the second skew sextupole have been set with a radial aperture of  $9\sigma$ , and those downstream of the second skew sextupole with a  $7\sigma$  aperture. See the schematic of Figure 6.10.

Figure 6.11 compares the half gap of the collimators for the linear and the alternative nonlinear collimation systems. The total number of active collimators in IR7 is 14 for the nonlinear system and 19 for the linear system (Phase-I system). The empty space in the histogram of Figure 6.11 in-

dicates the space reserve for future system upgrades. For the nonlinear collimation system we have eliminated the collimators #1 to #11, which are in front of the nonlinear system's spoilers/primary collimators. Moreover, we have added the secondary collimators #14, #15 and #17 using that existing space reserve.

Table 6.2: Data of primary and secondary collimators in the proposed two-stage nonlinear collimation insertion IR7: reference number in cleaning insertion, name of the collimator (maintaining the same nomenclature as in Phase-I), collimator material, collimator length, distance from IP7 taken as a reference point, skew angle in  $x$ - $y$  space (0. corresponding to a horizontal collimator), and half gaps in units of  $\sigma$ . The names with the superindex <sup>(\*)</sup> indicate additional collimators, which are not present in the baseline linear collimation system of Phase-I.

#	Name	Material	Length [m]	Distance from IP7 [m]	Azimuth [rad]	Half gap [ $\sigma_\beta$ ]
<b>Primary</b>						
12	TCSG.A4L7.B1	C	0.6	-3.	0.	16
13	TCSG.A4R7.B1	C	0.6	1.	1.571	8
<b>Secondary</b>						
14	TCSG.B4R7.B1 <sup>(*)</sup>	C	1.0	53.190	1.571	9
15	TCSG.A5R7.B1 <sup>(*)</sup>	C	1.0	88.256	0.651	9
16	TCSG.B5R7.B1	C	1.0	92.256	2.47	9
17	TCSG.C5R7.B1 <sup>(*)</sup>	C	1.0	104.256	1.571	9
18	TCSG.D5R7.B1	C	1.0	108.256	0.897	9
19	TCSG.E5R7.B1	C	1.0	112.256	2.277	9
20	TCSG.6R7.B1	C	1.0	146.861	0.009	9
21	TCLA.A6R7.B1	W	1.0	153.927	1.571	9
22	TCLA.C6R7.B1	W	1.0	184.801	0.	9
23	TCLA.E6R7.B1	W	1.0	218.352	1.571	7
24	TCLA.F6R7.B1	W	1.0	220.351	0.	7
25	TCLA.A7R7.B1	W	1.0	237.698	0.	7

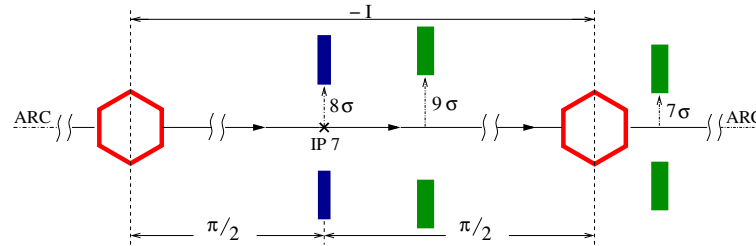


Figure 6.10: Schematic of a two-stage nonlinear collimation layout for the LHC. The primary collimator is drawn with blue colour, and the secondary collimators are drawn with green colour.



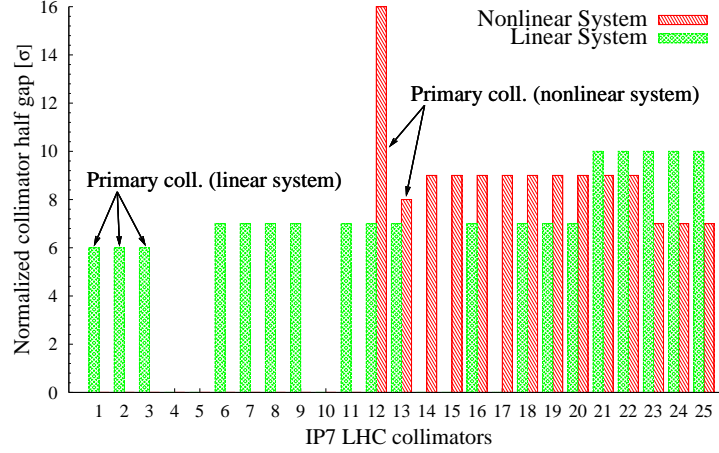


Figure 6.11: Comparison of the normalized collimator apertures for the nonlinear and the linear collimation systems. In the nonlinear case, the collimators [#1, #11] are not used, and collimators #12 with  $n_{x2} = 16$  and #13 with  $n_{y2} = 8$  play the role of primary spoilers at IP7.

### 6.2.5 Cleaning Efficiency

Tracking studies have been performed for the nonlinear and linear collimation systems by using a modified version of the tracking code SixTrack [144, 145]. This tool allows us to calculate the cleaning inefficiency of the collimation system and to save the particles trajectories for an off-line analysis of beam losses. For example, Fig. 6.12 compares the trajectory of a halo particle in the case of linear and nonlinear optics. For the nonlinear optics, the first sextupole gives a kick which increases the transversal amplitude in the region where the collimators are located. The second sextupole cancels the effect induced by the former.

The cleaning inefficiency  $\eta_c(A_0)$  of the collimation system is defined by [144]

$$\eta_c(A_0) = \frac{N_p(A > A_0)}{N_{\text{abs}}}, \quad (6.7)$$

with  $N_p(A > A_0)$  the number of beam protons with amplitude above  $A_0$  and  $N_{\text{abs}}$  the total number of absorbed protons in the cleaning insertion.

Sample beam halos have been generated by tracking initial distributions of  $N_p \simeq 5 \times 10^6$  protons for 200 turns. At first, initial horizontal and vertical halos were separately considered. The initial horizontal distribution in normalized phase space is an annulus with radii  $A_x = \sqrt{X^2 + X'^2} = 6.003$  and  $A_y = \sqrt{Y^2 + Y'^2} = 0$  and thickness  $\delta\sigma = 0.0015\sigma$  (see Fig. 6.13). Similarly, for the vertical halo we used  $A_x = 0$  and  $A_y = 6.003$ . In a second step, a square particle distribution (see Fig. 6.14) with diagonal amplitude  $A_r = \sqrt{A_x^2 + A_y^2} = 8.503$  ( $A_x = A_y \simeq 6$ ) has been considered to study the skew halo components.

The resulting inefficiency  $\eta_c(A_0)$  for the nonlinear collimation system compared with the linear

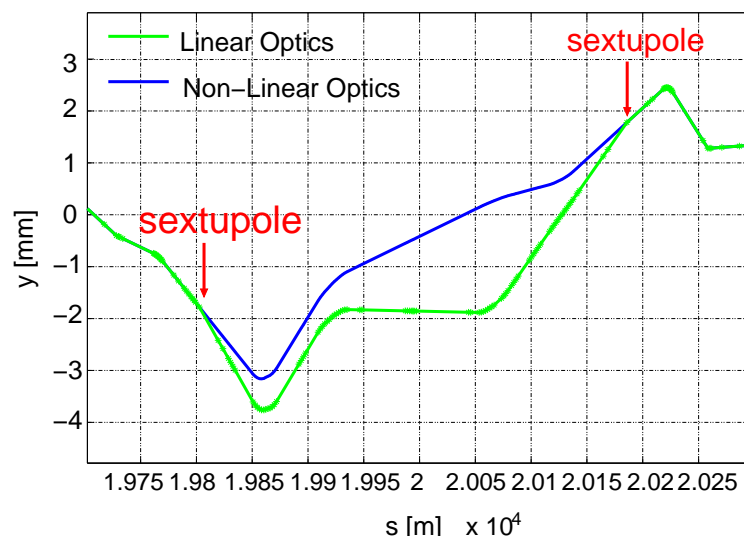


Figure 6.12: trajectory of a halo particle in LHC IR7 for the case of the linear optics (blue curve) and the optics with the sextupole pair (green curve).

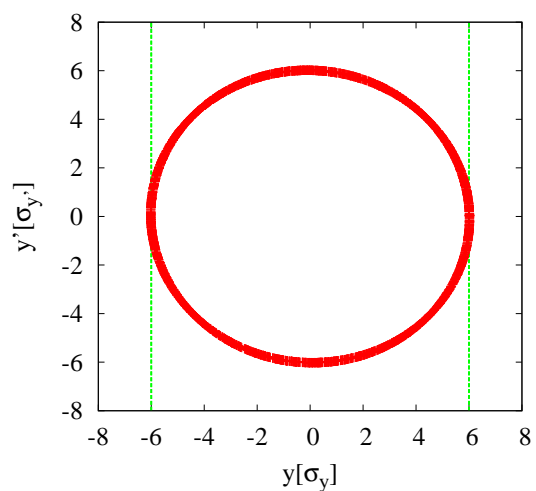


Figure 6.13: Example of an input vertical halo model for tracking with Sixtrack.

one is shown in Figure 6.15. The nonlinear system presents a better cleaning efficiency (lower cleaning inefficiency) for  $A_0 \in [6\sigma, 7.4\sigma]$  and  $A_0 \in [9.5\sigma, 15\sigma]$  for the vertical halo. In the range  $(7.4\sigma, 9.5\sigma)$  the linear system is more efficient by less than a factor 2. However, for a horizontal halo, the inefficiency of the nonlinear system in the range  $[7.5\sigma, 15\sigma]$  is higher by approximately

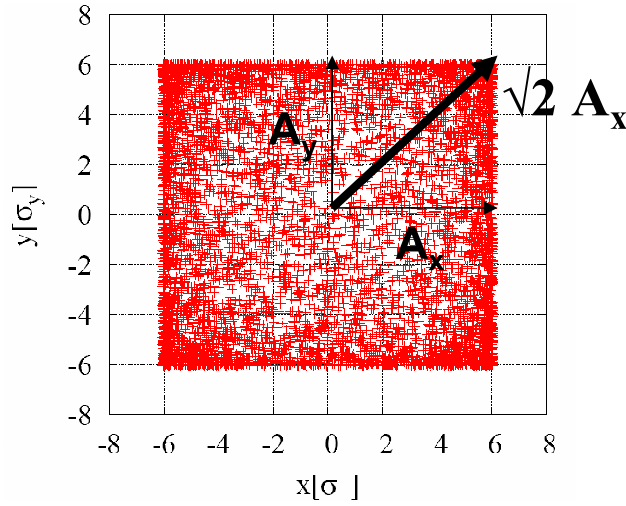


Figure 6.14: Example of an input radial halo model for tracking with Sixtrack.

a factor 10. In the case of a radial halo, the present version of the nonlinear system is less efficient by a factor 3.

The number of impacts and absorptions at every collimator of the nonlinear and linear systems is displayed in Figure 6.16 for the vertical halo, Figure 6.17 for the horizontal halo and Figure 6.18 for the radial halo. Unlike the linear system, that registers the peak of impacts and absorptions at the beginning of the insertion, the nonlinear system registers the peak at the collimator #13, located close to the IP7.

### 6.2.6 Decreasing the LHC Impedance

#### Coherent coupled-bunch tune shifts because of collimator impedances

Most of the LHC collimators in Phase-I will be made of graphite. This material is a poor conductor (its electrical conductivity is  $1.7 \times 10^{-3}$  that of copper). In addition, the collimator jaws of Phase-I will be located close to the beam ( $a \sim 6\sigma$ ). These conditions will contribute to a dramatic increase of the machine impedance. Calculations [133, 134] have shown that the achievable LHC beam intensity, and therefore the luminosity, will be limited by the impedances introduced by the collimators.

A nonlinear collimation system, allowing larger aperture for most of the collimators, could be a cure overcoming the performance limitations associated with the collimator impedances.

The transverse impedance of each collimator has been calculated by using the Burov-Lebedev theory [146, 147]. The contribution from the collimators rotated by an azimuthal angle  $\alpha$  has been considered applying the corresponding matrix rotation to a diagonal  $2 \times 2$  tensor impedance. More details are given in the Appendix F. The resistive-wall transverse impedance can generate coherent

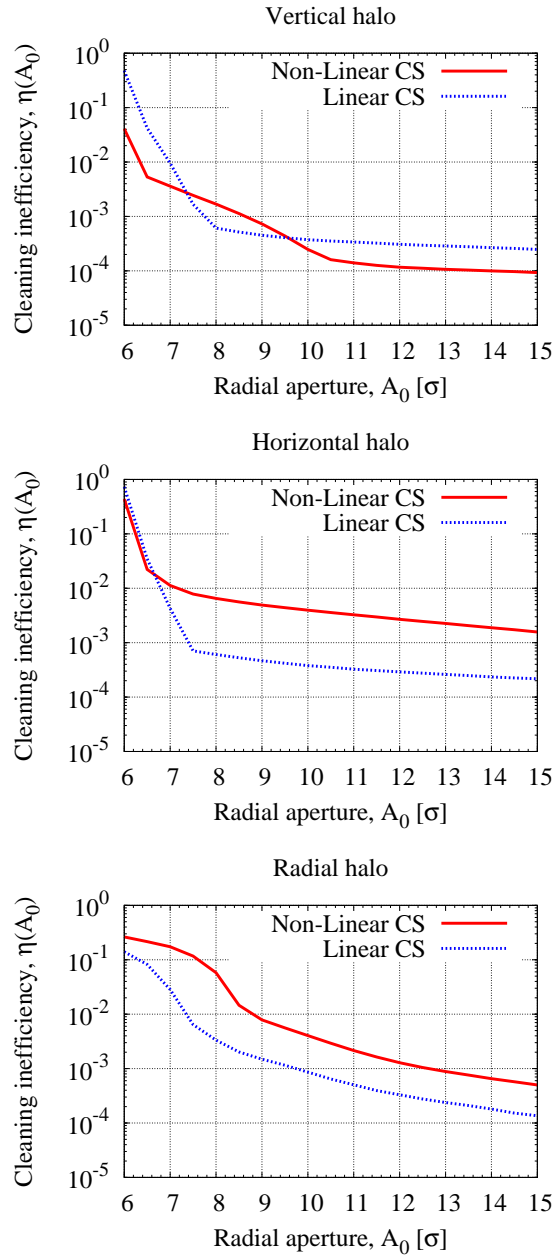


Figure 6.15: Cleaning inefficiency,  $\eta_c(A_0)$ , as a function of the radial amplitude  $A_0$  for the nonlinear collimation system (red solid line), compared with  $\eta_c(A_0)$  for the conventional linear system (dotted blue line) considering a vertical halo (top), a horizontal halo (middle) and a radial halo (bottom) at 7 TeV.

coupled-bunch tune shifts, which can be written in terms of an effective impedance  $Z_{\perp}^{\text{eff}}$  as [148]

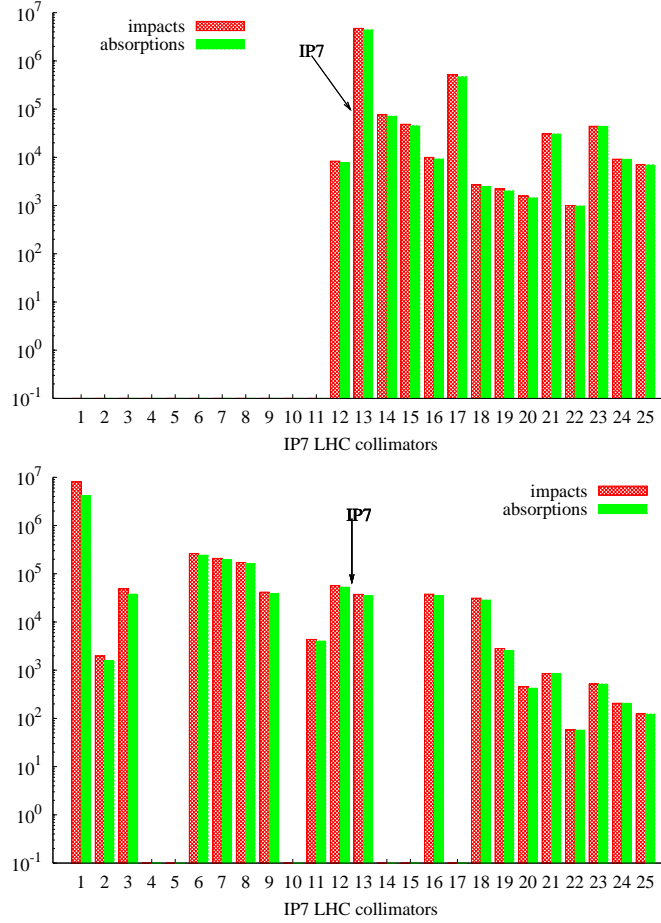


Figure 6.16: Number of particle impacts and absorptions in the collimators of the LHC insertion IR7 for nonlinear collimation (top) and for linear collimation (bottom), considering a vertical halo at 7 TeV.

$$\Delta Q_{\perp}(\omega_k - \omega_{\xi}) = -i \frac{N_b N e \omega_0 \beta_{\perp}}{8\pi^2 E} \frac{\Gamma(m + \frac{1}{2})}{2^m m!} Z_{\perp}^{\text{eff}}(\omega_k - \omega_{\xi}), \quad (6.8)$$

where  $N$  is the bunch population,  $N_b$  the number of equi-distant bunches and  $E$  the beam energy. It is important to stress the dependence on the frequency  $\omega_k = \omega_{\beta} + k\omega_0 + m\omega_s$ , depending on the following oscillation modes: the head-tail mode, characterized by the number  $m$ , and the coupled-bunch mode, characterized by the number  $l = k - N_b k'$  with  $-\infty \leq k' \leq +\infty$  and  $0 \leq l \leq N_b - 1$ . The frequency  $\omega_{\beta} = Q_{\beta}\omega_0$  denotes the betatron frequency as a function of the unperturbed betatron tune  $Q_{\beta}$  and the revolution frequency of the particles  $\omega_0$ ;  $\omega_s$  denotes the synchrotron angular frequency and  $\omega_{\xi} = \xi\omega_{\beta}/\eta$  is the chromatic frequency depending on the chromaticity  $\xi$  and the slippage factor  $\eta$ . The expression for the effective impedance  $Z_{\perp}^{\text{eff}}$  can be found in the Appendix F. By definition the effective impedance measures the degree at which the impedance overlaps the mode spectrum.

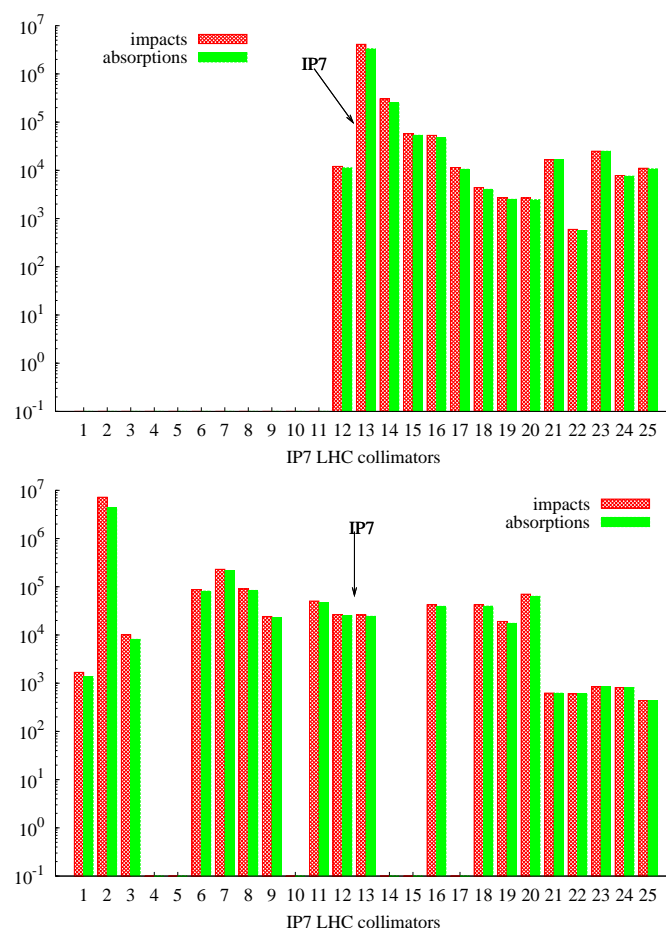


Figure 6.17: Number of particle impacts and absorptions in the collimators of the LHC insertion IR7 for nonlinear collimation (top) and for linear collimation (bottom), considering a horizontal halo at 7 TeV.

We have computed, using *Mathematica* [149], the total coherent tune shift for both cases, namely the baseline linear system of Phase-I and the nonlinear system proposed in this chapter. In a first step, we added exclusively the contribution of the collimators belonging to the IR7 insertion (for both cases linear and nonlinear system). In a second step, we also included the contribution from the total list of collimators, including the insertions IR7, IR3 (momentum collimation) and the tertiary collimators for local protection and cleaning at the triplets in IR1, IR2, IR5 and IR8 (experimental insertions), and IR6 (dump insertion). Other contributions such as the broad-band (BB) impedance and the resistive wall (RW) impedance for the rest of the ring without collimators have also been considered.

In order to select the most unstable case, we have computed the tune shift versus the coupled-bunch modes. The most critical mode is generally that which gives the maximum modulus of the

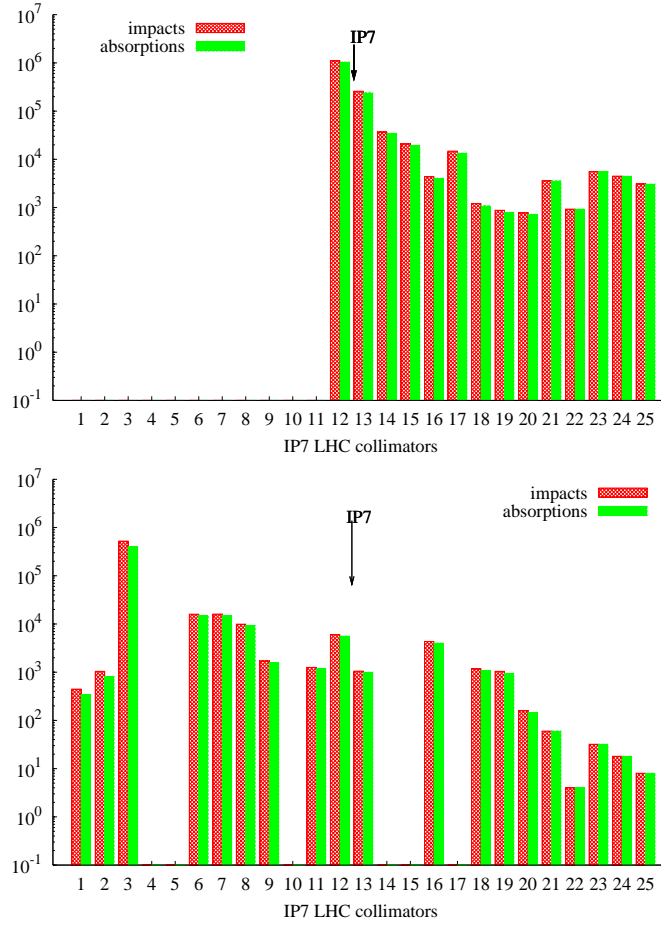


Figure 6.18: Number of particle impacts and absorptions in the collimators of the LHC insertion IR7 for nonlinear collimation (top) and for linear collimation (bottom), considering a radial halo at 7 TeV.

tune shifts. Figure 6.19 shows the modulus of the horizontal and vertical tunes shifts as a function of the mode number  $l$  for the case of the nonlinear IR7. A similar scan is presented in Figure 6.20 for the linear IR7. The maximum values of  $|\Delta Q_{\perp}|$  are found at  $l = 0$  or  $l = 3564$ . The corresponding imaginary part of the tune shift is plotted in Figure 6.21.

For all calculations we have taken the head-tail mode  $m = 0$ , related to rigid dipole oscillations, zero chromaticity and the LHC parameters of Table 6.3. In order to consider a pessimistic case, and since the theory assumes equi-distant bunches, we have used  $N_b = 3564$  instead of the nominal number of bunches  $N_b = 2808$ . Results of  $Z_{\perp=x,y}^{\text{eff}}$  and  $\Delta Q_{\perp=x,y}$  are summarized in Table 6.4 for each of the different contributions.

It is worthwhile to point out that when the nonlinear IR7 insertion is used,  $|Z_x^{\text{eff}}|$  is reduced by about a factor 2 and  $|Z_y^{\text{eff}}|$  by about a factor 3 with respect to the linear IR7 insertion of Phase-I.

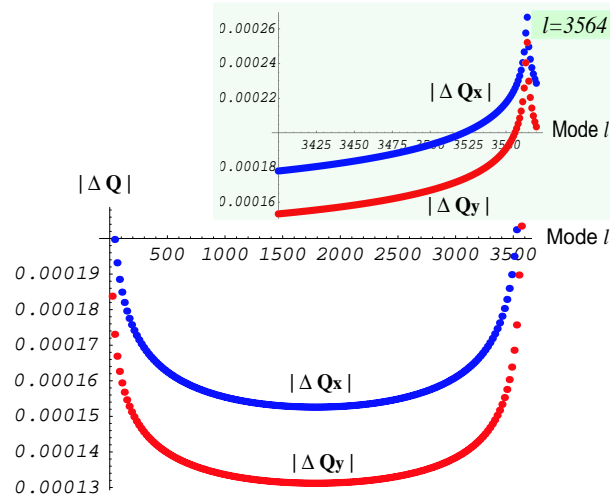


Figure 6.19: Module of the horizontal and the vertical coherent coupled-bunch tune shifts ( $|\Delta Q_x|$  and  $|\Delta Q_y|$  respectively) as a function of the coupled-bunch mode  $l$  for the case of the nonlinear IR7. The figure on the top shows a zoom of the region  $l \in [3400, 3575]$ . The maxima are found at  $l = 0$  and  $l = 3564$ . The results have been obtained assuming  $m = 0$  and  $\xi = 0$ .

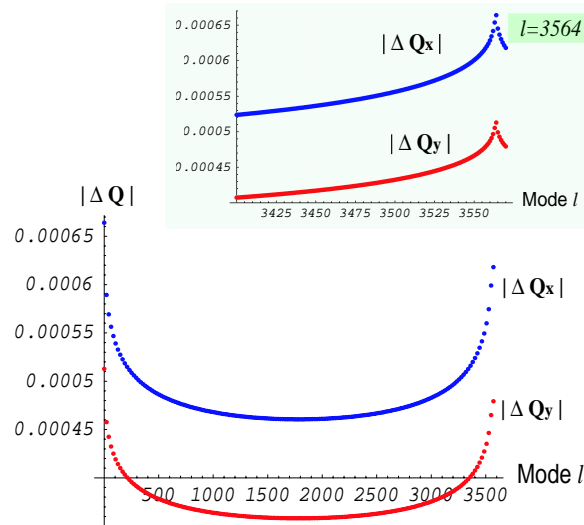


Figure 6.20: Module of the horizontal and the vertical coherent coupled-bunch tune shifts ( $|\Delta Q_x|$  and  $|\Delta Q_y|$  respectively) as a function of the coupled-bunch mode  $l$  for the case of the linear IR7. The figure on the top shows a zoom of the region  $l \in [3400, 3575]$ . The maxima are found at  $l = 0$  and  $l = 3564$ . The results have been obtained assuming  $m = 0$  and  $\xi = 0$ .

### Transverse stability diagrams

Landau damping [150] of the coherent beam oscillation modes due to the tune spread provides a possible cure against instabilities. Because of Landau damping, coherent modes which are present



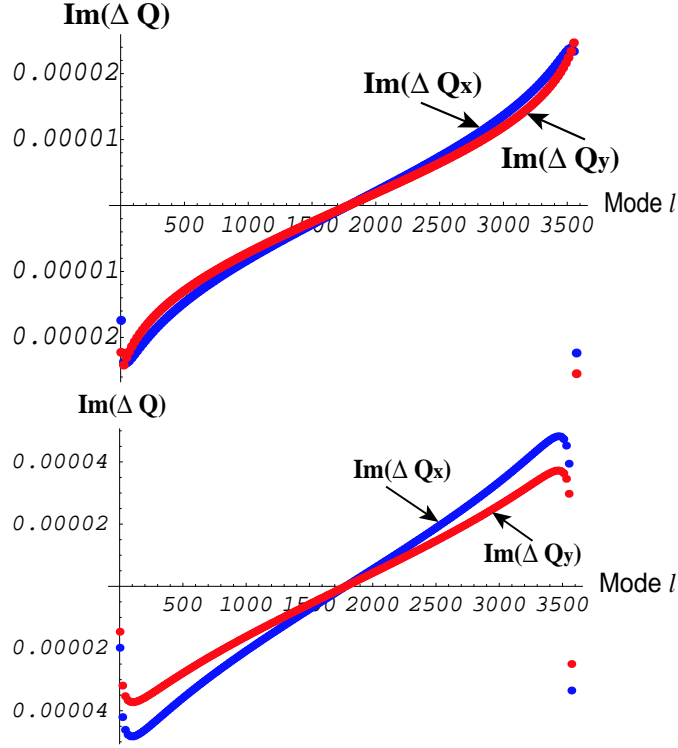


Figure 6.21: Imaginary part of the horizontal and the vertical coherent coupled-bunch tune shifts ( $\text{Im}(\Delta Q_x)$  and  $\text{Im}(\Delta Q_y)$  respectively) as a function of the coupled-bunch mode  $l$ , for the case of the nonlinear IR7 (top) and the case of the linear IR7 (bottom). The results have been obtained assuming  $m = 0$  and  $\xi = 0$ .

Table 6.3: LHC nominal parameters used in the tune shift calculation.

parameter	value
proton energy (at collision): $E$ [TeV]	7.
bunch length: $\sigma_z$ [mm]	75.5
bunch population: $N$	$1.15 \times 10^{11}$
number of bunches: $N_b$	2808
bunch spacing: $\Delta t_b$ [ns]	25
revolution frequency: $\omega_0 = 2\pi f_0$ [kHz]	70.6544
betatron tune: $Q_\beta$	65.32
machine slippage factor: $\eta$	$3.22 \times 10^{-4}$

when there is no incoherent tune shift may be absent when such a shift exists. In this way, Landau damping can be considered as a bridge between incoherent and coherent beam collective effects.

In the LHC arcs there are two families of magnetic octupoles which control betatron detuning and provide Landau damping of coherent beam oscillation modes [1]. Potentially unstable

Table 6.4: Transverse effective collimator impedance  $Z_{x,y}^{\text{eff}}$  and transverse coherent coupled-bunch tune shift  $\Delta Q_{x,y}$  for the IR7 Phase-I (linear), for our proposed nonlinear IR7, and for other additional contributions from: IR3 (momentum collimation insertion), other tertiary collimators for local protection (in IR1, IR2, IR5, IR6 and IR8), broad-band (BB) impedance and resistive wall (RW) impedance without collimators. These results have been obtained considering the most unstable case  $m = 0$ ,  $l = 0$  and  $\xi = 0$ .

	$Z_x^{\text{eff}}(m = 0, l = 0, \xi = 0)$ [M $\Omega$ /m]	$Z_y^{\text{eff}}(m = 0, l = 0, \xi = 0)$ [M $\Omega$ /m]
IR7 Phase-I (linear)	$9.309 - 272.321i$	$8.795 - 303.901i$
IR7 (nonlinear)	$9.068 - 120.62i$	$7.084 - 113.64i$
IR3	$1.955 - 38.841i$	$1.089 - 19.917i$
Others (tertiary)	$10.059 - 58.508i$	$9.19 - 47.8i$
RW (w/o collimators)	$41.272 - 8.334i$	$56.994 - 11.508i$
BB (w/o collimators)	$9.237 \times 10^{-6} - 2945.66i$	
	$\Delta Q_x(m = 0, l = 0, \xi = 0)$	$\Delta Q_y(m = 0, l = 0, \xi = 0)$
IR7 Phase-I (linear)	$-(6.637 + 0.197i) \times 10^{-4}$	$-(5.127 + 0.146i) \times 10^{-4}$
IR7 (nonlinear)	$-(2.662 + 0.174i) \times 10^{-4}$	$-(2.512 + 0.223i) \times 10^{-4}$
IR3	$-(0.2729 + 0.0217i) \times 10^{-4}$	$-(0.973 + 0.0375i) \times 10^{-4}$
Others (tertiary)	$-(1.259 + 0.222i) \times 10^{-4}$	$-(1.208 + 0.185i) \times 10^{-4}$
RW (w/o collimators)	$-(0.0867 + 0.43i) \times 10^{-4}$	$-(0.12 + 0.593i) \times 10^{-4}$
BB (w/o collimators)	$-(0.438 + 0.i) \times 10^{-4}$	

oscillation modes with negative imaginary tune shifts can be stabilized by this method.

In order to compare the complex transverse coherent tune shift generated by the collimator impedances from the nonlinear and the linear collimation system, we use the so-called stability diagrams, introduced first by J. S. Berg and F. Ruggiero [151]. This kind of diagrams represents the limits of the stable beam area in the  $[-\text{Im}(\Delta Q_{\perp})]$ – $[\text{Re}(\Delta Q_{\perp})]$  plane (or equivalently in the  $[\text{Re}(Z_{\perp})]$ – $[\text{Im}(Z_{\perp})]$  plane), granted by the octupole system.

Figure 6.22 compares the complex tune shift due to the impedances of the nonlinear IR7 and the linear IR7 systems with the Landau damping stability curves, assuming maximum available octupolar strength. The stable area is below the two curves in the figure. Figure 6.22 shows that the nonlinear system reduces the coherent tune shift by a factor 2–3, compared with the linear system.

Similarly, Figure 6.23 compares the tune shifts introduced by the nonlinear and linear IR7 plus the contribution of the IR3 insertion (momentum collimation) and other tertiary collimators in IR1, IR2, IR5, IR6 and IR8 for local protection. The contributions from BB impedance and RW impedance without collimators have also been added. Including all these contributions the nominal LHC beam may be unstable for both the linear and the nonlinear collimation systems in IR7 though in the latter case it is closer to the stability border.

The largest contribution to the real part of the remaining tune shift comes from the tertiary collimators and from resistive wall (see Table 6.4). Extending the nonlinear scheme and adding further nonlinear elements close to those tertiary collimators might move the maximum coherent

tune shift into the stable area for the nominal beam.

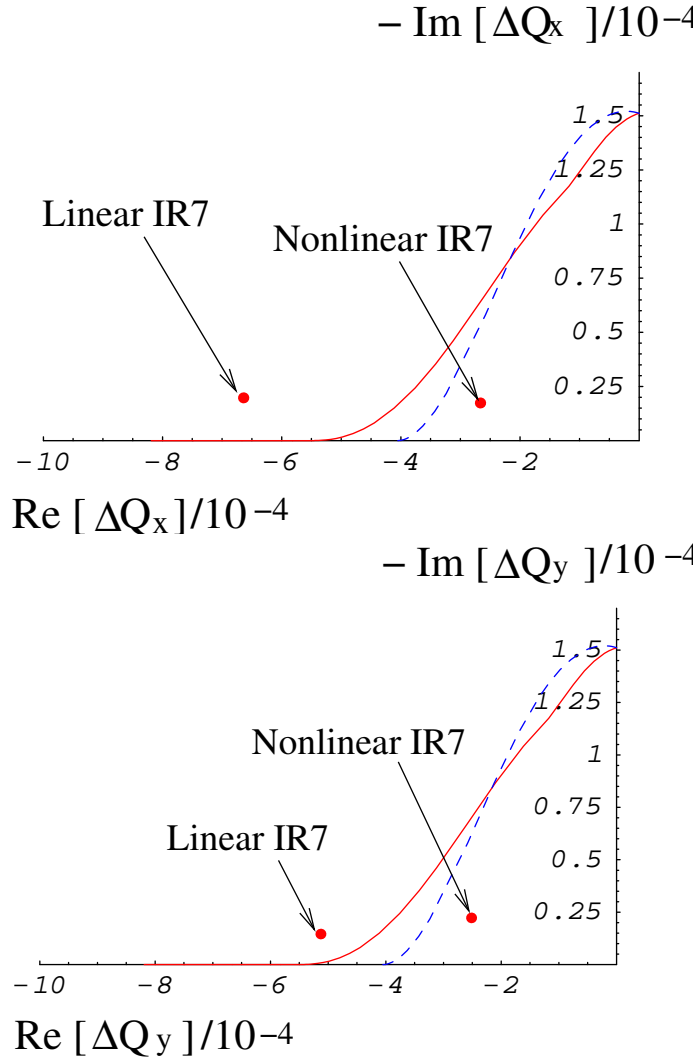


Figure 6.22: The transverse stability diagram in LHC at 7 TeV, with the nominal bunch population  $N = 1.15 \times 10^{11}$  protons. The horizontal and vertical axes represent the real part and the negative imaginary part of the transverse tune shift respectively (horizontal on the top and vertical on the bottom). The points for the nonlinear and linear collimation system are compared. The dashed (blue) curve is the stability for maximum Landau octupole current with negative anharmonicity; the solid (red) curve with positive anharmonicity.

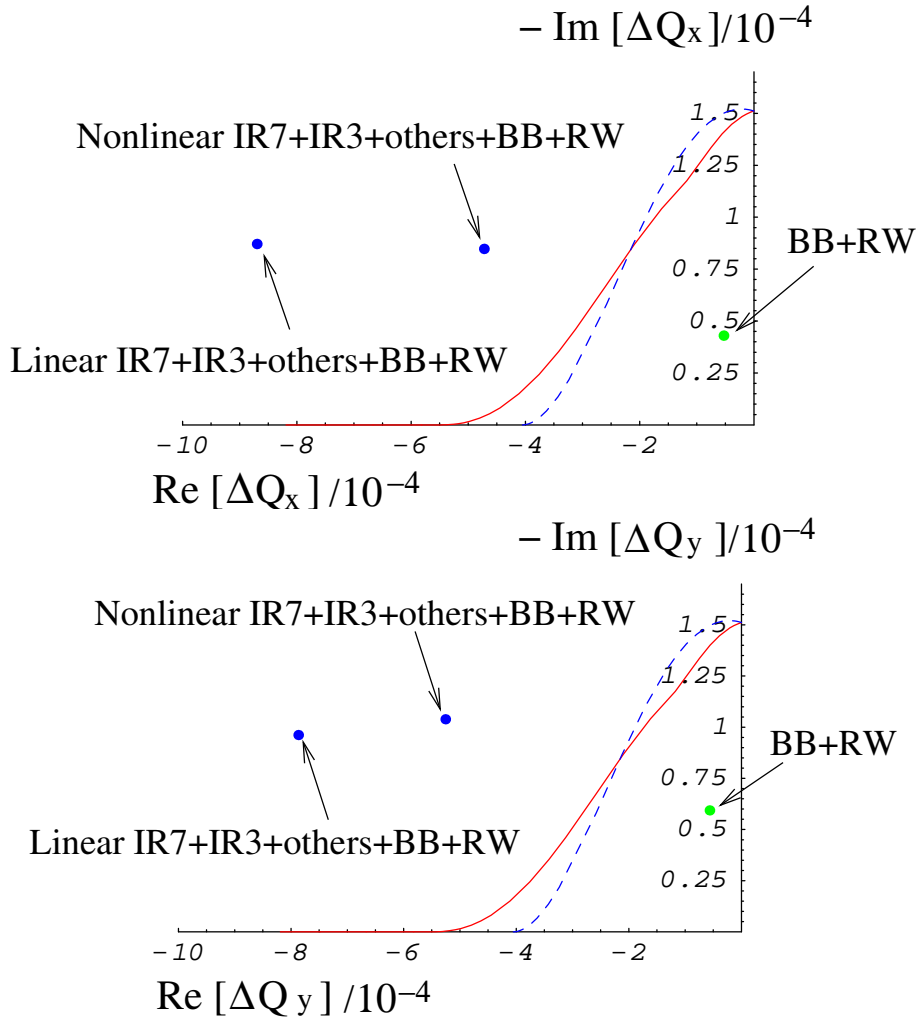


Figure 6.23: The transverse stability diagram in LHC at 7 TeV, with the nominal bunch population  $N = 1.15 \times 10^{11}$  protons. The horizontal and vertical axes represent the real part and the negative imaginary part of the transverse tune shift respectively (horizontal on the top and vertical on the bottom). The points compare the tune shift introduced by the nonlinear and the linear collimation systems, adding all contributions from Table ?? . The dashed (blue) curve is the stability for maximum Landau octupole current with negative anharmonicity; the solid (red) curve with positive anharmonicity.

# First Experimental Test on Nonlinear Collimation in the SPS

## 7.1 Introduction

The Super Proton Synchrotron (SPS) is the second biggest accelerator at CERN. The largest one will be the LHC, which will be supplied by a chain of proton accelerators (see Fig. 7.1). The SPS receives the proton beam from the PS (CERN Proton Synchrotron) at a energy of 26 GeV and will accelerate the beam up to 450 GeV in order to inject it into the LHC. Currently the SPS is an important experimental test bed for beam physics. It allows testing most of the beam design features which will later be required in the LHC.

A first experimental test of nonlinear collimation has been performed in the SPS at CERN on 8th November 2006. The aim of this chapter is to show some preliminary results from the analysis of the data recorded during this pioneering experiment.

## 7.2 Experimental setup

In order to demonstrate the required functionalities of the LHC collimator design, a prototype LHC Phase-I secondary collimator was installed in the SPS by the LHC Collimation Team in 2004 [152]. This collimator is still available for collimation related experiments in the SPS, and it has been used in the present test.

The extraction sextupoles of the SPS, which in normal operation are employed for the slow or resonant extraction of the beam, have been used to create nonlinear bumps in a region upstream of the collimator. Table 7.1 lists some relevant data for the SPS extraction sextupoles.

The main goal of this experiment was to study the sextupolar effect on the beam loss pattern

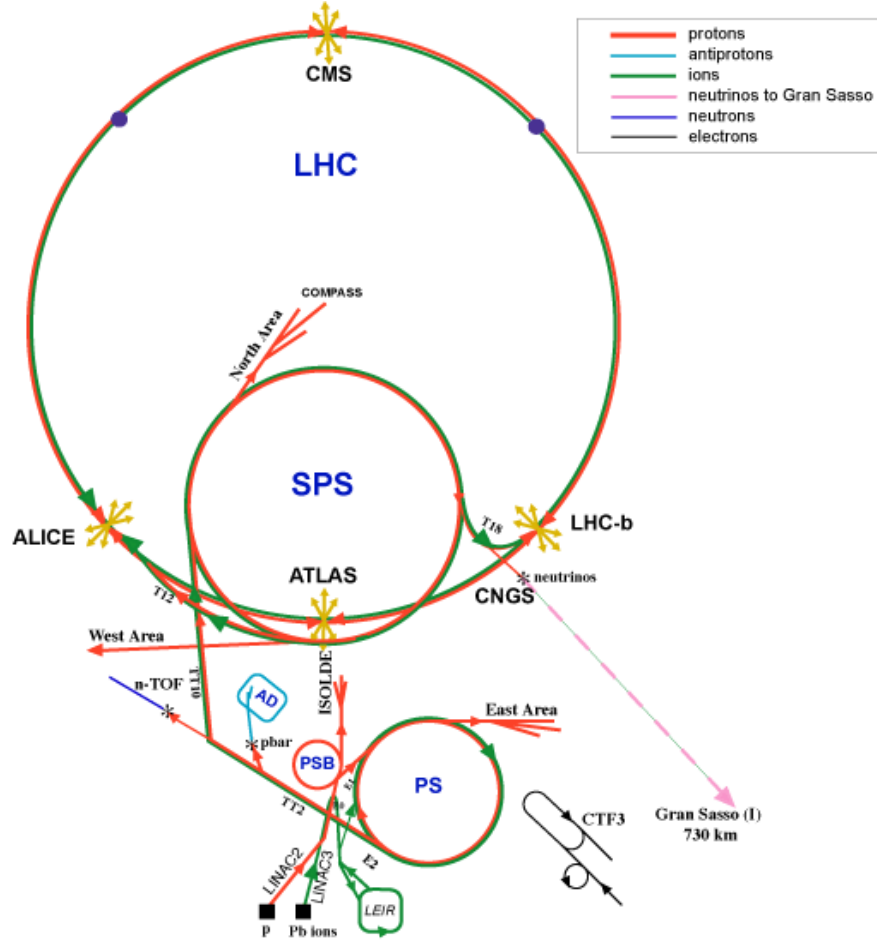


Figure 7.1: Accelerator complex in CERN.

Table 7.1: Relevant lattice parameters at the SPS extraction sextupoles.  $K_2$  is the integrated sextupole strength.

Name	$s$ [m]	$\beta_x$ [m]	$\mu_x$ [ $2\pi$ ]	$\beta_y$ [m]	$\mu_y$ [ $2\pi$ ]	$K_2$ [ $\text{m}^{-2}$ ]
LSE.10602	190.313	97.761	0.737	21.775	0.729	0.13875
LSE.12402	766.272	97.718	2.955	21.827	2.942	0.13875
LSE.20602	1342.231	97.748	5.173	21.797	5.158	0.13875
LSE.22402	1918.189	97.754	7.390	21.812	7.371	0.13875
LSE.40602	3646.065	97.663	14.047	21.782	14.018	-0.1665
LSN.42402	4222.023	97.764	16.265	21.864	16.233	-0.162
LSE.50602	4797.983	97.676	18.484	21.760	18.449	-0.111
LSE.52402	5373.941	97.780	20.703	21.866	20.664	-0.111

along the lattice. The beam parameters for the test are compiled in Table 7.2.

Table 7.2: SPS beam parameters for the nonlinear collimation test.

parameter	value
beam energy [GeV]	270
bunch population	$1.1 \times 10^{11}$
number of bunches	72
transverse norm. emittance [ $\mu\text{m}$ ]	$\sim 3$
longitudinal emittance [eV·s]	0.35

### 7.2.1 Sextupolar bumps

Using the Campbell-Baker-Hausdorf theorem (see Appendix A), the one turn map of an accelerator can be expressed as  $\mathcal{M} = e^{i\mathcal{H}}R$ , with  $\mathcal{H}$  the Hamiltonian kick. This Hamiltonian can be expanded in terms of Hamiltonian coefficients  $h_{jklm}$ , containing the contributions from all the multipoles of order  $n = j + k + l + m$ . The Hamiltonian coefficients coming from normal sextupoles are:  $h_{3000}$  and  $h_{2100}$ .

Alternatively the so-called Normal Form can be used for analyzing circular accelerators. It involves a change of coordinates that transforms the map into a simpler form. This change of coordinates is accomplished by a transformation  $e^{-iF}e^{i\mathcal{H}}Re^{iF}$ , where  $F$  is the generating function for the transformation. This function can be expressed as an expansion in generating function terms  $f_{jklm}$ , which are related to  $h_{jklm}$  via:

$$f_{jklm} = \frac{h_{jklm}}{1 - e^{-i2\pi[(j-k)Q_x + (l-m)Q_y]}} , \quad (7.1)$$

where  $Q_x$  and  $Q_y$  are the horizontal and the vertical tunes respectively. See for example [153] for a detailed introduction to the Normal Form applied to accelerators.

The eight sextupoles of extraction, listed in Table 7.1, have been used to excite the resonance terms  $f_{3000}$  and  $f_{2100}$ . Figure 7.2 represents both of these sextupolar terms along the lattice. The higher peaks correspond to  $f_{2100}$ .

### 7.2.2 The Beam Loss Monitor (BLM) data acquisition system

A total number of 216 BLMs (one for each of the 36 quadrupoles of each SPS sextant) were installed around the vacuum chamber along the lattice in order to measure and record the losses of the circulating beam. The data from the BLMs' electronics are received by the control room computers and processed by a real-time plotting software [154].

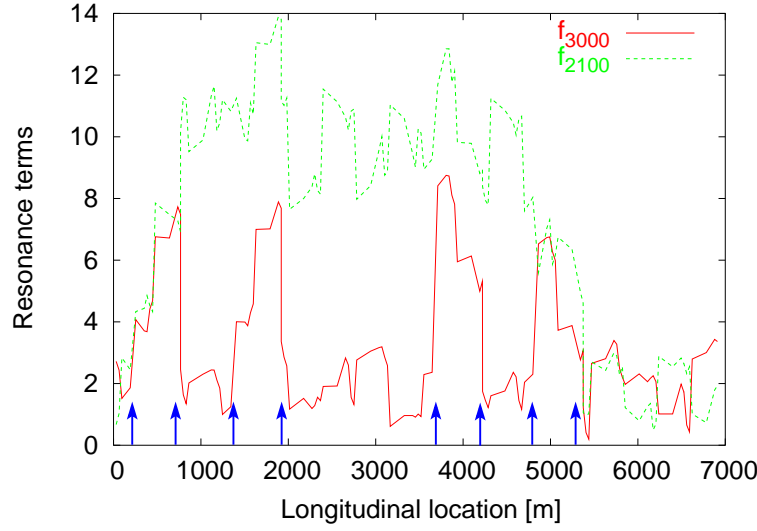


Figure 7.2: Generating function terms  $f_{3000}$  and  $f_{2100}$  along the SPS lattice. Courtesy of R. Tomás. The arrows indicate the positions of the extraction sextupoles.

### 7.2.3 Beam intensity during the test

The evolution of the beam current during the test is shown in Fig. 7.3. The upper horizontal axis in the figure represents the Central European Time (CET) during the development of the experiment. This started at approximately 4:18 h (CET), using an initial beam current of  $\approx 76 \times 10^{11}$  protons. During a first part (4:18–4:29 h), the sextupoles were switched off. The jaws of the collimator were then closed step by step in order to scrape the beam. Once the BLMs recorded a significant quantity of losses, we opened the jaws to the initial point, until the losses stopped. During a second part (from 4:29 h on), the sextupoles were switched on. Similar to before, the jaws were again moved until large losses were observed.

We have compared the loss maps of the two cases, and looked for important pattern differences.

## 7.3 Preliminary results

Important differences in the beam loss pattern are observed between the two cases with sextupoles switched-off and switched-on. It is worthwhile to mention that the same differences persisted at different times of the test run. For the two cases, we have found the following patterns:

- *Pattern of integrated beam loss maps with sextupoles OFF*: one can clearly distinguish four main loss peaks. The biggest one is located at the collimator position ( $\sim 5.2$  km). The others are registered upstream of the collimator position: at  $\sim 0.6$  km,  $\sim 1.7$  km and  $\sim 2.6$  km. It is necessary to point out that this pattern was repetitive when measured at different times



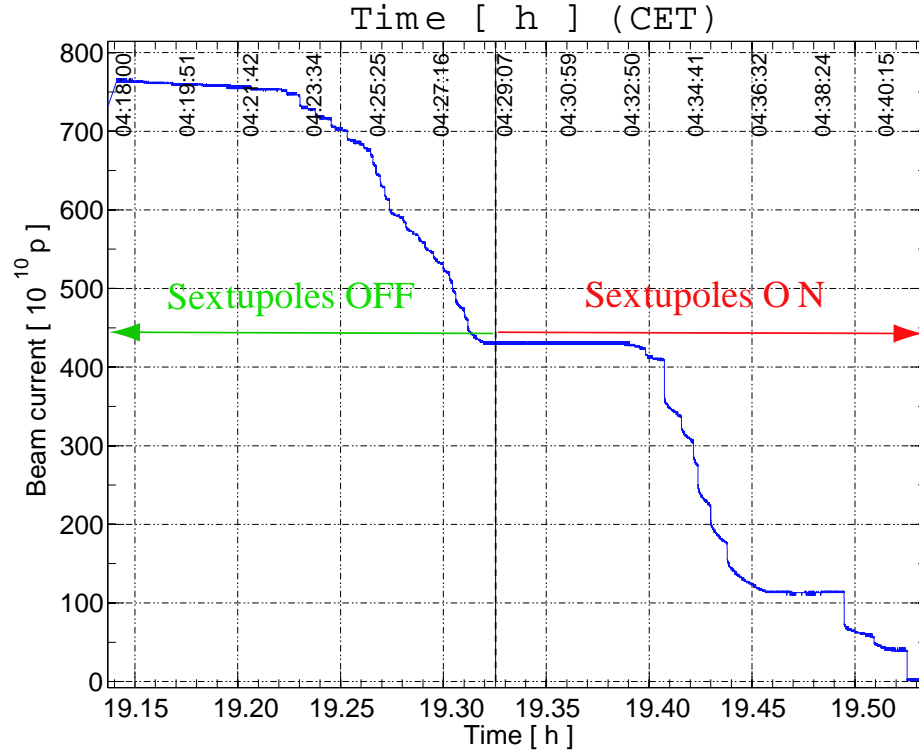


Figure 7.3: Beam current as a function of time (central european time (CET)) during the experiment, while the beam is being scraped with the collimator. The time intervals with sextupoles OFF and with sextupoles ON are indicated. The CET time is shown on the upper horizontal axis.

during the experiment. Two samples from different times are displayed in Fig. 7.4.

- *Pattern of integrated beam loss maps with sextupoles ON*: the loss peaks are observed at similar positions as in the previous case (with sextupoles OFF). Apart from this, additional peaks appear at positions where the sextupolar resonance term  $f_{2100}$  is high, and therefore they can be considered as peaks induced by the sextupolar effect. Fig. 7.5 and 7.6 show two example loss patterns recorded at different times.

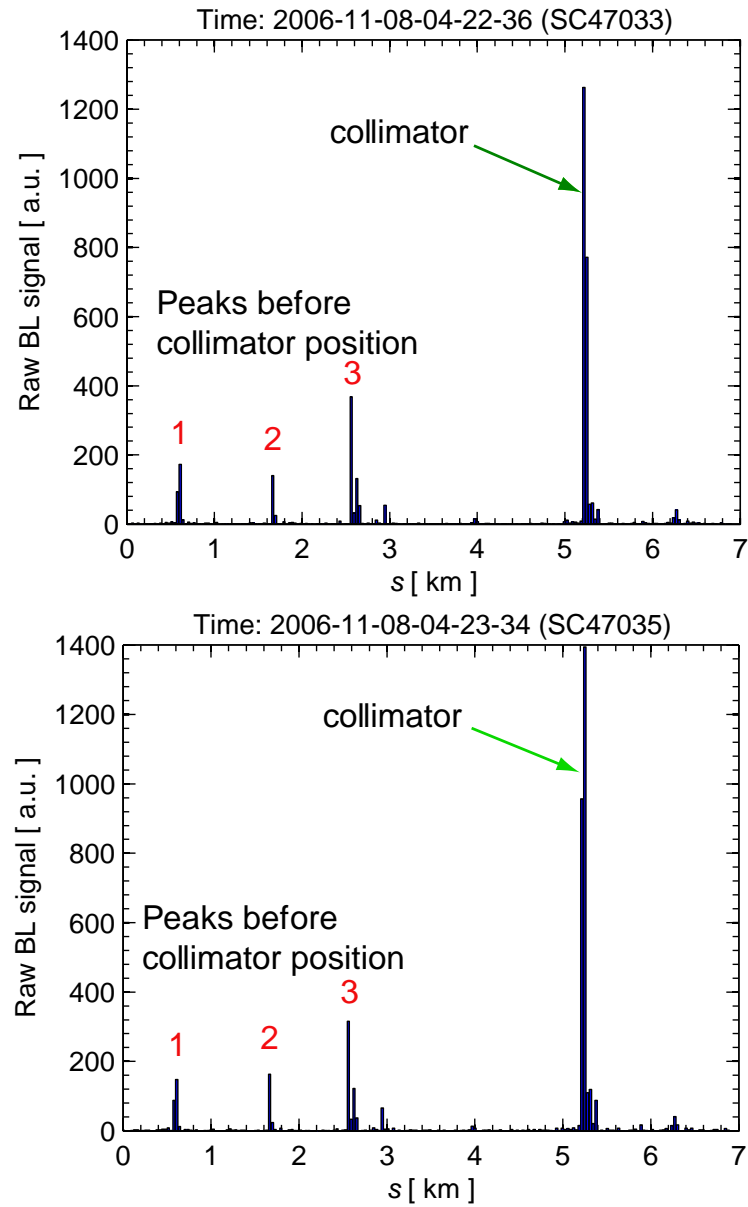


Figure 7.4: Measured loss map around the ring recorded by the BLMs at time 4:22:36 h (top). Integrated loss map at time 4:23:34 h (bottom). The sextupoles are switched off.

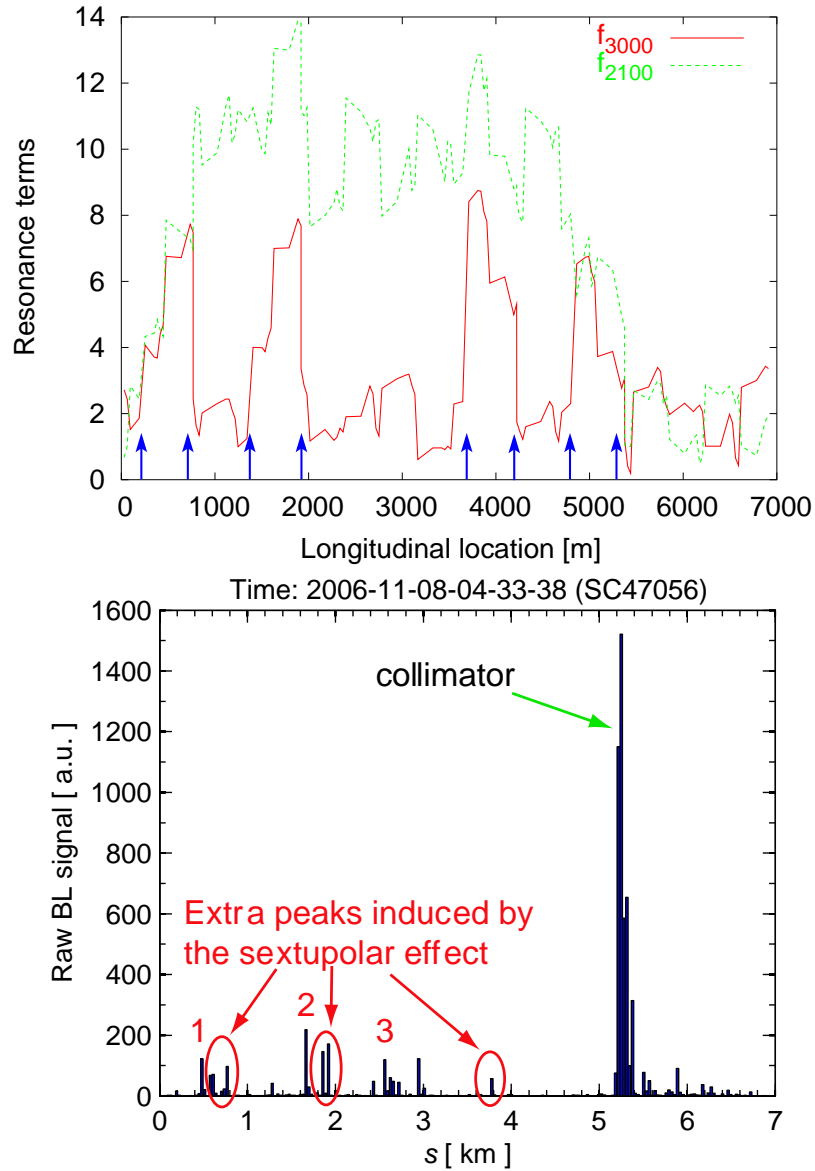


Figure 7.5: Measured loss map around the ring recorded at time 4:33:38 h (bottom), when the sextupoles were switched on. Note that extra loss peaks were registered at positions with large resonance term  $f_{2100}$  (top).

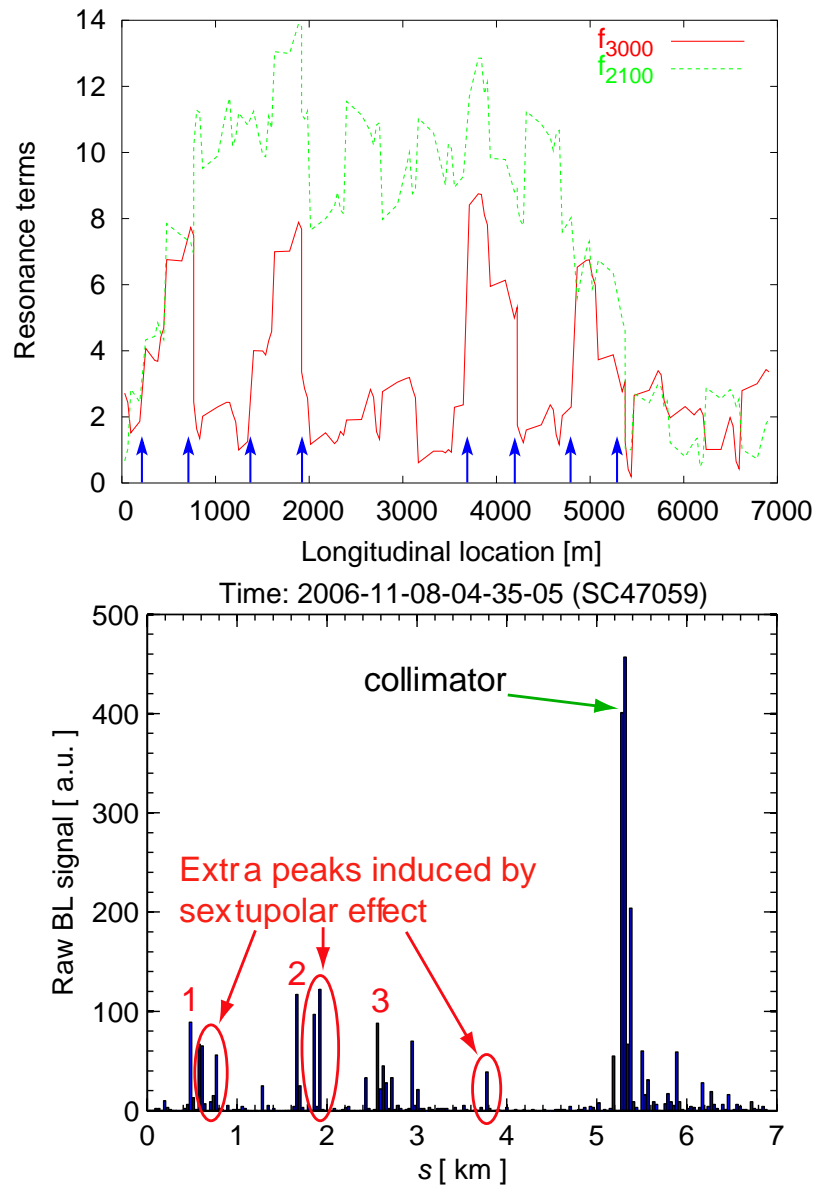


Figure 7.6: Measured loss map around the ring recorded at time 4:35:05 h (bottom), when the sextupoles were switched on. Note that extra loss peaks were registered at positions with large resonance term  $f_{2100}$  (top).

## Summary and Conclusions

The beam collimation systems are an essential part of the high energy colliders operating at center-of-mass energies around TeV, with high beam intensity and high luminosity. A collimation system should reduce the detector background at the interaction point by cleaning the beam halo particles. Another important function of the beam collimation is the machine protection against failure scenarios. Mis-steered or errant beams should be intercepted by the collimator system.

The mechanical and optics design of collimator systems is not simple, and they should fulfil some often conflicting constraints and requirements: high cleaning efficiency, high mechanical robustness, and low wakefields (impedances). Large wakefields effects and high optics aberrations may compromise the beam stability, reducing thereby the luminosity.

The conventional collimation systems are generally based on linear optics. Nevertheless, several alternative concepts of collimation have been proposed in the literature.

In this thesis report we have studied in detail nonlinear collimation systems for high energy colliders. These are based on a scheme with pair of skew sextupoles. It is important to point out that this nonlinear optics scheme is general, and it can be adapted to both linear and circular colliders.

In particular we have designed a nonlinear energy collimation system for CLIC. Its performance have been evaluated by means of tracking studies using the codes MAD, and PLACET. The luminosity has been computed using the beam-beam interaction code Guinea-Pig. This system fulfils the function of machine protection against mis-steered or errant beams with energy offset  $\gtrsim 1.5\%$ . Other important feature of this system is the spoiler survival in case of direct beam impact of a beam with a centroid energy error  $\gtrsim 1.5\%$ . By the sextupolar effect the beam transverse energy density is reduced at the energy spoiler, increasing thereby the spoiler survival probability.

The optics of the CLIC nonlinear collimation system has further been optimized by local correction of high order aberrations (2nd, 3rd and 4th order) using two additional nonlinear elements: a skew octupole and a normal sextupole. In this way we got a luminosity and energy bandwidth

comparable to those for the conventional linear optics.

The collimator wakefield effects on the luminosity due to the horizontal collimators misalignment are very similar for both linear and nonlinear systems. In this case similar luminosity acceptance curves have been obtained. However, the wakefield effects due to the vertical collimators misalignment are lower for the nonlinear collimator system, because of its higher betatronic collimator apertures.

Table 8.1 summarizes and compares the performance for both linear and nonlinear collimation systems.

Table 8.1: Summary of the performance of the nonlinear collimation system #4 versus the linear collimation system for CLIC.

	<b>nonlinear collimation #4</b>	<b>linear collimation</b>
Length [km]	2.0	2.0
Luminosity [ $\times 10^{34} \text{ cm}^{-2} \text{ s}^{-1}$ ]	5.1	7.0
Energy bandwidth	$-0.5 \% \lesssim \delta_0 \lesssim +0.5 \%$	$-0.5 \% \lesssim \delta_0 \lesssim +0.5 \%$
Transverse beam spot size at spoiler ( $\delta_0 = 1.5 \%$ ) $\sigma_{r,\text{rms}} = \sqrt{\sigma_{x,\text{sp}}\sigma_{y,\text{sp}}} [\mu\text{m}]$	470.544	150.241
Transverse energy density at spoiler ( $\delta_0 = 1.5 \%$ ) $\max(\rho_E(x, y)) [\text{KJ}/(\text{mm}^2 \text{ bunch})]$	12.659	30.08
Cleaning inefficiency $\eta_l$ for horizontal halo	$10^{-5} \lesssim \eta_l \lesssim 10^{-2}$	$10^{-5} \lesssim \eta_l \lesssim 10^{-2}$
Cleaning inefficiency $\eta_l$ for vertical halo	$10^{-2} \lesssim \eta_l \lesssim 10^{-1}$	$\sim 10^{-4}$
Wakefield jitter amplification $A_\beta$	0.000144 (vertical)	0.000505 (horizontal)
Wakefield jitter amplification $A_\delta$ ( $\delta_0 = 1 \%$ )	0.298 (vertical)	0.0668 (horizontal)

Since the collimation requirements for linear colliders designed to operate at center-of-mass energy around TeV are similar to those for the LHC, it is thus a close thought to apply a similar LHC nonlinear collimation scheme as that designed for CLIC. We have explored this possibility, and have presented an alternative nonlinear system for the Phase-II betatronic cleaning in the LHC. Its performance and cleaning efficiency have been studied by tracking using the code *Sixtrack*. By adjusting optics and collimator settings, we obtained a considerable improvement of the cleaning efficiency up to the level of the linear system for the vertical direction. However, a careful study is still necessary to further optimize the orientation and positions of secondary collimators to achieve the same level of efficiency as the linear system ( $\eta_c \lesssim 10^{-4}$ ) for the cleaning of the horizontal and radial halo components.

A nonlinear collimation system allows larger aperture for the mechanical jaws and thereby

reduces the collimator impedance. We have shown how the module of the horizontal effective impedance is reduced about a factor 2 and the vertical one about a factor 3 compared to the Phase-I IR7 insertion. Consequently, using the nonlinear collimation system, the coherent tune shift for the most critical coupled bunch mode has been reduced by about a factor 2 with respect to the Phase-I IR7 insertion.

A comparison of the features of the nonlinear collimation system IR7 and the linear collimation system IR7 of the LHC is summarized in Table 8.2.

Table 8.2: Summary of the performance of the nonlinear IR7 and the linear IR7 for the LHC.

	<b>nonlinear IR7</b>	<b>linear IR7</b>
Vertical primary collimator half gap $n_y$ [ $\sigma_y$ ]	8	6
Horizontal primary collimator half gap $n_x$ [ $\sigma_x$ ]	16	6
Cleaning inefficiency $\eta_c$ for vertical halo	$\approx 10^{-4}$	$\approx 2.5 \times 10^{-4}$
Cleaning inefficiency $\eta_c$ for horizontal halo	$\approx 2 \times 10^{-3}$	$\approx 2 \times 10^{-4}$
Cleaning inefficiency $\eta_c$ for radial halo	$\approx 4.5 \times 10^{-4}$	$\approx 1.5 \times 10^{-4}$
Hor. effective collimator impedance $ Z_x^{\text{eff}} $ [M $\Omega$ /m]	120.960	272.48
Vert. effective collimator impedance $ Z_y^{\text{eff}} $ [M $\Omega$ /m]	113.861	304.028
Hor. coherent coupled-bunch tune shift $ \Delta Q_x $	$2.668 \times 10^{-4}$	$6.64 \times 10^{-4}$
Vert. coherent coupled-bunch tune shift $ \Delta Q_y $	$2.522 \times 10^{-4}$	$5.129 \times 10^{-4}$

According to the results obtained for CLIC and LHC, we can conclude that a nonlinear collimation system using skew sextupoles for the case of linear and circular colliders appears to be competitive with the corresponding linear systems.

Finally, a first experimental test of nonlinear collimation has been performed in the SPS at CERN. For this experiment the SPS extraction sextupoles have been employed to create nonlinear bumps in a region upstream of a collimator. The goal has been to study the sextupolar effect in the pattern loss along the machine. Notable differences in the beam loss pattern have been observed between the two cases with sextupoles switched off and on. In the two cases, loss peaks are observed at similar positions. However, in the case with sextupoles switched on, additional peaks appear at positions where the created sextupolar resonances are large. Another goal of this experiment has been to inspire new ideas for performing more sophisticated tests in the future. These should be focused on the improvement of collimator cleaning efficiency using the extraction

sextupoles and a larger collimator aperture.



## Maps in accelerators

### A.1 Reference system

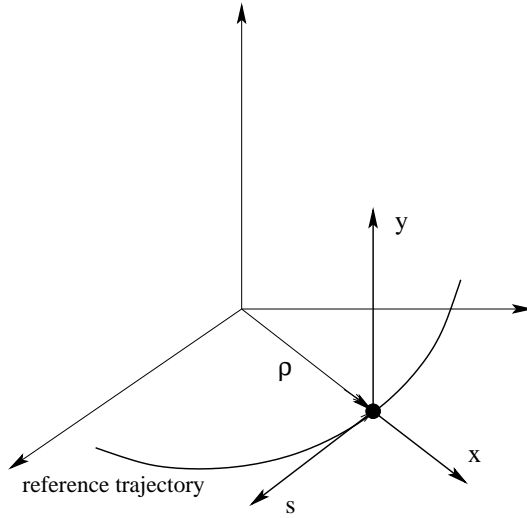


Figure A.1: Schematic of the coordinate system used to measure the particle positions.

Let  $z$  be a vector of six phase space variables,

$$z = (x, x', y, y', t, \delta) , \quad (\text{A.1})$$

which describes the particle motion in an accelerator. The coordinate system shown in Figure A.1 is generally used by convention for accelerators. The longitudinal coordinate  $s$  gives the particle location along the lattice and the local tangent to  $s$  points in the direction of the beam line. The

coordinates  $x$  and  $y$  measure the transverse horizontal and vertical (respectively) particle deviation from the ideal particle trajectory. The value  $t$  is the temporal coordinate and  $\delta$  the deviation of particle energy  $E$  with respect to the nominal energy  $E_0$ ,  $\delta \equiv (E - E_0)/E_0$ . Variations in slope of particle trajectories are denoted as  $x' \equiv dx/ds$  and  $y' \equiv dy/ds$ .

The beam transport between an initial lattice location  $z^i$  and a final lattice location  $z^f$  can be formally expressed through a transfer map  $\mathcal{M}$ ,

$$z^f = \mathcal{M}z^i . \quad (\text{A.2})$$

## A.2 Taylor maps

The transfer map  $\mathcal{M}$  has a Taylor representation [155]

$$z_j^f = \sum_k R_{jk} z_k^i + \sum_{k\ell} T_{jk\ell} z_k^i z_\ell^i + \sum_{k\ell m} U_{jk\ell m} z_k^i z_\ell^i z_m^i + \sum_{k\ell mn} V_{jk\ell mn} z_k^i z_\ell^i z_m^i z_n^i + \dots . \quad (\text{A.3})$$

The coefficients  $R_{jk}$  ( $j, k = 1, 2, \dots, 6$ ) are called first order matrix elements corresponding to the linear optics, which is composed of drifts, quadrupoles and dipoles. The quantities  $T_{jk\ell}$ ,  $U_{jk\ell m}$ ,  $V_{jk\ell mn}$ , etc., are called higher order transfer matrix elements, and contain the information about the optics aberrations of the lattice. For example, the second order matrix elements  $T_{jk\ell}$  describe the sextupole effects.

When a map  $\mathcal{M}$  has a jacobian matrix  $\mathbf{M}$  that is symplectic at all points, the map itself is said to be a symplectic map, i.e.,  $\mathbf{M}$  satisfies the matrix relations [156]

$$\tilde{\mathbf{M}}(z^i) \mathbf{J} \mathbf{M}(z^i) = \mathbf{J} , \quad (\text{A.4})$$

where  $\tilde{\mathbf{M}}$  denotes the transpose of  $\mathbf{M}$  and  $\mathbf{J}$  is a  $2n \times 2n$  matrix defined by the equation

$$\mathbf{J} = \begin{pmatrix} 0 & I \\ -I & 0 \end{pmatrix} , \quad (\text{A.5})$$

with  $I$  the  $n \times n$  identity matrix ( $n = 3$  in our case), and all other entries zero. A symplectic map is equivalent to a canonical transformation.

The truncated Taylor series has the disadvantage that it violates the symplectic condition [157, 158]. This violation is usually not important for studying single-pass systems such as final focus systems of linear collider, where have been shown that fourth order maps are usually sufficient [159]. However, it can be important for long-term particle tracking simulations such as following  $10^6$  to  $10^8$  turns in a storage ring [157].

### A.3 Lie algebra and symplectic maps

The map methods and the Lie algebra provide an extension of linear concepts into the nonlinear optics, including multipolar magnetics effects. See for example [157, 158, 161] for more details.

A symplectic map  $\mathcal{M}$  can be expressed by

$$\mathcal{M} = e^{i f \cdot} , \quad (\text{A.6})$$

where  $: f(z) :$  is a Lie operator defined by its action on a phase space function  $g(z)$ ,

$$: f(z) : g(z) = [f(z), g(z)] . \quad (\text{A.7})$$

The expression  $[f(z), g(z)]$  denotes the Poisson brackets of the functions  $f$  and  $g$ , i.e.,

$$[f(z), g(z)] = \sum_{i=1}^3 \frac{\partial f}{\partial q_i} \frac{\partial g}{\partial p_i} - \frac{\partial f}{\partial p_i} \frac{\partial g}{\partial q_i} , \quad (\text{A.8})$$

Here the phase space variables  $z = (x, x', y, y', t, \delta) \equiv (q_1, p_1, q_2, p_2, q_3, p_3)$  have been considered.

If  $: f :$ ,  $: g :$  and  $: h :$  are Lie operators, they satisfy the following relations:

- Antisymmetry:

$$[: f :, : g :] = -[: g :, : f :] . \quad (\text{A.9})$$

- Jacobi condition:

$$[: f :, [: g :, : h :]] + [: g :, [: h :, : f :]] + [: h :, [: f :, : g :]] = 0 . \quad (\text{A.10})$$

Then the Lie operators form a Lie algebra and the Poisson bracket operation can be viewed as the Lie product of this Lie algebra. Complementary rules can be found for example in Ref. [160].

The exponential  $e^{i f \cdot}$  is called the Lie transformation associated with the generator function  $f$ . The Lie transformation is also an operator and is formally defined by the exponential series:

$$e^{i f \cdot} = \sum_{n=0}^{\infty} \frac{[: f :]^n}{n!} . \quad (\text{A.11})$$

The action of  $e^{i f \cdot}$  on any function  $g$  is given by

$$e^{i f \cdot} g = g + [f, g] + \frac{1}{2} [f, [f, g]] + \cdots . \quad (\text{A.12})$$

Two remarkable properties of the Lie transformation are the exchange rule,

$$e^{i f \cdot} e^{i g \cdot} = e^{i g \cdot} e^{i e^{-i g \cdot} f \cdot} , \quad (\text{A.13})$$

and the Baker-Campbell-Hausdorff theorem,

$$e^{i f} e^{i g} = e^{i f + i g + \frac{1}{2} [f, g] + \frac{1}{12} [f, [f, g]] + \dots} \quad (\text{A.14})$$

Using the Dragt-Finn factorization theorem (which is well explained in Ref. [160]),  $\mathcal{M}$  can be factorized as

$$\mathcal{M} = e^{i f_1} e^{i f_2} e^{i f_3} \dots e^{i f_m} \dots, \quad (\text{A.15})$$

where the functions  $f_m$  are homogeneous polynomials of degree  $m$  in the variables of the vector  $z$ ,

$$f_m = f(q_i^m, p_j^m, q_i^m p_j^{m-n}, q_i^{m-n} p_j^n), \quad (\text{A.16})$$

with  $n < m$  and  $i, j = 1, 2, 3$ .

On a physical interpretation, the factor  $e^{i f_1}$  reproduces a translation in phase space as those produced by magnet misplacement errors and dipole powering errors; the factor  $e^{i f_2}$  produces linear transformation describing linear transport in drifts, quadrupoles and dipoles; the factor  $e^{i f_3}$  produces second and higher order aberrations terms describing the sextupole magnets effects;  $e^{i f_4}$  produces third and higher order aberrations describing the octupole magnets effects, etc. In general, the polynomials  $f_m$  describe aberrations of order  $(m - 1)$ .

If we does not consider the translation in phase space, the symplectic map  $\mathcal{M}$  can be factorized in a dynamic linear part and a nonlinear part:

$$\mathcal{M} = \mathcal{R} e^{i f_3} \dots e^{i f_n} \dots \quad (\text{A.17})$$

Here  $\mathcal{R}$  represents the linear matrix of elements  $R_{ij}$  ( $i, j = 1, 2, \dots, 6$ ) and the infinite product of Lie transformations  $e^{i f_m}$  ( $m = 3, 4, \dots$ ) represents the nonlinear part.

Unlike Taylor series, the factorized product of Eq. (A.17) can be truncated at any point while remaining symplectic. In relation to the Taylor map of Eq. (A.3),  $e^{i f_2}$  generates coefficients  $R_{ij}$ ;  $e^{i f_3}$  generates coefficients  $T_{jkl}$ ,  $U_{jklm}$ , etc.;  $e^{i f_4}$  generates  $U_{jklm}$ , etc. The coefficients  $R_{ij}$ ,  $T_{jkl}$ , etc. are strongly interrelated by a large number of nonlinear conditions, while the polynomials  $f_m$  are all independent.

It is easy to demonstrate that

$$[q_i^n, q_j] = 0, \quad (\text{A.18})$$

$$[p_i^n, p_j] = 0, \quad (\text{A.19})$$

$$[q_i^n, p_j] = n q_i^{n-1} \delta_{ij} \quad (\text{A.20})$$

$$[p_i^n, q_j] = -n p_i^{n-1} \delta_{ij} \quad (\text{A.21})$$

Taking into account the dependence of the functions  $f_n$  (see Eq. (A.16)), these expressions are

useful to evaluate easily the action of the Lie operator :  $f_n$  : on the phase space variables  $q_i$  and  $p_i$  .

### A.3.1 Examples

- **Drift:**

Consider the polynomial function  $f_2 = -l/2p^2$ , with  $l$  a parameter and  $p = x', y'$  the conjugated variables of  $q = x, y$  respectively. If we evaluate the transformation  $z^f = \mathcal{M}z^i$ , using Eqs. (A.12), (A.18), (A.19), (A.20) and (A.21) one finds:

$$q^f = e^{-\frac{l}{2}:p^2:} q^i = q^i - \frac{l}{2}[p^2, q^i] = q^i + lp^i , \quad (\text{A.22})$$

$$p^f = e^{-\frac{l}{2}:p^2:} p^i = p^i - \frac{l}{2}[p^2, p^i] = p^i . \quad (\text{A.23})$$

This result corresponds to the transfer map for a drift of length  $l$ .

- **Quadrupole:**

Consider  $f_2 = -k/2q^2$ , with  $k$  a parameter. Similarly, evaluating the transformation  $z^f = \mathcal{M}z^i$ , we find

$$q^f = e^{-\frac{k}{2}:q^2:} q^i = q^i - \frac{k}{2}[q^2, q^i] = q^i , \quad (\text{A.24})$$

$$p^f = e^{-\frac{k}{2}:q^2:} p^i = p^i - \frac{k}{2}[q^2, p^i] = p^i - kq . \quad (\text{A.25})$$

In this case, this corresponds to the transfer map for a quadrupole magnet of strength  $k$ .

- **Sextupole:**

Consider  $f_3 = k_s/3q^3$ , with  $k_s$  a parameter. One finds the following result:

$$q^f = e^{\frac{k_s}{3}:q^3:} q^i = q^i + \frac{k_s}{3}[q^3, q^i] = q^i , \quad (\text{A.26})$$

$$p^f = e^{\frac{k_s}{3}:q^3:} p^i = p^i + \frac{k_s}{3}[q^3, p^i] = p^i + k_sq^2 , \quad (\text{A.27})$$

which corresponds to the action of a sextupole magnet of strength  $k_s$  in the thin lens kick approximation.



# Appendix B

## Material properties

Table B.1: Table of material properties at room temperature:  $\varrho$  is the material density,  $C$  the specific heat,  $K$  the thermal conductivity, and  $\sigma$  the electrical conductivity. Data obtained from [?, ?, ?, 48].

<b>Material</b>	$\varrho$ [gm <sup>-3</sup> ]	$C$ [Jg <sup>-1</sup> K <sup>-1</sup> ]	$K$ [Wm <sup>-1</sup> K <sup>-1</sup> ]	$\sigma$ [ $\Omega^{-1}$ m <sup>-1</sup> ]
Be	$1.84 \times 10^6$	1.825	200	$1.67 \times 10^7$
C	$2.26 \times 10^6$	0.709	119-165	$7.27 \times 10^4$
Ti	$4.54 \times 10^6$	0.523	30.7	$2.0 \times 10^6$
Cu	$8.96 \times 10^6$	0.385	401	$6.0 \times 10^7$
W	$19.3 \times 10^6$	0.132	173	$1.81 \times 10^7$

Table B.2: Table of material properties:  $L_{\text{rad}}$  is the radiation length,  $L_{\text{rad}} \cdot (dE/dz)_{\text{min}}$  the minimum energy deposition for ionization per radiation length, and  $T_{\text{melt}}$  the melting point temperature. Data obtained from [48].

<b>Material</b>	$L_{\text{rad}}$ [m]	$L_{\text{rad}} \cdot (dE/dz)_{\text{min}}$ [MeV]	$T_{\text{melt}}$ [K]
Be	0.353	103.98	1560
C	0.188	74.38	3800
Ti	0.036	23.87	1941
Cu	0.014	18.04	1358
W	0.0035	7.74	3695





# Appendix C

## Horizontal beam size at the spoiler considering up to third order dispersion

In the next calculation we assume that the first order dispersion  $D_x$  is much higher than the transverse betatronic amplitudes  $x_\beta$  and  $y_\beta$  (additionally flat beams are assumed, i.e.  $x_\beta \gg y_\beta$ ) at the sextupoles and spoiler positions. If the second and third order dispersion,  $T_{166}$  and  $U_{1666}$  respectively in the transport notation of appendix A, then the horizontal mean squared position of particles is given by

$$\begin{aligned} \langle x_{\text{sp}}^2 \rangle \simeq & D_{x,\text{sp}}^2 \langle \delta^2 \rangle + R_{12}^2 K_s^2 D_{x,s}^2 \langle \delta^2 \rangle \langle x_{\beta,s}^2 \rangle + T_{166}^2 \langle \delta^4 \rangle + U_{1666}^2 \langle \delta^6 \rangle \\ & + 2T_{166} U_{1666} \langle \delta^5 \rangle + 2T_{166} D_{x,\text{sp}} \langle \delta^3 \rangle + 2U_{1666} D_{x,\text{sp}} \langle \delta^4 \rangle, \end{aligned} \quad (\text{C.1})$$

and the average horizontal beam offset is given by

$$\langle x_{\text{sp}} \rangle \simeq D_{x,\text{sp}} \langle \delta \rangle + T_{166} \langle \delta^2 \rangle + U_{1666} \langle \delta^3 \rangle. \quad (\text{C.2})$$

The angled brackets  $\langle \rangle$  indicate an average (or expectation) value. Let consider an arbitrary momentum distribution  $P(\delta)$ . From statistics we know that the raw moment of  $n$ th order can be computed by the integral

$$\langle \delta^n \rangle = \int_{-\infty}^{\infty} \delta^n P(\delta) d\delta, \quad (\text{C.3})$$

For instance, considering a *Gaussian distribution* with a width  $\sigma_\delta$  and with an average momentum offset  $\delta_0$ ,

$$P(\delta) = \frac{1}{\sqrt{2\pi}\sigma_\delta} e^{-1/2\left(\frac{\delta-\delta_0}{\sigma_\delta}\right)^2}, \quad (\text{C.4})$$

the six first raw moments are

$$\langle \delta \rangle = \delta_0, \quad (\text{C.5})$$

$$\langle \delta^2 \rangle = \sigma_\delta^2 + \delta_0, \quad (\text{C.6})$$

$$\langle \delta^3 \rangle = 3\sigma_\delta^2\delta_0 + \delta_0^3, \quad (\text{C.7})$$

$$\langle \delta^4 \rangle = 3\sigma_\delta^4 + 6\sigma_\delta^2\delta_0^2 + \delta_0^4, \quad (\text{C.8})$$

$$\langle \delta^5 \rangle = 15\sigma_\delta^4\delta_0 + 10\sigma_\delta^2\delta_0^3 + \delta_0^5, \quad (\text{C.9})$$

$$\langle \delta^6 \rangle = 15\sigma_\delta^6 + 45\sigma_\delta^4\delta_0^2 + 15\sigma_\delta^2\delta_0^4 + \delta_0^6. \quad (\text{C.10})$$

Next, using the expressions (C.1) and (C.2) and the above raw moments from expressions (C.5)–(C.6) we obtain the following horizontal rms beam size at the spoiler:

$$\begin{aligned} \sigma_{x,\text{sp}} \simeq & \left( D_{x,\text{sp}}^2 \sigma_\delta^2 + R_{12}^2 K_s^2 D_{x,s} (\sigma_\delta^2 + \delta_0^2) \beta_{y,s} \epsilon_y + 4D_{x,\text{sp}} T_{166} \sigma_\delta^2 \delta_0 \right. \\ & + 2T_{166}^2 (\sigma_\delta^4 + 2\sigma_\delta^2 \delta_0^2) + 9U_{166}^2 (3\sigma_\delta^6 + 4\sigma_\delta^4 \delta_0^2 + \sigma_\delta^2 \delta_0^4) \\ & \left. + 6D_{x,\text{sp}} U_{166} (\sigma_\delta^4 + 3\sigma_\delta^2 \delta_0^2) + 12T_{166} U_{166} (2\sigma_\delta^4 \delta_0 + \sigma_\delta^2 \delta_0^3) \right)^{1/2}, \quad (\text{C.11}) \end{aligned}$$

If we consider an *uniform distribution*

$$P(\delta) = \begin{cases} 0 & \text{for } \delta < -\frac{\delta_{\text{flat}}}{2} + \delta_0 \\ \frac{1}{\delta_{\text{flat}}} & \text{for } -\frac{\delta_{\text{flat}}}{2} + \delta_0 < \delta < \frac{\delta_{\text{flat}}}{2} + \delta_0 \\ 0 & \text{for } \delta > \frac{\delta_{\text{flat}}}{2} + \delta_0, \end{cases}$$

the raw moments of the distribution up to 6th order are

$$\langle \delta \rangle = \delta_0 , \quad (C.12)$$

$$\langle \delta^2 \rangle = \frac{\delta_{\text{flat}}^2}{12} + \delta_0^2 , \quad (C.13)$$

$$\langle \delta^3 \rangle = \frac{\delta_{\text{flat}}^2}{12} + \delta_0^2 , \quad (C.14)$$

$$\langle \delta^4 \rangle = \frac{\delta_{\text{flat}}^4}{80} + \frac{1}{2} \delta_{\text{flat}}^2 \delta_0^2 + \delta_0^4 , \quad (C.15)$$

$$\langle \delta^5 \rangle = \frac{\delta_{\text{flat}}^4 \delta_0}{16} + \frac{5}{6} \delta_{\text{flat}}^2 \delta_0^3 + \delta_0^5 , \quad (C.16)$$

$$\langle \delta^6 \rangle = \frac{\delta_{\text{flat}}^6}{448} + \frac{3}{16} \delta_{\text{flat}}^4 \delta_0^2 + \frac{5}{4} \delta_{\text{flat}}^2 \delta_0^4 + \delta_0^6 . \quad (C.17)$$

In this case we obtain the following horizontal rms beam size at the spoiler:

$$\begin{aligned} \sigma_{x,\text{sp}} \simeq & \left( D_{x,\text{sp}}^2 \frac{\delta_{\text{flat}}^2}{12} + R_{12}^2 K_s^2 D_{x,s}^2 \left( \frac{\delta_{\text{flat}}^2}{12} + \delta_0^2 \right) \beta_y \epsilon_y + 2T_{166} D_{x,\text{sp}} \frac{\delta_{\text{flat}}^2 \delta_0}{6} \right. \\ & + T_{166}^2 \left( \frac{\delta_{\text{flat}}^4}{180} + \frac{\delta_{\text{flat}}^2 \delta_0^2}{3} \right) + U_{166}^2 \left( \frac{\delta_{\text{flat}}^6}{448} + \frac{\delta_{\text{flat}}^4 \delta_0^2}{8} + \frac{3}{4} \delta_{\text{flat}}^2 \delta_0^4 \right) \\ & \left. + 2D_{x,\text{sp}} U_{166} \left( \frac{\delta_{\text{flat}}^4}{80} + \frac{\delta_{\text{flat}}^2 \delta_0^2}{4} \right) + 2T_{166} U_{166} \left( \frac{\delta_{\text{flat}}^4 \delta_0}{24} + \frac{\delta_{\text{flat}}^2 \delta_0^3}{2} \right) \right)^{1/2} . \quad (C.18) \end{aligned}$$



# Appendix D

## Baseline Phase-I Collimation Database at Collision (7 TeV)

Table D.1: Parameters of the collimators installed on the linear momentum collimation insertion **IR3** of the Beam line 1 at collision energy (7 TeV).

Name	Material	Length [m]	Azimuth [rad]	Half gap [mm]	Half gap [ $\sigma$ ]	$\beta_x$ [m]	$\beta_y$ [m]
Primary							
TCP.6L3.B1	C	0.6	0.000	3.862	15.0	133	142
Secondary							
TCSG.5L3.B1	C	1.0	0.000	2.986	18.0	55	295
TCSG.4R3.B1	C	1.0	0.000	2.066	18.0	26	403
TCSG.A5R3.B1	C	1.0	2.980	2.672	18.0	36	350
TCSG.B5R3.B1	C	1.0	0.189	2.995	18.0	46	318
Tertiary							
TCLA.A5R3.B1	W	1.0	1.571	5.959	20.0	144	179
TCLA.B5R3.B1	W	1.0	0.000	5.529	20.0	153	172
TCLA.6R3.B1	W	1.0	0.000	5.105	20.0	130	167
TCLA.7R3.B1	W	1.0	0.000	3.649	20.0	66	93

Table D.2: Parameters of the collimators installed on the linear betatron collimation insertion **IR7** of the Beam line 1 at collision energy (7 TeV).

#	Name	Material	Length [m]	Azimuth [rad]	Half gap [mm]	Half gap [ $\sigma$ ]	$\beta_x$ [m]	$\beta_y$ [m]
Primary								
1	TCP.D6L7.B1	C	0.6	1.571	1.178	6.0	169	73
2	TCP.C6L7.B1	C	0.6	0.000	1.668	6.0	160	78
3	TCP.B6L7.B1	C	0.6	2.225	1.394	6.0	152	82
Secondary								
6	TCSG.A6L7.B1	C	1.0	2.463	1.669	7.0	43	217
7	TCSG.B5L7.B1	C	1.0	2.504	1.981	7.0	147	163
8	TCSG.A5L7.B1	C	1.0	0.710	2.022	7.0	171	143
9	TCSG.D4L7.B1	C	1.0	1.571	1.307	7.0	307	70
11	TCSG.B4L7.B1	C	1.0	0.000	1.837	7.0	131	139
12	TCSG.A4L7.B1	C	1.0	2.349	1.824	7.0	121	149
13	TCSG.A4R7.B1	C	1.0	0.808	1.832	7.0	112	160
16	TCSG.B5R7.B1	C	1.0	2.470	2.107	7.0	131	273
18	TCSG.D5R7.B1	C	1.0	0.897	2.115	7.0	228	160
19	TCSG.E5R7.B1	C	1.0	2.277	2.118	7.0	257	137
20	TCSG.6R7.B1	C	1.0	0.009	2.897	7.0	353	45
Tertiary								
21	TCLA.A6R7.B1	W	1.0	1.571	1.539	10.0	312	45
22	TCLA.C6R7.B1	W	1.0	0.000	2.841	10.0	164	73
23	TCLA.E6R7.B1	W	1.0	1.571	2.772	10.0	66	151
24	TCLA.F6R7.B1	W	1.0	0.000	1.791	10.0	63	158
25	TCLA.A7R7.B1	W	1.0	0.000	1.763	10.0	60	149

Table D.3: Parameters of the collimators installed for local protection and cleaning at the low- $\beta$  triplets in the experimental insertions of the Beam line 1 at collision energy (7 TeV).

Name	Material	Length [m]	Azimuth [rad]	Half gap [mm]	Half gap [ $\sigma$ ]	$\beta_x$ [m]	$\beta_y$ [m]
IR1							
TCL.5R1.B1	Cu	1.0	0.000	2.894	10.0	132	926
TCTH.4L1.B1	W	1.0	0.000	7.551	8.3	1649	625
TCTV.4L1.B1	W	1.0	1.571	4.775	8.3	1654	659
IR2							
TCTH.4L2.B1	W	1.0	0.000	1.326	8.3	51	50
TDI.4L2	C	4.0	1.571	142.2	900.0	113	50
TCTV.4L2.B1	W	1.0	1.571	1.413	8.3	133	58
TCLIA.4R2	C	1.0	1.571	227.1	900.0	55	127
TCLIB.6R2	C	1.0	1.571	112.1	900.0	272	31
IR5							
TCTH.4L5.B1	W	1.0	0.000	7.551	8.3	1646	624
TCTV.4L5.B1	W	1.0	1.571	4.774	8.3	1652	658
TCL.5R5.B1	Cu	1.0	0.000	2.898	10.0	129	908
IR6							
TCDQA.4R6.B1	C	3.0	0.000	3.924	8.0	481	161
TCDQB.4R6.B1	C	3.0	0.000	3.968	8.0	492	165
TCSG.4R6.B1	C	1.0	0.000	3.766	7.5	504	169
IR8							
TCTH.4L8.B1	W	1.0	0.000	1.279	8.3	47	48
TCTV.4L8.B1	W	1.0	1.571	1.352	8.3	129	53





# Appendix E

## Nonlinear Collimation IR7 Database at Collision (7 TeV)

Table E.1: Parameters of the collimators installed on the nonlinear betatron collimation insertion **IR7** of the Beam line 1 at collision energy (7 TeV).

#	Name	Material	Length [m]	Azimuth [rad]	Half gap [mm]	Half gap [ $\sigma$ ]	$\beta_x$ [m]	$\beta_y$ [m]
Primary								
12	TCSG.A4L7.B1	C	0.6	0.000	3.318	16.0	86	73
13	TCSG.A4R7.B1	C	0.6	1.571	1.58	8.0	81	78
Secondary								
14	TCSG.B4R7.B1	C	1.0	1.571	2.796	9.0	66	193
15	TCSG.A5R7.B1	C	1.0	0.651	2.649	9.0	167	184
16	TCSG.B5R7.B1	C	1.0	2.47	2.737	9.0	195	169
17	TCSG.C5R7.B1	C	1.0	1.571	2.286	9.0	292	129
18	TCSG.D5R7.B1	C	1.0	0.897	2.843	9.0	329	117
19	TCSG.E5R7.B1	C	1.0	2.277	2.96	9.0	368	106
20	TCSG.6R7.B1	C	1.0	0.009	4.464	9.0	492	83
21	TCLA.A6R7.B1	W	1.0	1.571	1.972	9.0	434	96
22	TCLA.C6R7.B1	W	1.0	0.000	3.019	9.0	225	179
23	TCLA.E6R7.B1	W	1.0	1.571	2.778	7.0	82	315
24	TCLA.F6R7.B1	W	1.0	0.000	1.373	7.0	77	325
25	TCLA.A7R7.B1	W	1.0	0.000	1.222	7.0	61	276



# Coherent coupled-bunch head-tail tune shift

## F.1 Burov-Lebedev theory of linear resistive-wall wake field

In [146, 147] Burov and Lebedev (BL) calculated the linear resistive-wall impedance including the effect of the finite chamber thickness. They assumed that the beam wave length is large compared to the beam pipe inner aperture ( $c/\omega \gg a$ ), that the structure is long compared to the aperture ( $L \gg a$ ), and also the relativistic limit  $\beta_v \gamma \gg 1$  (here  $\beta_v$  is the relativistic ratio  $v/c$ , with  $v$  the particle velocity and  $c$  the speed of light). From the BL theory for a flat chamber (flat collimator) of thickness  $d$  with inner aperture  $a$  at an arbitrary transverse plane (1), surrounding by vacuum extending to infinity, the transverse resistive-wall impedance can be approximated by [146]

$$Z_{\perp(1)}^{\text{flat}}(\omega_k) \simeq -i \frac{\pi^2}{12} \frac{Z_0}{2\pi a^2} \frac{1}{1 + \tau/2} , \quad (\text{F.1})$$

with an accuracy better than 5 % for arbitrary  $0 \leq \tau \leq \infty$ , where  $\tau = \kappa a \tanh(\kappa d)$ , and  $|\kappa|a \gg 1$  is assumed. The value of  $\kappa$  is obtained from

$$\kappa = (i + \text{sgn}(\omega_k)) \sqrt{\frac{\mu_0 \sigma |\omega_k|}{2}} . \quad (\text{F.2})$$

The frequency  $\omega_k$  is given by  $\omega_k = \omega_\beta + k\omega_0 + m\omega_s$ , with  $-\infty \leq k \leq +\infty$  for a single bunch beam, and  $k = l + N_b k'$  with  $-\infty \leq k' \leq +\infty$  for a multi-bunch beam (such as in the case of the LHC). Here,  $\omega_\beta = Q_\beta \omega_0$ , with  $Q_\beta$  the unperturbed betatron tune and  $\omega_0 = 2\pi f_0$  the average revolution frequency of the particles and  $\omega_s = 2\pi f_s$  the synchrotron angular frequency. The number  $m = -\infty, \dots, -1, 0, 1, \dots, +\infty$  is called the *head-tail mode* number,  $l = 0, 1, \dots, N_b - 1$  the *coupled-bunch* mode and  $N_b$  the number of equi-populated equi-spaced bunches.

The impedance in a plane (2), orthogonal to the plane (1), can be obtained from the Yokoya prescription [162]  $Z_{\perp(2)}^{\text{flat}} = (1/2)Z_{\perp(1)}^{\text{flat}}$ , i.e.,

$$Z_{\perp(2)}^{\text{flat}} \simeq -i \frac{\pi^2}{24} \frac{Z_0}{2\pi a^2} \frac{1}{1 + \tau/2} . \quad (\text{F.3})$$

On the other hand, the transverse impedance of a round chamber (round collimator) can be obtained by dividing the expressions (F.1) and (F.3) with the factor  $\pi^2/12$  and  $\pi^2/24$  respectively [162], i.e.,

$$Z_{\perp(1)}^{\text{flat}} = \frac{\pi^2}{12} Z_{\perp}^{\text{round}} , \quad Z_{\perp(2)}^{\text{flat}} = \frac{\pi^2}{24} Z_{\perp}^{\text{round}} . \quad (\text{F.4})$$

## F.2 Coherent tune shift

Questions such as what modes are more critically excited by the impedance and the corresponding tune shift of these modes can be more directly addressed using the so-called effective impedance [148, 163], defined as

$$Z_{\perp}^{\text{eff}}(m, l, \xi) \equiv \frac{\sum_{k'=-\infty}^{+\infty} Z_{\perp}(\omega_{kl}) h_m(\omega_{kl} - \omega_{\xi})}{\sum_{k'=-\infty}^{+\infty} h_m(\omega_{kl} - \omega_{\xi})} , \quad (\text{F.5})$$

where the transverse impedance  $Z_{\perp}$  is essentially weighted by the beam power spectrum  $h_m$  for a head-tail mode number  $m$ . The frequency  $\omega_{kl}$  is given by  $\omega_{kl} = \omega_{\beta} + (l + N_b k')\omega_0 + m\omega_s$ . The variable  $\omega_{\xi} = \xi\omega_{\beta}/\eta$  is the transverse chromatic frequency, which is a function of the chromaticity  $\xi$ , the betatron frequency  $\omega_{\beta}$  and the slippage factor  $\eta = (\Delta T/T_0)(\Delta p/p_0)$ , with  $T$  and  $p$  the revolution period and the momentum of the particle respectively. In the case of a gaussian beam,

$$h_m(\omega) = \left( \frac{\omega \sigma_z}{c} \right)^{2m} e^{-\omega^2 \sigma_z^2 / c^2} . \quad (\text{F.6})$$

Figure F.1 shows the power spectrum of a gaussian beam for the first three head-tail modes  $m = 0, 1$  and 2 depending on the coupled-bunch mode  $l$

The transverse coherent tune shift because of the collimator impedances can be calculated in terms of the effective impedance (F.5) by using the following expression [148]:

$$\Delta Q_{\perp}(m, l, \xi) = -i \frac{N_b N_e \omega_0 \beta_{\perp}}{8\pi^2 E} \frac{\Gamma(m + \frac{1}{2})}{2^m m!} Z_{\text{eff}}(m, l, \xi) , \quad (\text{F.7})$$

where  $N$  is the number of particles per bunch and  $E$  the nominal beam energy.

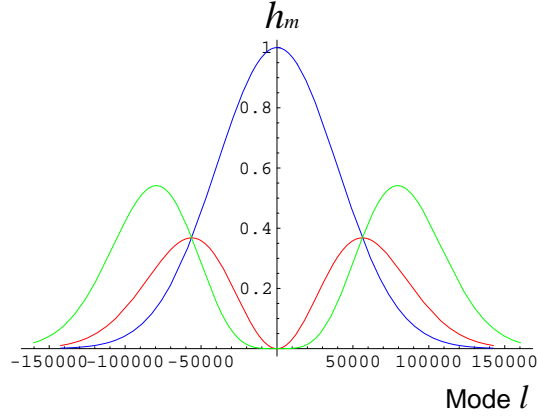


Figure F.1: Transverse power spectrum for the first three head-tail modes  $m = 0$  (blue),  $m = 1$  (red) and  $m = 2$  (green), assuming  $\xi = 0$  and  $p = 0$ , versus the coupled-bunch mode number  $l$ .

### F.3 Tilted collimator contribution

#### F.3.1 The transverse tensor impedance

In order to calculate the impedance contribution from a skew collimator, rotated by an angle  $\alpha$  around the longitudinal axis  $z$ , we use the tensor impedance [164]

$$\mathbf{Z}_{\perp} = \mathbf{R}^{-1} \mathbf{Z}'_{\perp} \mathbf{R} = \begin{pmatrix} Z_x & Z_{xy} \\ Z_{yx} & Z_y \end{pmatrix}, \quad (\text{F.8})$$

with the following matrix elements:

$$Z_x = Z_{\perp(1)} \cos^2 \alpha + Z_{\perp(2)} \sin^2 \alpha, \quad (\text{F.9})$$

$$Z_y = Z_{\perp(2)} \cos^2 \alpha + Z_{\perp(1)} \sin^2 \alpha, \quad (\text{F.10})$$

$$Z_{xy} \equiv Z_{yx} = (Z_{\perp(1)} - Z_{\perp(2)}) \sin \alpha \cos \alpha. \quad (\text{F.11})$$

Here,  $\mathbf{Z}'_{\perp}$  is the tensor impedance diagonalized in a frame rotated by angle  $\alpha$  around the axis  $z$ , i.e.,

$$\mathbf{Z}'_{\perp} = \begin{pmatrix} Z_{\perp(1)} & 0 \\ 0 & Z_{\perp(2)} \end{pmatrix}, \quad (\text{F.12})$$

and  $\mathbf{R}$  is the usual  $2 \times 2$  rotation matrix

$$\mathbf{R} = \begin{pmatrix} \cos \alpha & \sin \alpha \\ -\sin \alpha & \cos \alpha \end{pmatrix}. \quad (\text{F.13})$$

For instance, for a horizontal collimator ( $\alpha = 0$ ) one has  $\mathbf{Z}_{\perp}(\alpha = 0) = \mathbf{Z}'_{\perp}$ , and for a vertical

collimator  $Z'_\perp(\alpha = \pi/2) = \text{adj}\{\mathbf{Z}'_\perp\}$ .

### F.3.2 The tensor tune shift

The corresponding tune shift tensor is given by

$$\Delta\mathbf{Q}_\perp = -i \frac{N_b N e \omega_0}{8\pi^2 E} \beta_\perp^{1/2} \mathbf{Z}_\perp \beta_\perp^{1/2}, \quad (\text{F.14})$$

where

$$\beta_\perp = \begin{pmatrix} \beta_x & 0 \\ 0 & \beta_y \end{pmatrix} \quad (\text{F.15})$$

defines the diagonal matrix of the betatron functions,  $\beta_x$  and  $\beta_y$  for the horizontal and vertical plane respectively.

If we consider a collimator in an arbitrary plane (1), whose impedance contribution is  $Z_{\perp(1)}$ , using the same prescription [162] as in Eq. (F.3), the collimator impedance at the corresponding orthogonal plane (2) can be obtained from the relation  $Z_{\perp(2)} = (1/2)Z_{\perp(1)}$ . Therefore, one can calculate the transverse coherent tune shift contribution from a collimator rotated an arbitrary angle  $\alpha$  using the following expression:

$$\Delta\mathbf{Q}_\perp = \begin{pmatrix} \Delta Q_x & \Delta Q_{xy} \\ \Delta Q_{yx} & \Delta Q_y \end{pmatrix}, \quad (\text{F.16})$$

with the following matrix elements:

$$\Delta Q_x = -i \frac{N_b N e \omega_0}{8\pi^2 E} \beta_x (\cos^2 \alpha + \frac{1}{2} \sin^2 \alpha) Z_{\perp(1)}, \quad (\text{F.17})$$

$$\Delta Q_y = -i \frac{N_b N e \omega_0}{8\pi^2 E} \beta_y (\frac{1}{2} \cos^2 \alpha + \sin^2 \alpha) Z_{\perp(1)}, \quad (\text{F.18})$$

$$\Delta Q_{xy} = -i \frac{N_b N e \omega_0}{8\pi^2 E} \frac{\sqrt{\beta_x \beta_y}}{2} \sin \alpha \cos \alpha Z_{\perp(1)}. \quad (\text{F.19})$$

The non-diagonal element  $\Delta Q_{xy} \equiv \Delta Q_{yx}$  corresponds to a coupling term, which would be compensated by the incoherent tune shift [164].

It is worthwhile to notice that in Eqs. (F.17), (F.18) and (F.19) the impedance  $Z_{\perp(1)}$  can be replaced by a more general effective impedance for an arbitrary head-tail mode  $m$ , adding a normalization factor  $\Gamma(m + 1/2)/(2^m m!)$ , such as in Eqs. (F.5) and (F.7).

# Bibliography

- [1] LHC Design Report, CERN-2004-003 (2004). See also <http://www.cern.ch/lhc>.
- [2] ILC Reference Design Report, [http://media.linearcollider.org/rdr\\_draft\\_v1.pdf](http://media.linearcollider.org/rdr_draft_v1.pdf).
- [3] M. Battaglia, *et al.*, “Physics at the CLIC-TeV Linear Collider: report of the CLIC Physics Working Group”, CERN-2004-005; hep-ph/0412251 (2004).
- [4] W. R. Assmann, *et al.*, “A 3 TeV  $e^+ / e^-$  Linear Collider based on CLIC technology”, CERN-2000-008 (2000); see also [http://ab-div.web.cern.ch/ab-div/Info/2006/CLIC\\_Web\\_Site/publication.htm](http://ab-div.web.cern.ch/ab-div/Info/2006/CLIC_Web_Site/publication.htm).
- [5] N. Phinney, “SLC final performance and lessons”, in *Proceedings of the 20th Intl. Linac Conference LINAC 2000*, Ed. A. W. Chao, eConf C00082 (2000) MO102, arXiv:physics/0010008.
- [6] LEP Design Report, Vol III, LEP2, CERN-AC/96-01 (LEP2), June 1996.
- [7] R. Assmann *et al.*, “Collimators and Cleaning, Could this Limit the LHC Performance?,” LHC Project Workshop-’Chamonix XII’ (2003). “Designing and Building a Collimation System for the High-Intensity LHC Beam,” PAC2003, Oregon, 2003.
- [8] R. W. Assmann, “The Final Collimation System for the LHC”, in *Proceedings of EPAC2006*, Edinburgh, 2006.
- [9] R. Assmann *et al.*, “Collimation for CLIC”, CERN-AB-2003-075 (2003).
- [10] M. Aleksa, “CLIC Beam Delivery System”, *Presented at the 26th Advanced ICFA Beam Dynamics Workshop on Nanometre-Size Colliding Beams (Nanobeam2002)*, Lausanne, September, 2002; CLIC Note 551.
- [11] R. Appleby, *et al.*, EuroTeV report 2006-001-01.

- [12] C. Adolphsen, *et al.*, “Zeroth-Order Design Report for the Next Linear Collider”, SLAC Report 474 (1996); LBNL-5424 (1996).
- [13] O. Napoly, “Collimation Depth Requirements for the TESLA Interaction Region”, DAPNIA/SEA-01-02 (2001); DESY TESLA-01-18 (2001).
- [14] P. Raimondi and A. Seryi, “Novel Final Focus Design for Future Linear Colliders”, Phys. Rev. Lett. **86** (2000) 3779.
- [15] R. Brinkmann, N. J. Walker and G. A. Blair, “The TESLA Post-linac Collimation System,” DESY TESLA-01-12 (2001).
- [16] NLC Post-Linac Collimation Task Force, “New Post-Linac Collimation System for the Next Linear Collider”, LCC-Note-0052, 2001.
- [17] T. Trenkler and J. B. Jeanneret, Particles Accelerators **50** (1995) 285.
- [18] J. B. Jeanneret, “Optics of a two-stage collimation system,” Phys. Rev. ST Accel. Beams **1** (1998) 081001.
- [19] J. Frisch, E. Doyle, K. Skarpaas, “Advanced Collimator Prototype Results for the NLC”, SLAC-PUB-8463 (2000).
- [20] Y. Cai, *et al.*, “RC1 Conceptual Design Report”, see the web:  
<https://dms.uslarp.org/AcceleratorSystems/Collimation/Phase2/RotatingCollimatorRD>.
- [21] A. G. Afonin, *et al.*, Phys. Lett. B **435**, 240 (1998).
- [22] A. G. Afonin, *et al.*, in *Proceedings of PAC 1999*,
- [23] G. Arduini, *et al.*, Phys. Rev. Lett. **79**, (1997) 4182.
- [24] R. P. Fliller, *et al.*, Phys. Rev. ST AB **9**, (2006) 013501.
- [25] R. A. Carrigan, *et al.*, Fermilab-Conf-06-306-AD (2006).
- [26] W. Scandale, “H8-RD22 Experiment to test Crystal Collimation for the LHC”, INFN CSN1 Meeting, Frascati, 28 November 2006, see the presentation in the web: <http://care-hhh.web.cern.ch/care-hhh/publications.htm>.
- [27] A. M. Taratin and S. A. Vorobiev, Phys. Lett. A **119** (1987) 425; and A. M. Taratin and S. A. Vorobiev, NIM in PR B **26** (1987) 512.
- [28] F. Zimmermann, *et al.*, “New Final Focus Concepts at 5TeV and Beyond”, in *Proceedings of 8th Workshop on Advanced Accelerator Concepts*, Baltimore, Maryland, USA, 5–11 July, 1998; SLAC-PUB-7883.



- [29] V. Shiltsev, *et al.*, in *Proceedings of PAC 2005*, Knoxville, TN, USA, pp. 2083.
- [30] V. Shiltsev, “LHC Electron Lenses: What Are They Good For?”, to be published in *Proceedings of LHC-LUMI 2006*, Valencia, 16-20 October 2006.
- [31] N. Merminga *et al.*, “Collimation Systems in the Next Linear Collider”, SLAC-PUB-5436 (1991).
- [32] N. Merminga *et al.*, “Optimizing a Nonlinear Collimation System for Future Linear Colliders”, SLAC-PUB-5507 (1991).
- [33] N. Merminga, *et al.*, “Collimation systems for a TeV linear collider”, Part. Accel. **48** (1994), 85; SLAC-PUB-5165, May 1994.
- [34] F. Zimmermann, NLC Acc. Phys. Note, July 14, 1998.
- [35] R. Pitthan, SLAC-PUB-8402, 1999.
- [36] R. Brinkmann, *Proceedings of BDIR2000 workshop*, 2000.
- [37] R. Brinkmann, P. Raimondi, and A. Seryi, “Halo Reduction by Means of Non Linear Optical Elements in the NLC Final Focus System”, in *Proceedings of PAC2001*, Chicago, USA, 2001.
- [38] K. Thompson, R. Pitthan, F. Zimmermann, *et al.*, “NLC Collimation Meetings, in particular 22.05.98, 29.05.98, and 31.08.98; see the web side: <http://www-project.slac.stanford.edu/lc/bdir/meetings-collimation.asp>.
- [39] A. Faus-Golfe, and F. Zimmermann, “A Nonlinear Collimation System for CLIC”, CERN-SL-2002-032 (AP), CLIC Note 52.
- [40] H. Burkhardt and R. Kleiss, “Beam Lifetime in LEP”, in *Proceedings of the EPAC 1994*, pp. 1353 (1994).
- [41] H. Burkhardt, “Beam Tails in LEP”, in *Proceedings of EPAC96*, Sitges, Spain, 1996.
- [42] I. Reichel, “Study of Transverse Beam Tails at LEP”, CERN-Thesis-98-017 (1998).
- [43] I. Reichel, “Transverse Beam Tails at LEP”, in *Proceedings of ICFA Beam Dynamics Workshop on  $e^+e^-$  Factories*, Frascati, 1997, Ed. by L. Palumbo, G. Vignola (Frascati Phys. Series, Vol. X, Frascati, 1997).
- [44] P. Tenenbaum, T. O. Raubenheimer and M. Woodley, “Sources of Beam Halo in the Next Linear Collider Main Linac”, in *Proceedings of PAC 2001*, Illinois, USA, 2001; SLAC-PUB-8935 (2001).

- [45] Nuria Catalan-Lasheras, “Transverse and Longitudinal Beam Collimation in a High-Energy proton Collider (LHC)”, PhD Thesis, CERN-THESIS-2000-019.
- [46] R. Cimino, *et al.*, “Can Low-Energy Electrons affect High-Energy Physics Accelerators?”, *Phys. Rev. Lett.* **93** (2004) 014801.
- [47] E. Benedetto, G. Franchetti, and F. Zimmermann, “Incoherent effects of electron clouds in proton storage rings”, *Phys. Rev. Lett.* **97** (2006) 034801.
- [48] Particle Data Group, *Journal of Physics G* **33** (2006) 1.
- [49] H. Burkhardt, I. Reichel, and G. Roy, “Transverse beam tails due to inelastic scattering”, *Phys. Rev. ST-AB* **3** (2000) 091001.
- [50] A. W. Thomas, and W. Weise, “The Structure of the Nucleon”, Wiley-VCH, 2001.
- [51] A. Drozdin, *et al.*, “Backgrounds in the Tevatron Collider Detectors due to Nuclear Elastic Beam-Gas Scattering”, in *Proceedings of PAC2003*, Portland, Oregon, USA, 2003.
- [52] A. Schiz, *et al.*, *Phys. Rev. D* **21** (1980) 3010.
- [53] A.F. Martini, M. J. Menon and J. Montanha, “Correlations between total cross sections and slopes”, *Brazilian Journal of Physics* **34** (2004) 263.
- [54] TOTEM collaboration, “Total cross section, elastic scattering and diffraction dissociation at the LHC”, CERN/LHCC 97-49, pp. 10-21, 1997.
- [55] W.-M. Yao *et al.*, Particle Data Group: “Plots of cross sections and related quantities”, *J. Phys. G* **33** (2006).
- [56] H. Bethe, and J. Ashkin, “Experimental Nuclear Physics, Vol. 1, edited by E. Segre (Wiley, New York, 1953), p. 166.
- [57] W. R. Leo, “Techniques for Nuclear and Particle Physics Experiments, A How-to Approach”, Springer-Verlag, 1994.
- [58] A. N. Kalinovskii, N. V. Mokhov, and Yu. P. Nikitin, “Passage of High -Energy Particles through Matter, AIP (1989).
- [59] K. Goulios, “Diffractive interactions of hadrons at high energies”, *Physics Reports* **101** (1983) 171.
- [60] T. J. Roberts, *et al.*, “Neutron-nucleus inelastic cross-sections from 160 to 375 GeV/c”, *Nuclear Physics* **159** (1979) 56.
- [61] V. I. Telnov, “Scattering of Electrons on Thermal Radiation Photons in Electron-Positron Storage Rings”, *NIM A* **260** (1987) 304.

- [62] C. Bernardini, *Phys. Rev. Letters* **10** (1963) 407.
- [63] J. Le Duff, “Single and Multiple Touschek Effects”, in *Proceedings of CERN Accelerator School (CAS)*, Rhodes, Greece, 1993, v.I, pp. 573.
- [64] A. Wrulich, “Single-Beam Lifetime”, in *Proceedings of CERN Accelerator School (CAS)*, 1994, v.II, pp. 409.
- [65] A. Piwinski, “The Touschek Effect in Strong Focusing Storage Rings”, DESY-98-179, 1998.
- [66] F. Zimmermann, “Coherent Synchrotron Radiation and Touschek Scattering in the CLIC Damping Ring”, CLIC Seminar, 14 January 2005; see slides in <http://clic-meeting.web.cern.ch/clic-meeting/>.
- [67] F. Zimmermann and M. P. Zorzano, “Touschek Scattering in HERA and LHC”, LHC Project Note 244, 2000.
- [68] A. Piwinski, in *Proceedings of 9th International Conf. on High Energy Accel.*, pp. 405–409, SLAC, 1974.
- [69] J. D. Bjorken, and S. K. Mtingwa, “Intrabeam Scattering”, *Part. Accel.* **13** (1983) 115.
- [70] F. Zimmermann, “Intrabeam Scattering with Non-Ultrarelativistic Corrections and Vertical Dispersion for MAD-X”, CERN-AB-2006-002.
- [71] W. Herr, “Beam-Beam interactions”, in *Proceedings of CERN Accelerator School (CAS)*, DESY, Zeuthen, Germany, 2003. Edited by D. Brandt, CERN-2006-002.
- [72] J. Irwin, “Diffusive Losses from SSC Particles Bunches due to Long-Range Beam-Beam interactions”, SSC-233 (1989).
- [73] F. Zimmermann “Halo Formation due to Beam-Beam Interaction”, in *Proceedings of the 29th ICFA HALO’03 Workshop*, Montauk, Long Island, 2003; CERN-AB-2003-076 (ABP) (2003).
- [74] V. B. Berestetskii, E. M. Lifshitz, and L. P. Pitaevski, “Quantum Electrodynamics”, Pergamon Press, 1982.
- [75] S. I. Polityko, and V. G. Serbo, *Phys. Rev.* **E51**, 3, (1995) 2493; and “Coherent Bremsstrahlung at  $pp$  or  $p\bar{p}$  Colliders”, TPI-MINN-91/51-T (1991).
- [76] “Handbook of Accelerator Physics and Engineering”, Edited by A. Wu Chao, and M. Tigner, World Scientific, 1999, pp. 216-217.
- [77] S. Klein, “Localized Beampipe Heating due to e-Capture and Nuclear Excitation in Heavy Ion Colliders”, LBL-PUB-45566 (2000).

- [78] R. Hollebeek, Nucl. Instr. Methods **184** (1981) 333.
- [79] P. Chen, and K. Yokoya, Phys. Rev. D **38** (1988) 987.
- [80] R. J. Noble, Nucl. Instr. Methods A **256** (1987) 427.
- [81] M. Bell, and J. S. Bell, Part. Acc. **24** (1988) 1.
- [82] P. Chen, and K. Yokoya, Phys. Rev. Lett. **61** (1988) 2324.
- [83] D. Schulte, "Machine-Detector Interface at CLIC", CLIC Note 469 (2001); CERN/PS-2001-002 (AE) (2001).
- [84] D. Schulte, "Background at Future Linear Colliders", in *Proceedings of the Workshop on the Development of Future Linear Electron-Positron Colliders*, edited by G. Jarlskog, U. Mjörnmark and T. Sjöstrand, Lund, 1999, pp. 59-73 and CERN/PS 1999-066.
- [85] K. Yokoya, *et al.*, see <http://www-acc-theory.kek.jp/members/cain/>.
- [86] D. Schulte, *et al.* "Beam-Beam simulations with GUINEA-PIG", ICAP98, Monterey, CA., USA, 1998; CERN/PS/99-014-LP (1999).
- [87] S. Fartoukh, J. B. Jeanneret and J. Pancin, "Heat deposition by transient beam passage in spoilers", CERN-SL-2001-012 AP, CLIC Note 477, 2001.
- [88] X. E. Lin and D. H. Whittum, "Image current heating on a metal surface due to charged bunches", Phys. Rev. ST AB **3** (2000) 101001.
- [89] Milton Abramowitz and Irene A. Stegun, "Handbook of Mathematical Functions", Ed. National Bureau of Standards, Applied Mathematics Series-55, 1972.
- [90] R. H. Thomas, "Radiation effects and protection", in A. W. Chao, M. Tigner (Eds.), "Handbook of Acceleration Physics and Engineering", World Scientific (1999).
- [91] A. Fasso, *et al.*, "FLUKA: a multi-particle transport code", CERN-2005-10 (2005), INFN/TC-05/11, SLAC-R-773.
- [92] L. P. Keller, "Calculation of Muon Background in a 0.5 TeV Linear Collider", in *Proceedings of DPF Summer Study on High Energy Physics, Snowmass, Colorado, USA, 1990*.
- [93] H. Burkhardt, "Background in future linear  $e^+e^-$  colliders", CERN-SL-99-057 AP, CLIC Note 416 (1999).
- [94] H. Burkhardt, "Muon Background Simulations and Geant4", in *Proceedings of ICFA Nanobeam 2002 Workshop*, Lausanne, Switzerland, 2002.
- [95] J. D. Jackson, "Classical Electrodynamics", 2nd ed. (Wiley, 1975).

- [96] W. K. H. Panofsky, and W. A. Wenzel, "Some Considerations Concerning the Transverse Deflection of Charged Particles in Radio-Frequency Fields", *Rev. Sci. Instrum.* **27** (1956) 967.
- [97] G. V. Stupakov, "Geometrical Wake of a Smooth Taper", SLAC-PUB-95-7086 (1995).
- [98] K. F. L. Bane, and P. B. Wilson, "Longitudinal and Transverse Wake Potentials in SLAC", in *Proceedings of the 11th International Conference on High-Energy Accelerators*, Geneva, Switzerland, 1980, edited by W. S. Newman (Birkhäuser Verlag, Basel), pp. 592-596.
- [99] K. F. L. Bane, "Wakefield Effects in Linear Colliders", SLAC-PUB-4169.
- [100] K. Yokoya, "Impedance of Slowly Tapered Structures", CERN SL/90-88 (AP) (1990).
- [101] G. V. Stupakov, "Geometrical Wake of a Smooth Flat Collimator", SLAC-PUB-7167 (1996).
- [102] A. Piwinski, "Wake Fields and Ohmic Losses in Flat Vacuum Chambers", DESY HERA 92-04 (1992).
- [103] A. Piwinski, "Wake Fields and Ohmic Losses in Round Vacuum Chambers", DESY HERA 92-11 (1992).
- [104] A. Piwinski, "Impedances in Lossy Elliptical Vacuum Chambers", DESY-94 068 (1994).
- [105] I. Agapov, *et al.*, "BDSIM-Beamline Simulation Toolkit Based on Geant4", EUROTeV-Report-2006-035 (2006).
- [106] F. Jackson, "Collimation Optimization in the Beam Delivery System of the International Linear Collider", *Proceedings of EPAC2006*, Edinburgh, UK, June 2006.
- [107] M. Sands, "Emittance Growth from Radiation Fluctuations", SLAC/AP-47, December 1985.
- [108] R. .H. Helm, M. J. Lee, and P. .L. Morton, "Evaluation of Synchrotron Radiation Integrals", SLAC-PUB-1193, March 1973.
- [109] F. Tecker, *et al.* for the CLIC study team, "Updated CLIC Parameters 2005", CLIC Note 627; CERN-OPEN-2006-022 (2006).
- [110] F. Zimmermann, *et al.*, "Final-Focus Schemes for CLIC at 3 TeV", in *Proceedings of the 18th International Conference on High Energy Accelerators (HEACC2001)*, Tsukuba, Japan, CERN-SL-2001-010 AP; CLIC Note 476 (2001).
- [111] A. Drozhdin, *et al.*, "Comparison of the TESLA, NLC and CLIC Beam Delivery System Performance", 2002.

- [112] D. Schulte and F. Zimmermann, “Failure Modes in CLIC”, PAC2001, Chicago, USA, 2001, CLIC Note 492 (2001), and CERN-SL-2001-034 (AP) (2001).
- [113] H. Braun, “Parameters and the Costs of CLIC”, presentation in CLIC Parameter Away Day, 28-03-2006. See slides in:  
<http://indico.cern.ch/conferenceDisplay.py?confId=1607>.
- [114] H. Grote and F. C. Iselin, “The MAD Program, User’s Reference Manual”, CERN-SL-90-13 (AP) (1996); H. Grote and F. Schmidt, “MAD-X - An upgrade from MAD8”, CERN-AB-2003-024, ABP; see web site: <http://mad.home.cern.ch/mad/> and <http://frs.home.cern.ch/frs/Xdoc/mad-X.html>.
- [115] K. L. Brown, *et al.*, “TRANSPORT - A Computer Program for the Designing Charged Particle Beam Transport Systems”, CERN-80-04, Geneva (1980).
- [116] K. Hirata, “An introduction to SAD”, *Proc. Advanced ICFA Beam Dynamics Workshop, Lugano 1988*, CERN Yellow Report, pp.62-65; see work site: <http://acc-physics.kek.jp/SAD/sad.html>.
- [117] S. Redaelli, *et al.*, “Comparison of Simulation Tools for Beam Delivery System of linear Colliders”, *Proceedings of EPAC2002*, Paris, France, 2002; S. Redaelli, *et al.*, “Comparative Assessment of Simulations Tools for Beam Delivery Systems of linear Colliders”, NANOBEAM2002, Lausanne, Switzerland, 2002, CERN-AB-2003-072, CLIC Note 577 (2003).
- [118] T. Asaka and J. Resta López, “Characterization and Performance of the CLIC Beam Delivery System with SAD, MAD and Placet”, CLIC-Note-637, CERN-OPEN-2005-019 (2005).
- [119] D. Schulte *et al.*, “Simulation Package based on PLACET”, PAC2001, Chicago (2001); CERN/PS 2001-028 (AE), CLIC Note 482 (2001) see web site: <http://dschulte.home.cern.ch/dschulte/placet.html>.
- [120] K. Ohmi, *et al.*, Phys. Rev. E **49** (1994) 751.
- [121] F. Barbarin, F. C. Iselin and J. M. Jowett, “Particle dynamics in LEP at very high-energy”, *Proceedings of EPAC94*, London, England.
- [122] H. Burkhardt, private communication (2005).
- [123] D. Schulte, *et al.*, “CLIC Simulations from the Start of the Linac to the IP”, *Proceedings of EPAC2002*, Paris, France (2002).
- [124] H. Burkhardt, “Monte Carlo Generator for Synchrotron Radiation”, LEP Note 632, CERN, Geneva, 1990.

- [125] R. Tomás, “MAPCLASS:a code to optimize high order aberrations”, CERN-AB-Note-2006-017.
- [126] R. Tomás, “Non-Linear Optimization of Beam Lines”, Phys. Rev. ST AB9 (2006) 081001, CLIC Note 659.
- [127] F. Schmidt, “MAD-X PTC Integration”, *Proceedings of the PAC2005*, Knoxville, USA, pp. 1272.
- [128] G. A. Blair, H. Burkhardt and H. J. Schreiber, “Background simulation for the CLIC Beam Delivery System with Geant”, CERN-SL-2002-029 (AP), CLIC Note 519.
- [129] G. Rumolo and A. Latina, “Effects of Wake Fields in the CLIC BDS”, *Proceedings of EPAC2006*, Edinburgh, UK, June 2006.
- [130] A. Latina *et al.*, “Recent Improvements of PLACET”, CERN-AB-2006-048.
- [131] A. Bertarelli, *et al.*, “The mechanical design for the LHC collimators”, in *Proceedings of EPAC04*, Lucerne, Switzerland, 2004; A. Bertarelli, *et al.*, “Mechanical design for robustness of the LHC collimators”, in *Proceedings of PAC05*, Knoxville, USA, 2005.
- [132] B. Goddard, *et al.*, “Protection of the LHC against unsynchronised beam aborts”, in *Proceedings of EPAC06*, Edinburgh, Scotland, UK, 2006.
- [133] J. B. Jeanneret and E. Metral, “Operational constraints in the LHC due to collimation”, LHC Project Workshop-’Chamonix XIII’ (2004).
- [134] E. Metral, R&D and LHC Collective Effects (RLC) Meeting, 21.04.06, see web site: [http://ab-abp-rlc.web.cern.ch/ab-abp-rlc/Meetings/2006/2006.04.21/CBI&SBIAtLHCInjection&TopEnergy\\_RLC\\_21-04-06.pdf](http://ab-abp-rlc.web.cern.ch/ab-abp-rlc/Meetings/2006/2006.04.21/CBI&SBIAtLHCInjection&TopEnergy_RLC_21-04-06.pdf).
- [135] R. Tomás, *et al.*, “CLIC Final Focus Studies”, *Proceedings of EPAC06*, Edinburgh, 2006.
- [136] P. Emma, *et al.*, “Nonlinear Resonant Collimation for Future Linear Colliders”, SLAC-PUB-7958 (1998).
- [137] A. Faus-Golfe, J. Resta-Lopez and F. Zimmermann, “Non-linear Collimation in Linear and Circular Colliders”, *Proceedings of EPAC2006*, Edinburgh, 2006.
- [138] J. Resta Lopez, A. Faus-Golfe, and F. Zimmermann, “Optics design for a nonlinear collimation system in the LHC”, *Proceedings of the HHH2004*, Geneva, Switzerland, 2004.
- [139] J. Resta, *et al.*, “Exploring a Nonlinear Collimation System for the LHC”, *Proceedings of PAC2005*, Knoxville, USA, 2005; CERN-LHC-PROJECT-REPORT-842, 2005.
- [140] J. Resta Lopez, *et al.*, “An Alternative Nonlinear Collimation System for the LHC”, *Proceedings of EPAC2006*, Edinburgh, 2006; CERN-LHC-PROJECT-REPORT-939, 2006.

- [141] R. W. Assmann, private communication.
- [142] V. Vlachoudis, see slides at  
[http://www.cern.ch/lhc-collimation/files/VVlachoudis\\_06Feb2004.pdf](http://www.cern.ch/lhc-collimation/files/VVlachoudis_06Feb2004.pdf).
- [143] J. B. Jeanneret *et al.*, “Beam loss and collimation at LHC,” Proceedings of Beam Halo Dynamics Diagnostics, and Collimation, AIP 2003.
- [144] S. Redaelli *et al.*, “LHC Aperture and Commissioning of the Collimation System,” Chamonix XIV (2005).
- [145] G. Ripken and F. Schmidt, CERN SL 95-12 (AP)(1995) and DESY 95-063 (1995).
- [146] A. Burov and V. Lebedev, “Transverse resistive wall impedance for multi-layer flat chambers,” EPAC2002, Paris, 2002; FERMILAB-CONF-02-101, June 2002.
- [147] A. Burov and V. Lebedev, “Transverse resistive wall impedance for multi-layer round chambers,” EPAC2002, Paris, 2002; FERMILAB-CONF-02-100, June 2002.
- [148] A. W. Chao, “Physics of Collective Beam Instabilities in High Energy Accelerators,” J. Wiley & Sons, Inc, 1993.
- [149] S. Wolfram, “Mathematica,” Addison-Wesley, 1991.
- [150] H. G. Hereward, “Landau Damping,” Proceedings of International School of Particle Accelerators, CERN 77-13, p. 219-230, Geneva, 1977; A. Hofmann, “Landau Damping,” CERN Accelerator School (CAS), p. 271-304, Zeuthen, Germany, 2003.
- [151] J. Scott Berg and F. Ruggiero, “Landau damping with two dimensional betatron tune spread,” CERN SL-AP-96-71 (AP), 1996.
- [152] S. Redaelli, R. Assmann, and G. Robert-Demolaize, “LHC Aperture and Commissioning of the Collimation System”, in *Proceedings of LHC Project Workshop—Chamonix XIV*, pp. 268, 2005.
- [153] R. Tomás, “Direct Measurement of Resonance Driving Terms in the Super Proton Synchrotron (SPS) of CERN using Beam Position Monitors”, PhD Thesis, Valencia University, January 2003.
- [154] RtPlot – Real Time Plotting Utility, see the web:  
<http://members.surfbest.net/dbai@surfbest.net/RtPlot/>.
- [155] K. Brown, “A First- and Second- order matrix Theory for the Design of Beam Transport Systems and Charged particles Spectrometers”, SLAC-PUB-3381, July 1984.
- [156] H. Goldstein, “Classical Mechanics”, Addison-Wesley, 1980.



- [157] A. J. Dragt, *et al.*, Ann. Rev. Nucl. Part. Sci **38** (1988) 445.
- [158] A. J. Dragt and J. M. Finn, J. Math. Phys. **17** (1976) 2215.
- [159] G. J. Roy, "Analysis of the Optics of the Final Focus Test Beam using Lie Algebra Based Techniques", SLAC-397, Ph. D. Thesis, Sep. 1992.
- [160] A. J. Dragt and E. Forest, "Computation of Nonlinear Behavior of Hamiltonian Systems using Lie Algebraic Methods", J. Math **24** (1983) p. 2734.
- [161] E. Forest, "Beam Dynamics: A New Attitude and Framework", Harwood Academic (1998).
- [162] K. Yokoya, Part. Acc., **41**, 221 (1993).
- [163] F. Sacherer, "Single beam collective phenomena-transverse (bunched beams)," Proceedings of First Course International School on Accelerators, Erice, 1976; Theoretical Aspects of the Behaviour of Beams in Accelerators and Storage Rings, CERN 77-13, p. 210, 1977.
- [164] F. Ruggiero, LHC Collective Effects (LCE) Meeting, 03.10.06, see web site: <http://ab-abp-rlc.web.cern.ch/ab%2Dabp%2Drlc/Meetings/2003/2003.10.03/TensorImpedanceFR.pdf>.



## Acknowledgments

I would like to express my gratitude to the European Organization for Nuclear Research (CERN), where my work has been carried out, for the financial support. This work has also been made possible by the constant support from the Instituto de Física Corpuscular (Centro Mixto Universidad de Valencia – CSIC).

In particular I would like to sincerely acknowledge Dr. Ángeles Faus Golfe, Dr. Daniel Schulte and Dr. Frank Zimmermann for their continuous interest, support and supervision, making this work possible. I have taken a lot of profit from their wide experience and knowledge.

I would like to acknowledge the members of the LHC Collimation Group. In particular, I would like to thank Dr. Ralph Assmann, Dr. Stefano Redaelli and Dr. Guillaume Robert-Demolaize for providing me with the tracking code `Sixtrack`, and for very fruitful discussions and suggestions. I would also like to thank Dr. Rogelio Tomás for providing me with the optimization code `MAPCLASS`. They made possible the first experimental test on nonlinear collimation.

I would like to thank all my colleagues from the CLIC Beam Dynamics Group for many useful discussions. In particular I would like to thank Helmut Burkhardt and Lionel Neukermans for discussions and advice on beam halo and tail generation.

Special thanks to Dr. Takao Asaka, for his fruitful collaboration and for many coffee discussions.

Many thanks to Dr. Andrea Latina and Dr. Giovanni Rumolo for providing me with the last version of `Placet`, which includes the collimator wakefields effects.

Many and special thanks to my friends and colleagues Peder Eliasson and Tatiana Pieloni, who were my officemates during all my doctoral period, for their support and for many happy moments.

Thanks to my friend and colleague Matteo Magistris for supplying me some collimator information, and for many good conversations about music and musicians.

I would like to have a special mention to Dr. Francesco Ruggiero, who always supported students at CERN.

Un profundo agradecimiento va dirigido a mis padres, quienes me apoyan incondicionalmente en todo momento. También quisiera añadir un agradecimiento especial para Nerina por todo su apoyo, inestimable ayuda y paciencia.

